

©2017

KATHERINE KOH

ALL RIGHTS RESERVED

DESIGN AND SYNTHESIS OF NANOCATALYSTS ENABLING HYDROGEN  
STORAGE, RELEASE AND ELECTROCATALYSIS

By

KATHERINE KOH

A dissertation submitted to the  
Graduate School-New Brunswick  
Rutgers, The State University of New Jersey

In partial fulfillment of the requirements

For the degree of

Doctor of Philosophy

Graduate Program in Chemistry and Chemical Biology

Written under the direction of

Tewodros Asefa

And approved by

---

---

---

---

New Brunswick, New Jersey

October, 2017

## ABSTRACT OF THE DISSERTATION

### DESIGN AND SYNTHESIS OF NANOCATALYSTS ENABLING HYDROGEN STORAGE, RELEASE AND ELECTROCATALYSIS

by KATHERINE KOH

Dissertation Director:

Prof. Dr. Tewodros Asefa

In light of the given limited available energy resources and the constant increase in energy consumption and demand worldwide, the development of sustainable alternative energy sources has never become more vital. Among the conceivable renewable energy choices, hydrogen has been considered as one of the most promising energy carrier especially in the fuel-cell technology. Based on the concept of “hydrogen economy”, as coined by Bockris in 1970,<sup>1</sup> efficient storage, large-scale production and convenient distribution of hydrogen are of the utmost importance for successful utilization of this energy carrier. One of the most promising strategies to achieve the sustainable hydrogen carriers is through the hydrogenation/dehydrogenation interconversion reactions involving substances such as formic acid ( $\text{H}_2 + \text{CO}_2 \rightleftharpoons \text{HCOOH}$ ) or formate ( $\text{HCO}_2^- + \text{H}_2\text{O} \rightleftharpoons \text{HCO}_3^- + \text{H}_2$ ).<sup>2</sup> Other reactions that are also important for fuel cell applications are the hydrazine oxidation (HOR), oxygen reduction reaction (ORR), or hydrogen evolution reaction (HER). In this thesis, I

reported the design and synthesis of various nanocatalysts for several important fuel cell applications including formic acid dehydrogenation, formate/bicarbonate reversible cycle, and hydrazine oxidation reaction (HOR).

In chapter 2, I have developed a facile synthetic route to amine-functionalized nanoporous silica-supported ultrasmall Pd nanoparticles (Pd/SBA-15-Amine) that are proven to be highly active catalysts for formic acid dehydrogenation, producing hydrogen at ambient temperature with a high turn-over-frequency (TOF). The TOF values reported for the materials therein are among the highest TOFs ever reported for the reaction. I have also shown that the catalyst could be easily recyclable multiple times, without losing their catalytic activity. The catalyst may, therefore, contribute to some of the solutions of our current renewable energy and sustainability challenges (by enabling the so-called hydrogen economy).

In chapter 3, I have synthesized new types of palladium nanoparticles (Pd NPs) supported on amine-functionalized SBA-15, which have high catalytic activity for formic acid dehydrogenation. In this case, I have also demonstrated the synthesis of SBA-15 mesoporous silica materials grafted with three different amine groups (primary, secondary, and tertiary amine) and the interactions between the Pd NPs and the grafted amine groups to create favorable synergistic catalytic effects toward the reaction. The effects of the different amine types, their grafted density on the chemical and catalytic activities of the supported Pd NPs in formic acid dehydrogenation are then thoroughly investigated using various state-of-the-art characterization techniques. The study has also allowed some understanding of structure-catalytic activity relationship of such catalytic materials.

In chapter 4, the formate and bicarbonate reversible reactions are discussed.

Those reversible cycle can be used to store, release and allow hydrogen (H<sub>2</sub>) to serve as an effective energy carrier in energy systems such as fuel cells. However, to feasibly utilize these reactions for renewable energy applications, efficient catalysts are necessary to promote the formate-bicarbonate reversible reactions. I have reported the synthesis of novel polyaniline (PANI)-derived mesoporous carbon-supported Pd NPs that can efficiently catalyze these reversible reactions. The resulting nanomaterials has been shown efficiently catalyze both reactions, i.e., the dehydrogenation of formate ( $\text{HCO}_2^- + \text{H}_2\text{O} \rightarrow \text{H}_2 + \text{HCO}_3^-$ ) and the hydrogenation of bicarbonate ( $\text{H}_2 + \text{HCO}_3^- \rightarrow \text{H}_2\text{O} + \text{HCO}_2^-$ ). The study further revealed that having an optimum density of N dopant species in the catalysts could improve Pd's catalytic activity toward both reactions. Among the different materials studied here, the one synthesized at 800 °C with relatively high amount of colloidal silica templates gave the best catalytic activity and these TOF and TON values are among the highest reported for heterogeneous catalysts for these reversible reactions so far.

Lastly, nitrogen and oxygen co-doped metal-free, rice-derived mesoporous carbons (RDMCs) have been successfully synthesized by a combination of three synthetic processes: *i*) a low temperature hydrothermal treatment (HTC), *ii*) followed by a high pyrolysis temperature in presence of colloidal silica templates and *iii*) finally removal of the silica templates from the carbonized products. The obtained mesoporous carbons effectively electro-catalyzed the hydrazine oxidation reaction (HOR) with negative onset and/or peak potentials and high peak current densities, and show long-term stability. By optimizing the synthetic parameters, such as the amount of colloidal silica templates and pyrolysis temperatures used for the synthesis, RDMCs possessing the high electrocatalytic performances have been obtained. It has also been found that

the catalytic activities of the materials would depend on the BET surface area and amount of dopants in the materials. The material pyrolyzed at 800 °C along with hydrothermal reaction with moderate silica amount, in particular, gave the best activity toward hydrazine electrooxidation.

#### Reference

1. Bockris, J. O. *Science* **1972**, *176*, 1323-1323.
2. Grasmann, M.; Laurenczy, G. *Energy Environ. Sci.* **2012**, *5*, 8171-8181.

## **DEDICATIONS**

Dedicated to my parents,

**Seok Keun Koh and Mi Hwa Choo.**

Brother, **Jay Koh.**

My lovely doggy, **Cherry (Bbuzzy).**

## ACKNOWLEDGEMENTS

I thank God for giving me this opportunity and joyful moments with good advisor and friends. I've learned not only about research but also how to enjoy research from Dr. Tewodros Asefa, and I want to express my sincere thank you to such a great research and life advisor.

I also thank to my committee members, Dr. Jing Li and Dr. Deirdre O'Carroll for having the time to review and give insightful advice on my research proposals, thesis, and yearly progress reports. I also extend a big thank to our sister lab's advisor and my outside committee member, Dr. Manish Chhowalla, for his support.

I appreciate my previous advisors and good collaborators, Dr. Chang Won Yoon and Dr. Suk Woo Nam, in South Korea for their valuable advice and support during our collaborations. I've also learned and received a lot of valuable help from Dr. Yoon and his group members: Dr. Mina Jeon, Dr. Jin Hee Lee, and Yong Min Kim.

Moreover, I really appreciate my precious group members who fully supported and encouraged me every moment of research career at Rutgers, especially Dr. Taís Larissa Silva and Dr. Heveline Follmann. I also acknowledge our previous group members including Dr. Anandarup Goswami, Dr. Rafael Silva, Dr. Xiaoxi Huang, Dr. Yuying Meng, Dr. Vitor C. Almeida, and present research members, particularly Tao Zhang and Viktor Dubovoy. I also thank Dr. Damien Voiry, Dr. Xingquan (Andy) He, Weiming (Isabella) Wang, Jonathan Colón for their helps and supports. I would like to give special thanks and express my love to my best friend, Pamela (Dr. Jieun Yang), for all her advice and kindly support.

Finally, I want to express much thanks to Choo's family, Koh's family, and my best friends (Julia and Hanna) for their continuous love and help.

## TABLE OF CONTENTS

ABSTRACT OF DISSERTATION.....	ii
DEDICATION.....	vi
ACKNOWLEDGEMENT.....	vii
TABLE OF CONTENTS.....	ix

### CHAPTER 1

#### *Introduction to Nanocatalysis and Their Applications in Renewable Energy*

1.1. Introduction to chemical hydrogen storage.....	1
1.2. Introduction to fuel cells.....	4
1.3. Nanocatalysts.....	6
1.4. Mesoporous silica .....	11
1.5. Mesoporous carbon.....	16
1.6. Palladium nanocatalyst.....	20
1.7. Summary and outlook.....	24
1.8. Reference.....	26

### CHAPTER 2

#### *Ultrasmall Palladium Nanoparticles (Pd NPs) Supported on Amine-Functionalized SBA-15 Efficiently Catalyze Hydrogen Evolution from Formic Acid*

2.1. Overview.....	28
2.2. Introduction.....	29
2.3. Experimental section.....	31
2.4. Result and discussion.....	36
2.5. Conclusion.....	49

2.6. Reference.....	50
---------------------	----

### CHAPTER 3

#### *Formic Acid Dehydrogenation over Palladium Nanoparticles (Pd NPs) Supported on Amine Functionalized SBA-15s: Structure-Activity Relationships*

3.1. Overview.....	52
3.2. Introduction.....	53
3.3. Experimental section.....	57
3.4. Result and discussion.....	64
3.5. Conclusion.....	94
3.6. Reference.....	95

### CHAPTER 4

#### *Novel Nanoporous N-doped Carbon-supported Ultrasmall Pd Nanoparticles: Efficient Catalysts for Hydrogen Storage and Release*

4.1. Overview.....	97
4.2. Introduction.....	98
4.3. Experimental section.....	101
4.4. Result and discussion.....	107
4.5. Conclusion.....	136
4.6. Reference.....	137

### CHAPTER 5.

#### *N- and O-Doped Mesoporous Carbons Derived from Rice Grains: Efficient Metal-Free Electrocatalysts for Hydrazine Oxidation*

5.1. Overview.....	139
5.2. Introduction.....	140

5.3. Experimental section.....	144
5.4. Result and discussion.....	149
5.5. Conclusion.....	176
5.6. Reference.....	177
CHAPTER 6.	
Conclusions and Perspectives.....	179
Appendix.....	183

## Chapter 1

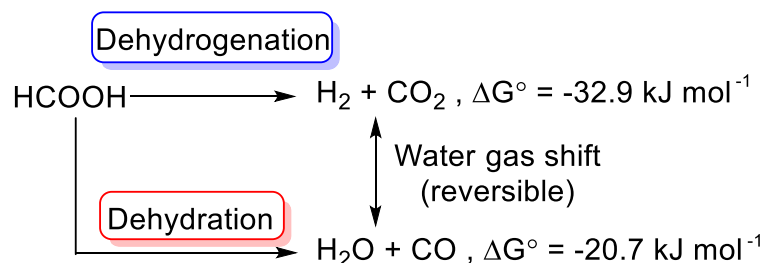
# Introduction to Nanocatalysis and Their Applications in Renewable Energy

### 1.1. Introduction to chemical hydrogen storage

The demands for sustainable and renewable energy sources have been increasingly rising, as the issues associated with the negative environmental impacts from fossil fuels have also been growing. One of alternative and ideal solution to meet these problems is hydrogen.<sup>1</sup> Hydrogen is considered as promising energy source because it generates electricity through a fuel cell, in clean and renewable manner by producing only water as a byproduct. Research efforts to consume and apply hydrogen in the fuel cell systems have been devoted and well developed so far; however, delivering and storing hydrogen is still tacking.<sup>2</sup> In these days, most common methods to deliver hydrogen are either in the form of cryogenic liquid hydrogen or compressed hydrogen, which are expensive to be commercialized and still pose major safety issues. In this regard, based on the concept of hydrogen economy,<sup>3</sup> developing efficient and safe storage has been placed as a main issue to become a practical and sustainable fuel cell. Several attractive alternatives to store and deliver hydrogen in a safe and efficient manner have been developed by using metal hydrides, complex hydrides, sorbent, or chemical hydrides. Among them, chemical hydrides have been received great attention because such systems, especially liquid phase hydrogen, can easily be transported, stored, and refilled and release hydrogen under mild condition when it is needed. Liquid

phase hydrogen storage media include ammonia borane ( $\text{NH}_3\text{BH}_3$ ), borohydrides ( $\text{NaBH}_4$ ), hydrazine ( $\text{N}_2\text{H}_4$ ), formic acid ( $\text{HCOOH}$ ) or formate ( $\text{HCOO}^-$ ).

Formic acid (FA) is considered as one of the promising chemical hydrogen storage systems because of its high volumetric density (4.4 wt.%), which is suitable for Department of Energy (DOE) 2017 onboard target.<sup>2</sup> Moreover, FA has several interesting and advantageous properties than many other chemical hydrogen storage systems. When FA is heated, it produces carbon monoxide and water (*Dehydration pathway* in **Scheme 1.1**). However, upon exposure to catalysts, FA can decompose to hydrogen and carbon dioxide (*Dehydrogenation pathway* in **Scheme 1.1**). Although it must be handled safely, unlike more traditional fuels, FA is not flammable in 85 % concentration. It is also generally non-toxic so FA is also considered a carbon neutral, renewable energy source, and can be obtained by aqueous catalytic partial oxidation of wet biomass.



**Scheme 1.1.** Two pathways of FA decomposition.

However, FA has some issues as well. First and foremost, FA does not exist naturally, and it has to be derived from somewhere. Currently, FA processes are mainly from two routes: via methyl formate hydrolysis, or free FA from formate.<sup>4</sup> although recent developments indicate it can be made from biomass via the Fischer-Tropsch

process and CO<sub>2</sub> hydrogenation, possibly using solar-fuel hydrogen.<sup>5</sup> If these can be realized, they will constitute renewable and sustainable sources for FA and it requires good and sustainable catalysts to have FA release hydrogen on it.

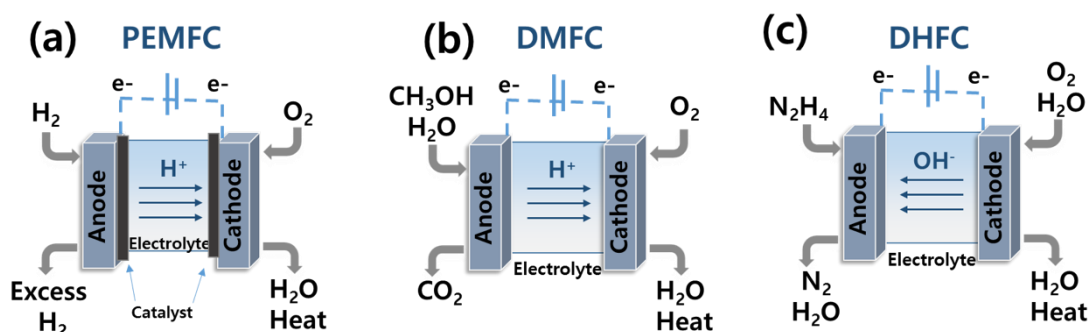
FA can undergo two possible decomposition pathways (**Scheme 1.1**). One produces H<sub>2</sub> and CO<sub>2</sub>, which is a desired process to generate H<sub>2</sub> from FA as discussed above. The second one is decarbonylation, or sometimes also referred to as dehydration process, and it produces H<sub>2</sub>O and CO (**Scheme 1.1**). However, this process is undesired during usage of FA as a fuel, because it forms H<sub>2</sub>O rather than the desired H<sub>2</sub>. Furthermore, the CO can lead to poisoning of catalysts, both of catalysts used for the reaction as well as in the fuel cells during formic acid's uses in the fuel cells. To utilize FA as a hydrogen storage and release media, catalysts that facilitate and selectively promote the first desired reaction ( $\text{HCOOH} \rightarrow \text{H}_2 + \text{CO}_2$ ) are among the major requirements. Similarly, catalysts that allow the production of FA, especially from CO<sub>2</sub>, and capable of promoting the reverse reaction are necessary. The CO<sub>2</sub> for the reversible reaction could be taken from that generated by many various power plants.

To be an ideal hydrogen carrier for FA/CO<sub>2</sub> system, the back-reaction from carbon dioxide to FA ( $\text{H}_2 + \text{CO}_2 \rightarrow \text{HCOOH}$ ) should be achieved but trapping and using the gaseous carbon dioxide product during FA dehydrogenation has not been developed yet.<sup>6</sup> To overcome this, the formate/bicarbonate system was introduced to meet a rechargeable hydrogen storage. Compared to carbon dioxide, bicarbonate species are more easy to handle and soluble in aqueous media (NaHCO<sub>3</sub>, 96 g/L at 20 °C in H<sub>2</sub>O). Moreover, formate is also a stable and nontoxic neutral compound with hydrogen content of 2.4 wt. % (based on NaHCO<sub>2</sub>/H<sub>2</sub>O). So, some researchers have focused on

formate/bicarbonate reversible system and investigated the potential of this reversible reaction to store and release hydrogen on demand in presence of suitable catalysts.

## 1.2. Introduction to fuel cells

In various fuel cells, many substances such as hydrogen, methanol, ethanol, hydrazine, low molecular weight hydrocarbon etc. have been applied as a fuel.<sup>7</sup> For example, proton exchange membrane fuel cell (PEMFC, **Scheme 1.2a**) is most commonly used at room temperature but it requires the expensive noble metal catalysis such as Pt catalysts, which can easily be poisoned by carbon monoxide.

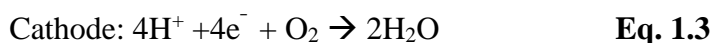
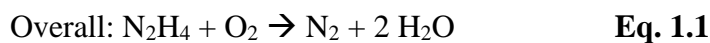


**Scheme 1.2.** Diagram of (a) proton exchange membrane fuel cell (PEMFC), (b) direct methanol fuel cell (DMFC), and (c) direct hydrazine fuel cell (DHFC).

Besides hydrogen based PEMFC, direct fuel cells (DFCs) have been interested because of using a liquid or vapor form of fuel directly without any reforming step.<sup>7d</sup> Among different types of DFCs, methanol has received attention as a candidate fuel due to its higher energy density (~20 MJ/kg) and because it can be regenerated from sources such as natural gas, coal, or biomass. However, there are several disadvantages in utilization of methanol as a fuel in direct methanol fuel cell (DMFC). Methanol is

toxic and DMFC still suffers from low efficiency due to adsorbed CO intermediate, which makes the reaction to require high potential to take place.

Hydrazine ( $\text{N}_2\text{H}_4$ ) can be a promising fuel among the series of DFCs because hydrazine 1) is less costly and less toxic, 2) has no carbon atoms and does not form CO poison, 3) can be easily generated from mass production of ammonia and decomposed to  $\text{N}_2$  and water, which is environmentally free and 4) it consists of high theoretical electromotive force value of 1.56 V, followed by **Eq. 1.1-1.3**.<sup>7</sup>



Recent research efforts to sustainable and inexpensive material to catalyze hydrazine oxidation reaction and several novel metals such Au, Pd, Ag, etc., few of non-metals including Fe, or Ni, and metal-free carbon materials of polypyrrole derive mesoporous carbon have been developed.<sup>7c</sup> However, the demand for developing sustainable and finding most efficient catalyst is still required for DHFC.

### 1.3. Nanocatalysts

Catalysts have been generally used as dependent source in nature, industry, and in our life. The catalysts can be defined as transforming from fine chemicals into value-added chemicals or synthetic chemicals with efficient ways: 1) giving fewer un-wanted byproduct, 2) lower energy consumption and 3) obtaining the desired products in larger amount with short time.<sup>8</sup> Moreover, the catalysts often contribute to solve environmental problems, i.e., destruction of pollutants through catalytic converters, so called three-way catalyst (TWC) on the exhaust system in the vehicles. Besides these applications, more importantly, catalysts are being developed for the production of renewable energy and reducing of limited fossil fuel resources.

Two different criteria—homogenous (substrate presents in same phase) and heterogeneous (substrate presents in the different phase) catalysts have been developed although their objectives are same: Obtaining a better catalytic performance. The homogenous catalysts have been considered as attractive materials due to their high activity and superior selectivity toward formation of a desired product but their recovery and recyclability are still having difficulties. On the other hand, heterogeneous catalysts have significant advantage over homogeneous catalysts, which is relatively easier to handle, separate from reaction mixture and reuse, although their activity and selectivity are often limited than homogenous catalysts. Interestingly, development of the nanoscience, which dwells on the 1- 100 nm ranged materials has the unique and fascinating properties. Moreover, this nanocatalysts have been placed at the interface between homogenous and heterogeneous catalyst divisions with possessing both

benefits of them, containing excellent catalytic activity, selectivity, stability as well as ease of separation/recycling.

### ***1.3.1. Catalysis for formic acid and its related chemical hydrogen***

The first work on the decomposition of formic acid generating hydrogen was reported in the late 1960 using iridium phosphine complex as homogeneous catalyst at relatively high temperature. Following this work, several other research groups demonstrated similar reactions using other catalysts using noble metals such as Ru, Rh or Ir. e.g.,  $\text{RuCl}_2(\text{PPh})_3$ ,<sup>9</sup>  $[\{\text{RuCl}_2(\text{benzene})\}_2]$ <sup>10</sup> and  $\text{RuBr}_3 \cdot \text{H}_2\text{O}$ ,<sup>11</sup> in the presence of different amines and different phosphine ligands.<sup>2</sup> More recently, besides non noble metal-based catalysis, non-noble metal ones that can give high efficiency for such recyclable reactions have been pursued. These materials are actually more preferable if they can be made to have good activity and selectivity in the reactions. In this context, Boddien et al. firstly demonstrated iron-based homogenous catalyst,  $\text{Fe}(\text{BF}_4)_2 \cdot 6\text{H}_2\text{O}$  with additive of 4 eq. of  $[\text{P}(\text{CH}_2\text{CH}_2\text{PPh}_2)_3, \text{PP}_3]$  and showed a TOF of  $9425 \text{ h}^{-1}$ .<sup>12</sup>

As mentioned above, homogeneous catalysts usually give excellent catalytic activity, but their recovery is hard. On the other hand, many heterogeneous catalysts for FA dehydrogenation including nanostructured metallic systems have recently been found to have good catalytic activity, some rivaling those of homogenous catalysts, while being more easily recyclable. Most heterogeneous catalyst systems involve metallic nanoparticles supported on stable nanostructured support materials. For example, Solymosi et al. examined vapor-phase catalytic decomposition of FA on several transition metals, such as Ir, Pt, Pd, Ru, and Rh. Only Ir catalysts showed the best catalytic activity and selectivity at 383-473 K.<sup>13</sup> Ojeda et al. studied Au-based

catalysts and proved that catalytic activities of the materials were dependent on the metal's particle size ( $<5$  nm).<sup>14</sup> Furthermore, they showed that Au/Al<sub>2</sub>O<sub>3</sub> shows better catalytic activity than Pt/Al<sub>2</sub>O<sub>3</sub> catalysts at 343-383 K, which was opposite direction from previous studies. Compared with gas based reaction, liquid based reaction is more favorable because the former needs higher temperature and inert carrier gas. Several research works devoted to increase catalytic activity of the materials in liquid phase reaction, and Pd and Pd based catalysts have been particularly found to be among most active and suitable catalysts in terms of selectivity and conversion for such reactions.<sup>19</sup>

Although the exact roles and key factors of secondary metal in Pd based alloy catalysts are not clarified and still being debated, several Pd alloy catalysts including AuPd<sup>15</sup> and AgPd<sup>16</sup> have showed enhanced activity and selectivity than pure metals. For examples, AuPd showed a higher turnover frequency (TOF) of 230 h<sup>-1</sup> than Pd (TOF value of 30 h<sup>-1</sup>) or Au (TOF value of 80 h<sup>-1</sup>),<sup>15c</sup> and AgPd-NH<sub>2</sub>-SBA-15 showed enhanced TOF of 1555 h<sup>-1</sup> than Pd/NH<sub>2</sub>-SBA-15 (TOF of 293 h<sup>-1</sup>) or Ag/NH<sub>2</sub>-SBA-15 (no reaction) itself, too.<sup>16</sup> Few experimental and computational studies were conducted to understand the relationship between structure and catalysis. Mullin et al. verified that the geometrical (ensemble) effect through distinct surface atomic arrangement on the Au(111) surface is an important factor for both the reactivity and selectivity of the catalysts. However, Lee et al.<sup>15a</sup> demonstrated the roles of PdAu alloys for facilitating FA dehydrogenation arise from both ensemble effects and ligand effects. Furthermore, Hu et al.<sup>17</sup> also showed that the enhanced catalytic activity by PdAg bimetallic catalysts is due to both geometric and electronic effects. Besides alloy catalysts, several core-shell nanocatalysts have been developed. Tsang's group<sup>18</sup> studied several different metal cores such as Ru, Rh, Pt, Ag, Au and Pd shell They found that Ag-Pd core-shell

structure has better catalytic activity than AgPd alloy due to strong electronic promotion from Ag (core) to Pd (shell), which is ligand effect.

One of drawbacks in most of mono- and multi-metallic catalysts is that they often require bases or additives for FA dehydrogenation, which are however difficult to separate after the reactions. To overcome this issue, strongly metal-support interacted Pd based catalysts have been developed under ambient temperatures without any additives at room temperature. Lee et al.<sup>19</sup> demonstrated Pd catalyst supported on mesoporous graphitic carbon nitride (Pd/mpg-C<sub>3</sub>N<sub>4</sub>) catalyzes the decomposition of formic acid with TOF of 144 h<sup>-1</sup>. Due to Lewis basic sites located at mpg-C<sub>3</sub>N<sub>4</sub>, electron density is transferred from the nitrogen atoms to Pd NPs, stabilizing the Pd NPs as well as synergistically initiating the decomposition of formic acid (**Figure 1.1**). Another seminal work was demonstrated for Pd NPs supported on amine functionalized SBA-15 mesoporous silica (detail in Chapter 2), in which the amine functional groups stabilized Pd NPs and also resulted in charge transfer from amine functional groups to Pd NPs. This gave the material a high catalytic activity (TOF of 293 h<sup>-1</sup>).<sup>20</sup> Moreover, the materials showed better activity than Pd catalysts with external bases (Pd/SBA-15 with n-propylamine).

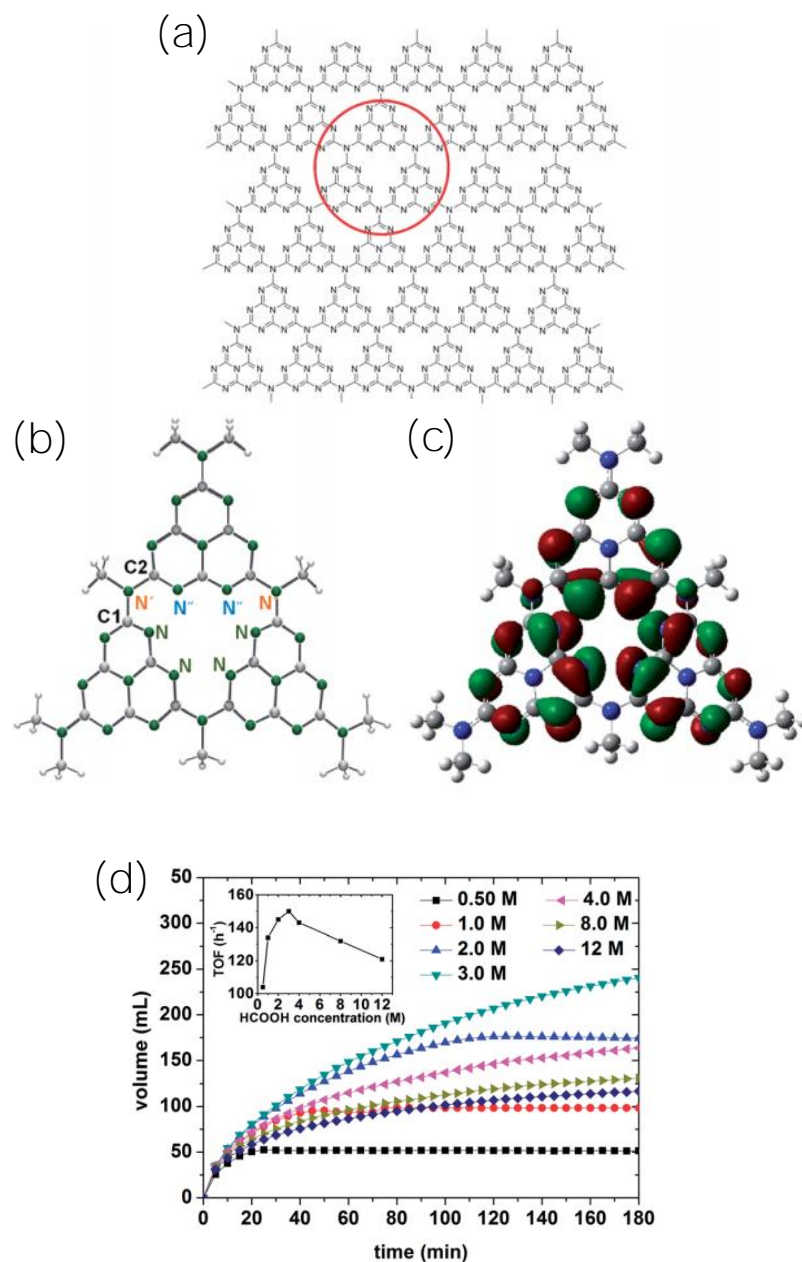
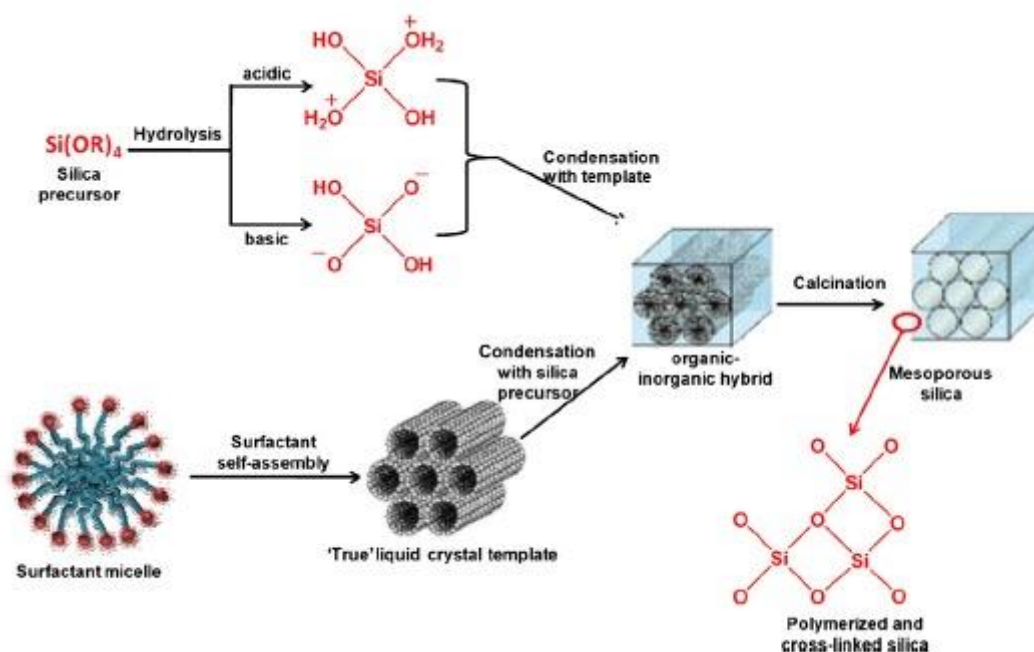


**Figure 1.1.** (a) Molecular structure of graphitic carbon nitride (mpg-C<sub>3</sub>N<sub>4</sub>), (b) DFT-optimized structure, (c) the calculated HOMOs of mpg-C<sub>3</sub>N<sub>4</sub>, and their catalytic activity for formic acid dehydrogenation after loading Pd NPs (Pd/mpg-C<sub>3</sub>N<sub>4</sub>). Reproduction from reference. <sup>15a</sup>

## 1.4. Mesoporous Silica (Soft Template Method)

### 1.4.1. Synthesis of mesoporous silica

Due to their high surface area ( $>600 \text{ m}^2/\text{g}$ ), narrow pore size distribution, tunable pore size (1.5-10 nm), and high thermal stability, mesoporous materials have been considered as suitable inorganic nanomaterial to support catalytic group or host bioactive guest molecules.<sup>21</sup> Synthesis of mesoporous materials are preferably achieved by supramolecular assembly of surfactant (S) and inorganic (I) sol-gel precursors. In briefly, self-assembly undergoes through the hydrolysis and condensation of silica precursors (e.g., tetraethoxysilane or tetraethyl orthosilicate (TEOS)) in presence of surfactant templates at aqueous solution (soft template method). Followed by removal of surfactant templates via calcination at air above  $350 \text{ }^\circ\text{C}$  or solvent extraction with acidic or organic solution, the mesoporous silica are obtained (**Scheme 1.3**).<sup>21b</sup>



**Scheme 1.3.** Stepwise formation of mesoporous silica. Reproduce from reference.<sup>20b</sup>

The synthesis pathways of mesoporous silica materials can be widely varied depending on synthetic conditions, such as temperature, pH, concentration of reagent, and organic surfactant molecules, employed in the synthesis. In basic condition (pH range of 9.5 to 12.5), during hydrolysis, the silica precursor remains as silicate anion. The silicate anion condenses with cationic surfactant, undergo polymerization and cross-linking and results in mesoporous MCM-41, MCM-48, etc.<sup>22</sup> depending on the type of surfactant and specific synthetic conditions used. Under acidic condition, silica precursor forms cationic species and condenses with non-ionic surfactant micelles such as P123, F127 or SDA to form SBA type mesoporous silica with thick pore walls and large pores (**Figure 1.2**).<sup>21,23</sup> Compared with the synthetic condition of MCM-41, condensation of silica in SBA-15 are under acidic condition and normally slower than that in basic conditions. Heteroatoms such as Ti, V, Co, Fe, Mn, Cr, Zn, Cu, or W, are often used for coordination site same as Si to incorporated into silica framework to give more stabile and high surface area mesoporous materials.<sup>21</sup>

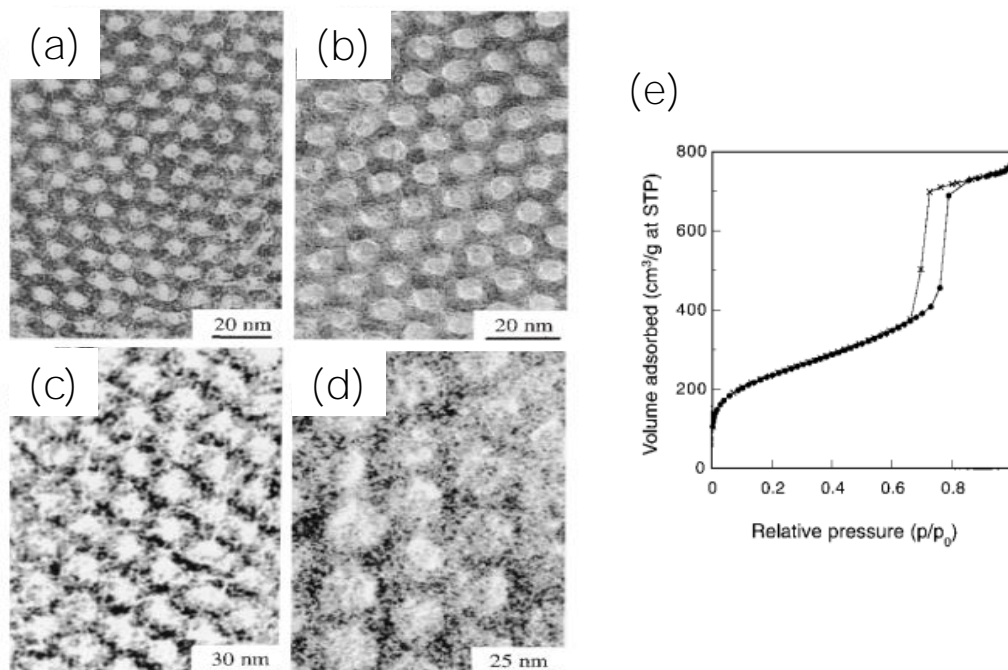
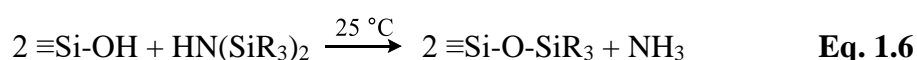
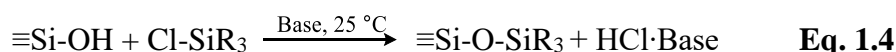


**Figure 1.2.** (a-d) TEM images of calcined hexagonal SBA-15 mesoporous silica with different average pore sizes and (e) their nitrogen adsorption/desorption curve. Reproduced from reference.<sup>23c</sup>

#### 1.4.2. *Functionalized mesoporous silica*

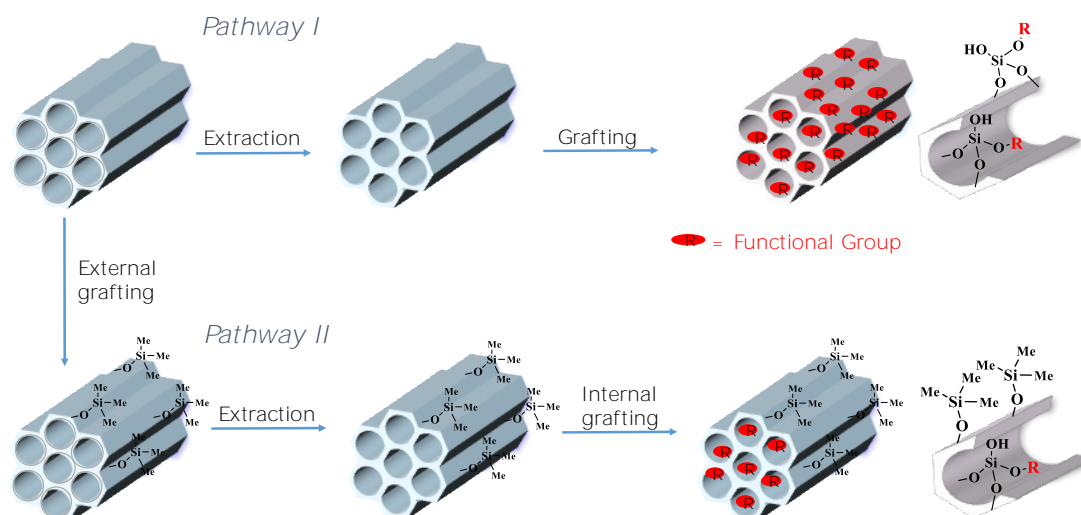
One of most important and easiest method to tailoring the physical and chemical properties of mesoporous silica is incorporating organic components on the mesoporous silica surface or wall through grafting. In post-synthesis modification, hybrid organic-inorganic mesoporous silica materials are obtained, in which different types of functional organic groups can be placed selectively on the internal or external surfaces of inorganic mesoporous silica. Organic functionalization can tune or improve the surface properties such as hydrophilicity, hydrophobicity, binding affinity to guest molecules, surface reactivity, stability and bulk properties of the mesoporous materials.<sup>21c</sup>

The typical post-grafting methods are held with extracted mesoporous silica (surfactant removed mesoporous silica). Surface silanol (Si-OH) group of mesoporous silica give convenient anchoring point for functionalization and the pathway of silylation is followed by one of **Eq. 1.4-1.6**.<sup>24</sup>



In this process, the extraction methods are important due to silylation occurring on free  $\equiv\text{Si-OH}$  and  $\equiv\text{Si}(\text{OH})_2$ . The common extraction method, calcination of the material at temperatures between 400 - 550 °C can strengthens the walls and increase surface reactivity; however, it may make many surface  $\equiv\text{Si}(\text{OH})_2$  groups to be lost. The silanol groups can be regenerated often through re-hydration by boiling the materials in water or acid or treating it in steam. Solvent extraction involving a mixture of acid and alcohol or using pure alcohols to remove the templates minimizes the loss of surface silanol; however, this method leaves behind some residual of surfactant after extraction.

In the typical grafting reactions, the external surface is more easily to be approached so functional groups are predominantly grafted more external surface than internal mesoporous surface (*Pathway I* in **Scheme 1.4**). Controlled functionalization internal wall rather than outer wall can achieve through passivating outer surface with hydrophobicity group prior to extracting surfactant and functionalized inner surface (*Pathway II* of **Scheme 1.4**).



**Scheme 1.4.** Selective grafting methods of mesoporous silica. Grafting functional group in external and internal surface (*pathway I*) and grafted selectively internal wall (*pathway II*).

The functionalized mesoporous silica materials can serve as good heterogeneous catalysts for several reactions as they offer high surface area and provide a significant number of accessible catalytic active sites. For example, tertiary amine functionalized SBA-15 show as an effective catalyst for Michael addition reaction between various nitro-alkenes and active methylene compounds (**Figure 1.3**).<sup>25</sup>

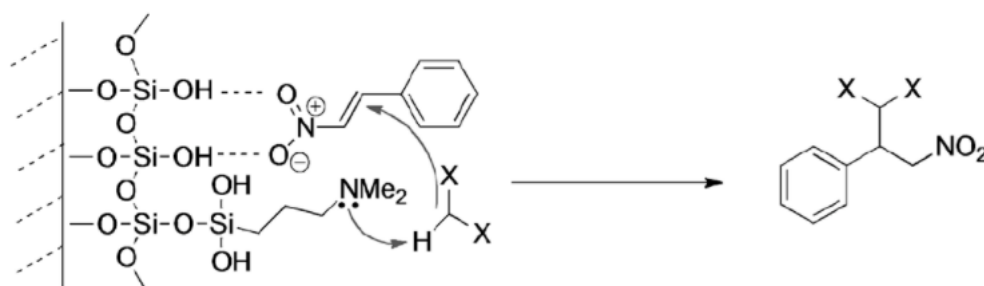
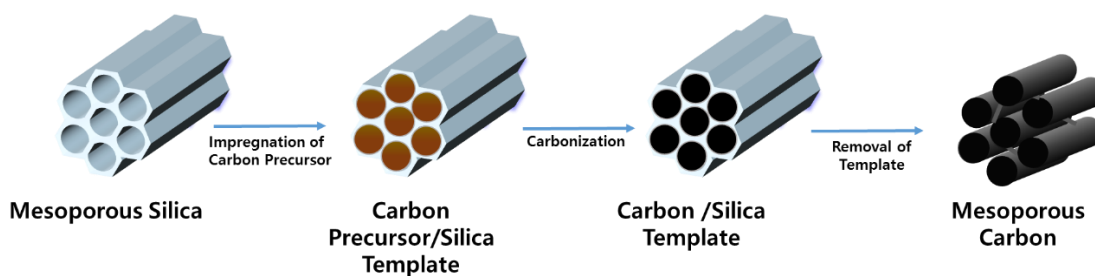


**Figure 1.3.** Schematic description of plausible mechanism of bifunctional mesoporous catalysts in Michael addition reaction. Reproduction from reference [25].

## 1.5. Mesoporous Carbon (Hard Template Method)

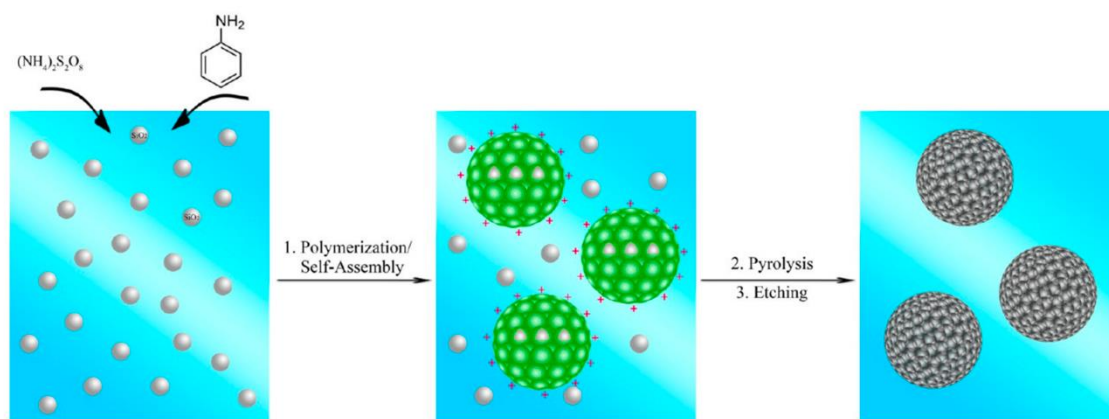
### 1.5.1. *Synthesis of Mesoporous Carbon*

Porous carbon materials have been received great attention due to their diverse application in several areas such as gas separation, water purification, catalyst support, or energy storage applications. These porous carbon materials are commonly made through several synthetic methods including: *i*) physical and chemical activation processes, *ii*) catalytic activation of carbon precursors using metal salts or organometallic compounds, or *iii*) carbonization of polymer, or polymer aerogel.<sup>26</sup> Although various synthetic methods have been developed to make carbon materials, making those with uniform pore structures still remains challenging. One of the most up-to-date synthetic procedures to make porous carbon materials with uniformly pore structures is utilizing mesoporous structured silica as hard template, as shown in **Scheme 1.5**. In this method, carbon precursors are first immobilized inside the pores of the inorganic mesoporous silica. This is followed by carbonization of the materials under desired temperature in inert gas atmosphere. Finally, the silica template is etched with HF or NaOH solution, e.g.,  $\text{SiO}_2 + 2\text{NaOH} \rightarrow \text{Na}_2\text{SiO}_3 + \text{H}_2\text{O}$ . Using this synthetic method with different mesoporous silica materials as hard templates (such as SBA-3, HMS, MSU-H, MCM-41, MCM-48, SBA-15, KIT-6, FDU-5, SBA-16), different types of porous carbon materials with different surface areas, pore sizes and uniformly ordered mesoporous structures can be obtained.<sup>27</sup>



**Scheme 1.5.** Schematic illustration of the synthesis of mesoporous carbon using mesoporous silica as hard templates. In this case, SBA-15 mesoporous silica use as a hard template to make a mesoporous carbon material designated as CMK-1.

Furthermore, colloidal silica are often used for as hard template to obtain porous carbon materials with narrow distribution of pore sizes, as shown in **Scheme 1.6**. This method also can obtain from different polymers carbon sources including sugar, polyaniline<sup>28</sup> or polypyrrole<sup>29</sup> and followed by pyrolysis at desired temperature and removal of silica and uniformly formed mesoporous carbon is obtained.



**Scheme 1.6.** Schematic description of colloidal silica templated mesoporous carbon from polyaniline. Reproduced by reference.<sup>28</sup>

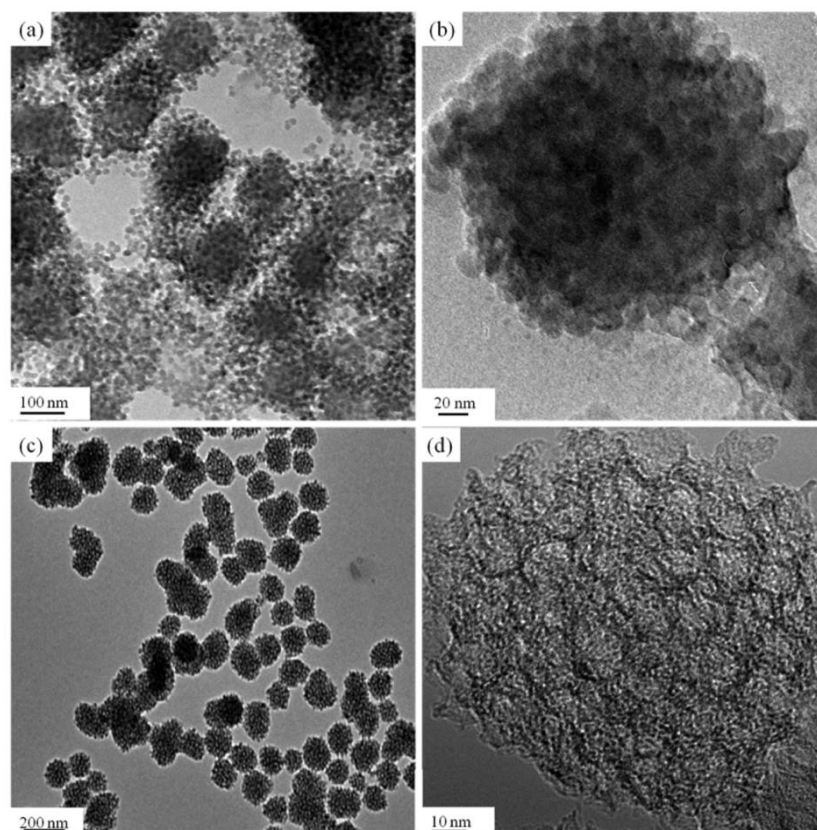


**Figure 1.3.** TEM images of polyaniline derived mesoporous carbon. Reproduced by reference.<sup>28</sup>

### ***1.5.2. Hetero-atom doped mesoporous carbon***

One of the major advantages for the hard templating strategy for synthesis of porous carbon materials is that it allows the synthesis from a variety of carbon precursors, including those already naturally possessing different elements, such as nitrogen, boron, sulfur, boron or iron. Various heteroatom-doped porous carbon materials, synthesized from this methods, often result in perturbation of the electronic structure of the carbon lattice, and generate partially positive or negative charged groups on the material.<sup>31</sup> So, heteroatom dopants endow the carbon species not only tailoring the chemical properties but also physical properties thereby giving the

sustainable materials with more controllable electronic features. This surface modification makes the materials to be more suitable for several applications, especially as catalysts in fuel cells. For example, although the exact mechanism is not well understood, heteroatom dopant often enhances the catalytic activity of carbon materials toward the oxygen reduction reaction (ORR).<sup>30a</sup> It is believed that the charge redistribution around the heteroatom dopants in carbon materials makes the materials more active in catalyzing the ORR. Similarly, boron-doped carbon material (e.g., B-CNT) is found to an effective catalyst for nitrobenzene reduction, again due to the boron species present in the material.<sup>30b</sup> Moreover, in the energy storage, nitrogen (or electron rich atoms) often donate electron to metal nanocatalysts (Pd, Pt, or Au) and perturb the electron density around the metals and thereby enhancing the catalytic activities of the latter for various reactions, e.g., formic acid dehydrogenation, formate/bicarbonate reversible cycle and so on.

Among the heteroatom doped carbon materials, electronegative nitrogen easily donates electrons and it delocalizes in the  $\pi$  system of carbon matrices which creates positive and negative charged groups on the materials to increase carbon's conductive properties.<sup>31</sup> In this case, nitrogen is ideal dopants due to its' similar size with carbon so it is easily replaced carbon atom. Moreover, nitrogen doped carbon has the n-type conductivity which increases the metallic properties and its' higher electron affinity causes their charge delocalization/distribution, changes in their spin density (doping-induced spin redistribution), and increases the density of donor states closed to the Fermi level of carbon. Nitrogen doped carbon materials can be divided by chemical nitrogen and structural nitrogen: The chemical types of nitrogen are either amines or nitro group, and different types of nitrogen (structural nitrogen) can be found with

varied nitrogen types and density of nitrogen through preferably pyrolysis procedure (**Figure 1.4**). The structural nitrogen types can be determined by X-ray photoelectron spectroscopy (XPS) and the pyridinic N species are located at ca. 398.4 eV, pyrrolic N species at 399.8 eV, quaternary N species are at 401.0 eV and N-oxide are at 402.9 eV.<sup>32</sup>

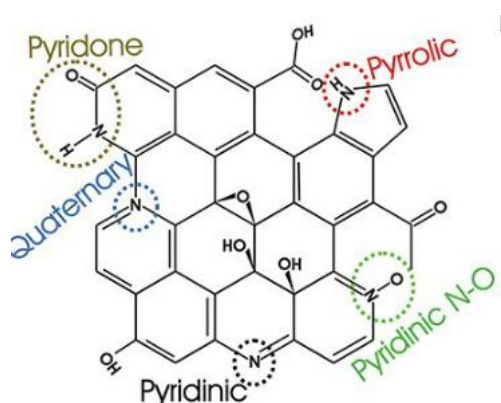


**Figure 1.4.** Schematic illustration of pyritic, pyridinic, quaternary and pyrrolic nitrogen species. Reprinted by reference.<sup>31</sup>

## 1.6. Palladium nanocatalyst

### 1.6.1. Pd nanocatalysts

The major advantages for metal nanoparticles (NP), comparing to their bulk counterpart, are high catalytic activity and excellent selectivity toward the desired products mainly due to their high surface area to volume ratios and thereby obtain the unique surface atom/surface faceted structures of nanoparticles. The history of nanoparticles dates back to the work of Michael Faraday, who discovered the wet chemical reduction method to make metal nanoparticles some 150 years ago. This wet chemistry method has been commonly used even today in synthesis of nanoparticles.<sup>7,33</sup>

After Faraday's attribution, Turkevich firstly prepared Au NPs from  $[\text{AuCl}_4]^-$  precursor by stepwise formations including: *i*) nucleation, *ii*) growth and *iii*) agglomeration (**Figure 1.5**). In this synthesis, the reducing agents such as hydrogen, alcohol, hydrazine or borohydride are involved and so stabilizer on (e.g., ligand, polymer or surfactant).<sup>33</sup>

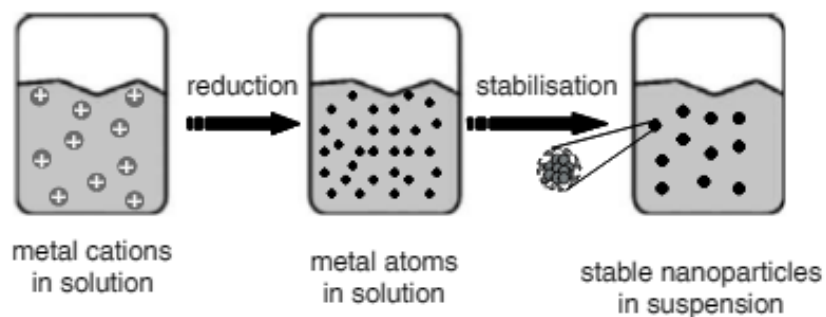


**Figure 1.5.** Synthesis of metallic nanoparticle through reduction of metal salt precursor. Reprinted from reference.<sup>33</sup>

Among several metal nanoparticles are well developed and used for many application, palladium catalysts are widely used as catalysts for such catalytic reactions, which are Suzuki reaction,<sup>34</sup> Heck coupling reaction,<sup>35</sup> hydrogenation and dehydrogenation of formic acid,<sup>2</sup> or other renewable energy application and several palladium nanocatalysts have been shown as similar catalytic activity as homogenous catalysts with ease of recycling.

### ***1.6.2. Palladium nanoparticles supported on functionalized mesoporous silica***

As mentioned previous section, Pd catalysts both homogeneous and heterogeneous catalysts, show interesting and promising catalytic activity so widely used in many reactions. Significant effort has been achieved to improve catalytic activity but several Pd nanocatalysts still have problems of leaching or aggregation,

which lead to the deactivation of the catalysts' activity. To solve these problems, one of commonly used solution is adapting stabilizer, which often strongly adsorbs between metal-stabilizer.<sup>7,33,36</sup>

To avoid and solve the Pd catalysts' leaching and losing their catalytic activity problems, functionalized solid support materials for Pd NPs are one of developed option. Among the various solid support materials ranging from polymer to ordered mesoporous and modified silica, silica remains among the top choices due to its wide accessibility, excellent stability, porosity and inert environmental for metal nanoparticles.<sup>7</sup> Furthermore, pre-functionalized mesoporous silica materials often role as ligands or stabilizer such as phosphines, carbenes, pincer ligands, or palladacycle, to name a few. For example, Gao group functionalized highly branched and well defined polyamidoamine (PAMAM) onto SBA-15 mesoporous silica and loaded palladium nanoparticles (**Figure 1.6**).<sup>37</sup> The Pd nanoparticles as catalysts were shown to catalyze the hydrogenation of ally alcohol high catalytic activity as well as selectivity.

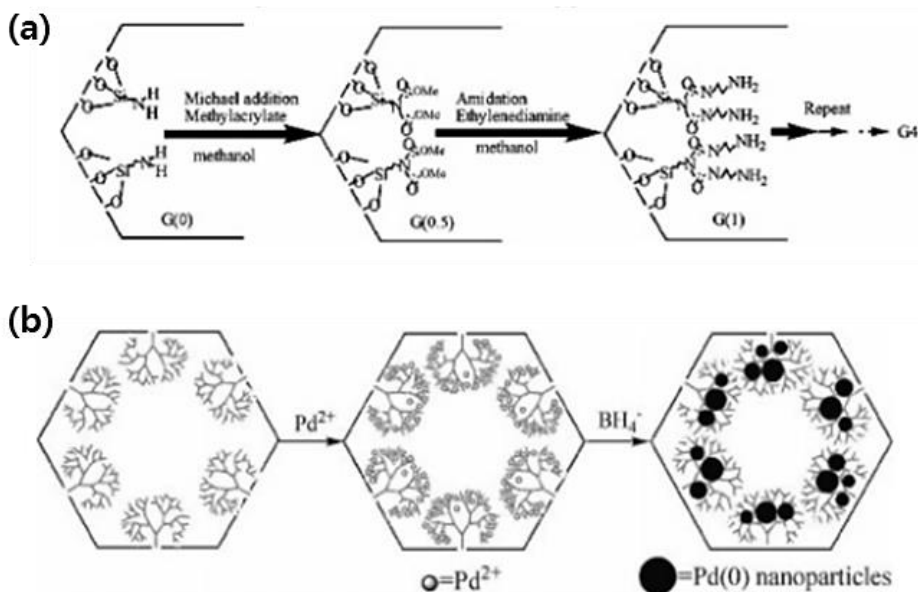


**Figure 1.6.** (a) Preparation of PAMAM dendrimers supported SBA-15 and (b) formation of Pd NPs onto PAMAM supported SBA-15 mesoporous silica. Reprinted from reference.<sup>37</sup>

### 1.6.3. Palladium nanocatalysts supported on N-doped carbon materials

As discussed above section, heteroatom such as N, B, P and S doped carbon materials are proven to have improved catalytic properties toward various reactions. Different structural nitrogen properties such as pyridinic, pyrrolic, and quaternary interact with metal nanoparticles and leading to unique catalytic behavior through *metal-support* and *metal-support-reactant* interactions. Arrigo et al.<sup>38</sup> studied the nature of interaction between the N species on the carbon support materials and the supported Pd centers. Pd loaded onto nitrogen doped carbon nanotubes (NCNTs), nature of N species immobilizing onto NCNT and doing  $\sigma$ -type donation from the filled  $\pi$  orbital to empty d-orbitals of Pd as well as  $\pi$  back-donation from the filled Pd atomic d orbital

to the  $\pi^*$  antibonding orbital of N atom. These  $\sigma$  donation and  $\pi$  back-donation induce the charge transfer with ionic character and results in chemical shift of Pd 3d level.

## 1.7. Summary and outlook

Despite various nanocatalysts have been developed for hydrogen storage and hydrazine oxidation, most of them still rely on noble metals such as Pt, Pd, or Au. However, these noble metals are expensive and less earth abundant. So most of catalytic research works over the past few years have focused on the development of sustainable nanocatalysts with optimized structures, high surface areas and efficient catalytic properties to enable these reactions.

One of drawback to be focused in transition and noble nanocatalysts is its' high surface area with high free energies, which tend to agglomerate to reduce their surface area. This often ends up with reducing their catalytic activities. For obtaining sustainable novel metal catalysts, stabilization of metal nanoparticles is one of important factors and the modified support materials can ideally contribute to this problem, i.e., functional groups on the support materials can serve as the role of stabilizer as well as provide favorable *strong metal-support interaction* (SMSI) to the catalytic sites. In next few chapters, the design and synthesis of the nanocatalysts supported on functionalized mesoporous silica and investigation of *strong metal-support interaction* (SMSI) along with their catalytic activity are described for the various fuel cell applications such as formic acid dehydrogenation, formate/bicarbonate reversible reaction, and hydrazine oxidation.

In conclusion, the development of sustainable and efficient catalyst for fuel cell applications can impact and make contributions to the next generation of energy systems. The studies in this thesis will provide some opportunities for developing similar or better catalysts for renewable energy systems involving formic acid dehydrogenation, formate/bicarbonate dehydrogenation/hydrogenation cycles, and hydrazine oxidation for fuel cells. The work would also document intricate details of reaction mechanisms and fundamental studies regarding these reactions as related to various alternative energy systems.

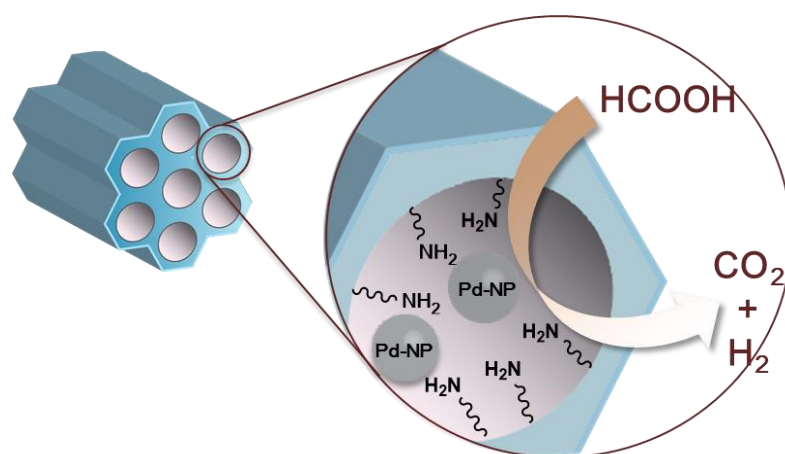
## 1.8. Reference

- (1) (a) Turner, J *Science*, **1999**, 285, 687-689. (b) Steele B. C. H.; Heinzl A. *Nature*, **2001**, 414, 345-352. (c) Grasemann, M.; Laurenczy G. *Energy Environ. Sci.*, **2012**, 5, 8171.
- (2) (a) Q. Zhu, Q. Xu, *Energy Environ. Sci.*, **2015**, 8, 478-512. (b) Yadav, M.; Xu, Q. *Energy Environ. Sci.*, **2012**, 5, 9698-9725. (c) Enthaler, S.; Langermann, J. V.; Schmidt T. *Energy Environ. Sci.*, **2010**, 3, 1207-1217.
- (3) Bockris, J. O. M. *Science*, **1972**, 176, 1323.
- (4) Reutemann, W.K.; Kieczka, H. *Ullmann's Encyclopedia of Industrial Chemistry*, Wiley-VCH, Weinheim, 2011
- (5) Albert, J.; Jess, A.; Kern, C.; Pöhlmann, F.; Glowienka K.; Wasserscheid, P. *ACS Sustain. Chem. Eng.* **2016**, 4, 5078-5086.
- (6) Boddien, A.; Gärtner, F.; Federsel, C.; Sponholz, P.; Mellmann, D.; Jackstell, R.; Junge, H.; Beller, M. *Angew. Chem. Int. Ed.* **2011**, 50, 6411-6414
- (7) (a) Serov, A.; Kwak, C. *Appl. Catal., B*, **2010**, 98, 1-9. (b) Soloveichik, G. L. *Beilstein J. Nanotechnol.* **2014**, 5, 1399-1418. (c) Fragal, E. H.; Fragal, V. H.; Huang, X.; Martins, A. C.; Cellet, T. S. P.; Pereira, G. M.; Mikmeková, E.; Rubira, A. F.; Silva, R.; Asefa, T. *J. Mater. Chem. A*, **2017**, 5, 1066-1077. (d) Qian, W.; Wilkinson, D.P.; Shen, J.; Wang, H.; Zhang, J. *J. Power Sources* **2006**, 154, 202-213.
- (8) Asefa, T.; Polshettiwar, V. *Nanocatalysis: Synthesis and applications*, 1<sup>st</sup> ed.; Wiley-VCH, Weinheim, 2013.
- (9) Loges, B.; Boddien, A.; Junge H.; Beller, M. *Angew. Chem., Int. Ed.*, **2008**, 47, 3962-3965.
- (10) Boddien, A.; Loges, B.; Junge, H.; Gaertner, F.; Noyes J. R.; Beller, M. *Adv. Synth. Catal.*, **2009**, 351, 2517-2520.
- (11) Boddien, A.; Loges, B.; Junge H.; Beller, M. *ChemSusChem*, **2008**, 1, 751-758.
- (12) Boddien, A.; Mellmann, D.; Gärtner, F.; Jackstell, R.; Junge, H.; Dyson, P.J.; Laurenczy, G.; Ludwig, R.; Matthias Beller, *Science*, **2011**, 333, 1733-1736
- (13) Solymosi, F.; Koós, Á.; Liliom, N.; Ugrai, I. *J. Catal.* **2011**, 279, 213-219.
- (14) Ojeda, M.; Iglesia, E. *Angew. Chem. Int. Ed.* **2009**, 48, 4800-4803.
- (15) (a) Lee, J.H.; Cho, J.; Jeon, M.; Ridwan, M.; Park, H.S.; Choi, S.H.; Nam, S.W.; Han, J.H.; Lim, T.-H.; Ham, H.C.; Yoon, C.W. *J. Mater. Chem. A*, **2016**, 4, 14141-14147. (b) Yu, W.; Mullen, G.M.; Flaherty, D.W.; Mullins C.B. *J. Am. Chem. Soc.*, **2014**, 136, 11070-11078. (c) Metin, Ö.; Sun, X.; Sun, S. *Nanoscale*, **2013**, 5, 910-912.
- (16) Zhu, Y.; Nakanishi, T.; Kanamori, K.; Nakanishi, K.; Ichii, S.; Iwaida, K.; Masui, Y.; Kamei, T.; Shimada, T.; Kumamoto, A.; Ikuhara, Y.H.; Jeon, M.; Hasegawa, G.; Tafu, M.; Yoon, C.W.; Asefa T. *ACS Appl. Mater. Interfaces*, **2017**, 9, 36-41.
- (17) Hu, C.; Mu, X.; Fan, J.; Ma, H.; Zhao, X.; Chen, G.; Zhou, Z.; Zheng, N. *ChemNanoMat* **2016**, 2, 28-32.
- (18) Tedsree, K.; Li, T.; Jones, S.; Chan, C.W.A.; Yu, K.M.K.; Bagot, P. A. J.; Marquis, E.A.; Smith, G.D.W.; Tsang, S.C.E. *Nat. Nanotechnol.* **2011**, 6, 302-307.
- (19) Lee, J.H.; Ryu, J.; Kim, J.Y.; Nam, S.W.; Han, J.H.; Lim, T.-H.; Gautam, S.; Chae K.H.; Yoon, C. W. *J. Mater. Chem. A*, **2014**, 2, 9490-9495.
- (20) Koh, K.; Seo, J.-E.; Lee, J.H.; Goswami, A.; Yoon, C.W.; Asefa T. *J. Mater. Chem. A*, **2014**, 2, 20444-20449.

- (21) (a) Tanev, P.T.; Pinnavaia, T.J. *Science* **1995**, *267*, 865–867. (b) Pal, N.; Bhaumi, A. *Adv. Colloid Interface Sci.* **2013**, *21*, 189–190. (c) Hoffmann, F.; Cornelius, M.; Morell, J.; Fröba, M. *Angew. Chem. Int. Ed.* **2006**, *45*, 3216–3251.
- (22) (a) Sayari, A. *Chem. Mater.* **1996**, *8*, 1840–1852. (b) Beck, J.S.; Vartuli, J.C.; Roth, W. J.; Leonowicz, M.E.; Kresge, C.T.; Schmitt, K.D.; Chu, C.T.-W.; Olson, D.H.; Sheppard, E.W.; McCullen, S.B.; Higgins, J.B.; Schlenker, J.L. *J. Am. Chem. Soc.*, **1992**, *114*, 10834–10843.
- (23) (a) Kresge, C.T.; Leonowicz, M.E.; Roth, W. J.; Vartuli, J.C.; Beck, J.S. *Nature* **1992**, *359*, 710–712. (b) Meng, Y.; Gu, D.; Zhang, F.Q.; Shi, Y.F.; Yang, H.F.; Li, Z. *Angew. Chem. Int. Ed.* **2005**, *44*, 7053–7059. (c) Zhao, D.; Feng, J.; Huo, Q.; Melosh, N.; Fredrickson, G.H.; Chmelka, B.F.; Stucky, G.D. *Science*, **1998**, *279*, 548–552.
- (24) Lickiss, P.D. *Adv. Inorg. Chem.*, **1995**, *42*, 147–262.
- (25) Das, S.; Goswami, A.; Murali, N.; Asefa, T. *ChemCatChem*, **2013**, *5*, 910–919.
- (26) (a) Wang, X.; Liang, C.; Dai, S. *Nano/Microporous Materials: Mesoporous and Surface-Functionalized Mesoporous Carbon* Wiley-VCH, Weinheim, 2011. (b) Lee, J.; Kim, J.; Hyeon, T. *Adv. Mater.* **2006**, *18*, 2073–2094.
- (27) Xu, R.; Pang, W.; Huo, Q. Synthetic chemistry of inorganic ordered porous material in *Modern Inorganic Synthetic Chemistry* 1<sup>st</sup> ed.; Elsevier, 2010.
- (28) Huang, X.; Zhou, L.; Voiry, D.; Chhowalla, M.; Zou, X.; Asefa, T. *ACS Appl. Mater. Interfaces*, **2016**, *8*, 18891–18903.
- (29) Meng, Y.; Voiry, D.; Goswami, A.; Zou, X.; Huang, X.; Chhowalla, M.; Liu, Z.; Asefa, T. *J. Am. Chem. Soc.*, **2014**, *136*, 13554–13557
- (30) (a) Zhang, J.; Dai, L.; ACS Catal. **2015**, *5*, 7244–7253. (b) Lin, Y.; Wu, S.; Shi, W.; Zhang, B.; Wang, J.; Kim, Y.A.; Endod, M.; Su, D. S. *Chem. Commun.* **2015**, *521*, 13086–13089. (c) Daems, N.; Sheng, X.; Vankelecom, I.F.J.; Pescarmona, P.P. *J. Mater. Chem. A*, **2014**, *2*, 4085–4110. (d) Wang, H.; Maiyalagan, T.; Wang, X. *ACS Catal.*, **2012**, *2*, 781–794.
- (31) (a) Jin, Z.; Yao, J.; Kitrell, C.; Tour, J.M. *ACS Nano*, **2011**, *5*, 4112–4117. (b) Sharifi, T.; Hu, G.; Jia, X.; Wagberg, T. *ACS Nano*, **2012**, *6*, 8904–8912.
- (32) Silva, R.; Voiry, D.; Chhowalla, M.; Asefa, T. *J. Am. Chem. Soc.*, **2013**, *135*, 7823–7826.
- (33) Pachón, L.D.; Rothenberg, G. *Appl. Organometal. Chem.* **2008**, *22*, 288–299
- (34) (a) Miyaura, N.; Yanagi, T.; Suzuki, A. *Synth. Commun.* **1981**, *11*, 513. (b) Kotha, S.; Lahiri, K.; Kashinath, D. *Tetrahedron* **2002**, *58*, 9633–9695.
- (35) (a) Beletskaya, I. P.; Cheprakov, A. V.; *Chem. Rev.* **2000**, *100*, 3009–3066. (b) Littke, A.F.; Fu, G.C. *Angew. Chem. Int. Ed.* **2002**, *41*, 4176–4211.
- (36) Polshettiwar, V.; Len, C.; Fihri, A. *Coord. Chem. Rev.* **2009**, *253*, 2599–2626.
- (37) Jiang, Y.; Gao, Q. *J. Am. Chem. Soc.* **2006**, *128*, 716–717.
- (38) Arrigo, R.; Schuster, M.E.; Xie, Z.; Yi, Y.; Wowsnick, G.; Sun, L.L.; Hermann, K.E.; Friedrich, M.; Kast, P.; Hävecker, M. Knop-Gericke, A.; Schlög, R. *ACS Catal.*, **2015**, *5*, 2740–2753.

## CHAPTER 2

### Ultrasmall Palladium Nanoparticles Supported on Amine-functionalized SBA-15 Efficiently Catalyze Hydrogen Evolution from Formic acid



#### 2.1. Overview

The success of the so-called “hydrogen economy” for large-scale applications will ultimately depend on efficient and sustainable production, storage and distribution of hydrogen. Owing to its low toxicity, high volumetric  $H_2$  storage capacity and availability both from renewable resources (e.g., biomass) as well as non-renewable resources (e.g., fossil fuel feedstocks), formic acid (FA) is one of the most favorable chemical hydrogen storage media for large-scale energy storage applications. However, for FA to become a viable hydrogen storage medium, efficient catalysts that enable it to release  $H_2$  at low cost are necessary. Herein I report a facile synthetic route to amine-functionalized nanoporous silica-supported ultrasmall Pd nanoparticles (Pd/SBA-15-

Amine) that are highly active catalysts for formic acid dehydrogenation, producing hydrogen at ambient temperature with a high turn-over-frequency (TOF) of  $293\text{h}^{-1}$ —which is among the highest TOFs ever reported for the reaction by a heterogeneous catalyst. I also show that the material is easily recyclable multiple times, without losing its catalytic activity. So, the catalyst I developed might contribute to some of the solutions of our sustainability challenges

## 2.2. Introduction

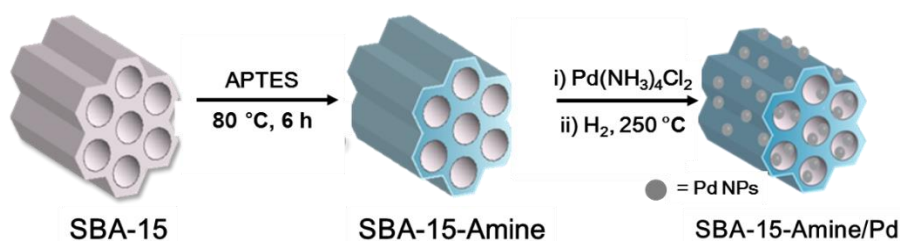
Given the current energy landscape, where the consumption of fossil fuels continues to rise while the negative environmental impacts associated with burning fossil fuels continues unabated, the search for alternative, benign and sustainable energy sources is a burgeoning interest. In this context, hydrogen—as one of the most promising clean energy carriers—can play pivotal roles to meet these challenging issues facing the world, as already successfully demonstrated with clean hydrogen-fed fuel cell technologies.<sup>1-4</sup> Despite the progress made since the 1970s, when the term "hydrogen economy" was coined by Bockris,<sup>2</sup> it has become apparent that the ultimate success of hydrogen-based energy cycle for large scale applications heavily hinges on efficient, large-scale production, storage, and distribution of hydrogen. In particular, the development of safe and reversible hydrogen storage systems is a key technical issue that must be fully addressed to successfully realize an "ideal" hydrogen economy.<sup>5-7</sup>

Because of its low toxicity and high availability both from renewable resources (e.g., biomass) as well as non-renewable resources (e.g., fossil-feedstock), formic acid (FA) has recently attracted significant attention for its potential as favorable chemical

hydrogen storage medium for large-scale energy storage applications.<sup>8-9</sup> FA's appeal as favorable hydrogen carrier also stems from the fact that it has a high volumetric H<sub>2</sub> storage capacity of 53 g/L, which is suitable for many on-board energy applications.<sup>10</sup> Moreover, FA can be dehydrogenated to produce hydrogen it carries under ambient conditions, making it auspicious for direct utilization within hydrogen-fed polymer electrolyte membrane-based fuel cells (PEMFCs).

For FA to be used as a viable hydrogen storage medium though, efficient catalysts that enable it to generate H<sub>2</sub> at low cost are critically needed. In recent years, various homogeneous catalysts based on metals such as Ru<sup>11-14</sup> and Ir<sup>15</sup> and heterogeneous catalysts including AuPd/C,<sup>16</sup> AgPd<sup>17</sup>, CoAuPd/C,<sup>18</sup> Pd/C<sub>3</sub>N<sub>4</sub><sup>19,20</sup> for dehydrogenation of FA have been reported. Generally, homogeneous catalysts are highly active and exhibit higher turnover frequencies (TOFs) than heterogeneous catalysts for many reactions including formic acid dehydrogenation. However, the heterogeneous catalysts are generally advantageous over homogeneous ones in terms of recoverability of the spent-catalysts from the reaction mixtures.<sup>21</sup> By immobilizing homogeneous catalysts onto solid support materials, the benefits attainable by both types of catalysts can sometimes be realized. This approach of 'heterogenization of homogeneous catalysts' can also be successfully applied for catalytically active ultrasmall metallic nanoclusters, which have been increasingly become promising catalysts for formic acid dehydrogenation.<sup>22-26</sup> Furthermore, functional groups such as amines could easily be supported on the surfaces of such heterogeneous catalysts to serve as interaction sites for supported metallic nanoclusters and serve as co-catalytic species, which in the case of FA-dehydrogenation can function as deprotonation sites

for FA molecules, synergistically assisting FA's catalytic dehydrogenation. This hypothesis, in conjunction with the recent success of other gold (Au) nanoparticles encapsulated in silica nanospheres<sup>26</sup> and Pd supported catalysts over materials such as silica microspheres<sup>22</sup> or metal-organic frameworks (MOFs)<sup>24</sup> for FA dehydrogenation, has prompted us to develop an efficient hybrid catalyst based on ultrasmall Pd nanoparticles (Pd NPs) supported on amine-functionalized mesoporous silica for FA dehydrogenation, as shown in **Scheme 2.1**.



**Scheme 2.1.** A synthetic scheme employed for making ultrasmall Pd nanoparticles supported on amine-functionalized SBA-15 mesoporous silica, which can efficiently catalyze formic acid (FA) dehydrogenation

## 2.3. Experimental section

### 2.3.1. Materials and reagents

Poly(ethylene glycol)-*block*-poly(propylene glycol)-*block*-poly(ethylene glycol) copolymer (Pluronic® 123, with an average molecular mass of 5800 Da) was purchased from BASF. (3-Aminopropyl)triethoxysilane (APTES), ammonium hydroxide (NH<sub>4</sub>OH), formic acid (HCOOH), anhydrous toluene, tetraethyl orthosilicate (TEOS), *n*-propylamine, and palladium chloride (PdCl<sub>2</sub>) were obtained from Sigma-Aldrich.

Hydrochloric acid (36.5%) was purchased from Fischer Scientific. Anhydrous ethanol was purchased from Pharmco-Aaper. All the reagents were used as received without further purification.

### **2.3.2. Instrumentation**

Transmission electron microscopy (TEM) and scanning transmission electron microscope (STEM) were performed with a FEI Tecnai™ F20 instrument equipped with Schottkey FEG electron gun and operating at 200 kV. FA dehydrogenation experiments were performed using a laboratory-made customized system (please see the procedure above for details). Gaseous products were identified using an in situ FT-IR spectrometer (Nicolet iS10, Thermo Scientific) equipped with an MCT detector and a customized gas cell. Spectral data were collected using a scan rate of 8 scans min<sup>-1</sup> with a resolution of 4 cm<sup>-1</sup>. Elemental analysis (EA) and inductively coupled plasma atomic emission spectrometer (ICP-AES) were done at Korea Institute of Science and Technology Advanced Analysis center. ICP-AES analyses of all samples were done using a Varian 710-ES (Varian, Australia). X-ray Photoelectron spectroscopy (XPS) were performed using a PHI 5000 VersaProbe (Ulvac-PHI) instrument, equipped with Al K $\alpha$  (1486.6 eV) monochromator, Anode (25W, 15kV), operating at background pressure is 6.7x10<sup>-8</sup> Pa and has 100  $\mu$ m x 100  $\mu$ m sample size.

### **2.3.3. Synthesis of materials**

#### *Synthesis of SBA-15 Mesoporous Silica*

SBA-15 was synthesized using Pluronic® 123 as templating agent in acidic solution, as reported previously by Zhao et al.<sup>27</sup> Typically, a solution of Pluronic® 123

/ 12 M HCl / tetraethyl orthosilicate (TEOS) / H<sub>2</sub>O (2:12:4.3:26, mass ratio in grams) was prepared and stirred at 40 °C for 24 h. The solution was then aged at 65 °C for another 24 h. The resulting solution was filtered, and the solid material was washed with copious amount of water and dried, giving a white powder labeled as “as-synthesized SBA-15”. As-synthesized SBA-15 (1 g) was then dispersed in ethanol (100 mL) and diethyl ether (100 mL) and stirred at 50 °C for 5 h to remove Pluronic®123. After filtration and washing with ethanol, the final solid material was dried in oven, giving the template extracted SBA-15 mesoporous silica, denoted as “SBA-15.”

*Synthesis of ultrasmall Pd nanoparticles-loaded amine-functionalized SBA-15*

100 mg of SBA-15 was mixed and stirred with 1.37 mmol of (3-aminopropyl)-triethoxysilane (APTES) in 50 mL of anhydrous toluene for 6 h at 80 °C to graft the mesoporous channel surfaces of SBA-15 with primary amine groups. After filtration the mixture, the solid product was washed with toluene and ethanol and let to dry at ambient condition, producing amine-functionalized SBA-15 that was denoted as “SBA-15-Amine”.

A solution of PdCl<sub>2</sub> (56.3 μmol) in 100 μL of 14 M of ammonium hydroxide (NH<sub>4</sub>OH) and 5 mL ethanol:DI water (1:4 v/v) was prepared. After mixing this solution with SBA-15-Amine, the mixture was stirred at 80 °C for 3 h. The solid material was recovered by filtration, washed with water and ethanol, and finally dried, yielding Pd(II)-functionalized SBA-15-Amine. The resulting material was then treated at 250 °C for 3 h with 10% H<sub>2</sub> : 90% N<sub>2</sub> affording ultrasmall Pd-NPs-containing SBA-15-Amine, denoted as Pd/SBA-15-Amine.

### *Synthesis of palladium nanoparticles (control sample)*

$\text{PdCl}_2$  (56.3  $\mu\text{mol}$ ) of Palladium chloride ( $\text{PdCl}_2$ ) was dissolved in 100  $\mu\text{L}$  of 14 M of ammonium hydroxide ( $\text{NH}_4\text{OH}$ ) and sonicated until a colorless solution was obtained. The resulting solution was allowed to undergo reduction under the same conditions as above, i.e., at 250  $^\circ\text{C}$  for 3 h with 10%  $\text{H}_2$  : 90%  $\text{N}_2$ , yielding palladium nanoparticles, denoted as “Pd NPs”.

### *Catalytic formic acid dehydrogenations*

Formic acid dehydrogenation reactions in the presence of the materials synthesized above were conducted in a modified glass reactor (volume, 40 mL) possessing two necks (one for inlet and another for outlet). The inlet was employed to purge the reactor with  $\text{N}_2$  gas. During consecutive  $\text{H}_2$  generation tests, the outlet goes directly to gas burette system for real-time measurement of the rate of  $\text{H}_2 + \text{CO}_2$  release as well as the accumulative amount of  $\text{H}_2$ , as I have demonstrated previously. The overall experimental apparatus for  $\text{H}_2$  measurement is shown in **Figure 2.1**. The reactions were performed using 10 mL of 1 M formic acid at room temperature. 50 mg of catalyst was used in each reaction. The reactor was stirred at room temperature (299 K) with vigorous stirring at a rate of 300 rpm. The gases evolved from the reaction were directly delivered into a gas burette system and their volumes were quantified.



**Figure 2.1.** An experimental set up used for measuring volume of  $\text{H}_2 + \text{CO}_2$  (mL).

#### *Recyclability Studies of Catalysts*

After the initial catalytic test involving 50 mg of Pd/SBA-15-Amine and 10 mL of 1 M FA was performed, the catalyst was recovered and washed with copious D.I water and dried under vacuum for 4 h. It was then used in the next reaction cycle in the same way as above and by keeping the same ratio of substrate to catalyst.

#### *Leaching Studies in Catalysis*

To determine whether or not palladium nanoparticles or some palladium species leach into the reaction mixture during the catalytic reaction or not, the supernatant was taken 50 min after FA dehydrogenation reaction started. The recovered Pd/SBA-15-Amine catalyst was analyzed for the amount of palladium in it using ICP-AES.

## 2.4. Result and Discussion

First, SBA-15 type mesoporous silica was synthesized using soft templating-based, supramolecular self-assembly synthetic technique, as demonstrated by Zhao et al.<sup>27</sup> By using the residual surface silanols ( $\equiv\text{Si-OH}$ ) located on the pore walls of SBA-15, the material was functionalized with organic functionalities, which were then utilized to anchor metal ions onto the surfaces of the nanoporous material.<sup>28,29</sup> In this current effort, primary amine groups were anchored on SBA-15 by grafting (3-aminopropyl)triethoxysilane (APTES) onto the surfaces of SBA-15, producing a material denoted as SBA-15-Amine (**Scheme 2.1**). Then,  $\text{Pd}^{2+}$  ions were supported onto the surfaces of SBA-15-Amine by mixing the latter with ammonical palladium solution ( $\text{Pd}(\text{NH}_3)_4\text{Cl}_2$ ).<sup>30</sup> Subsequent reduction of the resulting material using  $\text{H}_2/\text{N}_2$  mixture (1:9 v/v) at 250 °C for 3 h afforded SBA-15-Amine-supported Pd NPs (denoted hereafter as Pd/SBA-15-Amine) that are highly catalytically active for FA dehydrogenation (*see detailed experiment in experimental section*).

The structures and morphology of Pd/SBA-15-Amine were first analyzed by high-resolution transmission electron microscopy (HRTEM) and high-angle annular dark-field scanning transmission electron microscopy (HAADF-STEM). The Pd nanoparticles in Pd/SBA-15-Amine were found to be ultrasmall, having an average size of 1.9 nm (**Figure 2.2** a-b). In contrast, the unmodified Pd/SBA-15 prepared under otherwise identical synthetic conditions afforded relatively bigger Pd NPs (**Figures 2.2** c-d). The latter is not surprising since ultrasmall Pd NPs are often too difficult to obtain with conventional reduction methods employing  $\text{NaBH}_4$  and/or without capping agents because they tend to aggregate easily due to their relatively high surface energies (*vide*

*infra*). In our other control experiment, the Pd NPs formed following the reduction of the ammonical Pd(II) species in the absence of SBA-15-Amine were also, unsurprisingly, significantly bigger in size, having particle sizes as high as 150 nm (**Figure 2.3**). Thus, the amine functional groups inside the mesoporous silica and their ability to stabilize the Pd NPs must have played important roles in keeping the Pd NPs quite small during reduction of Pd<sup>2+</sup> ions under H<sub>2</sub> at 250 °C. The amounts of Pd in the Pd/SBA-15-Amine and Pd/SBA-15, as characterized by ICP-AES, were found to be identical (0.32 mmol/g<sub>cat</sub>, 3.4 wt. %). On the basis of other previous report,<sup>31</sup> it is conceivable that the amine functional groups grafted in our Pd/SBA-15-Amine could serve as Brønsted basic sites, facilitating the deprotonation of FA into formate intermediate, while the ultrasmall Pd NPs around them catalytically activate the C-H bonds of the resulting formate species. Besides this, the amine groups help with both the formation as well as stabilization of the ultrasmall Pd NPs (or protect them from undergoing aggregation during the catalytic reactions (*see below*)).

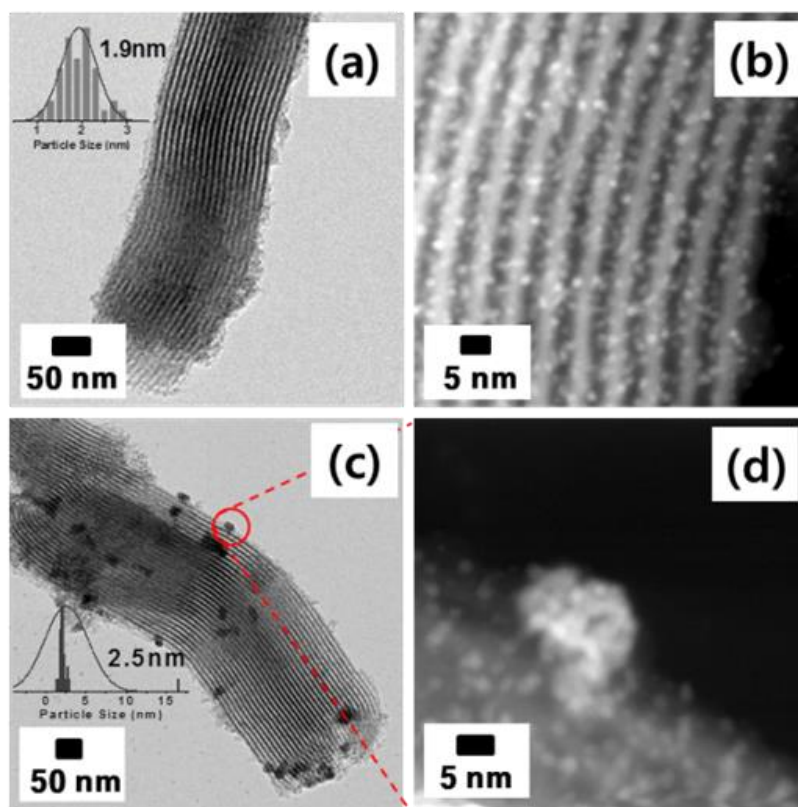


**Figure 2.2.** TEM (a) and STEM (b) images of Pd/SBA-15-Amine. TEM (c) and STEM (d) images of Pd/SBA-15. The insets show the size distributions of the particles obtained from the TEM images.

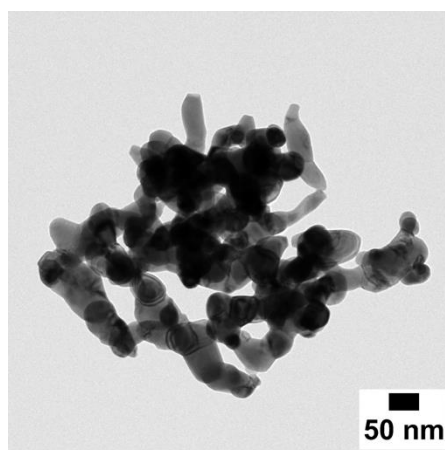


**Figure 2.3.** TEM image of Pd NPs synthesized using any support materials such as

SBA-15 and SBA-15-Amine.

Furthermore, the amine groups supported onto the SBA-15 can donate electron density to Pd, thereby enhancing the Pd's catalytic activity of towards FA dehydrogenation.<sup>31</sup> To elucidate this possible electronic effect of the amine groups on Pd, X-ray photoelectron spectroscopy (XPS) was employed to analyze the materials and the results are displayed in **Figure 2.4-2.7**. As depicted in **Figures 2.4-2.7**, while the peaks corresponding to Pd(0) in Pd/SBA-15 with maxima are centered at 341.0 eV ( $3d_{3/2}$  state) and 335.8 eV ( $3d_{5/2}$  state),<sup>32</sup> the corresponding peaks in the case of Pd/SBA-15-Amine are shifted into lower binding energies of 340.1 eV and 335.0 eV, respectively. This is likely due to the interaction between Pd NPs and amine groups in Pd/SBA-15-Amine; *i.e.*, the amine groups donating some electron density to Pd NPs and producing electron- rich Pd centers with lower binding energies. These electronically perturbed Pd centers in Pd/SBA-15-Amine could thus be partly responsible for the material's improved catalytic activity towards FA dehydrogenation compared with that of Pd/SBA-15 (*vide infra*). It is worth-adding here that the Pd<sub>3d</sub> spectra for both materials showed two small peaks corresponding to Pd<sup>2+</sup> centered at 343.2 eV and 337.9 eV, respectively, clearly indicating negligible presence of Pd<sup>2+</sup> species.

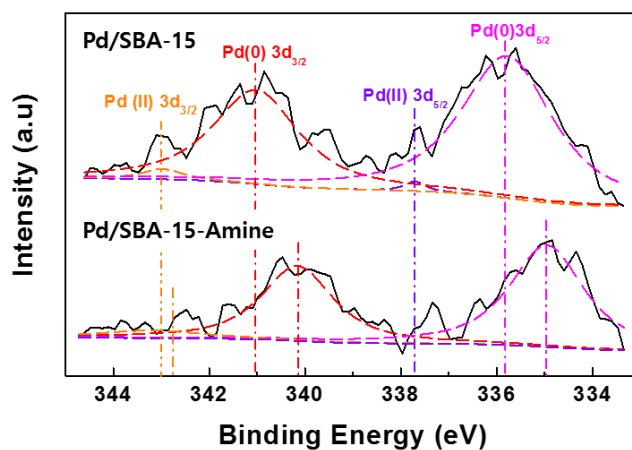


**Figure 2.4.** The high resolution Pd<sub>3d</sub> peaks in the XPS spectra of Pd/SBA-15-Amine and Pd/SBA-15.

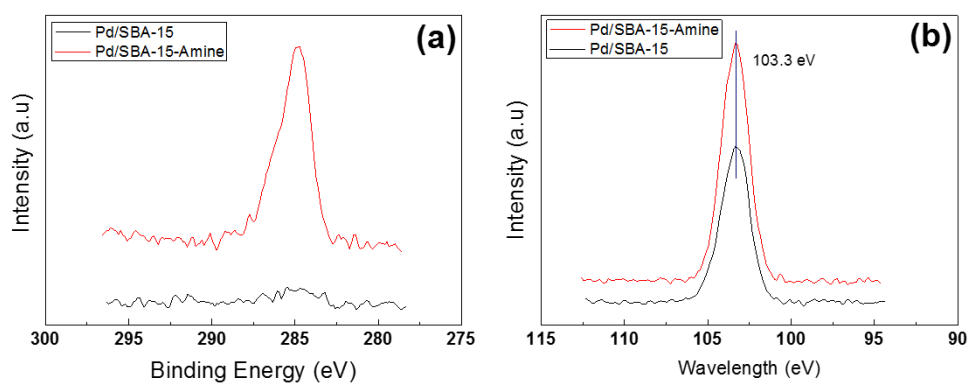


**Figure 2.5.** The high-resolution C1s peaks (a) and Si2p (b) in the XPS spectra of Pd/SBA-15 and Pd/SBA-15-Amine.

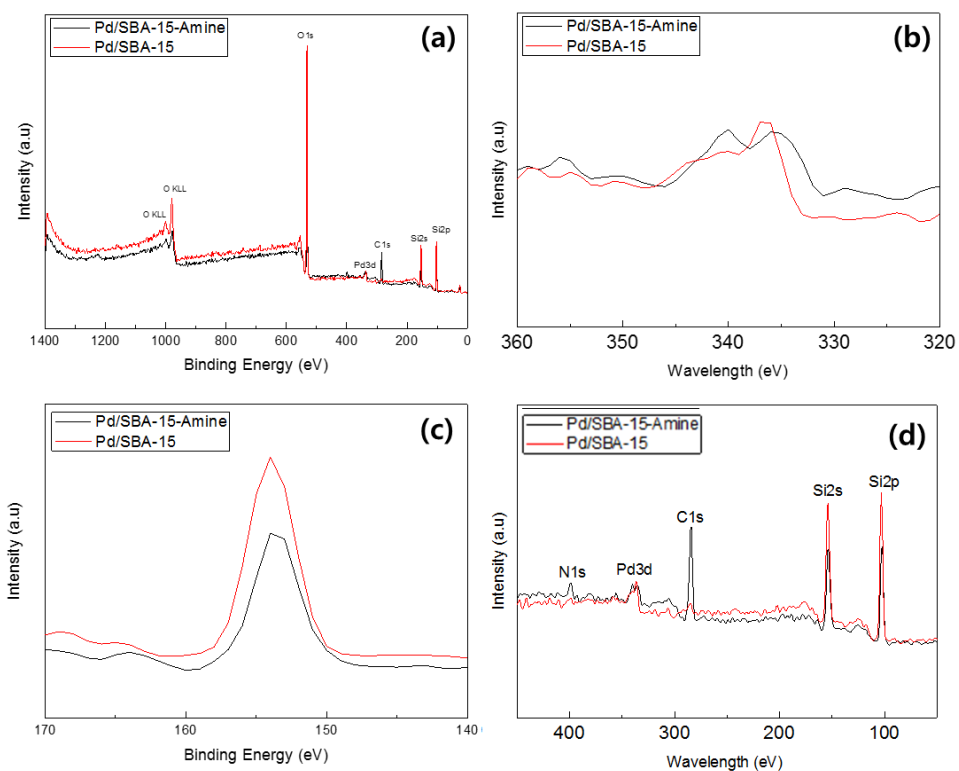


**Figure 2.6.** The survey spectrum of (a) Pd/SBA-15-Amine and Pd/SBA-15. Enlarged (b) Pd3d peaks and (c) Si2s peaks of the survey spectra. The peaks are assigned using Si2p peak as reference. (d) Enlarged XPS survey spectra of the materials with some of the important peaks.

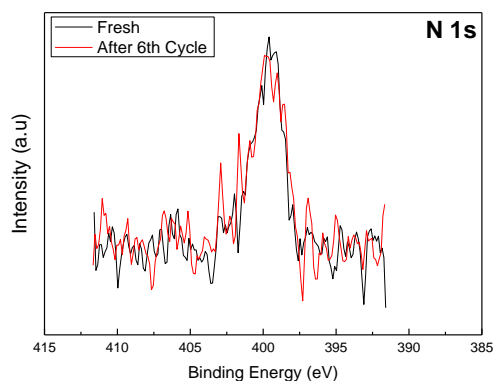


**Figure 2.7.** N1s XPS results of Pd/SBA-15-Amine catalysts after 0<sup>th</sup> and 6<sup>th</sup> cycle of the reaction.

Next, I evaluated the catalytic activities of Pd/SBA-15-Amine, SBA-15-Amine, Pd/SBA-15, and bare Pd NPs toward FA dehydrogenation at room temperature in the absence of external bases using the set-up shown in **Figure 2.1**. As illustrated in **Figure 2.8**, among these various materials I investigated Pd/SBA-15-Amine showed superior activity towards FA dehydrogenation. The rate and amount of total H<sub>2</sub>-release from FA over Pd/SBA-15-Amine were quite good with an initial TOF of 293 h<sup>-1</sup> in 10 min, which is among the highest TOF for FA dehydrogenation compared with the TOF values previously reported for other heterogeneous catalysis under ambient condition without bases.<sup>11-20</sup> The TOFs of recently developed heterogeneous catalysts without additives at ambient temperature are compared in **Figure 2.9** and **Table 2.1** entries 1-6. It is also valuable to compare with recent most active palladium catalyst, Pd/MSO-30, under ambient condition with using base (sodium formate) (**Table 2.1**, entry 7)<sup>34</sup> The control materials, Pd/SBA-15 and Pd NPs, showed only little catalytic activity, again supporting that the amine functional groups in Pd/SBA-15-Amine play a pivotal role in

accelerating FA dehydrogenation. It is also worth noting that the mesoporous silica material has no activity on its own towards the reaction.

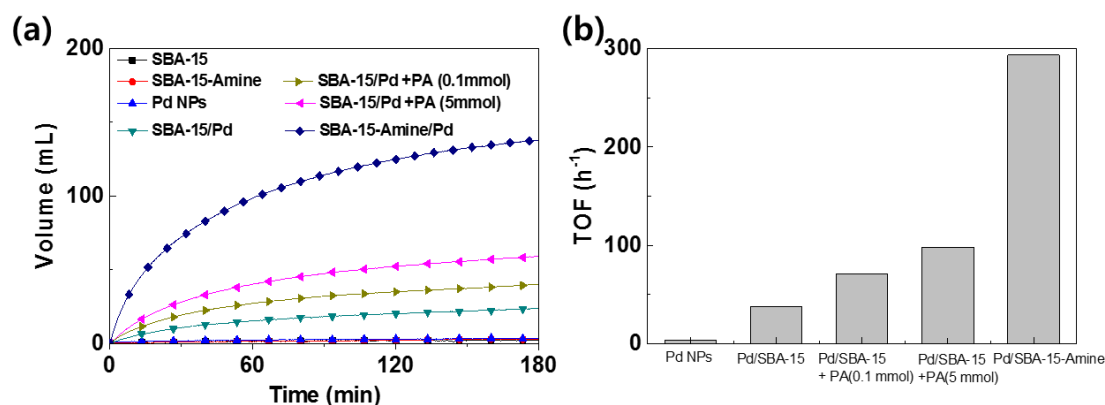


**Figure 2.8.** FA dehydrogenation catalyzed by the various materials synthesized and investigated here. (a) The volume of total gases produced versus time (min) curves. (b) TOFs at 10 min calculated based on the mol of Pd in the materials (catalysts). Reaction condition: 10 mL of 1 M FA was stirred with 50 mg of a desired catalyst (16  $\mu$ mol of palladium) at room temperature at 300 rpm.

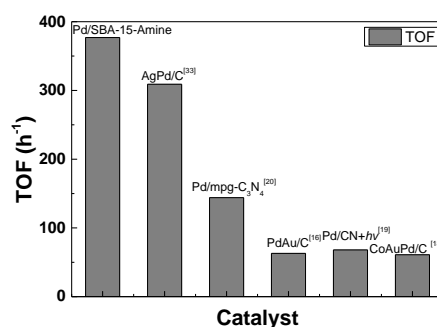


**Figure 2.9.** Comparison of TOFs at 10 min of Pd/SBA-15-Amine catalyst with other recently reported catalysts.

**Table 2.1.** Comparison of TOFs at 10 min of Pd/SBA-15-Amine catalyst with other recently reported catalysts without additives.<sup>[a]</sup>

<i>Entry</i>	<i>Catalyst</i>	<i>Temp.</i> [K]	<i>Volume</i> [mL]	<i>TOF</i> [h <sup>-1</sup> ]	<i>Additives</i>	<i>Ref.</i>
1a	Pd/SBA-15-Amine	299	38.5	300	None	This work
1b	Pd/SBA-15-Amine <sup>[b]</sup>	299	38.5	377	None	This work
2	AgPd/C	298	80	309	None	[33]
3	Pd/mpg-C <sub>3</sub> N <sub>4</sub>	298	52	144	None	[20]
4	PdAu/C	298	30	63	None	[16]
5	Pd/C <sub>3</sub> N <sub>4</sub> (+ <i>hν</i> )	288 <sup>[c]</sup>	8	68	None	[19]
6	CoAuPd/C	298	50	61	None	[18]
7	Pd/MSU-30	298	440	600	SF <sup>[d]</sup>	[34]

<sup>[a]</sup> The TOFs of some of the materials were calculated based **Eq. 2.1-2.2** in below. <sup>[b]</sup>

For recycled catalyst (activity increased due to its treatment with H<sub>2</sub>, see discussion). <sup>[c]</sup>

Please note that the temperature is different from others. <sup>[d]</sup> The ratio of Formic acid :

Sodium formate (SF) was 1:1.

$$\text{Moles of HCOOH at 10 min (n)} = \frac{PV}{RT} = \frac{1 \times \text{Total Volume at 10min}}{0.082 \times \text{Temperature}} \times \frac{1}{2} \quad \text{Eq. 2.1}$$

$$TOF \text{ (h}^{-1}\text{)} = \frac{\text{moles of HCOOH at 10 min}}{\text{moles of metal used} \times \text{time}} \quad \text{Eq. 2.2}$$

To further scrutinize the potential roles of the covalently tethered amine functional groups in the catalytic activity of the material towards FA dehydrogenation, I carried additional controlled experiments by using the physical mixtures of Pd/SBA-15 and various quantities of *n*-propylamine (PA) as catalyst. Compared with Pd/SBA-15, the physical mixture of Pd/SBA-15 and 0.1 mmol of PA showed an increased catalytic activity (**Figures 2.8** a-b). Note that the amount of amine or PA added is 0.1 mmol, which is almost equal to that covalently tethered amines in Pd/SBA-15-Amine. Upon addition of higher amount (5 mmol) of PA (**Figure 2.8a**, indicated with pink triangles), the corresponding activity increased slightly, but was still significantly lower than that obtained with Pd/SBA-15-Amine. Nevertheless, these results strongly imply that the added amine clearly acted as a Brønsted base, helping the deprotonation of FA. The results also suggest that the amine functional groups on the pore walls of Pd/SBA-15-Amine play multiple functions; *i.e.*, effectively deprotonating FA, besides allowing the synthesis of well-dispersed, electron rich, and catalytically active ultras-small Pd NPs for FA. As a result, the rate of dehydrogenation of FA over the Pd/SBA-15-Amine is much more enhanced.

FA is known to decompose *via* two possible pathways: (1) dehydrogenation ( $\text{HCOOH} \rightarrow \text{H}_2 + \text{CO}_2$ ) and dehydration ( $\text{HCOOH} \rightarrow \text{H}_2\text{O} + \text{CO}$ ).<sup>35</sup> To obtain better FA dehydrogenation systems for hydrogen production, catalysts that favor the former and suppress the latter are unquestionably preferred. This is because the second (dehydration) process does not produce  $\text{H}_2$ , not to mention it forms CO—a common poison for many catalysts, including the Pt catalysts typically used in hydrogen-fed

PEMFCs.<sup>36-40</sup> To examine the selectivity of the overall reaction to the one leading to the desired product, *i.e.*, H<sub>2</sub>, as defined as [moles of H<sub>2</sub>/moles of (H<sub>2</sub> +CO)]×100, FT-IR spectroscopy was employed to detect CO directly (**Figure 2.10**). The FT-IR spectrum obtained using Pd/SBA-15-Amine after 50 min gave a doublet peak located at ca. 2300 cm<sup>-1</sup>, indicating the evolution of CO<sub>2</sub>. The peak at ca. 2100 cm<sup>-1</sup> corresponding to CO was barely observable, strongly suggesting that H<sub>2</sub> selectivity is close to ca. 100 %.

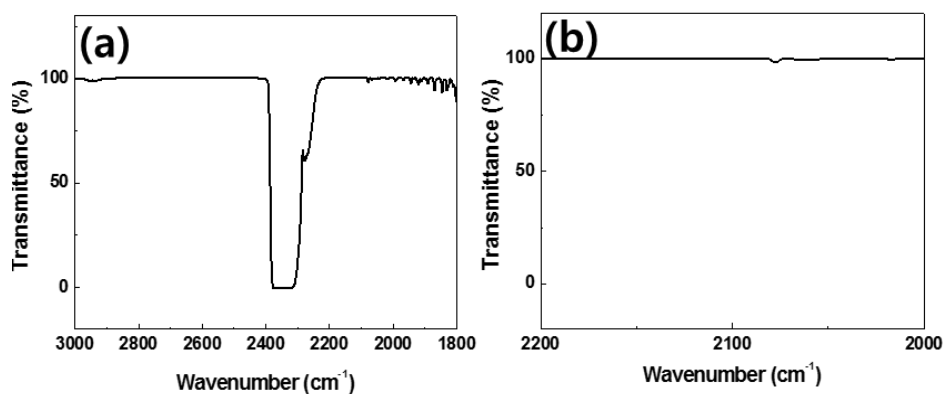


**Figure 2.10.** *In situ* FT-IR spectra of gases generated during FA dehydrogenation over Pd/SBA-15-Amine after 50 min: (a) CO<sub>2</sub> and CO stretch ranges (3000-1800 cm<sup>-1</sup>). (b) Enlarged area of CO stretching range (2200-2000 cm<sup>-1</sup>).

Recyclability studies of the catalytic material were additionally carried out for Pd/SBA-15-Amine. The result revealed that the catalyst was reusable at least six times without losing its activity (**Figure 2.11**). Interestingly, the TOFs were, in fact, found to increase after the 1<sup>st</sup> run becoming nearly identical for 2<sup>nd</sup> – 6<sup>th</sup> runs, reaching values as high as 377 h<sup>-1</sup>. Consistent with these results, the TEM images of Pd/SBA-15-Amine revealed no appreciable change in the structure of mesoporous silica even following completion of 6<sup>th</sup> catalytic recycle run. Moreover, the size of Pd NPs also remained

unchanged (**Figure 2.12**). The improved performance of the recycled catalysts particularly after the first cycle can be attributed to the reductive environment (due to the  $H_2$  produced by the reaction) that the catalyst is exposed to during the catalytic reactions, which can convert any surface-oxidized PdO possibly present on the original catalyst back to the catalytically active Pd-NPs. The condition which can convert any possibly oxidized PdO back to catalytic be active Pd and also prevents the Pd NPs from undergoing oxidation and losing their activity. Finally, to determine possible leaching of Pd from Pd/SBA-15-Amine during the reactions, the supernatant obtained after 150 min was examined by ICP-AES. The amount of Pd in the supernatant was found to be only ca. 10 ppm, indicating that the Pd NPs remain supported on Pd/SBA-15-Amine during the dehydrogenation reaction. In amine case, analyzed by atomic percentage of XPS (**Table 2.2**), the nitrogen after 6th recycle, the amount of amine (based on nitrogen) remains almost constant.

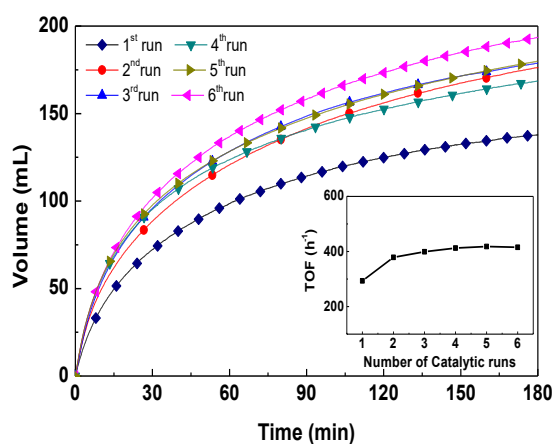


**Figure 2.11.** Recyclability results of Pd/SBA-15-Amine used in FA dehydrogenation: Volume (mL) of gas products ( $H_2 + CO_2$ ) versus time (min). Inset shows a plot of initial TOFs versus catalytic recycle runs.

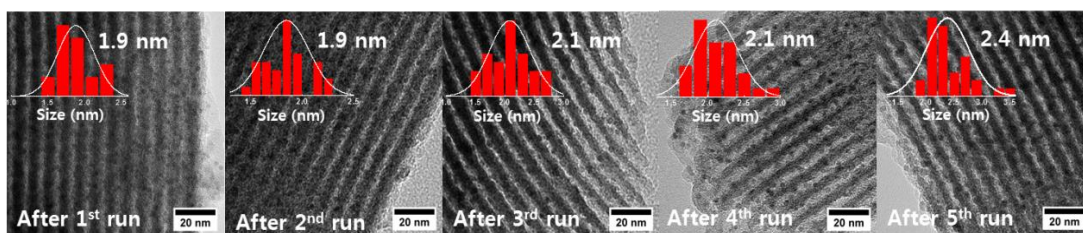


**Figure 2.12.** TEM images of spent Pd/SBA-15-Amine catalysts after each catalytic reaction cycle.

**Table 2.2.** Atomic percentages of elements as obtained from XPS results of the catalyst Pd/SBA-15-Amine after 0<sup>th</sup> and 6<sup>th</sup> cycle.

<i>No. of Cycle</i>	<i>Cl<sub>s</sub></i>	<i>N<sub>1s</sub></i>	<i>O<sub>1s</sub></i>	<i>Si<sub>2p</sub></i>	<i>Pd<sub>3d</sub></i>
0 <sup>th</sup>	30.2	2.40	47.4	19.5	0.44
6 <sup>th</sup>	22.3	2.98	52.4	21.9	0.54

## 2.4. Conclusion

In conclusion, amine-functionalized SBA-15-supported ultrasmall Pd NPs are synthesized and shown to have excellent activity towards FA dehydrogenation at room temperature in the absence of any external base, giving an initial TOF of  $293 \text{ h}^{-1}$ —one of the highest values reported so far for heterogeneous catalysts, to the best of our knowledge (**Table 2.1** and **Figure 2.9**). Despite the difference in synthetic strategies, the support materials, the metals involved and the catalytic procedures used in our case and in some of the previous related works, based on the catalytic outcomes there appears to be the so-called “*strong metal–molecular support interaction (SMMSI)*” reported by Xu group<sup>26</sup> at play in our material as well, or is more likely to be responsible for the enhanced catalytic activities attained in it. But some other subtle metal-ligand interactions may have also additionally contributed to the higher catalytic activity in our case as compared with the non-ligand counterparts because: 1) the surface properties, the size of the metal-nanoparticles of the amine-grafted catalysts and non-amine catalysts like ours are quite different and 2) based on recently reported mechanistic details<sup>31</sup> as well as some of our ongoing work, I also believe, the supported amine groups play an additional role as a base.

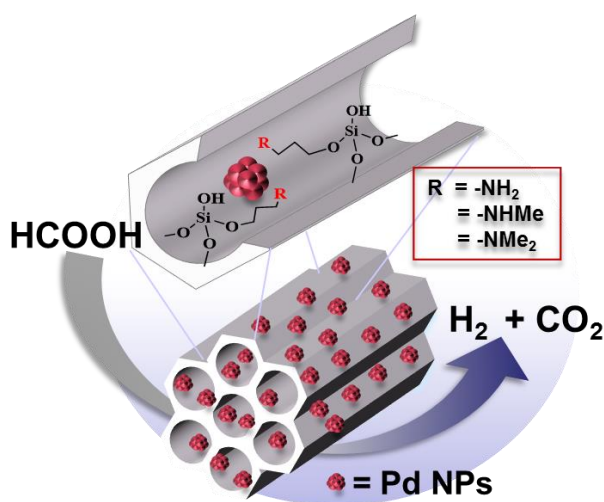
## 2.5. Reference

- (1) Haryanto, A.; Fernando, S.; Murali, N.; Adhikari, S. *Energy Fuels* **2005**, *19*, 2098–2106.
- (2) Bockris, J. O.M. *Science* **1972**, *176*, 1323.
- (3) Stolten, D. *Hydrogen and Fuel Cells. Fundamentals, Technologies and Applications*, Wiley-VCH, Weinheim, 2010.
- (4) Yadav, M.; Xu, Q. *Energy Environ. Sci.*, **2012**, *5*, 9698–9725.
- (5) Yang, J.; Sudik, A.; Wolverton, C.; Siegel, D. J. *Chem. Soc. Rev.*, **2010**, *39*, 656–675.
- (6) Zou, X.; Huang, X.; Goswami, A.; Silva, R.; Sathe, B. R.; Asefa, T. *Angew. Chem. Int. Ed.*, **2014**, *53*, 4372–4376.
- (7) Xie, G.; Zhang, K.; Guo, B.; Liu, Q.; Fang, L.; Gong, J. R. *Adv. Mater.* **2013**, *25*, 3820–3839.
- (8) Dapía, S.; Santos, V.; Parajó, J.C. *Biomass Bioenergy* **2002**, *22*, 213–221
- (9) Reutemann, W.; Kieczka, H. in *Ullmann's Encyclopedia of Industrial Chemistry*, Wiley-VCH, Weinheim, 2011.
- (10) Grasemann, M.; Laurenczy, G. *Energy Environ. Sci.* **2012**, *5*, 8171–8181.
- (11) Loges, B.; Boddien, A.; Junge, H.; Beller, M. *Angew. Chem. Int. Ed.* **2008**, *47*, 3962–3965.
- (12) Adhikari, S.; Fernando, S.; Haryanto, A. *Int. J. Hydrogen Energy*, **2007**, *32*, 2875–2880.
- (13) Gao, Y.; Kuncheria, J. K.; Jenkins, H. A.; Puddephatt, R. J.; Yap, G. P. A. *J. Chem. Soc., Dalton Trans.* **2000**, *18*, 3212–3217.
- (14) Adhikari, S.; Fernando, S.; Haryanto, A. *Catal. Today.* **2007**, *129*, 355–364.
- (15) Himeda, Y. *Green Chem.* **2009**, *11*, 2018–2022.
- (16) Metin, Ö.; Sun, X.; Sun, S. *Nanoscale* **2013**, *5*, 910–912.
- (17) Tedsree, K.; Li, T.; Jones, S.; Chan, C.W.A.; Yu, K.M.K.; Bagot, P.A.J.; Marquis, E.A.; Smith, G. D. W.; Tsang, S. C. E. *Nat. Nanotechnol.* **2011**, *6*, 302–307.
- (18) Wang, Z.-L.; Yan, J.-M.; Ping, Y.; Wang, H.-L.; Zheng, W.-T.; Jiang, Q. *Angew. Chem. Int. Ed.* **2013**, *52*, 4406–4409.
- (19) Cai, Y.-Y.; Li, X.-H.; Zhang, Y.-N.; Wei, X.; Wang, K.-X.; Chen, J.-S. *Angew. Chem. Int. Ed.* **2013**, *52*, 11822–11825.
- (20) Lee, J. H.; Ryu, J.; Kim, J.Y.; Nam, S.-W.; Han, J.H.; Lim, T.-H.; Gautam, S.; Chae, K.H.; Yoon, C.W. *J. Mater. Chem. A* **2014**, *2*, 9490–9495.
- (21) Cole-Hamilton, D. J. *Science* **2003**, *299*, 1702–1706.
- (22) Zhao, Y.; Deng, L.; Tang, S.-Y.; Lai, D.-M.; Liao, B.; Fu, Y.; Guo, Q.-X. *Energy Fuels* **2011**, *25*, 3693–3697.
- (23) Martis, M.; Mori, K.; Fujiwara, K.; Ahn, W.-S.; Yamashita, H. *J. Phys. Chem. C* **2013**, *117*, 22805–22810
- (24) Vicente, J.; Ereña, J.; Oar-Arteta, L.; Olazar, M.; Bilbao, J.; Gayubo, A. G. *Ind. Eng. Chem. Res.*, **2014**, *53*, 3462–3471
- (25) Zhu, W.; Michalsky, R.; Metin, Ö.; Lv, H.; S. Guo, C. Wright, X. Sun, A. A. Peterson, S. Sun, *J. Am. Chem. Soc.* **2013**, *135*, 16833–16836.
- (26) Yadav, M.; Akita, T.; Tsumoriab, N.; Xu, Q. *J. Mater. Chem.*, **2012**, *22*, 12582–12586.

- (27) Zhao, D.; Feng, J.; Huo, Q.; Melosh, N.; Fredrickson, G. H.; Chmelka, B. F.; Stucky, G. D. *Science* **1998**, *279*, 548–552.
- (28) Hoffmann, F.; Cornelius, M.; Morell, J.; Froba, M. *Angew Chem. Int. Ed.* **2006**, *45*, 3216–3251.
- (29) Margelefsky, E.L.; Zeidan, R.K.; Davis, M.E. *Chem. Soc. Rev.* **2008**, *37*, 1118–1126.
- (30) Li, C.; Zhang, Q.; Wang, Y.; Wan, H. *Catal. Lett.* **2008**, *120*, 126–136.
- (31) Mori, K.; Dojo, M.; Yamashita, H. *ACS Catal.* **2013**, *3*, 1114–1119.
- (32) Kumar, G.; Blackburn, J. R.; Albridge, R. G.; Moddeman, W. E.; Jones, M. M. *Inorg. Chem.* **1972**, *11*, 296–300.
- (33) Zhang, S.; Metin, Ö.; Su, D.; Sun, S. *Angew. Chem. Int. Ed.* **2013**, *52*, 3681–3684.
- (34) Zhu, Q.; Tsumori, N.; Xu, Q. *Chem. Sci.*, **2014**, *5*, 195–199.
- (35) Akiya, N.; Savage, P. E. *AIChE J.* **1998**, *44*, 405–415.
- (36) Winther-Jensen, B.; Fraser, K.; Ong, C.; Forsyth, M.; MacFarlane, D. R. *Adv. Mater.* **2010**, *22*, 1727–1730.
- (37) Camara, G.A.; Ticianelli, E.A.; Mukerjee, S.; Lee, S.J.; McBreen, J. *J. Electrochem. Soc.* **2002**, *149*, A748–A753
- (38) Manasilp, A.; Gulari, E. *Appl. Catal. B* **2002**, *37*, 17–25
- (39) Lee, J.S.; Locatelli, S.; Oyama, S.T.; Boudart, M. *J. Catal.* **1990**, *125*, 157–170
- (40) Li, Q.; He, R.; Gao, J.-A.; Jensen, J.O.; Bjerrum, N.J. *J. Electrochem. Soc.* **2003**, *150*, A1599–A1605.

## CHAPTER 3

### Formic Acid Dehydrogenation over Pd NPs Supported on Amine-Functionalized SBA-15 Catalysts: Structure-Activity Relationships



#### 3.1. Overview

Palladium nanoparticles (Pd NPs) supported on organoamine-functionalized SBA-15 mesoporous silica are known to have higher catalytic activity for formic acid dehydrogenation than Pd NPs supported on plain, unmodified SBA-15 mesoporous silica (chapter 1). The organoamine groups present around the Pd NPs play important roles in stabilizing the Pd NPs, providing *strong metal-molecular support interaction* (SMMSI) to the Pd NPs, and rendering enhanced catalytic activities to the materials toward formic acid dehydrogenation. However, detailed studies on the effects of different types of amine groups on the catalytic activities of mesoporous silica-supported Pd NPs toward formic acid dehydrogenation have not

been reported. Herein, I describe the synthesis of SBA-15 mesoporous silica grafted with three types of organoamine groups (primary, secondary, and tertiary amine), whose pores are further introduced with tetraamine palladium(II) complexes that are then reduced to Pd NPs *in situ* with 10 % of H<sub>2</sub>/N<sub>2</sub> at 250 °C. The effects of the different compositional and steric properties associated with the amine groups on *i*) the electronic properties of the Pd NPs, *ii*) the size of the Pd NPs, and *iii*) the structure-property relationships of the materials were closely examined. Based on the results, the materials' catalytic activities toward dehydrogenation of formic acid to generate hydrogen (H<sub>2</sub>) for fuel cells were determined.

### 3.2. Introduction

To address current energy and environmental issues associated with the rapid consumption of fossil fuels, major research on alternative, clean and sustainable energy sources is continuing worldwide.<sup>1,2</sup> Among the plausible alternative energy sources and carriers that have received significant attentions and that are expected to contribute to the solutions of these issues in the future, hydrogen (H<sub>2</sub>) stands out. In fact, H<sub>2</sub> has long been considered as one of the most notable and propitious energy carriers for portable and stationary energy systems. Furthermore, successful usage of H<sub>2</sub> as a plausible energy carrier in fuel cells for transportation applications and many other commercial alternative energy systems has long been proven.<sup>1-6</sup> However, H<sub>2</sub>-based energy systems have so far not made it into large scale applications, mainly due to the unavailability of efficient and economically feasible technologies that allow sustainable production, reliable storage, and cost-effective distribution of H<sub>2</sub>. So, the development of safe and

inexpensive hydrogen storage systems is one of the major requirements to enable hydrogen energy technologies to become a reality in a wide range of applications.<sup>6,7</sup> This has therefore led to extensive investigations, over the last decade, of numerous types of potential chemical-based H<sub>2</sub> storage compounds and materials.

Owing to its high stability, relatively low toxicity, high volumetric hydrogen storage density (53 g/L), and ease of portability, formic acid (FA) has recently been recognized as a good liquid phase chemical hydrogen storage medium. Furthermore, compared with H<sub>2</sub>, FA can easily be stored, transported and delivered to desired sites more economically using existing infrastructures.<sup>6-9</sup> In addition, FA can readily release H<sub>2</sub> on demand under ambient conditions in the presence of the right catalysts through the reaction:  $\text{HCOOH} \rightarrow \text{H}_2 + \text{CO}_2$ . Moreover, FA can potentially be regenerated by catalytic hydrogenation of CO<sub>2</sub>—the greenhouse gas that is often released by power plants and other industries—using the reaction:  $\text{H}_2 + \text{CO}_2 \rightarrow \text{HCOOH}$ .<sup>10</sup> This whole process will be appealing especially if the H<sub>2</sub> needed to carry out this reaction comes from water *via* renewable energy-driven water electrolysis. FA can also be produced from biomass by various processes such as biomass gasification, the Fischer-Tropsch process, etc.<sup>11</sup> Hence, FA is a highly attractive hydrogen carrier for decentralized fuel cell power generation sites, hydrogen refueling stations, large-scale renewable energy storage systems, and so forth.

To make FA-based hydrogen storage systems usable in practical fuel cells, the rate of H<sub>2</sub>-release from FA needs to be sufficiently fast though. While the dehydrogenation process of FA can be accelerated by increasing the reaction temperature, this process often leads to an undesired dehydration pathway that releases

CO *via* the reaction:  $\text{HCOOH} \rightarrow \text{H}_2\text{O} + \text{CO}$ . This reaction is undesired because one of its products, CO, is detrimental to the catalysts used in many fuel cells. Besides, the reaction does not generate the desirable product  $\text{H}_2$  anyway, but rather  $\text{H}_2\text{O}$ . So, it is of significant importance to develop selective catalysts that can promote only the desirable dehydrogenation pathway, besides being able to do so with high activity.<sup>6</sup> To attain this goal, a number of homogeneous and heterogeneous catalysts, which work either in the absence or in the presence of external bases, have been explored for FA dehydrogenation. Among them, heterogeneous mono- and bi-metallic materials, particularly those containing Pd, such as Pd,<sup>12–16</sup> PdAg,<sup>17</sup> and AuPd NPs,<sup>16,20</sup> were found to be excellent catalysts for the release of  $\text{H}_2$  from FA, in addition to being convenient to use.

In chapter 2, I recently demonstrated that the surface functional groups around Pd NPs could boost Pd's catalytic activity toward FA dehydrogenation reaction, besides stabilizing the Pd NPs (*i.e.*, the catalytically active sites).<sup>12</sup> In particular, ultrasmall Pd NPs supported on primary amine-functionalized SBA-15 were found to exhibit high catalytic activity and selectivity for dehydrogenation of FA at room temperature, even in the absence of external base in the reaction mixture. Similarly, several other studies demonstrated that multifunctional heterogeneous catalysts modified with primary amine groups, such as Pd-Amine-MIL-125,<sup>14</sup> Au-Amine-SiO<sub>2</sub>,<sup>21</sup> and Pd/PDA-rGO (PDA= 1,4, phenylene diamine)<sup>22</sup> had good catalytic activity toward FA dehydrogenation. Moreover, the immobilization of ultrafine metal nanoparticles on high surface area materials and their catalytic application including FA were reviewed by Q. Zhu et al.<sup>23</sup> Meanwhile, some studies indicated that modifying the electronic

properties and geometries of Pd active sites using amine-containing polymers could improve Pd's catalytic activity toward FA dehydrogenation.<sup>24</sup> Despite these interesting previous studies, the effects of different amine ligands and their structures on the size of Pd NPs as well as the materials' electronic properties and catalytic activities toward FA dehydrogenation have not yet been profoundly established.

In this contribution, a series of nanoporous silica materials modified with different types of amine groups and Pd NPs are synthesized, and the relationships among the types of amine functionalities, the Pd NPs forming in the materials, and the materials' catalytic properties toward FA dehydrogenation are elucidated. The materials include SBA-15 functionalized with different amine groups and Pd NPs, named Pd/SBA-15-Amine, where "Amine" represents primary, secondary, or tertiary amines. After investigating the structures and compositions of the materials obtained after each synthetic step, their catalytic properties are studied with particular focus being paid to the relationships among the amine functionality, the size of Pd NPs, and the materials' catalytic properties. Based on the results, the roles of the amine groups and the structural features of the Pd NPs in the materials toward the catalytic dehydrogenation reaction are determined.

### 3.3. Experimental section

#### 3.3.1. Materials and reagents

Poly(ethylene glycol)-*block*-poly(propylene glycol)-*block*-poly(ethylene glycol) (Pluronic® P123) was obtained from BASF. (3-Aminopropyl)trimethoxysilane (APTMS), ammonium hydroxide solution (NH<sub>4</sub>OH, 28-30 %, NH<sub>3</sub> basis), formic acid (HCOOH), anhydrous toluene, tetraethyl orthosilicate (TEOS), methylamine solution (CH<sub>3</sub>NH<sub>2</sub>, 40 wt.% in H<sub>2</sub>O), dimethylamine solution ((CH<sub>3</sub>)<sub>2</sub>NH, 40 wt.% in H<sub>2</sub>O) and palladium(II) chloride (PdCl<sub>2</sub>) were all purchased from Sigma-Aldrich. *N*-methylaminopropyltrimethoxysilane (MAPTMS) and 3-(*N,N*-dimethylaminopropyl)-trimethoxysilane (DMAPTMS) were acquired from Gelest, Inc. Hydrochloric acid (36.5 %) was purchased from Fischer Scientific. Anhydrous ethanol was acquired from Pharmco-Aaper. Different deuterated formic acids (DCOOH and HCOOD) were purchased from Cambridge Isotope Laboratories, Inc. All the reagents were used as received without further purification.

#### 3.3.2. Instrumentations

The following analytical instruments and methods were used to characterize the structures and compositions of materials and to evaluate their catalytic properties.

(A) Thermogravimetric analyses of the materials were performed with TGA 7 (PerkinElmer) in a temperature range of 50 to 900 °C and at a heating rate of 10 °C/min in air.

(B) The N<sub>2</sub> adsorption/desorption data for the materials were obtained with a Micrometrics ASAP 2000 instrument using N<sub>2</sub> at 77 K. Based on the data, the surface

areas of the materials were calculated using the Brunauer-Emmett-Teller (BET) method. The pore volume and pore size distributions of the materials were determined based on the amount of N<sub>2</sub> adsorbed at a relative pressure of 0.99 and with the Barrett-Joyner-Halenda (BJH) method, respectively.

(C) High-resolution transmission electron microscopy (HRTEM) and scanning transmission electron microscopy (STEM) images were acquired using a field emission FEI Tecnai microscope G2 F20 operating at 200 kV.

(D) X-ray photoelectron spectroscopy (XPS) was performed with a PHI 50000 VersaProbe instrument (ULVAC PHI) operating with an Al K $\alpha$  X-ray beam at a background pressure of  $6.7 \times 10^{-8}$  Pa. The spectra were calibrated using C1s's peak at 284.6 eV.

(E) The amount of Pd in the catalysts was determined by means of inductively coupled plasma-optical emission spectrometry (ICP-OES) (Varian 720ES, Agilent), and the amount of nitrogen in the materials was analyzed with an elemental analyzer (EA) (FLASH 2000, Thermo Scientific).

(F) All gaseous products generated by the catalytic reactions were analyzed by an *in situ* FT-IR spectrometer (Nicolet iS10, Thermo Scientific) equipped with a MCT detector and a customized gas cell. Spectral data were collected using a scan rate of 8 scans min<sup>-1</sup> with a resolution of 4 cm<sup>-1</sup>.

(G) UV-Vis diffuse reflectance spectroscopy was carried out with a Cary 5000 UV-Vis spectrometer (Agilent).

(H) Gas chromatography (GC) used by a Model 7890A instrument (Agilent

Technologies) equipped with a TCD detector and two columns: Hayesep D and MS13X.

### 3.3.3. *Synthesis of catalysts*

#### *Synthesis of SBA-15 mesoporous silica (Ext-SBA-15)*

SBA-15 was synthesized in acidic solution using Pluronic® 123 as a templating agent according to a previously reported procedure.<sup>25</sup> In a typical experiment, Pluronic® 123, HCl (12 M), TEOS, and deionized (D.I.) water were mixed with a mass ratio of 2:12:4.3:26, and stirred together at 40 °C for 24 h. The solution was then aged at 65 °C for an additional 24 h. After filtration of the solution, a solid product was recovered and washed several times with D.I. water. To remove the Pluronic® 123 templates from the resulting dried white powder product, 1.0 g of the material was taken and dispersed in a solution containing ethanol (100 mL) and diethyl ether (100 mL), and the mixture was stirred at 50 °C for 5 h. After filtering the mixture, then washing the resulting solid product with copious amount of diethyl ether and then ethanol, and letting it to dry at 40 °C in vacuum, a surfactant-extracted powder SBA-15 mesoporous silica material, named Ext-SBA-15, was obtained.

#### *Synthesis of SBA-15-functionalized with three different types of amines (SBA-15-Amine, where Amine is PA, SA, or TA) (Step I)*

To introduce different types of organoamine functional groups onto the surfaces of Ext-SBA-15, 1.0 g of Ext-SBA-15 was dispersed in anhydrous toluene (50 mL) containing 1.4 mmol of APTMS, MAPTMS, or DMAPTMS, and the mixtures were stirred at 80 °C for 6 h. The mixtures were then filtered, and the resulting solid products were washed with toluene and then ethanol, and let to dry at 40 °C in a vacuum oven.

White powder products, denoted as SBA-15-PA, SBA-15-SA, and SBA-15-TA, respectively, in which PA, SA, and TA stand for primary amine (PA,  $-\text{NH}_2$ ), secondary amine (SA,  $-\text{NHCH}_3$ ), or tertiary amine (TA,  $-\text{N}(\text{CH}_3)_2$ ) groups, were finally obtained. The three resulting amine-functionalized SBA-15 materials were generally labeled also as “SBA-15-Amine”. The synthetic procedure leading to the materials and their structures are illustrated in **Scheme 3.1**.

#### *Synthesis of Pd(II)/SBA-15-Amine materials (Step II)*

First, tetraaminepalladium(II) complex was synthesized by mixing  $\text{PdCl}_2$  ( $5.6 \times 10^{-2}$   $\mu\text{mol}$ ) with 1.0 M of ammonium hydroxide ( $\text{NH}_4\text{OH}$ , 1.8  $\mu\text{mol}$   $\text{NH}_3$ ) and then sonicating the solution until the dark red solution associated with  $\text{PdCl}_2$  turned colorless (or until complete complexation occurred). The resulting solution was added into a flask containing ethanol (1.0 mL), D.I. water (4.0 mL), and SBA-15-Amine (1.0 g), where Amine is PA, SA, or TA. Pd/SBA-15 were synthesized with using tetraaminepalladium(II) complex with Ext-SBA-15. The mixtures were stirred at 80 °C for 3 h. Pd/SBA-15 was synthesized by mixing the solution of tetraaminepalladium(II) chloride, was prepared above, with Ext-SBA-15 and stirring the two together at 80 °C for 3 h. After the mixtures were filtered, the solid products were washed with copious amounts of water and let to dry at 40 °C under vacuum. This led to different Pd(II)-anchored SBA-15-Amine materials (Pd(II)/SBA-15-Amine), as shown in *step II* in **Scheme 3.1**. The latter gave the corresponding control material Pd(II)/SBA-15.

#### *Reduction to Pd (0)/SBA-15-Amine (Step III)*

The Pd(II)/SBA-15-Amine and Pd(II)/SBA-15 materials prepared above were all subjected to reduction using 10 % of  $\text{H}_2/\text{N}_2$  at 250 °C for 3 h to convert the Pd(II) ions

in them into Pd NPs, and then yield Pd(0)/SBA-15-Amine or Pd(0)/SBA-15 materials. Here, the respective materials obtained were named as Pd(0)/SBA-15-PA (**1**), Pd(0)/SBA-15-SA (**2**), Pd(0)/SBA-15-TA (**3**), and Pd(0)/SBA-15 (a control material).

#### *Synthesis of control materials*

Control materials containing Pd(II) species supported on unfunctionalized (or unmodified) Ext-SBA-15 were synthesized by immobilizing three different tetraaminepalladium(II) complexes into the mesopores of amine-free Ext-SBA-15. Specifically, different tetraaminepalladium(II) complexes were synthesized by mixing PdCl<sub>2</sub> ( $5.6 \times 10^{-2}$   $\mu\text{mol}$ ) with solutions containing three different amines (1.8  $\mu\text{mol}$  of ammonia (NH<sub>4</sub>OH), methylamine (NH<sub>2</sub>CH<sub>3</sub>), or dimethyl amine (NH(CH<sub>3</sub>)<sub>2</sub>). The solutions were sonicated until they turned colorless, or the desired palladium(II)-amine complexes formed. The resulting different tetraaminepalladium(II) complexes were mixed and stirred with 1.0 g of unmodified Ext-SBA-15 at 80 °C for 3 h. This led to [Pd(NH<sub>3</sub>)<sub>4</sub>Cl<sub>2</sub>]/SBA-15, [Pd(NH<sub>2</sub>CH<sub>3</sub>)<sub>4</sub>Cl<sub>2</sub>]/SBA-15, and [Pd(NH(CH<sub>3</sub>)<sub>2</sub>)<sub>4</sub>Cl<sub>2</sub>]/SBA-15 materials, respectively. These control materials containing Pd<sup>2+</sup> complexes (*i.e.*, Pd(NH<sub>3</sub>)<sub>4</sub>Cl<sub>2</sub>-SBA-15, Pd(NH<sub>2</sub>CH<sub>3</sub>)<sub>4</sub>Cl<sub>2</sub>-SBA-15 and Pd(NH(CH<sub>3</sub>)<sub>2</sub>)<sub>4</sub>Cl<sub>2</sub>-SBA-15) were prepared mainly for comparative studies of the potential effect of organoamine ligands on the electronic properties or UV-Vis absorption properties of the Pd(II)-amine complexes vis-à-vis those of SBA-15-Amine-supported Pd(II)'s species before being subjected to reduction.

#### *Catalytic dehydrogenation to release H<sub>2</sub> from FA*

Catalytic FA dehydrogenation reactions were performed in a modified glass reactor (volume, 40 mL) containing an aqueous solution of FA (1.0 M, 10 mL) and the

catalyst (**1**, 50 mg; **2**, 46 mg; or **3**, 43 mg). Note that different masses of catalysts were used in the three cases in order to keep the amount of N (or amine groups) in them the same (*i.e.*, 64  $\mu\text{mol}$  of N in each case, based on EA). The reactor was kept at room temperature for 15 min under  $\text{N}_2$  atmosphere, and the quantity of the gas produced by the reaction was determined using an automatic gas burette system. To examine whether or not CO formed during the reaction, a portion of the gaseous products generated by the reaction was taken and analyzed by *in-situ* FT-IR spectroscopy and gas chromatography (GC). Unless otherwise noted, the catalytic activities for FA dehydrogenation reaction presented here were for catalysts prepared from the same batch of Ext-SBA-15. The values of catalytic turnover frequency (TOF) were calculated using **Eq. (3.1-3)** below.

$$\text{moles of hydrogen in 10 min, } n_{\text{H}_2} = P_{\text{atm}}(V_{\text{gas}}/2)/RT \quad \text{Eq. 3.1}$$

where  $P_{\text{atm}}$  is pressure,  $V_{\text{gas}}$  is the total volume of gases,  $R$  is the gas constant, and  $T$  represents a reaction temperature in Kelvin.

$$\text{Turnover frequency (TOF, } h^{-1}) = \frac{\text{moles of hydrogen in 10 min}}{(\text{moles of metal used}) * \text{time}} \quad \text{Eq. 3.2}$$

The selectivity of the FA dehydrogenation reaction in giving  $\text{H}_2$  as a product was examined *in-situ* using a FT-IR spectrometer and quantified using equation (**3**) below.

$$\text{H}_2 \text{ selectivity} = [\text{moles of H}_2 / \text{moles of (H}_2 + \text{CO})] \times 100 \quad \text{Eq. 3.3}$$

#### *Recyclability tests*

During the recovery of solid catalysts for recycling tests, it is common to lose a small amount of the catalysts. To minimize possible experimental errors arising from such possible loss of catalyst during the catalytic FA dehydrogenation tests, the

following procedure was employed. The same amount of catalyst (50 mg of **1**, for example) was added into four different identical reactors containing aqueous solution of FA (1.0 M, 10 mL). After letting the FA dehydrogenation reaction run for 2.5 h, D.I. water (10 mL) was added into each reactor. The spent catalysts were recovered by filtration and then washed with copious amount of D.I. water. The resulting recycled catalysts were let to dry in a vacuum oven before being used in the next cycle. Typically, they were combined, and the same procedure as the ones described above was performed in three reactors this time, with each containing 50 mg of the recovered catalyst **1**.

#### *Kinetic isotope effect (KIE) studies*

For kinetic studies, similar catalytic dehydrogenation reactions using deuterated FA (DCOOH and HCOOD), instead of FA, were carried out. Typically, 10 mL of 1.0 M of deuterated FA and the required amount of catalyst (**1**, 50 mg; **2**, 46 mg; or **3**, 43 mg) were used. The remaining steps and characterizations were the same as those employed above.

### 3.4. Result and discussion

#### 3.4.1. *Synthesis and characterization of amine-functionalized SBA-15 mesoporous silica*

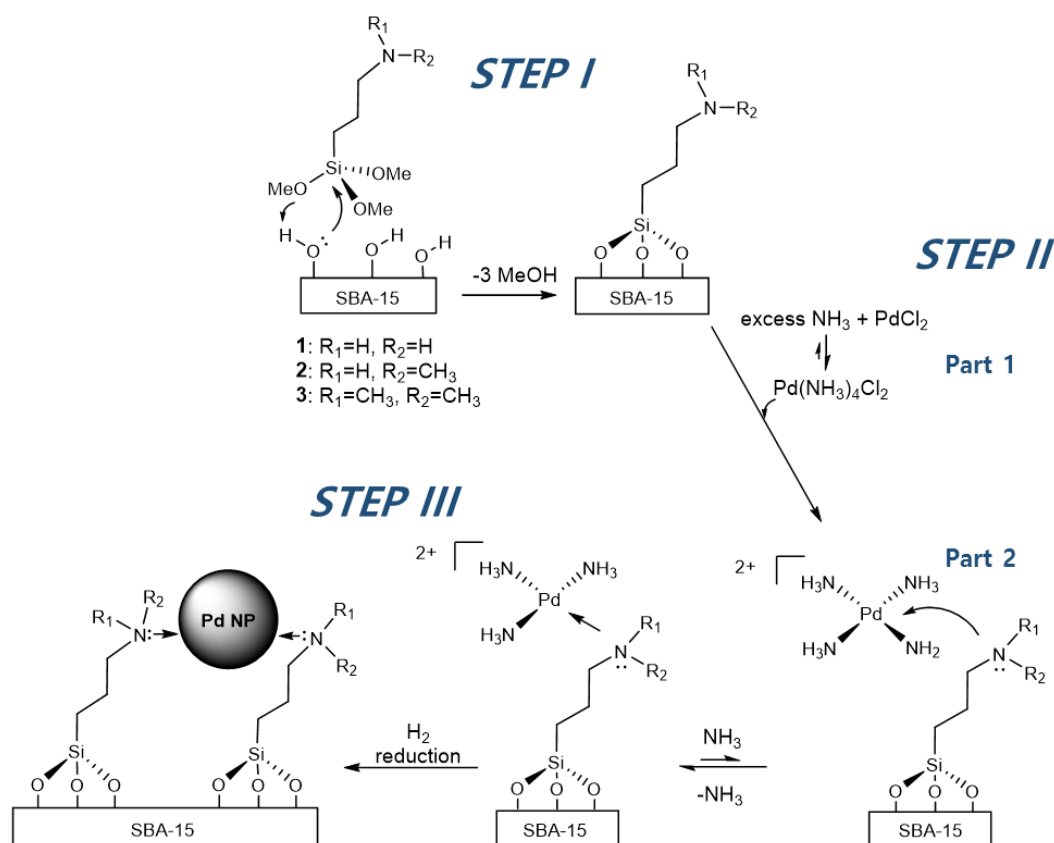
A series of SBA-15 mesoporous silica materials functionalized with primary amine (PA), secondary amine (SA), and tertiary amine (TA) were synthesized by following a procedure reported previously,<sup>12</sup> with a slight modification. In short, the surface Si-OH groups of surfactant-extracted SBA-15 mesoporous silica (Ext-SBA-15) were grafted with three different 3-aminoalkoxysilanes, namely ATPMS, MAPTMS, and DMAPTMS, in toluene at 80 °C for 6 h.

The Ext-SBA-15 was prepared by removing the Pluronic® P123 templates from the as-prepared mesostructured silica with a solvent-extraction method. This solvent extracted method was purposely chosen for removing the templates, because it leaves behind the much-needed, especially higher density of Si-OH groups. A higher density of Si-OH groups are necessary as they enable higher concentration of organoamine groups grafted onto the SBA-15 material, which those amine groups that can serve as co-catalysts in formic acid dehydrogenation catalysis (*vide infra*). Furthermore, higher concentration of organoamine groups helped for loading the materials with a larger density of Pd(II) ions, and thereby Pd nanoparticles, the actual groups that catalyze the dehydrogenation reaction. Besides, a substantial amount of the remaining P123 templates after the solvent-extraction process come off the material during the subsequent grafting step at 80 °C for 6 h, followed by washing, and then reduction step at 250 °C for 3 h while producing the Pd nanoparticles. Based on TGA analysis, Pluronic P123 is known to start to undergo degradation around 250 °C,<sup>26</sup> and over

longer time treatment even at 250 °C, a lot of the templates can be removed. So, there are negligible P123 remaining in the very final product or catalyst.

During this grafting process, the Si-OH groups of the Ext-SBA-15 materials act as nucleophiles and attack the 3-aminoalkoxysilanes, generating grafted organoamine groups covalently attached to the surfaces of Ext-SBA-15 through Si-O-Si bonds and methanol as byproduct (see *step I* in **Scheme 3.1**). By following this procedure, three different types of amine groups (PA, SA, and TA) were then anchored onto Ext-SBA-15 from their respective alkoxy silane precursors, resulting in three different types of amine-functionalized SBA-15 (*i.e.*, SBA-15-Amine, where “Amine” is PA, SA, or TA).

**Scheme 3.1.** Synthetic procedures leading to the different Pd/SBA-15-Amine materials/catalysts (in which “Amine” represents PA, SA, and TA) that were employed as catalysts for FA dehydrogenation.



The resulting SBA-15-Amine materials (where Amine represents PA, SA or TA) as well as the control material Ext-SBA-15 were all characterized by various analytical techniques including elemental analysis (EA), thermogravimetric analysis (TGA), and  $N_2$  porosimetry. EA showed the presence of similar amount of nitrogen (*ca.* 2.2 - 2.5 mmol/g<sub>cat</sub>) in all of the SBA-15-Amine materials (**Table 3.1**). The TGA results of the control material Ext-SBA-15 and all the SBA-15-Amine materials are depicted in **Figure 3.1**. In the case of the control material, the first weight loss (of *ca.* 0.62 %) was observed from room temperature (RT) to 120 °C, which is due to evaporation of

physisorbed water. A second weight loss (of *ca.* 16 %) was observed in the range of 120 °C to 700 °C, and it is most likely due to the loss of residual polymer templates and water as a result of condensation of Si-OH groups. In the case of the SBA-15-Amine materials, the TGA showed two distinct weight losses (**Figure 3.1a**). The first weight loss was observed from RT to 120 °C and attributed to the evaporation of physisorbed water from the surfaces of the materials. In all of SBA-15-Amine materials, a weight loss due to desorption of water (*ca.* 1.6 %) was also seen in the range of RT to 120 °C. The second weight loss was seen in the range of 120 °C to 700 °C, and it was due to the removal of residual polymer templates, water due to condensation of Si-OH groups, and more importantly, organoamine groups due to their combustion as:  $\text{NR}_1\text{R}_2(\text{CH}_2)_3\text{SiO}_{1.5} + x\text{O}_2 \rightarrow \text{SiO}_2 + \text{combustion products}$ .<sup>27</sup> After correcting for the loss of polymer templates and condensation of water, a weight loss due to the decomposition of organoamine moieties was determined to *ca.* 11 % for all these organoamine-functionalized materials. This result suggested that the three SBA-15-Amine materials had a similar amount of grafted organoamine moieties.

Based on N<sub>2</sub> adsorption/desorption measurements, the amine-functionalized SBA-15 generally showed lower surface areas than Ext-SBA-15 (**Table 3.1** and **Figure 3.1b-c**). Lower surface areas and pore diameters were to be expected in the former as the pores in the materials were partly occupied by surface organoamine groups, which resulted from organosilane grafting. Furthermore, the gas adsorption/desorption data of all the materials gave type IV isotherm with hysteresis loops, indicating the presence of mesoporosity or mesopores in the materials as well as the retention of the mesoporous structure in the materials after organoamine grafting. However, as organoamines were

grafted and as the grafted organoamines got bulkier, the pore sizes of the materials got increasingly reduced. Notably, the average BJH pore diameters of Ext-SBA-15, SBA-15-PA, SBA-15-SA and SBA-15-TA were found to be 6.4, 5.1, 4.4, and 3.3 nm, respectively (**Figure 3.1c** and **Table 3.1**). The materials also got concomitantly lower pore volumes (**Table 3.1**).

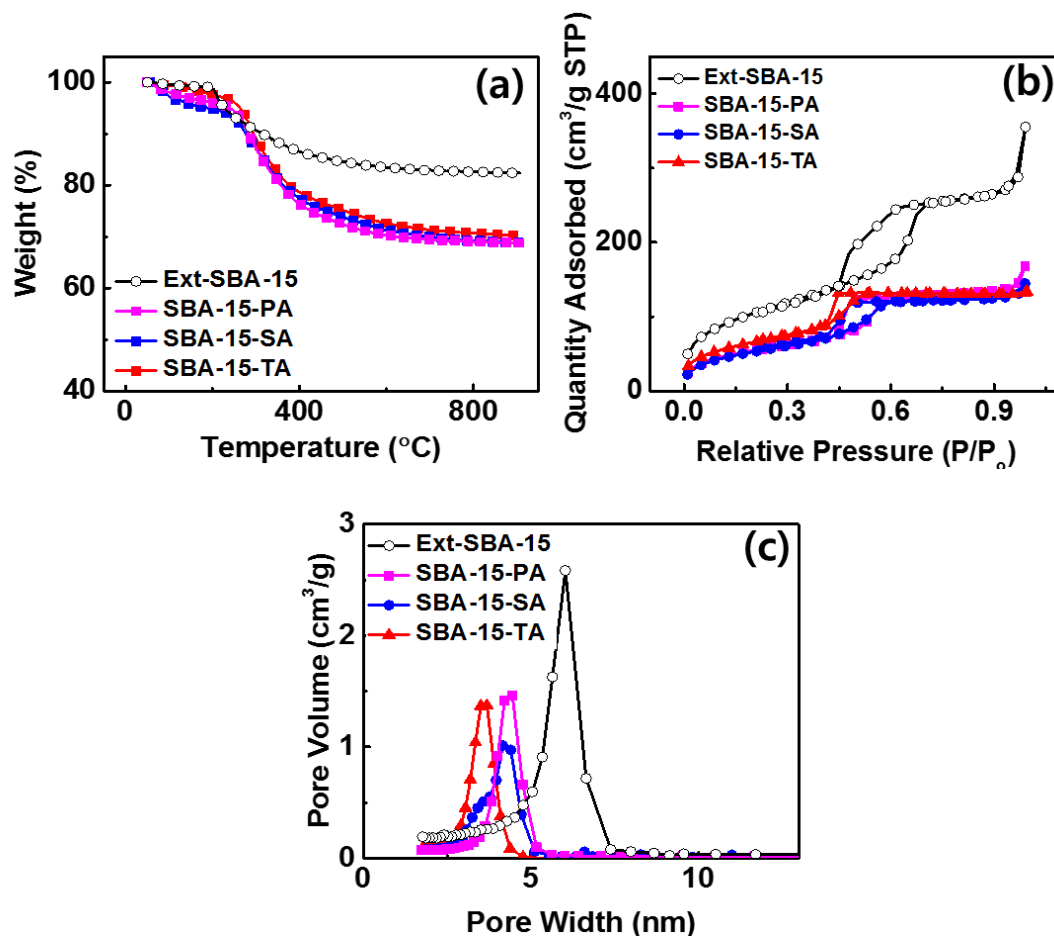


**Figure 3.1.** (a) Thermogravimetric analysis (TGA) traces, (b) N<sub>2</sub> Adsorption and desorption profiles and pores size distribution of amine-modified SBA-15 materials.

**Table 3.1.** Textural properties of Ext-SBA-15 (a control material) and the three SBA-15-Amine materials derived from it by grafting organosilane.

	<i>Amount of N</i>	<i>BET Surface Area</i>	<i>Pore Size</i>	<i>Pore</i>
	<i>(mmol/</i>	<i>Area</i>	<i>(nm)<sup>c</sup></i>	<i>Volume</i>
	<i>g cat)<sup>a</sup></i>	<i>(m<sup>2</sup>/g)<sup>b</sup></i>		<i>(cm<sup>3</sup>/g)<sup>c</sup></i>
Ext-SBA-15	N/A	378	6.4	0.48
SBA-15-PA	2.3	200	5.1	0.23
SBA-15-SA	2.2	195	4.4	0.19
SBA-15-TA	2.5	237	3.3	0.17

<sup>a</sup> Obtained based on EA. <sup>b</sup> Obtained based on N<sub>2</sub> adsorption/desorption data. <sup>c</sup> Obtained from the BJH adsorption branch of the isotherms.

Despite its containing bulkier grafted groups, the surface area of SBA-15-TA was found to be slightly higher than those of SBA-15-PA and SBA-15-SA. Part of the reason behind this intriguing trend may have to do with the fact that SBA-15-TA is functionalized with more non-polar groups than SBA-15-PA and SBA-15-SA. The modification of the silica surface with hydrophobic groups is known to complicate the value used for the cross-sectional area of the adsorbate molecules in the conventional BET surface area analysis of materials.<sup>28-30</sup> The degree of interaction of the non-polar adsorbate N<sub>2</sub> with the adsorbent is of great importance in adsorption and surfaces exhibiting weaker interactions can ultimately determine the effective molecular area of N<sub>2</sub> molecules occupying the surface. It was shown that the effective cross-sectional area for N<sub>2</sub> on silica surface could vary between 16.2 to 21 Å<sup>2</sup> depending on the surface modification of silica.<sup>28-30</sup> Furthermore, the adsorption isotherms for organic-modified

silicas in the low relative pressure region could be less convex than those of bare silica, and an extreme example of which would be the concave low-pressure regions seen with type III isotherms which are characterized by weak interactions.<sup>31</sup> Although several types of corrections to obtain the effective cross-sectional area of N<sub>2</sub> were considered or developed, the BET surface area analysis results by the very nature has been not be precise, especially for non-polar modified porous materials. So, I believe that the BET surface area calculation may have over-exaggerated the value for relatively hydrophobic sample SBA-15-TA (**3**) compared with those of SBA-15-PA (**1**) and SBA-15-SA (**2**).

#### **3.4.2. Synthesis and characterization of Pd(II)/SBA-15-Amine**

The immobilization of palladium(II) ions into SBA-15-Amine was achieved by contacting SBA-15-Amine materials with a solution containing tetraaminepalladium(II) chloride, or [Pd(NH<sub>3</sub>)<sub>4</sub>Cl<sub>2</sub>]. The latter was generated *in situ* by mixing PdCl<sub>2</sub> and NH<sub>3</sub> (aq) (Part 1 in *Step II* in **Scheme 3.1** and **Figure 3.2**). To monitor the interactions between the tetraaminepalladium(II) complexes and the amine groups (*i.e.*, PA, SA or TA) grafted onto Ext-SBA-15, all the resulting three different Pd(II)/SBA-15-Amine materials were analyzed by UV-Vis diffuse reflectance spectroscopy (**Figure 3.3a**). The Pd(II)/SBA-15-Amine materials exhibited an absorption maximum ( $\lambda_{\max}$ ) centered between *ca.* 285 to 300 nm, attributable ligand-metal (L-M) charge transfer or interband transitions in the metal-amine complexes.<sup>32,33</sup> Notably also, the absorption spectra of all the Pd(II)/SBA-15-Amine materials showed bathochromic shifts compared with that of the control material Pd(II)/SBA-15 (whose  $\lambda_{\max}$  was at *ca.* 282 nm). The extent of the shift in the absorption maxima increased as the number of methyl substituents on

the nitrogen atom of the amine group was increased: *i.e.*, Pd(II)/SBA-15-PA ( $\lambda_{\text{max}} = 285$  nm), Pd(II)/SBA-15-SA ( $\lambda_{\text{max}} = 292$  nm), and Pd(II)/SBA-15-TA ( $\lambda_{\text{max}} = 300$  nm). These results implied that a ligand exchange reaction between the tetraaminepalladium(II) ( $[\text{Pd}(\text{NH}_3)_4]^{2+}$ ) complexes and the amine moieties grafted on Ext-SBA-15 ( $\text{NR}_1\text{R}_2 \cdots \text{SBA-15}$ ) occurred, ultimately leading to  $[\text{Pd}(\text{NH}_3)_3(\text{NR}_1\text{R}_2)]^{2+} \cdots \text{SBA-15}$  materials (Part 2 of *Step II* in **Scheme 3.1**). Similar bathochromic shifts were seen in the three control materials prepared by mixing unmodified Ext-SBA-15 with different tetraaminepalladium(II) complexes, namely  $[\text{Pd}(\text{NH}_3)_4\text{Cl}_2]^{2+}$ ,  $[\text{Pd}(\text{NH}_2\text{CH}_3)_4\text{Cl}_2]^{2+}$ , and  $[\text{Pd}(\text{NH}(\text{CH}_3)_2)_4\text{Cl}_2]^{2+}$  (**Figure 3.3**).



**Figure 3.2.** Photographs of Ext-SBA-15 (1<sup>st</sup> row), Pd(II)/SBA-15-Amine (2<sup>nd</sup> row), and Pd(0)/SBA-15-Amine (3<sup>rd</sup> row). (a) Pd(II)/SBA-15-PA, (b) Pd(II)/SBA-15-SA, (c) Pd(II)/SBA-15-TA, (d) Pd(0)/SBA-15-SA, (e) Pd(0)/SBA-15-SA, and (f) Pd(0)/SBA-

15-TA materials.

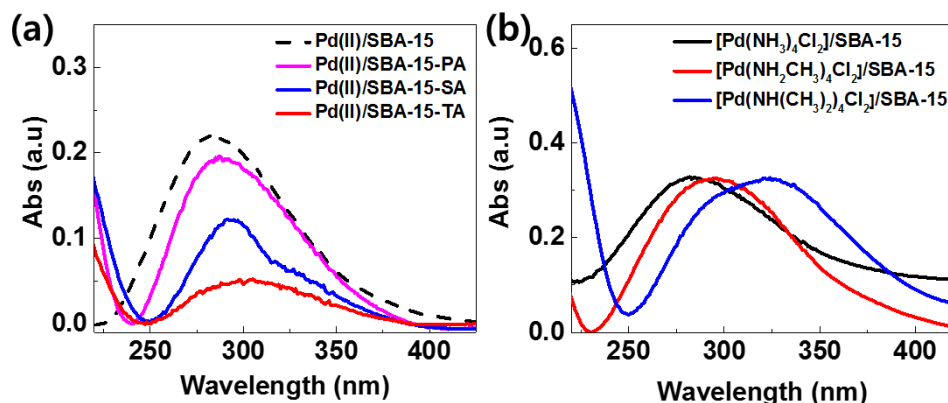


**Figure 3.3.** UV-Vis diffuse reflectance spectra of (a) Pd(II)/SBA-15-Amine materials and (b) Ext-SBA-15 immobilized with different tetraamine palladium(II) complexes ( $[\text{Pd}(\text{NH}_3)_4\text{Cl}_2]$ ,  $[\text{Pd}(\text{NH}_2\text{CH}_3)_4\text{Cl}_2]$ , and  $[\text{Pd}(\text{NH}(\text{CH}_3)_2)_4\text{Cl}_2]$ ).

The corresponding UV-Vis spectra for the Pd-amine complexes in solution are shown in **Figure 3.4**. The red shift in the absorption band of the complexes as the number of amine groups on the amine moiety is increased is not unusual. *N*-methylation of amino-ligands is known to induce a marked red shift of the L-M charge transfer bands of many metal complexes comprising Pd(II), Pd(I), Cu(II) ions, etc. and amine ligands.<sup>32,33</sup> This red shift is often due to the following three possible factors of: i) *N*-methylation of amine causes an anodic shift in the redox potential or a reduction in the electrode potential of the metal ions in the complexes. ii) The *N*-methyl groups decrease the degree of solvation of the complexes. iii) *N*-methylation of amine groups increases the electron density of the nitrogen donor atom, and makes the amine moiety a better  $\sigma$  donor and the metal-amine complex to have a lower optical electronegativity. In the presence of polar hydrogen bond capable solvents though, the methyl groups around the amines can make the latter a weaker  $\sigma$ -donor to the metal ions. As a result, tertiary

amines are widely reported to be poorer  $\sigma$ -donors and poorer ligands than the corresponding primary and secondary amines.<sup>33,34</sup> The effect of *N*-methylation on the  $\sigma$ -donating properties of the non-bonding electron pairs of the nitrogen atoms can, in turn, be attributed to two main factors: a) the formation of M-N-H $\cdots$ O hydrogen bonds to the solvent molecules make the nitrogen atoms of primary and secondary amines stronger  $\sigma$ -donors (conversely, the absence of this effect in the nitrogen atoms of tertiary amine ligands make them weaker  $\sigma$  donors) and b) the steric hindrance due to the insertion of methyl groups within the ligand framework which can cause elongation of the M-N bond and distortions of the coordination sphere around Pd(II) in the complexes. Since in our spectra the experiments were conducted on complexes in which the organoamine ligand molecules themselves are used as solvent or the complexes are present on dried powder materials, there is no additional effect due to the solvents. So, any possible effect due to solvents can be ruled out. This then leaves the observed red shift in the charge transfer band upon more *N*-methylation of the ligands to be exclusively due to the increasingly weakening  $\sigma$  electron-donating properties of the nitrogen atoms of the amine ligands and the anodic shift of the redox potential.<sup>33,34</sup>

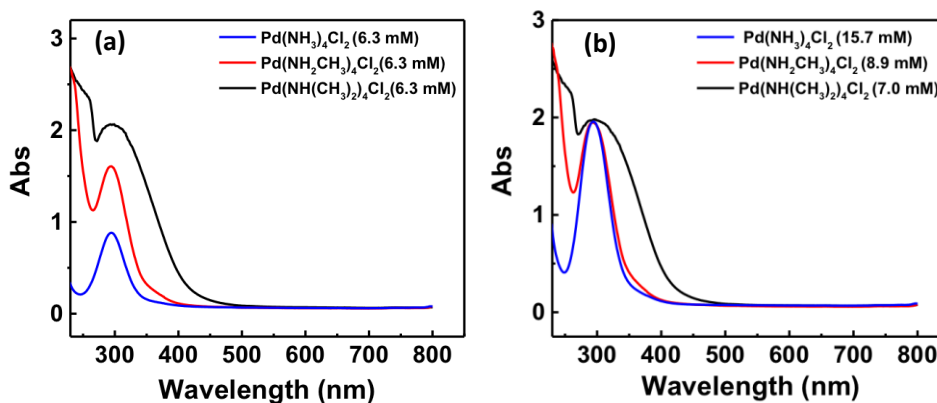


**Figure 3.4.** The UV-Vis spectra of the aqueous solutions containing three different tetraamine palladium(II) complexes,  $[\text{Pd}(\text{NH}_3)_4\text{Cl}_2]$ ,  $[\text{Pd}(\text{NH}_2\text{CH}_3)_4\text{Cl}_2]$ , and  $[\text{Pd}(\text{NH}(\text{CH}_3)_2)_4\text{Cl}_2]$ : (a) for the same concentrations and (b) for similar absorbance using different concentrations.

### 3.4.3. Synthesis and characterization of a series of Pd(0)/SBA-15-Amine materials/catalysts

Following the grafting of the organoamine groups and immobilization of Pd(II) ions into the Ext-SBA-15, the materials were reduced using  $\text{H}_2$  gas (10/90 % of  $\text{H}_2/\text{N}_2$ ) at 250 °C. This afforded black or greyish colored, powder SBA-15-Amine materials containing different amine groups and supported Pd NPs. The materials were named Pd(0)/SBA-15-Amine, where “Amine” is PA, SA or TA (see *Step III* in **Scheme 3.1** and **Figure 3.2**). The materials were characterized first by EA, ICP-OES, and  $\text{N}_2$  porosimetry, and the results are summarized in **Table 3.2** and **Figure 3.5**. The EA and ICP-OES results indicated the presence of different amounts of nitrogen and palladium in the materials. While the amount of nitrogen in the catalysts was nearly identical (*ca.* 1.4 mmol/ $g_{\text{cat}}$ ), the amount of palladium in them varied, where **1** had 0.41 mmol/ $g_{\text{cat}}$ , **2**

had 0.11 mmol/g<sub>cat</sub>, and **3** had 0.16 mmol/g<sub>cat</sub>.

**Table 3.2.** Textural properties and elemental compositions of Pd(0)/SBA-15-Amine materials.

	<i>Amount of N (mmol/ g<sub>cat</sub>)<sup>a</sup></i>	<i>Amount of Pd(0) (mmol/ g<sub>cat</sub>)<sup>b</sup></i>	<i>BET Surface Area (m<sup>2</sup>/g)<sup>c</sup></i>	<i>Pore Size (nm)<sup>d</sup></i>	<i>Pore Volume (cm<sup>3</sup>/g)<sup>d</sup></i>
Pd/SBA-15 <sup>e</sup>	N/A	0.32	166	8.1	0.27
<b>1</b>	1.3	0.41	186	7.5	0.29
<b>2</b>	1.4	0.11	196	4.6	0.26
<b>3</b>	1.5	0.16	242	4.4	0.30

<sup>a</sup> Analyzed by EA; <sup>b</sup> Analyzed by ICP-OES; <sup>c</sup> Obtained from the N<sub>2</sub> adsorption/desorption data using the BET method; <sup>d</sup> Obtained from the adsorption branch of the gas adsorption/desorption isotherm using the BJH method. <sup>e</sup> A control material made from unmodified SBA-15.

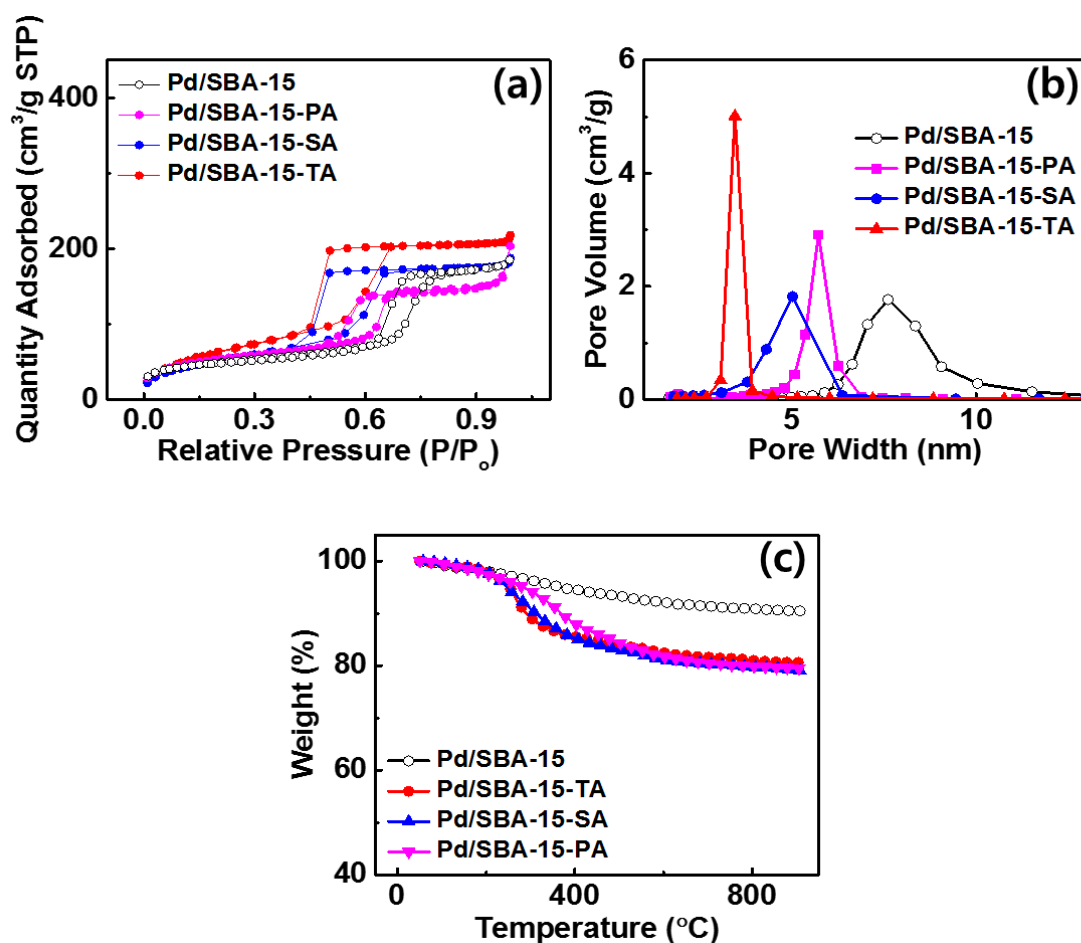


**Figure 3.5.** (a) N<sub>2</sub> Adsorption and desorption profiles and (b) thermogravimetric analysis (TGA) traces of Pd/SBA-15-Amine materials (where Amine = PA, SA, or TA groups).

Although I used identical amount of Pd(II) precursor moles during the synthesis of the materials **1**, **2**, and **3**, I found that the final amount of Pd loaded in the materials varied. These differences are likely to do with the differences in hydrophobicity of the organoamine groups grafted in the materials. More specifically, the loadings of Pd in **2** and **3** were lower than that in **1** (Table 3.2) because of the relatively weaker ability of [Pd(NH<sub>3</sub>)<sub>4</sub>]<sup>2+</sup> species to anchor onto SBA-15-grafted tertiary and secondary amine groups than SBA-15-grafted primary amine groups. In other words, the Pd(II)

complexes anchor less favorably in SBA-15-SA and SBA-15-TA than in SBA-15-PA. The slightly higher amount of Pd in **3** (0.16 mmol/g) compared with that in **2** (0.11 mmol/g) is because **3** has slightly more amount of amine groups than **2**.

Their N<sub>2</sub> adsorption/desorption data of these materials also gave a type IV isotherm with some hysteresis loops, again indicating that the original mesoporous structures of the materials remained intact even after they were treated at relatively high temperature in H<sub>2</sub>/N<sub>2</sub> to reduce the Pd(II) ions to Pd(0) (**Figure 3.2a**). Furthermore, the BET surface areas of the Pd(0)/SBA-15-Amine materials were found to reduce compared with the corresponding SBA-15-Amine materials or the materials before reduction (**Table 3.2**). Furthermore, these materials too showed increasingly lower average BJH pore diameter and pore volume, as the types of organoamine groups grafted in them were increasingly bulkier (**Table 3.2** and **Figure 3.5**).

Next, the three Pd(0)/SBA-15-Amine materials and the control material Pd(0)/SBA-15 were all analyzed by TGA (**Figure 3.5c**). All the Pd(0)/SBA-15-Amine materials exhibited an initial weight loss of *ca.* 0.75 % between RT to 120 °C and a second weight loss of 11% between 120 to 700 °C. The former was attributed to the loss of physisorbed water and the latter was attributed to the decomposition of organoamine groups, residual templates and water due to condensation of Si-OH groups in the materials. In contrast, the control material Pd(0)/SBA-15 showed a weight loss of *ca.* 1.1 % in the temperature range of RT to 120 °C (due to the removal of water) and a weight loss of *ca.* 7.5 % in a temperature range of 120 to 700 °C (due to the removal of residual Pluronic polymer templates and water due to condensation of Si-OH groups). The latter value was smaller because this material did not contain organoamines, as the Pd(0)/SBA-15-Amine materials did (**Figure 3.5c**).

To examine the effect of the type of amine groups in the SBA-15-Amine materials on the size and size distribution of the Pd NPs, high-angle annular dark-field scanning transmission electron microscopy (HAADF-STEM) was employed. As depicted in **Figure 3.6.**, the as-synthesized catalysts displayed well-dispersed, supported Pd NPs throughout their structures. However, the sizes of the Pd NPs were found to vary from material to material. The average size of Pd NPs in Pd/SBA-15 (**Figure 3.6**) was 2.5 nm, but those in catalysts **1** and **2** were almost similar in size and much smaller: 1.5 nm and 1.6 nm, respectively (**Figure 3.6b-c**). On the other hand, the average size of Pd NPs in **3** was much bigger (2.9 nm) (**Figure 3.6d**).

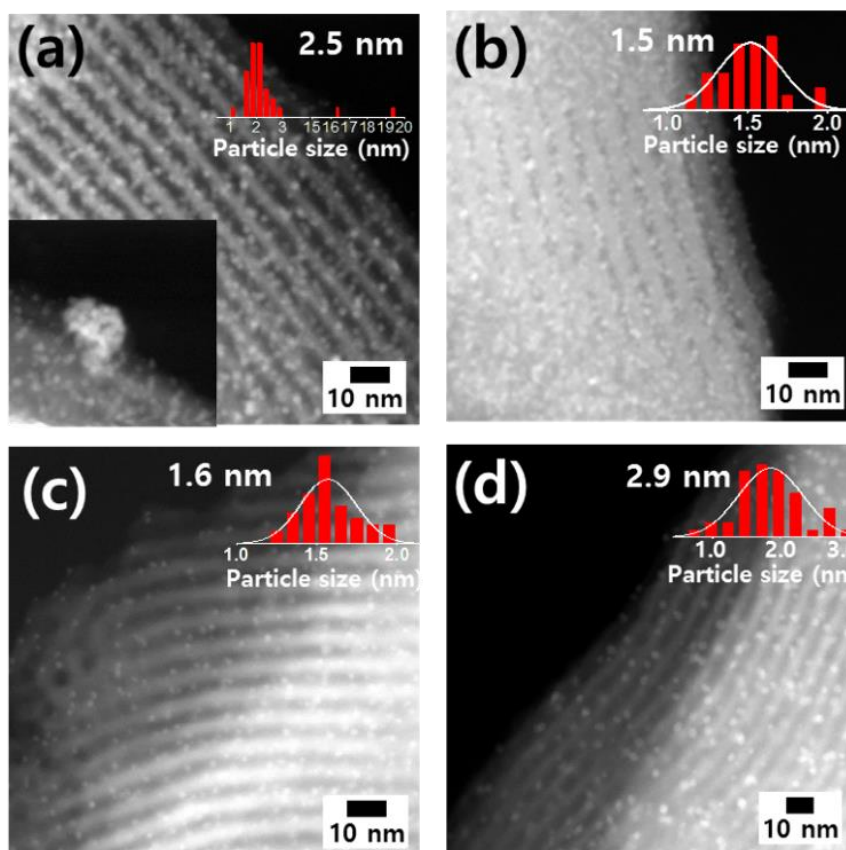


**Figure 3.6.** STEM images of different catalysts: (a) Pd/SBA-15, (b) Pd/SBA-15-PA (1), (c) Pd/SBA-15-SA (2), and (d) Pd/SBA-15-TA (3). The average size of Pd NPs in Pd/SBA15 (a) is taken from reference 13.

The observed difference in the size of Pd nanoparticles formed in the different catalysts can be accounted based on the relative ability of the SBA-15-grafted organoamine ligands in stabilizing the Pd(II) complexes, and then Pd NPs, just like many other organic ligands and surfactants, such as poly(ethylene glycol) (PEG), polyvinylpyrrolidone (PVP), etc., used as capping agents to synthesize various metallic nanoparticles do. The different amine functionalities existing in the as-prepared SBA-15 materials in our case can render different degrees of stability to the Pd species forming in the materials. In other words, the Pd(II) complexes or Pd nanoparticles in

the materials reported herein are expected to have different degree of interaction with different SBA-15 grafted amine ligands, and thus end up with different sizes. More specifically, compared with secondary and primary amine ligands, tertiary amine ligands are weaker  $\sigma$  electron donors to Pd(II) in solution, due to their poorer ability to undergo solvation, and also form less thermodynamically stable Pd(II) complexes.<sup>33</sup> *N*-methylation can also lead to a molecular crowding, more steric hindrance and stiffening, and elongated and relatively more distorted Pd-N bonds in the Pd(II)-amine complexes. Pd(II) has a higher tendency to impose its own geometry on the ligands as well, and this can in turn reduce the ability of the ligands to adapt to the stereochemical requirements of Pd(II) species well enough. Hence, Pd(II) complexes or metallic species (or Pd nanoparticles forming from the reduction) in the presence of more *N*-methylated ligands are less stable than their unmethylated counterparts. As a result, the tertiary amine ligands interact less strongly with the Pd nanoparticles than the primary amine groups do, resulting in less stabilized Pd nanoparticles that have greater chances to grow and form relatively bigger Pd particles.

To elucidate the potential electronic interaction between the amine groups and the Pd NPs, X-ray photoelectron spectroscopy (XPS) was applied and the peaks associated with Pd 3d in the spectra were carefully analyzed (**Figure 3.7**). When organoamine functional groups were present in the materials (or for Pd(0)/SBA-15-Amine materials), the peaks for Pd(0) 3d<sub>3/2</sub> and Pd(0) 3d<sub>5/2</sub> were shifted to lower binding energies of 340.6 eV and 335.3 eV compared with the corresponding peaks for Pd(0)/SBA-15 (341.2 and 335.7 eV, respectively). This indicated the presence of electron transfer from the amine functional groups (PA, SA, or TA) to the Pd centres,

which is consistent with the results reported previously for related systems.<sup>13</sup> However, there were barely any difference among the peak positions of the three materials functionalized with organoamine groups. In other words, as the number of methyl substituent in the Pd(0)/SBA-15-Amine was varied (PA, SA, or TA), there was barely any shift in the Pd(0) 3d<sub>3/2</sub> and Pd(0) 3d<sub>5/2</sub> peak positions or binding energies.

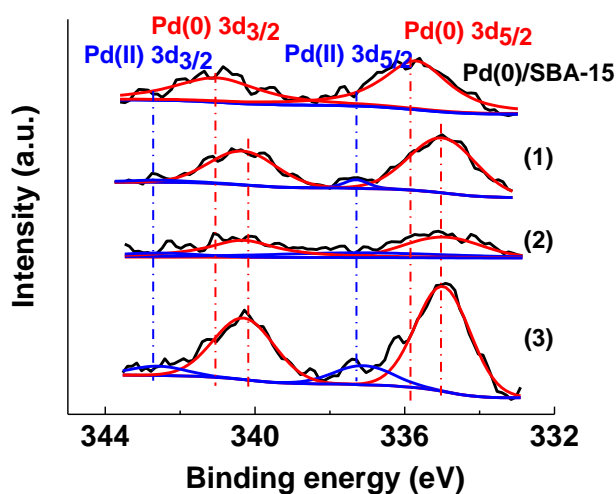


**Figure 3.7.** Comparison of Pd 3d peaks of Pd(0)/SBA-15 and different Pd(0)/SBA-15-Amine materials (where Amine = PA, SA, or TA groups).

#### ***3.4.6. Catalytic activities of the materials toward FA dehydrogenation and the effects of their structures and compositions***

FA dehydrogenation reaction was then carried out by placing the series of Pd/SBA-15-Amine materials (**1**, **2**, and **3**), with each containing identical amount of nitrogen (64  $\mu\text{mol}$ ), in 10 mL of 1 M of FA at room temperature. As illustrated in **Figure 3.8**, among the three catalysts, **1** exhibited the highest catalytic activity. The activity of the catalysts, as measured based on initial TOF and TON, decreased in the order of **1** (whose TOF was 355  $\text{h}^{-1}$ , TON value of 59) > **2** (whose TOF was 190  $\text{h}^{-1}$  and whose

TON was 32) > **3** (whose TOF value of 70 h<sup>-1</sup> and whose TON value was 12) (**Figure 3.8a-b**).

In order to probe the reasons behind the relative catalytic activity of these three catalysts, possible roles played by their structures and compositions were all taken into consideration. Recently, primary amine-functionalized mesoporous silica containing Pd NPs was found to have a good catalytic activity toward FA dehydrogenation.<sup>12</sup> The high catalytic activity of the material was due to the transfer of electron density from the primary amine groups to the Pd NPs, and thereby the electron-richness of the Pd centers in it. Similar electron transfer process from secondary and tertiary amine groups to Pd NPs and similar peak positions for Pd 3d in XPS were also seen in catalysts **2** and **3**; so, it is reasonable to expect high catalytic activity for these two materials as well. Indeed catalysts **2** and **3** also catalyzed FA dehydrogenation well enough. However, besides electronic effects between amine groups and Pd NPs, other factors such as the size of Pd NPs can affect the catalytic activity of the materials in FA dehydrogenation. This was found to be the case, especially when comparing catalysts **1** and **2** with catalyst **3** (**Figure 3.8c**). Catalyst **3** showed the lowest catalytic activity, which must largely be due to the relatively large sized Pd NPs it owned. Although catalyst **2** had similar sized Pd NPs (*ca.* 1.6 nm) as catalyst **1** (*ca.* 1.5 nm), catalyst **2** showed lower activity than catalyst **1** (**Figure 3.8c**). This, on the other hand, suggested that the type of amine functional groups in these materials also directly or indirectly dictated the materials' catalytic activities in FA dehydrogenation. More specifically, the organoamine groups appeared to have the ability to affect the size and the quantity of Pd active sites forming in the Ext-SBA-15 material, and also exert different degrees of steric hindrances around

the catalytic sites, as discussed further below. Furthermore, the organoamine groups dictated the pore diameters in the catalysts. So, the superior catalytic activity exhibited by catalyst **1** compared with catalyst **2** can be due mainly to combined effects of these (**Figure 3.8c**). On the other hand, Pd/SBA-15's poor catalytic activity compared with catalyst **3**, despite the former had smaller Pd NPs (2.5 nm) than the latter had (2.9 nm) (**Figure 3.8c**) must have largely been an indication of the importance of electronic effect in dictating the catalytic activity of these materials, like those reported in few previous studies.<sup>14,21</sup>

Additionally, the observed trend in catalytic activity between these three catalysts may also partly be due to the presence (or absence) of methyl groups on the grafted amine moieties. The methyl groups have an ability to increase the hydrophobicity of the ligand, and then indirectly influence the degree of formic acid (FA) dehydrogenation reaction. In other words, the hydrophilic formic acid/formate anion species would have difficulty to undergo mass diffusion into the pores of the catalysts in the initial step of the reaction, in the order of **3** > **2** > **1**. So, the hydrophobicity of the three organoamine groups should be another likely reason behind the trend in catalytic activity I observed for the three catalysts: **3** < **2** < **1** (or **1** > **2** > **3**).

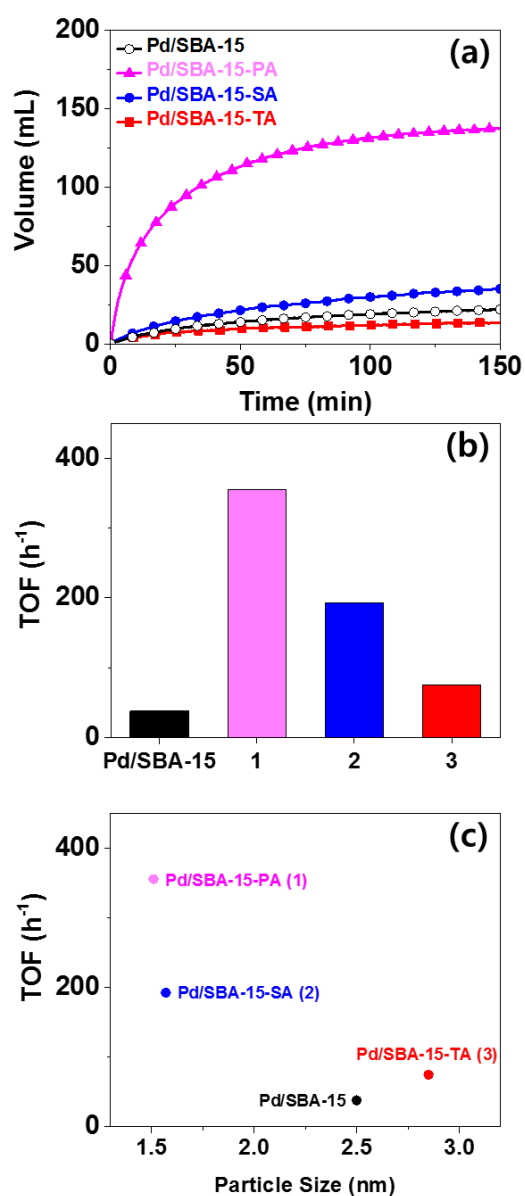


**Figure 3.8** FA dehydrogenation over the as-synthesized catalysts: (a) volume of the produced gases ( $\text{H}_2 + \text{CO}_2$ ) as a function of reaction time, (b) catalytic TOF of the reaction at 10 min, and (c) catalytic TOF as a function of size of Pd NPs on the catalysts.

#### 2.4.7. Governing factors for FA dehydrogenation over Pd(0)/SBA-15-Amine catalysts

To gain insight into the mechanism of the dehydrogenation reaction over the catalysts, the reaction was performed using HCOO-D and D-COOH, instead of FA (HCOOH). As depicted in **Figure 3.9**, the  $k_H/k_D$  values over catalysts **1**, **2**, and **3** obtained using HCOO-D were similar, suggesting that the Brønsted basicity of the amine functional groups in Pd(0)/SBA-15-Amine did not contribute much to the activity of the catalysts during FA dehydrogenation. On the other hand, the  $k_H/k_D$  values obtained using D-COOH were higher than those obtained using HCOO-D, indicating that C-H bond cleavage was likely the rate-determining step for all the Pd/SBA-15-Amine catalysts under the reaction conditions employed herein. In addition, the  $k_H/k_D$  values obtained with D-COOH increased in the order of **1** < **2** < **3**, which was in line with the catalysts' activity toward FA dehydrogenation: **1** > **2** > **3**.

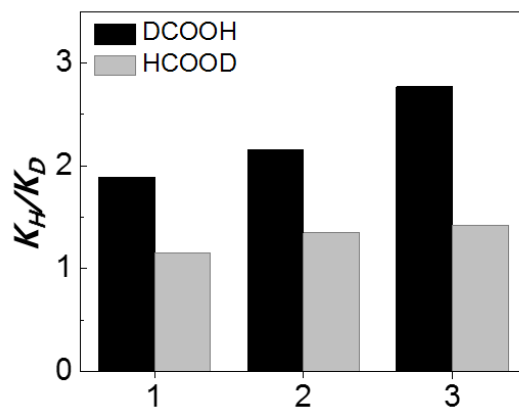
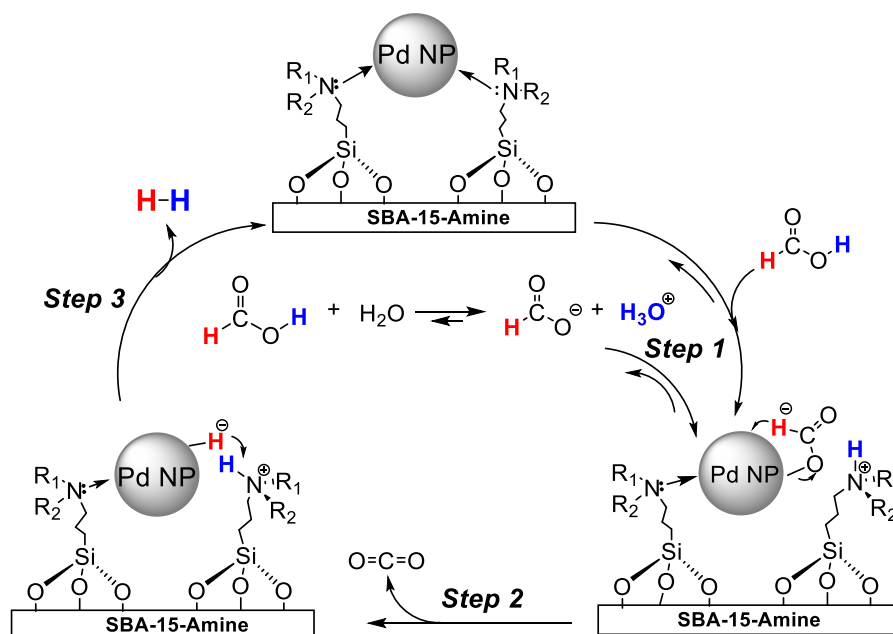


**Figure 3.9.** Comparison of the kinetic isotope effect (KIE) of the series of Pd catalysts synthesized and studied.

These differences in catalytic activity exhibited by the series of Pd(0)/SBA-15-Amine catalysts (**1**, **2**, and **3**) may have once again originated from the differences in (*i*)

the electronic effect, (ii) size of Pd NPs, (iii) steric effect in their tethered amine functional groups, and (iii) pore diameters in the materials. Given the relatively small differences in the size of Pd NPs and electronic effect a, as evidenced by XPS, among the three Pd(0)/SBA-15-Amine catalysts studied herein, the steric effect due to the organoamine groups appeared to have played more dominant roles in their catalytic properties (see further discussions below). However, it should be noted that the better catalytic activity exhibited by Pd(0)/SBA-15-Amine, compared with Pd/SBA-15 (the control material containing no amine groups), may have also partly originated from electronic interaction between Pd NPs and amine groups, as supported by XPS (see above), as well as the ability of the amine groups in being able to cooperatively dictate the reaction pathways as illustrated in **Scheme 3.2**.

Based on the results presented above, it is plausible that FA initially undergoes deprotonation due to the amine group, affording formate ( $\text{HCO}_2^-$ ) and ammonium ( $\text{NHR}_1\text{R}_2^+$ ) species as intermediates (**Scheme 3.2**, *Step 1*). Note that the formation of formate in the first step can also come from the chemical equilibrium between formic acid and formate ion in aqueous media ( $\text{HCO}_2\text{H}(\text{aq}) \leftrightarrow \text{HCOO}^-(\text{aq}) + \text{H}^+(\text{aq})$ ), which can lead to a small difference in the kinetic isotope effect among catalysts **1**, **2**, and **3** during dehydrogenation of  $\text{HCOO-H/HCOO-D}$ . Next, the C-H bond in the  $\text{H-COO}^-$  intermediate species can then cleave at the Pd sites and generate  $\text{CO}_2$  and Pd-H species (**Scheme 3.2**, *Step 2*). Lastly, the hydridic species (Pd-H) undergoes protonation by the acidic proton of the protonated amine species to release  $\text{H}_2$  (**Scheme 3.2**, *Step 3*).

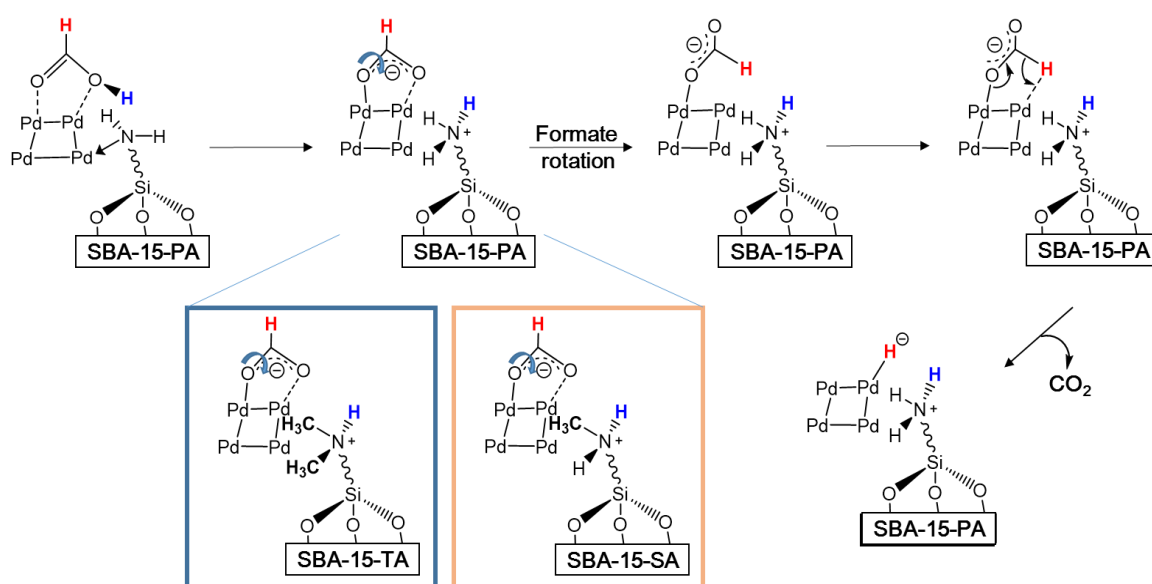


**Scheme 3.2.** A possible reaction pathway for FA dehydrogenation over Pd(0)/SBA-15-Amine catalysts (**1**, **2**, and **3**). Note that step 1 represents the deprotonation of FA both by water and amine group. Obviously, the latter is a more dominant reaction and is also more responsible for the formation of the formate species in the reaction. In **1**, R<sub>1</sub> and R<sub>2</sub> are H; in **2**, R<sub>1</sub> is CH<sub>3</sub> and R<sub>2</sub> is H; and in **3**, R<sub>1</sub> and R<sub>2</sub> are both CH<sub>3</sub>.

Recent detailed studies, however, have shown that the rate determining step (*Step 2* of **Scheme 3.2**) can have two sequential transition states, one of which involves the rotation of formate (HCOO\*) species over the Pd NPs.<sup>35,36</sup> So, in the as-developed catalysts reported herein, the rotation of the formate species can be the first step. This way, the Pd-H species generated by C-H bond activation can become near the acidic H atom present on NR<sub>1</sub>R<sub>2</sub>-H moiety and be able to interact with the latter, finally forming H<sup>+</sup> (due to H<sup>-</sup> atom approach H<sup>+</sup>) (**Scheme 3.3**). Consequently, it is believed that the degree of rotation of the formate species adsorbed on Pd can dictate the rate of the

reaction. The rotation of formate species adsorbed on **1** can be expected to have a lower activation energy than those adsorbed on **2** and **3** due to *i*) the less steric hindrance and *ii*) the better mass diffusion (due to the relatively bigger pores in **1**) the former experience. On the other hand, in the catalysts, which have one or two methyl groups on their amine groups (catalysts **2** or **3**), the adsorbed formate species require more energy to undergo the rotation due to the steric hindrance they experience, thanks to the methyl groups present around the N atoms of the amine groups in them (**Scheme 3.3**). These are most likely part of the reasons behind the trend in catalytic activity among catalysts **1**, **2** and **3** (or  $1 > 2 > 3$ ).

**Scheme 3.3.** Schematic description of detailed mechanism of the catalytic dehydrogenation of FA over Pd/SBA-15-PA (**1**). Inserted in the orange and cyan boxes are Pd/SBA-15-SA (**2**) and Pd/SBA-15-TA (**3**) catalysts, respectively.



### 3.4.8. Recyclability studies and analysis of by-products

Recyclability studies were additionally conducted on catalysts **1**, **2**, and **3** to determine their stability and reusability. Interestingly, in the case of catalyst **1**, the once and twice recycled catalysts actually showed higher catalytic activity for FA dehydrogenation than did the original catalyst (**Figure 3.10**). In the other two cases, the catalytic activities of the catalysts toward FA dehydrogenation remained almost unchanged for, at least, up to 3 cycles. Catalyst **1**'s higher catalytic activity after the 1<sup>st</sup> run was most likely due to the possible reduction of residual PdO species by the H<sub>2</sub> gas produced during the FA dehydrogenation, and the formation of more catalytically active Pd sites.<sup>12</sup> This possible reduction could be relatively insignificant in for catalysts **2** and **3** because these two produced much less amount of H<sub>2</sub> compared with that produced by catalyst **1**. In other words, most of the possible PdO species present on the former two catalysts remained more likely in oxidized forms even after FA dehydrogenation reaction. Although TEM analysis of the spent-catalysts indicated that the average sizes of Pd NPs increased after the 3<sup>rd</sup> cycle in all cases (for **1**, from 1.5 nm to 2.3 nm; for **2**, from 1.6 nm to 2.1 nm; and for **3**, from 2.9 nm to 4.4 nm), the catalysts largely retained their activity, and even became more active in some cases, for the reaction. This is possible due to most of amine protonated by formic acid at first step and thereby ligand strength between amine-palladium would be weaken.

Furthermore, *in-situ* FT-IR spectroscopy revealed that the reaction over the catalysts did not generate CO gas. In other words, the catalysts did not favor the undesired FA dehydration reaction ( $\text{HCOOH} \rightarrow \text{CO} + \text{H}_2\text{O}$ ) (**Figure 3.11**). The absence of CO byproduct during FA dehydrogenation was further confirmed by GC analysis (**Figure 3.12**) and comparison of recent catalysts were in **Table 3.3**.

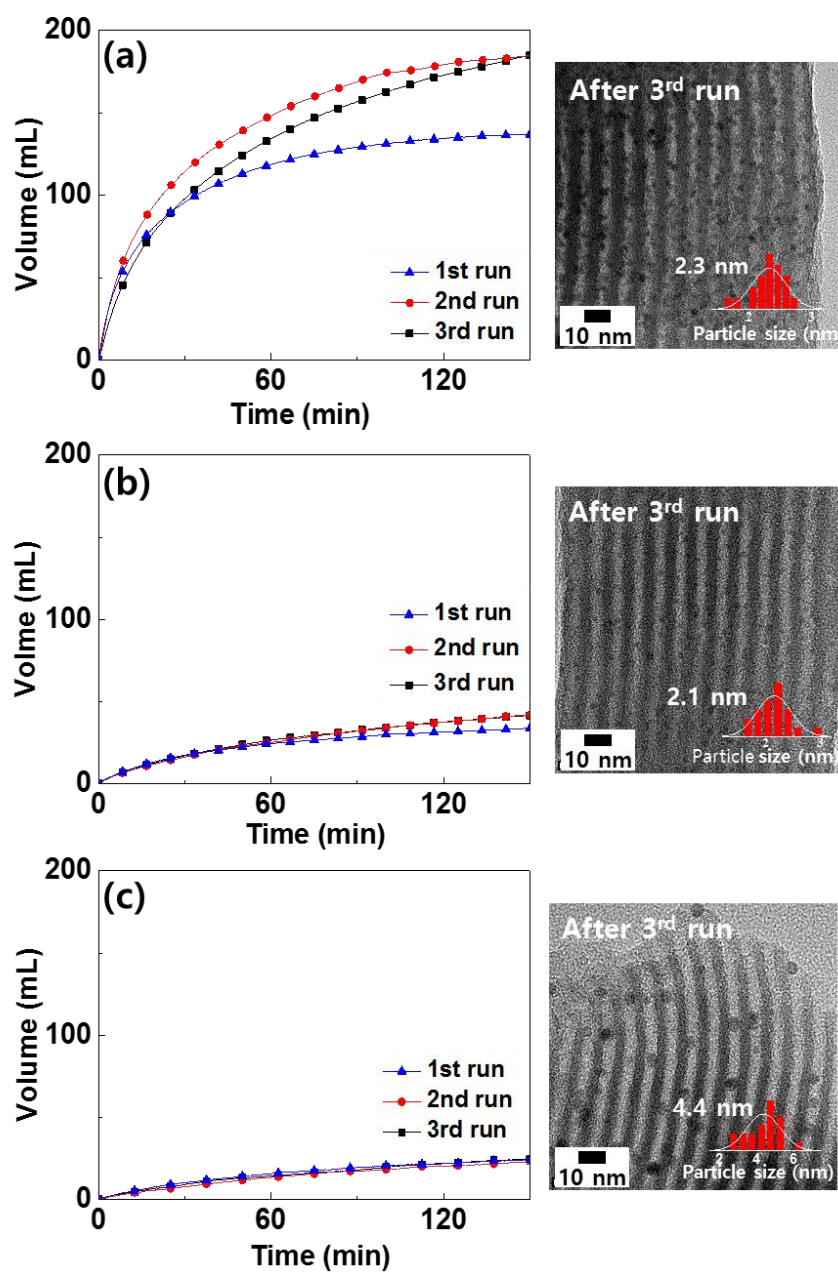


**Figure 3.10.** Recyclability test results of Pd/SBA-15-Amine: (a) Pd/SBA-15-PA (1), (b) Pd/SBA-15-SA (2), and (c) Pd/SBA-15-TA (3). The average sizes of Pd NPs after 3<sup>rd</sup> cycle were presented inside the TEM images.

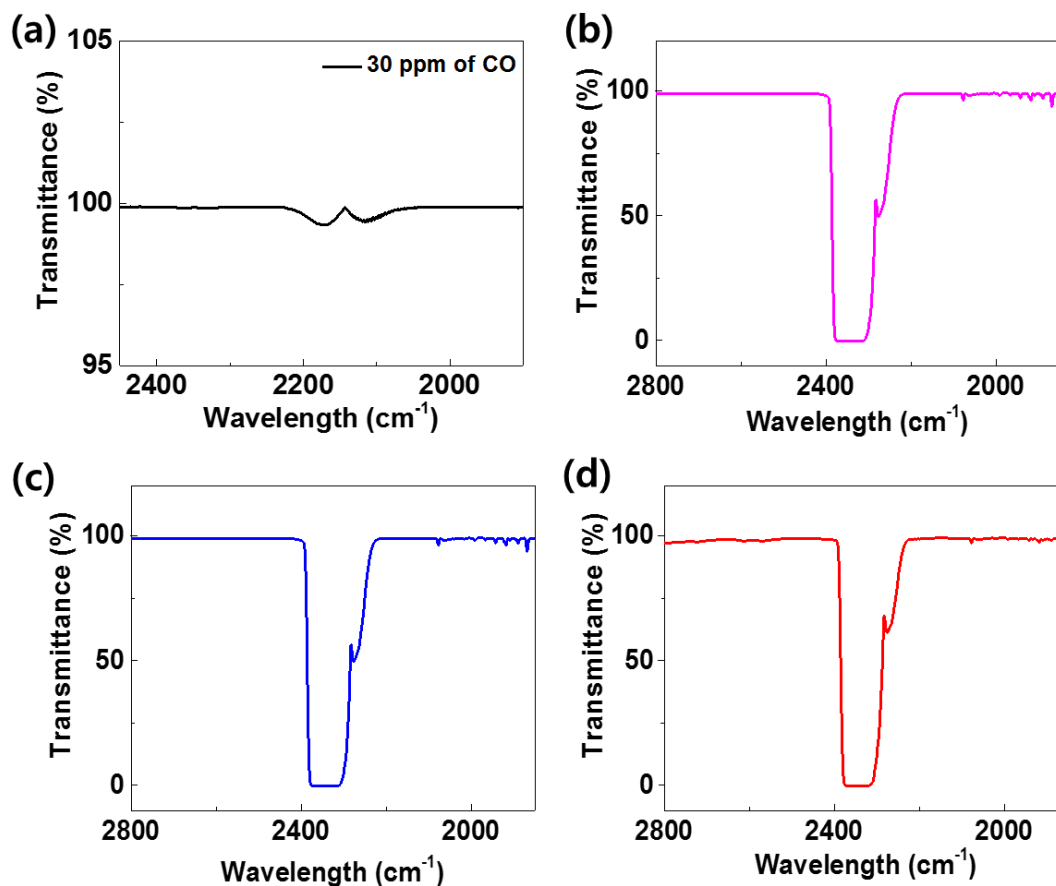


**Figure 3.11.** FT-IR results during reaction (at 50 min) for all catalysts. (a) 30 ppm of CO gas, (b) Pd/SBA-15-PA, (c) Pd/SBA-15-SA, and (d) Pd/SBA-15-TA.

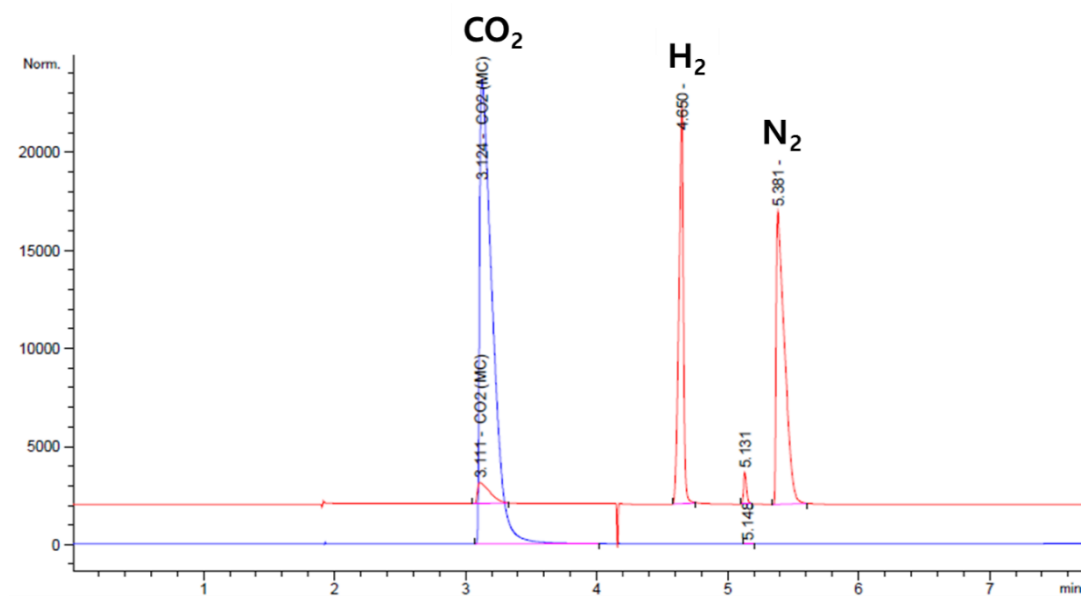


**Figure 3.12.** GC result after reaction (180 min) with Pd/SBA-15-PA for FA dehydrogenation. Blue line is peak of CO<sub>2</sub> and red line is peak of H<sub>2</sub>.

**Table 3.3.** Comparison of TOFs at 10 min of Pd/SBA-15-Amine catalysts with other recently reported catalysts without additives.<sup>[a]</sup>

<i>Entry</i>	<i>Catalyst</i>	<i>Temperature</i> [K]	<i>TOF</i> [h <sup>-1</sup> ]	<i>Reference</i>
1a	Pd/SBA-15-PA	299	355	This work
1b	Pd/SBA-15-SA	299	190	This work
1c	Pd/SBA-15-TA	299	70	This work
2	AgPd/C	298	309	[37]
3	Pd/mpg-C <sub>3</sub> N <sub>4</sub>	298	144	[20]
4	PdAu/C	298	63	[38]
5	Pd/C <sub>3</sub> N <sub>4</sub> (+ hν)	288 <sup>[b]</sup>	68	[19]
6	CoAuPd/C	298	61	[40]
7	Pd/CN	298	70	[41]
8	Pd <sub>0.5</sub> Au <sub>0.3</sub> Mn <sub>0.2</sub> /N-SiO <sub>2</sub>	298	295	[42]
9	Ag-Pd/UiO-66	298	183	[43]

---

<sup>[a]</sup> The TOFs of some of the materials were calculated based on information provided in the manuscripts. <sup>[b]</sup> Please note that the temperature is different from others.

The slight increase in the size of Pd nanoparticles after recycling can be explained based on the weakened interaction between the Pd nanoparticles and the grafted amine functional groups during the reactions. Given the fact that the adsorbed formic acid molecules undergo deprotonation with grafted organoamine groups (*via* Pd-HCOOH $\cdots$ NR<sub>2</sub>-SBA-15  $\rightarrow$  Pd-HCOO<sup>-</sup> + NHR<sub>2</sub><sup>+</sup>-SBA15; please also see Step 1 in Scheme 2), the resulting SBA-15-supported quaternary ammonium groups (NHR<sub>2</sub><sup>+</sup>) would have no ability to interact with and cap the Pd nanoparticles as much as the NR<sub>2</sub>-SBA-15 groups do. As a result, the Pd nanoparticles would have a greater chance to diffuse over the catalyst surface, aggregate with each other and grow into larger nanoparticles during catalysis. Note that unprotonated amine groups donate electron densities into Pd nanoparticles *via* Pd-N interaction, as evidenced by XPS (**Figure 3.7**)

### 3.5 Conclusion

In conclusion, I have successfully synthesized and characterized the structures, compositions and catalytic properties for FA dehydrogenation of a series of Pd/SBA-15-Amine materials containing different types of amine groups and Pd NPs. Using the results, the relationships between amine groups and the Pd NPs forming in the materials have been investigated. The catalytic activity of the materials have been found to directly and indirectly relate to the terminal amine functional groups present in the materials. Specifically, the types of amine functional groups are found to dictate the size of the Pd NPs forming in the materials, the electronic properties in the materials, and the pore diameters and pore volumes in the materials. These have, in turn, dictated the overall degree of catalytic activities of the materials toward FA dehydrogenation. The structural and composition parameters identified for the materials in relation to their catalytic properties toward FA dehydrogenation reaction here may provide valuable guidelines for the development of other efficient catalysts to generate H<sub>2</sub> on-board for H<sub>2</sub>-powered fuel cells.

### 3.6. References

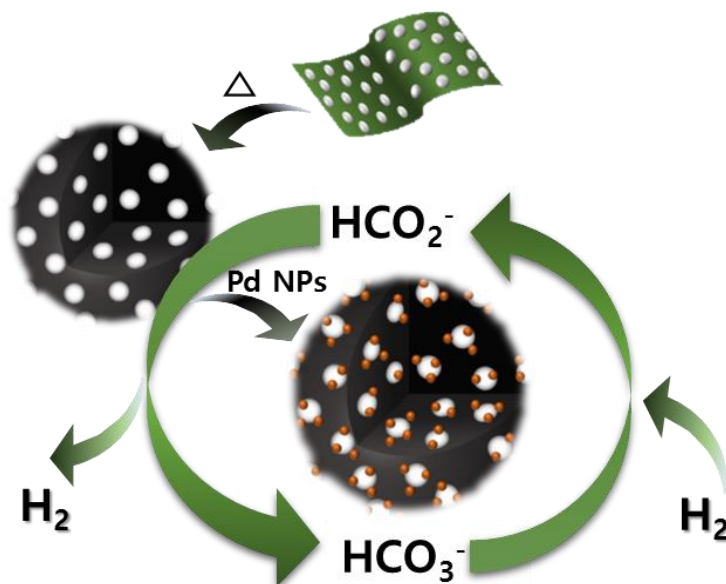
- (1) Turner, J. A. *Science*, **2004**, *305*, 972–974.
- (2) Steele, B.C.H.; Heinzl, A. *Nature*, **2001**, *414*, 345–351.
- (3) Enthaler, S. *ChemSusChem*, **2008**, *1*, 801–804.
- (4) Schlapbach, L.; Züttel, A. *Nature*, **2001**, *414*, 353–358.
- (5) Armaroli, N.; Balzani, V. *Angew. Chem. Int. Ed.*, **2007**, *46*, 52–66.
- (6) Grasemann, M.; Laurenczy, G. *Energy Environ. Sci.*, **2012**, *5*, 8171–8181.
- (7) (a) Loges, B.; Boddien, A.; Junge, H.; Beller, M. *Angew. Chem. Int. Ed.*, **2008**, *47*, 3962–3965; (b) Majewski, A.; Morris, D. J.; Kendall K.; Wills, M. *ChemSusChem*, **2010**, *3*, 431–434.
- (8) (a) Zhu, Y.; Nakanishi, T.; Kanamori, K.; Nakanishi, K.; Ichii, S.; Iwaida, K.; Masui, Y.; Kamei, T.; Shimada, T.; Kumamoto, A.; Ikuhara, Y. H.; Jeon, M.; Hasegawa, G.; Tafu, M.; Yoon, C.W.; Asefa, T. *ACS Appl. Mater. Interfaces*, **2017**, *9*, 36–41; (b) Koh, K.; Jeon, M.; Chevrier, D. M.; Zhang, P.; Yoon, C.W.; Asefa, T. *Appl. Catal. B*, **2017**, *203*, 820–828.
- (9) Loges, B.; Boddien, A.; Junge, H.; Beller, M. *Angew. Chem. Int. Ed.*, **2008**, *47*, 3962–3065.
- (10) Lu, X.; Leung, D.Y.C.; Wang, H.; Leung, M.K.H.; Xuan, J. *ChemElectroChem*, **2014**, *1*, 836–849.
- (11) Albert, J.; Jess, A.; Kern, C.; Pöhlmann, F.; Glowienka, K.; Wasserscheid, P. *ACS Sustain. Chem. Eng.* **2016**, *4*, 5078–5086.
- (12) Koh, K.; Seo, J.-E.; Lee, J. H.; Goswami, A.; Yoon, C.W.; Asefa, T. *J. Mater. Chem. A*, **2014**, *2*, 20444–20449.
- (13) Lee, J. H.; Ryu, J.; Kim, J. Y.; Nam, S.-W.; Han, J. H.; Lim, T.-H.; Gautam, S.; Chae, K.H.; Yoon, C.W. *J. Mater. Chem. A*, **2014**, *2*, 9490–9495.
- (14) Mori, K.; Dojo, M.; Yamashita, H. *ACS Catal.*, **2013**, *3*, 1114–1119.
- (15) Martis, M.; Mori, K.; Fujiwara, K.; Ahn, W.-S.; Yamashita, H. *J. Phys. Chem. C*, **2013**, *117*, 22805–22810.
- (16) Bi, Q.-Y.; Lin, J.-D.; Liu, Y.-M.; He, H.-Y.; Huang, F.-Q.; Cao, Y. *Angew. Chem. Int. Ed.*, **2016**, *55*, 11849–11859.
- (17) Hu, C.; Mu, X.; Fan, J.; Ma, H.; Zhao, X.; Chen, G.; Zhou, Z.; Zheng, N. *ChemNanoMat*, **2016**, *2*, 28–32.
- (18) Huang, Y.; Zhou, X.; Yin, M.; Liu, C.; Xing, W. *Chem. Mater.* **2010**, *22*, 5122–5128.
- (19) Weicheng, M.; Mori, K.; Kuwahara, Y.; Yamashita, H. *ACS Energy Lett.* **2017**, *2*, 1–7.
- (20) Lee, J. H.; Cho, J.; Jeon, M.; Ridwan, M.; Park, H.S.; Choi, S.H.; Nam, S.W.; Han, J.; Lim, T.; Ham, H.C.; Yoon, C.W. *J. Mater. Chem. A*, **2016**, *4*, 14141–14147.
- (21) Yadav, M.; Akita, T.; Tsumori, N.; Xu, Q. *J. Mater. Chem.*, **2012**, *22*, 12582–12586.
- (22) Song, F.-Z.; Zhu, Q.-L.; Tsumori, N.; Xu, Q. *ACS Catal.* **2015**, *5*, 5141–5144.
- (23) Zhu, Q.; Xu, Q. *Chem*, **2016**, *1*, 220–245.
- (24) Jones, S.; Qu, J.; Tedsree, K.; Tsang, S.C.E. *Angew. Chem. Int. Ed.* **2012**, *51*, 11275–11278.
- (25) Zhao, D.; Feng, J.; Huo, Q.; Melosh, N.; Fredrickson, G.H.; Chmelka, B.F.; Stucky, G.D. *Science*, **1998**, *279*, 548–552.

- (26) Wang, L.; Yang, R. T.; *J. Phys. Chem. C* **2011**, *115*, 21264–21272.
- (27) Hiyoshi, N.; Yogo, K.; Yashima, T. *J. Jpn. Pet. Inst.*, **2005**, *48*, 29–36.
- (28) Adamson, A. W.; Gast, A. P. In *Physical Chemistry of Surfaces*. Wiley-Interscience, NY, 1997, ch. 17, pp
- (29) Amati, D.; Kovats, E. S. *Langmuir*, **1987**, *3*, 687–695.
- (30) Amati, D.; Kovats, E. S. *Langmuir* **1988**, *4*, 329–337.
- (31) Kazakevich, Y.V.; Fadeev, A. Y. *Langmuir* **2002**, *18*, 3117–3122.
- (32) Spielbauer, D.; Zeilinger, H.; Knoezinger, H. *Langmuir*, **1993**, *9*, 460–466.
- (33) Bazzicalupi, C.; Bencini, A.; Cohen, H.; Giorgi, C.; Golub, G.; Meyerstein, D.; Navon, N.; Paoletti, P.; Valtancoli, B. *J. Chem. Soc., Dalton Trans.*, **1998**, *10*, 1625–1631.
- (34) Golub, G.; Cohen, H.; Paoletti, P.; Bencini, A.; Messori, L.; Bertini, I.; Meyerstein, D. *J. Am. Chem. Soc.*, **1995**, *117*, 8353–8361.
- (35) Yang, X. *Dalton Trans.*, **2013**, *42*, 11987–11991.
- (36) Aldeev, V.I.; Parmon, V. N. *J. Phys. Chem. C*, **2011**, *115*, 21755–21762.
- (37) Zhang, S.; Metin, Ö.; Su, D.; Sun, S. *Angew. Chem. Int. Ed.* **2013**, *52*, 3681–3684.
- (38) Metin, O.; Sun, X.; Sun, S. *Nanoscale* **2013**, *5*, 910–912.
- (39) Cai, Y.-Y.; Li, X.-H.; Zhang, Y.-N.; Wei, X.; Wang, K.-X.; Chen, J.-S. *Angew. Chem. Int. Ed.* **2013**, *52*, 11822–11825.
- (40) Wang, Z.-L.; Yan, J.-M.; Ping, Y.; Wang, H.-L.; Zheng, W.-T.; Jiang, Q. *Angew. Chem. Int. Ed.* **2013**, *52*, 4406–4409.
- (41) Bi, Q.; Lin, J.; Liu, Y.; He, H.; Huang, F.; Cao, Y. *Angew. Chem. Int. Ed.* **2016**, *128*, 12028–12032.
- (42) Karatasas, Y.; Bulut, A.; Yurderi, M.; Ertas, I. E.; Alal, O.; Gulcan, M.; Celebi, M.; Kivrak, H.; M. Kaya, M.; Zahmakiran, M. *Appl. Catal. B*, **2016**, *180*, 586–595.
- (43) Gao, S.; Liu, W.; Feng, C.; Shang, N.; Wang, C.; *Catal. Sci. Technol.*, **2016**, *6*, 869–874
- (44) Wang, Z. L.; Yan, J. M.; Zhang, Y. F.; Ping, Y.; Wang, H. L.; Jiang, Q. *Nanoscale*, **2014**, *6*, 3073–3077

## CHAPTER 4.

### Novel Nanoporous N-doped Carbon-supported Ultrasmall Pd

### Nanoparticles: Efficient Catalysts for Hydrogen Storage and Release



#### 4.1. Overview

The reversible reactions involving formate and bicarbonate can be used to store and release hydrogen ( $\text{H}_2$ ), allowing  $\text{H}_2$  to serve as an effective energy carrier in energy systems such as fuel cells. However, to feasibly utilize these reactions for renewable energy applications, efficient catalysts that can reversibly promote both reactions are required. Herein I report the synthesis of novel polyaniline (PANI)-derived mesoporous carbon-supported Pd nanoparticles, or materials that can efficiently catalyze these reversible reactions. The synthesis involves pyrolysis of PANI/colloidal silica composite materials at temperatures above  $500\text{ }^\circ\text{C}$  and then removal of the colloidal silica from the carbonized products with an alkaline solution. The resulting nanomaterials efficiently catalyze the reversible reactions, *i.e.*, the dehydrogenation of

formate ( $\text{HCO}_2^- + \text{H}_2\text{O} \rightarrow \text{H}_2 + \text{HCO}_3^-$ ) and the hydrogenation of bicarbonate ( $\text{H}_2 + \text{HCO}_3^- \rightarrow \text{H}_2\text{O} + \text{HCO}_2^-$ ). The porosity and the catalytic property of the materials can be tailored, or improved, by changing the synthetic conditions (in particular, the pyrolysis temperature and the amount of colloidal silica used for making the materials). The study further reveals that having an optimum density of N dopant species in the catalysts makes Pd to exhibit high catalytic activity toward both reactions. Among the different materials studied here, the one synthesized at 800 °C with relatively high amount of colloidal silica templates gives the best catalytic activity, with a turnover frequency (TOF) of 2,562 h<sup>-1</sup> for the dehydrogenation reaction and a turnover number (TON) of 1,625 for the hydrogenation reaction. These TOF and TON values are among the highest values ever reported for heterogeneous catalysts for these reversible reactions

## 4.2. Introduction

In the face of the rising energy consumptions worldwide and the continued negative environmental impacts caused by fossil fuels, there are burgeoning efforts to find alternative energy sources and carriers.<sup>1-3</sup> These efforts include research in hydrogen (H<sub>2</sub>), which has long been regarded as one of the most promising energy carriers, because it is a clean and renewable fuel.<sup>4,5</sup> While hydrogen's use in fuel cells has long been successfully demonstrated, finding efficient hydrogen storage systems that can make hydrogen-based energy technologies sustainable and widely applicable still remains a challenge.<sup>6,7</sup> To address these issues, several chemical systems that inherently possess high hydrogen density and that can release H<sub>2</sub> hydrolytically or thermally, such as sodium borohydride or ammonia borane, have been widely studied.<sup>8,9</sup>

However, the reaction pathways that these systems follow while releasing H<sub>2</sub> make them difficult to deploy, because their spent fuels are in solid phase or in slurry form, and are thus hard to regenerate back to fuels.<sup>10,11</sup> This is, in fact, one of the major stumbling blocks limiting the utilization of these systems as efficient, safe, and reversible hydrogen storage/release media.

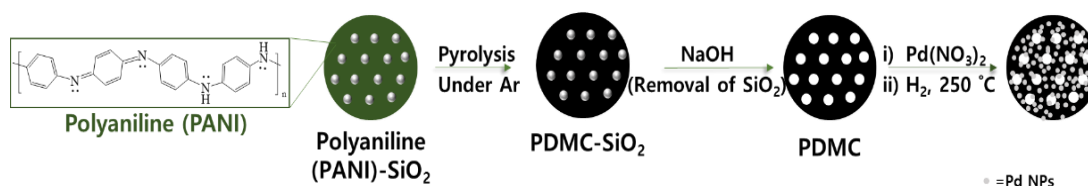
Owing to their regenerability and high volumetric hydrogen content, formic acid (HCO<sub>2</sub>H) and related compounds are more interesting reversible hydrogen storage/release systems.<sup>12,13</sup> Recently, the Beller<sup>14,15</sup> and the Joó<sup>16</sup> groups showed that the formate/bicarbonate (HCO<sub>2</sub><sup>-</sup>/HCO<sub>3</sub><sup>-</sup>) reversible reactions over *homogeneous* Ru-based catalysts enable a rechargeable hydrogen battery. In fact, compared with the HCO<sub>2</sub>H/CO<sub>2</sub> system, a system that has been more widely studied for H<sub>2</sub> storage/release, the HCO<sub>2</sub><sup>-</sup>/HCO<sub>3</sub><sup>-</sup> system can be more advantageous, especially for fuel cell applications. This is because the latter can: 1) release H<sub>2</sub> without producing CO, a known poison for the Pt and other catalysts commonly used in fuel cells, and 2) release the H<sub>2</sub> under non-acidic media, the media that is sometimes preferred for reactions employed in various fuel cells. However, so far only few *heterogeneous* catalysts have been studied for catalytic inter-conversions of HCO<sub>2</sub><sup>-</sup>/HCO<sub>3</sub><sup>-</sup>, and they include Pd/C<sup>17,18</sup> and reduced graphene oxide-supported Pd nanoparticles (Pd/r-GO).<sup>19</sup> More importantly, some of these previous studies have revealed that, when supported on carbon materials, Pd could give comparable catalytic activity as, and better selectivity and reversibility than, its homogenous counterparts for the HCO<sub>2</sub><sup>-</sup>/HCO<sub>3</sub><sup>-</sup> reversible reactions.<sup>17-21</sup>

Meanwhile, it has been reported that by doping the structure of carbon support

materials with heteroatoms (*e.g.*, N,<sup>22-24</sup> B,<sup>25</sup> or P<sup>26</sup>), not only the physical and chemical properties of the materials can be favorably tailored, but also the ability of the materials to assist supported catalytically active metallic species on them (*e.g.*, Pd nanoparticles or Ru complexes) can be improved.<sup>22-27</sup> Moreover, although the exact mechanisms are not yet well understood, N-based species in amine-functionalized mesoporous silicas or carbon nitrides have been known to provide some synergetic effects with various metallic catalytic groups, especially Pd nanoparticles, cooperatively promoting the deprotonation step involved in formic acid dehydrogenation.<sup>22-26</sup> Besides, many N-based moieties are known for their ability to stabilize Pd nanoparticles, increasing the latter's shelf-lives during catalysis. However, despite their similar, favorable surface properties as amine groups (such as polarity and basicity), the potential ability of the N-dopants of N-doped carbon materials to assist with the  $\text{HCO}_2^-/\text{HCO}_3^-$  reversible reactions have only been rarely explored.<sup>17-21</sup> In other words, generally the ease of tailorability of the properties of carbon support materials *via* heteroatom doping,<sup>27</sup> and the possible advantages this may have on the catalytic activity of the resulting heterogeneous catalysts toward  $\text{HCO}_2^-/\text{HCO}_3^-$  reversible reactions, have not been explored.

To this end, herein I report the synthesis of novel polyaniline (PANI)-derived mesoporous N-rich carbon materials with Pd nanoparticles (Pd/PDMCs) (**Scheme 4.1**) that show efficient catalytic activity toward  $\text{HCO}_2^-/\text{HCO}_3^-$  reversible reactions. To synthesize the catalysts, PANI is used as a precursor and silica nanoparticles are used as templates. PANI is purposely chosen as a precursor because it has a high N/C atomic ratio (0.167), and can thus give a high yield of N-dopant species in the carbon materials upon pyrolysis.<sup>28</sup> The silica nanoparticles are used as templates in order to render the

carbon support material high porosity and large surface area so that the catalyst can have better diffusion pathways for the reactants and products, and achieve better catalytic activity.<sup>29</sup> Additionally, by applying different pyrolysis temperatures, the density and the type of N-dopant species in the PANI-derived mesoporous carbon materials are tailored, and the materials' catalytic properties are further optimized and improved.



**Scheme 4.1.** Schematic illustration of the synthesis of PANI-derived mesoporous N-doped carbon-supported Pd nanoparticles (Pd/PDMC) materials.

## 4.2. Experimental Section

### 4.2.1. Chemicals and Materials

Aniline, ammonium persulfate ((NH<sub>4</sub>)<sub>2</sub>S<sub>2</sub>O<sub>8</sub>), colloidal silica (Ludox-HS-40, 40 wt. % suspension in H<sub>2</sub>O), formic acid (HCOOH), palladium on carbon (Pd/C, 10 wt. %), and palladium nitrate (Pd(NO<sub>3</sub>)<sub>2</sub>·2H<sub>2</sub>O) were obtained from Sigma-Aldrich. Sodium formate (HCOONa) and sodium bicarbonate (NaHCO<sub>3</sub>) were purchased from Alfa-Aesar. Sodium formate-d (DCOONa) and deuterium oxide (D<sub>2</sub>O), which were used for kinetic isotope effect (KIE) studies, were obtained from Sigma-Aldrich. All the reagents were used as received without further purification.

### 4.2.2. Instrumentations

The following analytical instruments and methods were used to characterize the

structures and compositions of materials and to evaluate their catalytic properties.

- (A) The Brunauer-Emmett-Teller (BET) surface area, the Barrett-Joyner-Helenda (BJH) pore size distribution, and the pore volumes of the materials were obtained with a Micrometrics ASAP 2000 instrument using N<sub>2</sub> at 77 K.
- (B) High-resolution transmission electron microscopy (HRTEM) and scanning transmission electron microscopy (STEM) images were acquired using a field emission, FEI Tecnai microscope G<sup>2</sup> F20 operating at 200 kV.
- (C) X-ray diffraction (XRD) studies of the materials was done using a Rigaku Mini Flex II instrument operating with Cu K $\alpha$  X-ray source at 40 kV and 20 mA.
- (D) XPS spectra were acquired with an XPS instrument equipped with a PHI 50000 Versa Probe operating with an Al K $\alpha$  X-ray beam at a background pressure of  $6.7 \times 10^{-8}$  Pa. The spectra were calibrated by using C1s's peak at 284.6 eV.
- (E) The amount of Pd in the catalysts was determined by means of inductively coupled plasma-optical emission spectrometry (ICP-OES) (Varian 720ES Agilent).
- (F) Gas chromatography (GC) was performed using a Model 7890A instrument (Agilent Technologies) equipped with a TCD detector and two columns: Hayesep D and MS13X.
- (G) High performance liquid chromatography (HPLC) analysis was performed using a (1200 series HPLC instrument from Agilent Technologies that is equipped with a UV detector at 210 nm. To analyze the concentration of formate (HCO<sub>2</sub><sup>-</sup>) in the reaction mixtures, samples were separated with an YMC-pack C18 column (250 X 4.6 mm I.D.), using H<sub>2</sub>O containing 0.1 % H<sub>3</sub>PO<sub>4</sub> as the mobile phase at a flow

rate of 1 mL/min.

- (H) Extended X-ray absorption fine structure (EXAFS) was performed at the Pd K-edge region using the 10C Wide-Energy XAFS beamline at the Pohang Light Source (PLS-II), Republic of Korea, in the 3.0 GeV storage ring, with a ring current of 320 mA. The measurement was conducted in the transmission mode. After subtracting its background, the EXAFS data were normalized and transformed to k- and R-space using standard data reduction protocols. A k-range of 3-13 Å<sup>-1</sup> was used for the Fourier transformation to R-space. Simulated Pd-O and Pd-Pd scattering parameters used to fit Pd K-edge EXAFS data were generated using FEFF8.2 computational software.<sup>37</sup>
- (I) Near edge X-ray absorption fine structure (NEXAFS) was performed with 10D XAS (X-ray absorption spectroscopy) using KIST B/L at the Pohang Light Source, South Korea, and the data were processed using the WinXAS program. The pre-edge background was subtracted by a linear function, and the post-edge background was not subtracted due to the complicated fine structure shape. For comparison purpose, the first peak was normalized to 1.

#### ***4.2.3. Synthesis of materials***

##### *Synthesis of polyaniline-derived mesoporous carbons (PDMCs)*

First, a polyaniline (PANI)/silica nanocomposite material was synthesized with oxidative polymerization<sup>30</sup> of aniline in the presence of silica nanoparticles. Typically, an aqueous solution (100 mL) containing 1.0 M formic acid was stirred with 20 mmol

of  $(\text{NH}_4)_2\text{S}_2\text{O}_8$  at 2 °C until all the reagents were completely dissolved. Then, various amounts (0, 4, 8 or 16 g) of Ludox® HS-40 colloidal silica (40 wt. % in  $\text{H}_2\text{O}$ ) were slowly added, drop-wise, into the solution under vigorous stirring. Into the stirring reaction mixture, 20 mmol of aniline was slowly added. The mixture was stirred at 2 °C for 24 h and then purified (*via* centrifugation at 15,000 rpm for 20 min, followed by decantation, and washing with  $\text{H}_2\text{O}$  (3 times) and EtOH (2 times)). The resulting material was dried at 60 °C in vacuum oven for 12 h. Finally, a dark blue-to-greenish colored product, *i.e.*, a PANI/silica nanocomposite material, was obtained.

The resulting material was subjected to pyrolysis under Ar atmosphere in a temperature-programmable tube furnace at various temperatures (500, 700, 800, 900, or 1000 °C). The pyrolysis process was programmed to involve: 1) heating at 300 °C at a heating rate of 1 °C·min<sup>-1</sup> and keeping the temperature at 300 °C for 3 h and 2) then increasing the pyrolysis temperature from 300 to 500, 700, 800, 900, or 1000 °C at a heating rate of 10 °C·min<sup>-1</sup> and keeping the temperature there for an additional 2 h.

The resulting black powdered products were treated with 1.0 M NaOH solution in an autoclave at 100 °C for 18 h to remove the silica templates in them. After filtration, the solid products were washed with copious amounts of water and EtOH, and let to dry at 40 °C under vacuum. This finally yielded a series of black powdered materials, labeled as PDMC-*T-x* (where *T* represents their pyrolysis temperature and *x* represents the amount of colloidal silica in g per 0.02 mole of aniline used to make the precursors of the PDMCs).

### *Synthesis of Pd/PDMC materials*

To generate supported Pd nanoparticles in the PDMCs materials, typically 200 mg of each one of the PDMC- $T$ - $x$  materials was placed in an aqueous solution (40 mL) containing Pd(NO<sub>3</sub>)<sub>2</sub>·2H<sub>2</sub>O (56 μmol). (For the synthesis of PDMC with a lower loading of Pd nanoparticles, 18 μmol of Pd(NO<sub>3</sub>)<sub>2</sub>·2H<sub>2</sub>O was used instead). The mixtures were stirred for 3 h at room temperature, and then centrifuged. The resulting solid products were washed with distilled H<sub>2</sub>O (*via* stirring, centrifugation and decantation) and then dried at 40 °C under vacuum. Finally, the Pd(II)-loaded PDMC- $T$ - $x$  materials were subjected to thermal treatment at 250 °C in N<sub>2</sub>/H<sub>2</sub> (90/10 %) atmosphere for 3 h to reduce the Pd(II) to Pd(0). This led to brown-colored, Pd nanoparticles-containing PDMC- $T$ - $x$  powder materials. The materials were denoted as Pd/PDMC- $T$ - $x$ , where again  $T$  represents their final pyrolysis temperature and  $x$  represents the amount of colloidal silica in g used per 0.02 mole of aniline to make the PDMCs.

### *Catalytic dehydrogenation of sodium formate*

To test the catalytic properties of the materials toward formate dehydrogenation, typically 25 mg of one of Pd/PDMC- $T$ - $x$  materials was added into a solution of 1.0 M sodium formate (HCO<sub>2</sub>Na) (5.0 mL). The reaction mixture was stirred, and the amount of H<sub>2</sub> evolved from the reaction was determined as follows. The gaseous products produced by the reaction were let to pass through a NaOH (10 M) trap to remove the CO<sub>2</sub> byproduct, and the remaining gaseous products were then measured using a gas burette in real time. The blank experiments with the same experiment set up (5 mL of

1 M of sodium formate) without a catalyst and checked possible errors involving H<sub>2</sub> evolution.

To analyze the type(s) of gaseous product(s) evolved, one of the outlets of the reactor was connected with gas sampling bag, and the product(s) collected there from the reaction was/were analyzed with gas chromatography (GC). For kinetic isotope effect (KIE) studies, two deuterated reagents (DCO<sub>2</sub>Na and D<sub>2</sub>O) were used instead of HCO<sub>2</sub>Na and H<sub>2</sub>O under otherwise similar experimental procedures.

#### *Catalytic hydrogenation of sodium bicarbonate*

Typically, a mixture of 50 mg of one of the Pd/PDMC-*T-x* catalysts and 10 mL of 1.0 M aqueous solution of sodium bicarbonate (HCO<sub>3</sub>Na) were mixed in a stainless steel reactor and then purged with N<sub>2</sub>. H<sub>2</sub> gas was then let to flow into the reactor till the pressure in the reactor reached 40 bar. The reaction mixture was heated to a desired temperature (*i.e.*, 80 °C in our case) and stirred for 24 h while continuously flowing H<sub>2</sub> gas in it and while maintaining the reactor's pressure constant (40 bar). After letting it to cool down to room temperature, the reactor was depressurized, and the reaction mixture was purged with N<sub>2</sub> before it was finally exposed to air. The catalyst was removed from the reaction mixture by a syringe filter, and the liquid collected was analyzed using high-performance liquid chromatography (HPLC).

#### *Recyclability tests of the catalysts*

The recyclability of the catalysts was evaluated by recovering them from the reaction mixtures. Typically, after the first reaction, the spent catalyst was recovered by

filtration, and washed several times with deionized water and then ethanol (*via* stirring, centrifugation, and decantation). The recovered catalyst was then dispersed in deionized water (100 mL) and stirred overnight to remove the products or reagents adsorbed on its surfaces. The catalyst was dried under vacuum oven after filtration, and then used as catalyst in the next reaction cycle. This procedure was repeated several times as necessary.

### 4.3. Results and Discussion

#### 4.3.1. *Synthesis and characterization of catalysts*

The synthetic procedure used to make Pd/PDMCs consists of three steps. First, *in-situ* polymerization of PANI within the void spaces of colloidal silica templates is carried out (**Scheme 5.1**). The resulting PANI-silica composite material is pyrolyzed at 300 °C for 3 h, and then at 500, 700, 800, 900 or 1000 °C for 2 h, under argon atmosphere. Following this, the silica nanoparticles in the carbonized products are etched with an aqueous NaOH solution. The resulting PANI-derived mesoporous carbons, denoted PDMCs, are immobilized with Pd(II) ions, and the Pd(II) ions-immobilized PDMCs are then subjected to reduction at 250 °C in H<sub>2</sub> atmosphere to generate Pd(0) nanoparticles in the PDMCs. Finally, Pd/PDMC-*T-x* materials, in which *T* represents the final pyrolysis temperature and *x* represents the amount of colloidal silica (in g) per 0.02 mole of aniline used to make the PDMCs, are obtained. The as-synthesized Pd/PDMC materials prepared using different (i) amounts of colloidal silica (see below) and (ii) calcination temperatures (see below) are then used as catalysts for formate-bicarbonate reversible reactions to provide valuable information about the

effect of the synthetic conditions on the structures, compositions, and catalytic properties of the materials.

#### ***4.3.2. Effect of colloidal silica on the structures of PDMC-T-x materials***

First, the effect of the added colloidal silica on the textural properties and morphology of the PDMC-T-x materials are examined by using N<sub>2</sub> gas adsorption/desorption, scanning transmission electron microscopy (STEM), and high-resolution transmission electron microscopy (HR-TEM). In all the cases, the adsorption/desorption isotherms are found to be Type IV with hysteresis loops, indicating the presence of mesoporous structure in them (entries 1-4 in **Table 4.1** and **Figure 4.1**). However, larger surface areas are found in the materials synthesized using colloidal silica as templates, and a relatively much lower surface area is obtained in the material prepared without colloidal silica template. These results are further confirmed by HR-TEM images. Similarly, while HR-TEM images indicate the presence of porosity in the materials (**Figure 4.2a,b** and **4.3**), higher porosity is observed in Pd/PDMC-1000-16 (the material synthesized using relatively higher amount of colloidal silica as template) and lower porosity is observed in Pd/PDMC-1000-0 (the control material synthesized without using colloidal silica as template). So, these results reveal that the structures of the Pd/PDMC materials vary depending on whether as well as how much colloidal silica is used as template for the synthesis of the materials.

**Table 4.1.** Textural properties of Pd/PDMC-*T-x* materials and their average size of their Pd nanoparticles as a function of the amount of colloidal silica templates and pyrolysis temperatures used to synthesize the materials.

Entry	Pd/PDMC- <i>T-x</i>		$A_{BET}$ [ $m^2 \cdot g^{-1}$ ] <sup>a</sup>	$D_{BJH}$ [nm] <sup>b</sup>	$V$ [ $cm^3 \cdot g^{-1}$ ] <sup>c</sup>	Pd [ $\mu mol/g_{cat}$ ] <sup>d</sup>	Size of Pd
	<i>T</i>	<i>x</i>					NPs [nm] <sup>e</sup>
1	1,000	0	260	2.5	0.2	70	16.0
2	1,000	4	817	7.4	1.5	230	1.5
3	1,000	8	919	8.0	1.8	200	1.5
4	1,000	16	994	9.7	2.4	180	1.7
5	900	16	934	9.2	2.2	150	1.6
6	800	16	1,080	9.4	2.5	140	1.6
7	700	16	845	8.4	1.8	150	1.5
8	500	16	510	3.4	0.4	130	1.7

<sup>a</sup>) BET surface area. <sup>b</sup>) Average pore diameter obtained from the desorption branch of N<sub>2</sub> absorption/desorption data. <sup>c</sup>) Pore volume. <sup>d</sup>) Measured by ICP-OES. <sup>e</sup>) Determined by STEM.

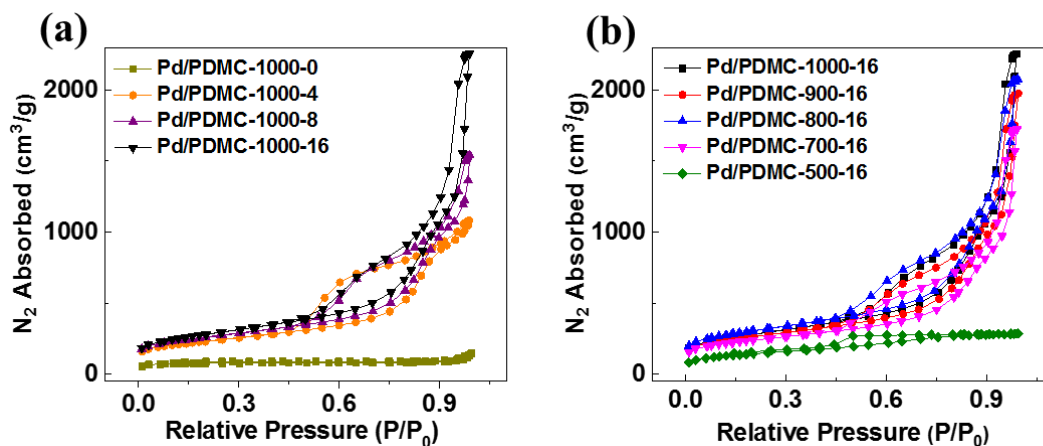


**Figure 4.1.**  $N_2$  adsorption/desorption isotherms of: (a) Pd/PDMC-1000- $x$  and (b) Pd/PDMC- $T$ -16 materials.

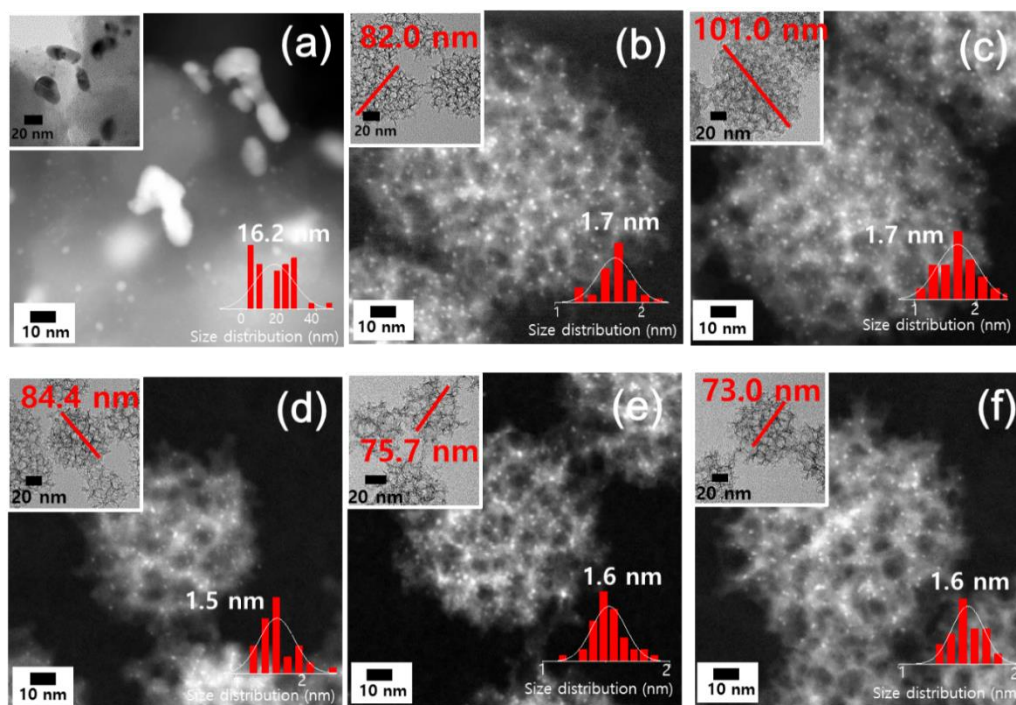


**Figure 4.2.** STEM and TEM images (inset) of Pd/PDMC- $T$ - $x$  materials: (a) Pd/PDMC-1000-0 (a control material), (b) Pd/PDMC-1000-16, (c) Pd/PDMC-500-16, (d) Pd/PDMC-700-16, (e) Pd/PDMC-800-16, and (f) Pd/PDMC-900-16.

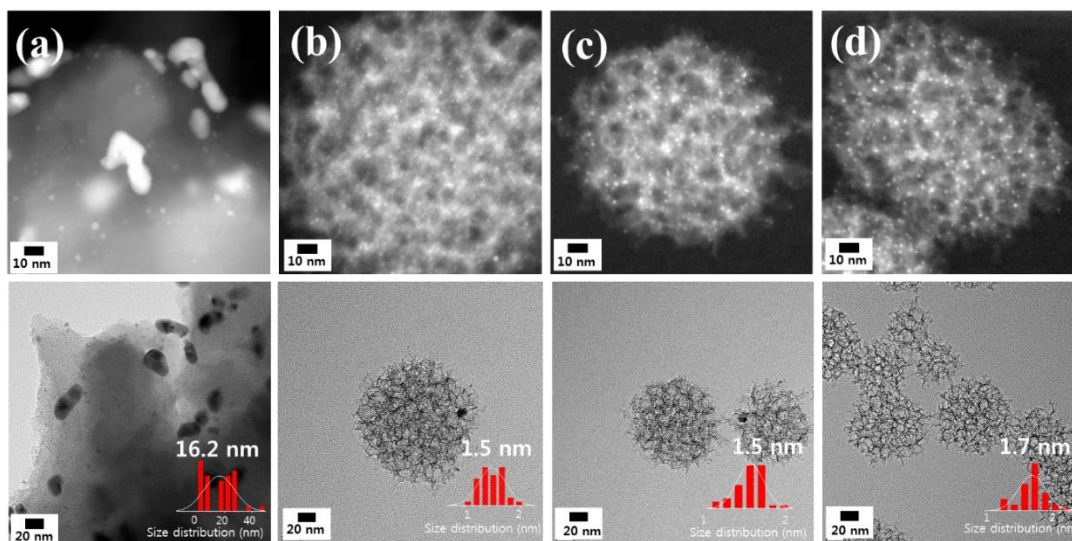


**Figure 4.3.** STEM images (Upper Panel) and HR-TEM images (Lower Panel) of the series of PDMC-1000- $x$  materials, where  $x$  is 0 g (a), 4 g (b), 8 g (c) and 16 g (d) of colloidal silica that were used with 20 mmol of aniline for the synthesis of the respective materials. The inset in each figure shows particle size distribution of the Pd nanoparticles (Pd NPs) in the materials.

Besides aiding with the formation of porous structures, the colloidal silica used as template in the syntheses of the materials appear to have indirectly played some roles in the formation of small Pd nanoparticles in the final materials. Specifically, when  $x$  (the amount of colloidal silica) is increased from 0 to  $\geq 4$  g, the size of the Pd nanoparticles in Pd/PDMC-1000- $x$  materials becomes smaller, and the average size of the Pd nanoparticles decreases from *ca.* 16 nm to *ca.* 1.5-1.7 nm (**Figure 4.3**). Additionally, results obtained by inductively coupled plasma optical emission spectrometry (ICP-OES) show that the colloidal silica templates seem to assist with the loading of Pd onto the PDMC materials. In other words, although  $282 \mu\text{mol Pd(II)}/g_{\text{catalyst}}$  is employed to synthesize the Pd nanoparticles in all the materials, the

$\mu\text{mol Pd/g}_{\text{cat}}$  that ended up residing in the final materials after the reduction step varies. More specifically, the amount of Pd in Pd/PDMC-1000-0 (made without silica templates) is much smaller ( $70 \mu\text{mol/g}_{\text{cat}}$ ) than the amounts ( $180\text{-}230 \mu\text{mol/g}_{\text{cat}}$ ) obtained in the materials synthesized using colloidal silica templates (*i.e.*, Pd/PDMC-1000-4, Pd/PDMC-1000-8 and Pd/PDMC-1000-16 (**Table 4.1**)).

#### 4.3.3. Effect of pyrolysis temperature on the structures of PDMC-T-x materials

The textural properties of the series of Pd/PDMC-T-16 materials prepared at different pyrolysis temperatures (500, 700, 800, 900, or 1000 °C) are then evaluated (**Figure 4.2** and entries 4-8 in **Table 4.1**). Compared with Pd/PDMC-500-16 (whose BET surface area is  $510 \text{ m}^2\cdot\text{g}^{-1}$ ), the materials obtained at 700 °C or higher pyrolysis temperatures all show significantly higher surface areas and porosity (with BET surface areas of  $845\text{-}1080 \text{ m}^2\cdot\text{g}^{-1}$ ). Close examination of the materials' morphologies by STEM and TEM reveal that Pd/PDMC-500-16 has larger, elliptical-shaped mesoporous carbon nanoparticles (*ca.* 101 nm) whereas those obtained at higher pyrolysis temperatures (700 °C and higher) have relatively smaller, spherical mesoporous carbon nanoparticles (with sizes ranging from 73 to 84 nm) (**Figure 4.2**). The size of the Pd nanoparticles in the materials is, however, reasonably similar in all of them (with an average size of *ca.* 1.6 nm), except in the one made without using colloidal silica as templates, in which case the size of then Pd nanoparticles is much higher and *ca.* 16 nm. The amount of Pd in the PDMC-T-16 materials ( $T = 500, 700, 800, 900$  and  $1000 \text{ }^\circ\text{C}$ ) determined by ICP-OES is *ca.*  $130\text{-}180 \mu\text{mol/g}_{\text{cat}}$  (**Table 4.1**). Furthermore, varying the loading amount of Pd(II) from 282 to  $94 \mu\text{mol/g}_{\text{cat}}$  on PDMC-800-16 support,  $80 \mu\text{mol/g}_{\text{cat}}$  of Pd(0)/PDMC-800-16 was obtain. The XRD patterns of the materials show a weak peak

at around  $2\Theta = 40^\circ$  corresponding to the (111) Bragg reflection of Pd, besides a peak at *ca.*  $2\Theta = 24^\circ$  corresponding to the (002) plane of amorphous/graphitic carbon (**Figure 4.4**).

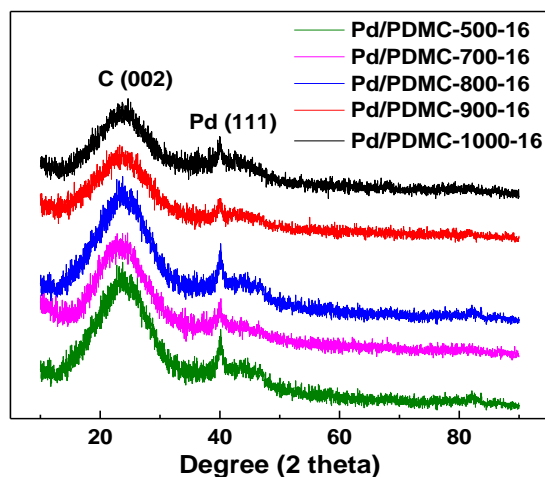


**Figure 4.4.** XRD patterns of the series of Pd/PDMC-*T*-16 materials synthesized.

#### 4.3.4. Catalytic properties of Pd/PDMC-*T*-*x* for $\text{HCO}_2^-$ dehydrogenation

Next the catalytic properties of the Pd/PDMC-*T*-*x* materials are tested, first for the  $\text{HCO}_2^-$  dehydrogenation reaction (**Table 4.2**). The control material (Pd/PDMC-1000-0, entry 1 in **Table 4.2**) shows barely any catalytic activity toward the reaction (**Figure 4.5**). On the other hand, the materials prepared using colloidal silica templates show good catalytic activity toward the reaction. Furthermore, their catalytic performance (conversion and turn-over-frequency (TOF)) increases when the amount of colloidal silica (*x*) used to make the materials is increased from 4 to 16 g (see entries 2-4 in **Table 4.2** and **Figure 4.5a,b**). Since the size of the Pd nanoparticles is nearly identical in all the Pd/PDMC-*T*-*x* materials, this trend in catalytic activity is most likely

to do with the increase in surface area in the Pd/PDMC-1000- $x$  (as the relative amount of colloidal silica used ( $x$ ) to synthesize them is increased).

**Table 4.2.** Catalytic TOF values for the dehydrogenation of sodium formate ( $\text{NaHCO}_2$ ) over the Pd/PDMC- $T$ - $x$  materials/catalysts.<sup>a)</sup>

<i>Entry</i>	<i>Pd/PDMC-T-x</i>		<i>TOF</i> [ $\text{h}^{-1}$ ] <sup>b)</sup>
	<i>T</i>	<i>X</i>	
1	1,000	0	N/A
2	1,000	4	813
3	1,000	8	1,054
4	1,000	16	1,396
5	900	16	1,570
6	800	16	1,854
7 <sup>c)</sup>	800	16	2,562
8	700	16	1,515
9	500	16	1,281
10 <sup>d),e)</sup>	Pd/C	N/A	1,034

All the reactions are carried out in 5 mL of 1 M of sodium formate with 25 mg of catalyst at 80 °C; <sup>b)</sup> TOF is calculated using the data obtained at 10 min using **Eq. 4.1-4.2**; <sup>c)</sup> 94  $\mu\text{mol}/\text{g}_{\text{cat}}$  of Pd (II) is loaded on the support material; <sup>d)</sup> 5.0 mg (4.7  $\mu\text{mol}$ ) of commercially available Pd/C (from Sigma-Aldrich, 10 wt. %) is used; <sup>e)</sup> Note that the surface area of this material is also high (745  $\text{m}^2/\text{g}$ ) or is comparable to those of most of the Pd/PDMC materials.

The equations used to determine the amount of the desired product (*i.e.*,  $\text{H}_2$ ) and the

reaction's turnover frequency (TOF) value are given as:

$$\text{mole of hydrogen (H}_2\text{) at 10 min, } n\text{H}_2 = P_{\text{atm}}(V_{\text{gas}})/RT \quad (\text{Eq. 4.1})$$

where  $P_{\text{atm}}$  is atmospheric pressure,  $V$  is total volume of gas generated by the reaction,  $R$  is gas constant, and  $T$  is temperature.

$$\text{Turnover frequency (TOF)} = \frac{\text{Total moles of hydrogen at 10 min}}{\text{moles of metal used } \times \text{ time}} \quad (\text{Eq. 4.2})$$

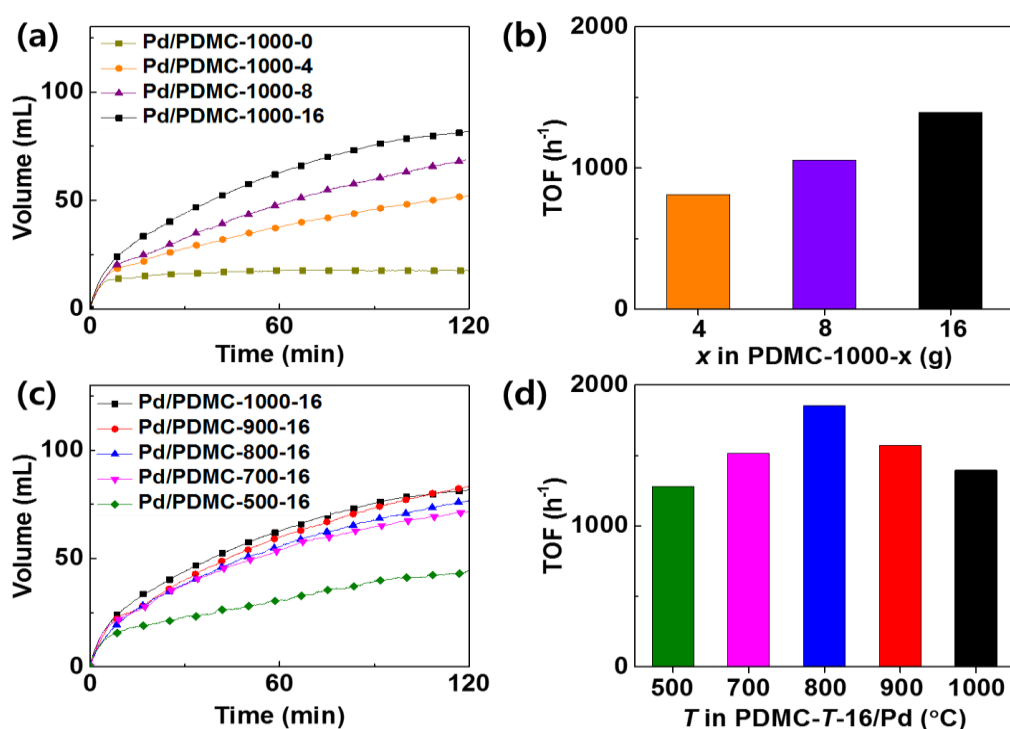


**Figure 4.5.** Amount of catalytically produced H<sub>2</sub> versus reaction time during the dehydrogenation of 1 M of aqueous NaHCO<sub>2</sub> over the different Pd/PDMC materials (left panels) and comparison of the relative catalytic activity of the materials in the catalytic reaction (right panels) for: (a,b) the series of Pd/PDMC-1000-x materials and (c,d) the series of Pd/PDMC-T-16 materials.

Additionally, the catalytic activity of the materials toward the reaction (*i.e.*,  $\text{HCO}_2^-$  dehydrogenation) is found to depend on the pyrolysis temperature used to synthesize them. The relationship follows a volcano type trend, where the catalytic activity of the materials increases as the pyrolysis temperature is raised from 500 to 800 °C, but then decreases afterwards (see entries 4-9 in **Table 4.2** and **Figure 4.5c-d**). Based on this result, it can be said that Pd/PDMC-800-16 is the best catalyst for  $\text{HCO}_2^-$  dehydrogenation reaction among the series of materials I have investigated here. Actually, when the loading of Pd(II) on PDMC-800-16 is lowered from 282 to 94  $\mu\text{mol/g}_{\text{cat}}$ , by decreasing the relative amount of Pd(II) used to synthesize the Pd nanoparticles, the TOF of the resulting material for  $\text{HCO}_2^-$  dehydrogenation is significantly higher, with a TOF value of 2,562  $\text{h}^{-1}$  (entry 7 in **Table 4.2**). Since the size of the Pd nanoparticles in the two materials is found to be about the same and the loading efficiency is effectively similar, there must have been relatively less number of Pd in the pores of the latter material. This, in turn, makes the latter material to provide better pathways for diffusion of reactants and products, and then yield better catalytic outcomes. This is what, I believe, is responsible for the higher TOF value obtained for the PDMC-800-16 material containing less amount of Pd compared with the one with higher amount of Pd.

Notably also, the catalytic activity of Pd/PDMC-800-16 is higher than those of Pd/C<sup>17,18</sup> and Pd/NMC<sup>20</sup> (or the few heterogeneous catalysts reported for the reaction in the literature) (**Table 4.3**). Moreover, Pd/PDMC-800-16's catalytic activity for the dehydrogenation reaction is better than that of the Pd/C material I have synthesized with no N dopants in its carbon structure as well (entry 10 in **Table 4.2**). So, based on these comparative results, it appears that the N sites incorporated into the PDMC

support material are instrumental to the enhanced catalytic activity exhibited by the Pd/PDMC-800-16 as well as the other Pd/PDMC materials. This point is discussed further in the sections to follow.

**Table 4.3.** Comparison of the catalytic activity of Pd/PDMC for formate dehydrogenation with respect to various notable heterogeneous Pd-based catalysts reported in the literature for the same reaction.

<i>Entry</i>	<i>Catalysts</i>	<i>Initial TOF at 10 min</i>	<i>Temp. (°C)</i>	<i>Type of formate (HCO<sub>2</sub><sup>-</sup>)</i>	<i>Reference</i>
1	Pd/C	375	70	KHCO <sub>2</sub> (10 M)	17 and 18
2	Pd/AC	250	80	NH <sub>4</sub> HCO <sub>2</sub> (1 M)	21
3	Pd/r-GO	12,235	80	KHCO <sub>2</sub> (4.8 M)	19
4	Pd/NMC-8	2,243	60	KHCO <sub>2</sub> (2 M)	22
<b>5</b>	<b>Pd/PDMC</b>	<b>2,562</b>	<b>80</b>	<b>NaHCO<sub>2</sub> (1 M)</b>	<b>This work</b>

It is worth adding that the dehydrogenation reaction over the Pd/PDMC-*T-x* materials does not release CO, as characterized by gas chromatography (GC) (**Table 4.4** and **Figure 4.6**). Conversely, the dehydrogenation over Pd/PDMC-*T-x* catalysts goes through the desirable process of  $\text{HCO}_2^- + \text{H}_2\text{O} \rightarrow \text{H}_2 + \text{HCO}_3^-$ , without forming the undesired byproduct CO, which sometimes forms by such reactions over some catalysts. In addition, the Pd/PDMC-*T-x* catalysts are proven to be easily recyclable and reusable several times without significant losing their catalytic activity. For example, Pd/PDMC-800-16 is recycled and reused up to at least three times, giving nearly similar

TOF values (of  $1854 \text{ h}^{-1}$ ,  $1753 \text{ h}^{-1}$  and  $1477 \text{ h}^{-1}$  for the 1<sup>st</sup>, 2<sup>nd</sup> and 3<sup>rd</sup> runs, respectively) (Figure 4.7). Consistent with this result, STEM indicates that the size of the Pd nanoparticles in the Pd/PDMC-*T-x* remain nearly unchanged after recycling (see, for example, the STEM image of Pd/PDMC-800-16 after the 3<sup>rd</sup> reaction cycle, Figure 4.7). Moreover, tests by ICP-OES for possible leached Pd species in the reaction mixture reveal only  $< 2 \text{ ppm}$  of Pd, indicating the high stability of the Pd/PDMCs catalysts during catalysis.

**Table 4.4.** The type and amount of gaseous products obtained/expected from the dehydrogenation reaction, as determined by GC.

<i>Pd/PDMC-1000-16</i>	$H_2$	$O_2$	$N_2$	$CO$	$CO_2$
<b>Result (%)</b>	38.7	7.6	48.1	0	0

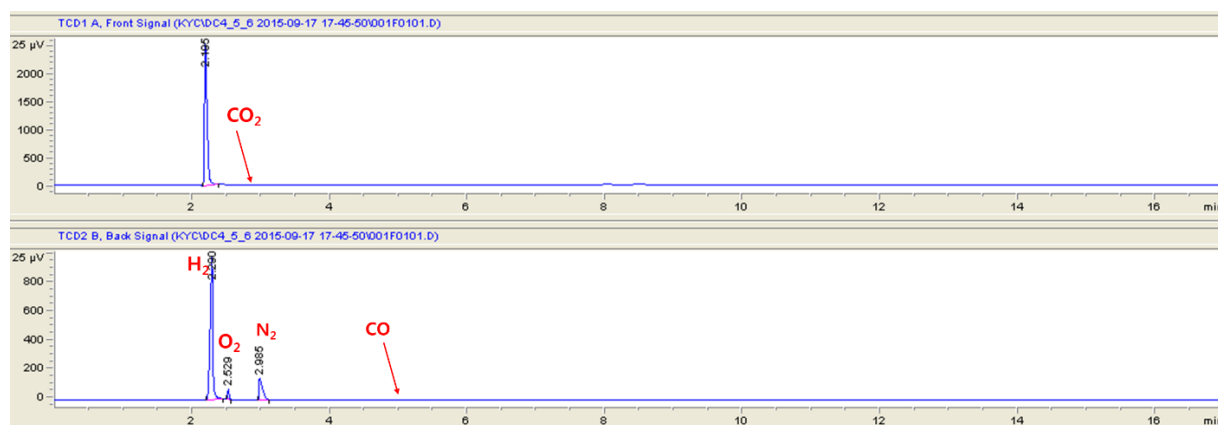


**Figure 4.6.** Typical gas chromatograms (GC) of the gaseous products formed during formate dehydrogenation using the Pd/PDMC catalysts.

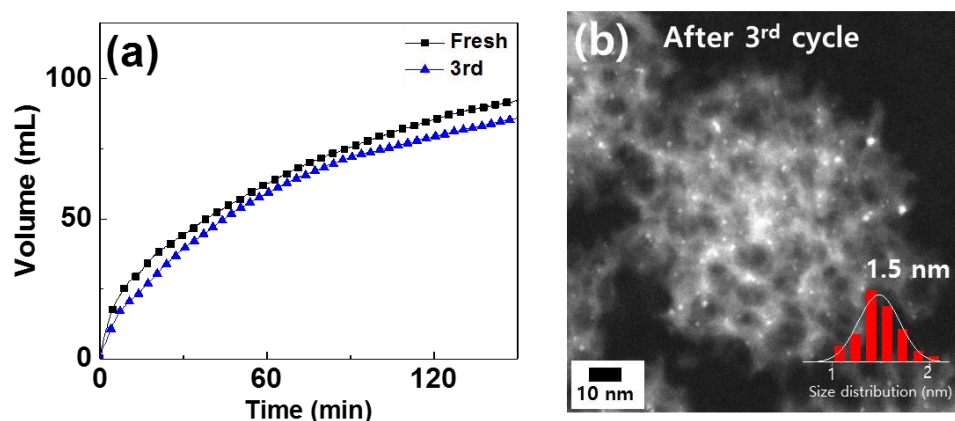


**Figure 4.7.** (a) Recyclability results of Pd/PDMC-800-16 catalyst in dehydrogenation reaction and (b) STEM image of the catalyst after 3<sup>rd</sup> cycle.

#### 4.3.5. Catalytic properties of Pd/PDMC-*T*-*x* for HCO<sub>3</sub><sup>-</sup> hydrogenation

To assess the ability of Pd/PDMC-*T*-16 materials to promote the H<sub>2</sub> recharging reaction, the hydrogenation of HCO<sub>3</sub><sup>-</sup> (to HCO<sub>2</sub><sup>-</sup>) in the presence of the materials is evaluated (**Table 4.5**). The catalytic activity of the materials toward this reaction as a function of their pyrolysis temperature also followed a volcano type trend, in the same way as the result obtained for the dehydrogenation reaction above. Moreover, the Pd/PDMC material synthesized at 800 °C (Pd/PDMC-800-16), once again, shows the best catalytic activity for this reaction, while those prepared either at lower or higher temperatures than 800 °C give lower catalytic activities. The general trend of the materials' catalytic activity for the HCO<sub>3</sub><sup>-</sup> hydrogenation reaction is found to be Pd/PDMC-800-16 > Pd/PDMC-700-16 > Pd/PDMC-900-16 > Pd/PDMC-1000-16 >> Pd/PDMC-500-16. Notably, the turnover numbers (TONs) of all the Pd/PDMC materials, even the poorly performing ones, is comparable to those of other previously reported Pd-based catalysts for the HCO<sub>3</sub><sup>-</sup> hydrogenation reaction (**Table 4.6**).<sup>17-21</sup>

**Table 4.5.** Turnover number (TON) values for the hydrogenation of sodium bicarbonate ( $\text{HCO}_3^-$ ) over Pd/PDMC-*T*-16.<sup>a)</sup>

<i>Entry</i>	<i>PDMC-T-x</i>		<i>Conv.</i> [%] <sup>b)</sup>	<i>TON</i> <sup>c)</sup>
	<i>T</i>	<i>x</i>		
1	500	16	22	338
2	700	16	74	987
3	800	16	82	1,171
4 <sup>d)</sup>	800	16	65	1,625
5	900	16	73	973
6	1,000	16	70	778
7 <sup>e),f)</sup>	Pd/C	N/A	52	369

<sup>a)</sup> Reaction conditions: 50 mg catalyst with 10 mL of 1 M of  $\text{HCO}_3\text{Na}$  at 80 °C with 40 bar for 24 h; <sup>b)</sup> Conversion values are calculated from the amount of formate produced from the reaction and measured by HPLC; <sup>c)</sup> TON values are calculated using **Eq. 4.3**; <sup>d)</sup> 94  $\mu\text{mol/g}_{\text{cat}}$  (*i.e.*, less amount) of Pd is loaded on same batch of PDMC-800-16 support material; <sup>e)</sup> 15.0 mg (14  $\mu\text{mol}$ ) of commercially available Pd/C (from Sigma-Aldrich, 10 wt. %) is used; <sup>f)</sup> Note that the surface area of this material is also high (745  $\text{m}^2/\text{g}$ ) or comparable to those of most of the Pd/PDMC materials.

**Table 4.6.** Comparison of the catalytic activity of Pd/PDMC for bicarbonate hydrogenation reaction with respect to the various notable heterogeneous Pd-based catalysts reported in the literature for the same reaction.

<i>Entr</i> <i>y</i>	<i>Catalysts</i>	<i>Press.</i> <i>(bar)</i>	<i>Temp.</i> <i>(°C)</i>	<i>Time</i> <i>(h)</i>	<i>Type of</i> <i>Bicarbonate</i>	<i>TON</i>	<i>Ref.</i>
1	Pd/AC	28	20	15	NH <sub>4</sub> HCO <sub>3</sub> (1 M)	1,769	18
2	Pd/r-GO	40	80	10	KHCO <sub>3</sub> (4.8 M)	1,555	19
3	Pd/NMC-8	60	80	4	KHCO <sub>3</sub> (4 M)	1,598	21
<b>4</b>	<b>Pd/PDMC</b>	<b>40</b>	<b>80</b>	<b>24</b>	<b>NaHCO<sub>3</sub></b> <b>(1 M)</b>	<b>1,625</b>	<b>This work</b>

The turnover number (TON) of the reaction was calculated by the following formula (Eq. 4.3). The moles of the catalysts for the equation were obtained by ICP-OES analyses.

$$\text{Turnover number (TON)} = \frac{\text{Total moles of formate}}{\text{Moles of catalyst used}} \quad \text{Eq. 4.3}$$

An additional control experiment involving a commercially available Pd/C (10 wt. %) that does not have N-dopants in its carbon (Figure 4.8). Despite its high surface area (745 m<sup>2</sup>/g) or comparable surface area as those of Pd/PDMC materials, the Pd/C (10 wt. %) shows a significantly lower catalytic activity and gives a lower TOF value

than most of the Pd/PDMC materials I have investigated, for the hydrogenation reaction (entry 7 in **Table 4.5**), just like in the hydrogenation reaction above.

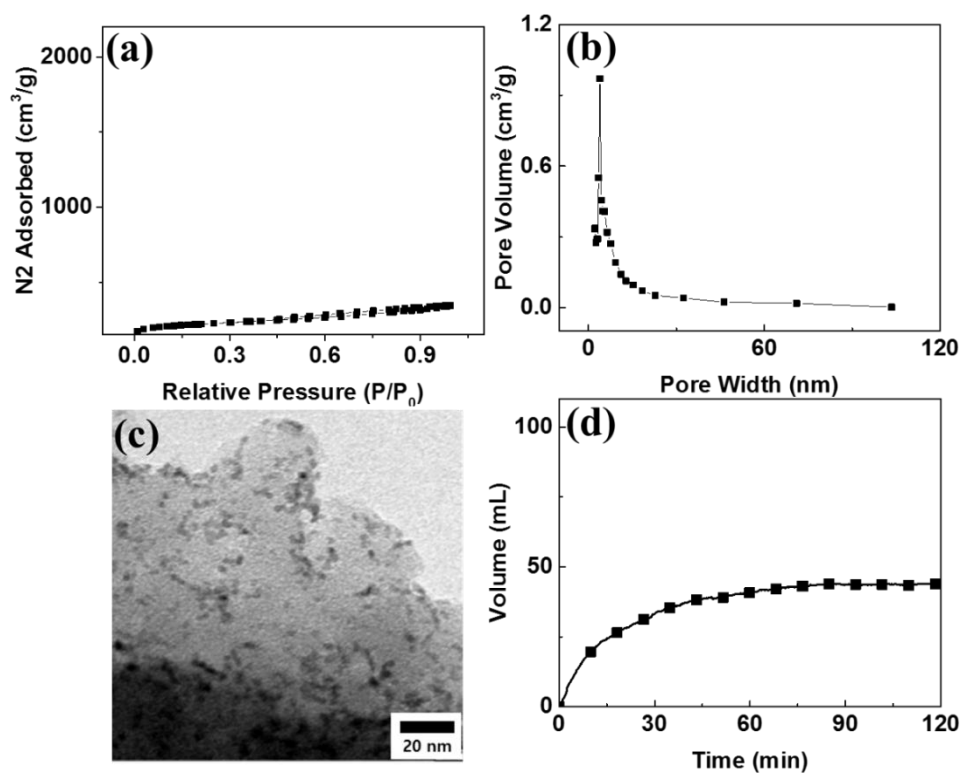


**Figure 4.8.** (a) N<sub>2</sub> adsorption/desorption isotherm, (b) BJH pore size distribution curve, (c) TEM image, and (d) catalytic activity toward HCO<sub>2</sub><sup>-</sup> dehydrogenation of a commercially available Pd/C (Sigma-Aldrich, 10 wt. %). The catalytic reaction conditions were: 4.7 μmol of Pd/C in 5 mL of 1 M of NaHCO<sub>2</sub>.

#### ***4.3.6. Investigation of chemical states of N-dopant sites and their effect on the materials' catalytic properties***

Although Pd nanoparticles remain the major species responsible for Pd/PDMCs' catalytic activity toward both reactions, the superior performances of the Pd/PDMC catalysts in both reactions appear to be due to the presence of N-dopant-related species on their carbon support materials. This hypothesis is further supported by the result obtained from an additional control experiment involving a commercially Pd/C (10 wt. %) that I discussed before.

To further elucidate the effect of N-dopant sites in the Pd/PDMC materials on the materials' catalytic activity, the density and chemical states of nitrogen in the catalysts are analyzed using X-ray photoelectron spectroscopy (XPS) and Raman spectroscopy. The XPS survey spectra show that the atomic ratios of N to C in the Pd/PDMC-*T*-16 catalysts decreases from 11 to 3 % when their pyrolysis temperature is raised from 500 to 1000 °C (**Figure 4.9a**). The N1s peak in the spectra can be deconvoluted into four distinct peaks, corresponding to pyridinic-N (398.7 eV), pyrrolic-N (400.3 eV), quaternary-N (401.2 eV), and pyridinic-N<sup>+</sup>-O<sup>-</sup> (403.3 eV) species.<sup>31</sup> The relative density of the different N-doped species in the materials varies as a function of pyrolysis temperature (**Figure 4.9b** and **Figure 4.10**). The best catalyst for both reactions, Pd/PDMC-800-16, has a relatively higher density of electron-rich pyrrolic-N and pyridinic-N groups than the other Pd/PDMC-*T*-16 materials. Moreover, the density of these groups is higher than the quaternary-N (electron-deficient) species not only in Pd/PDMC-800-16 but all also in all the other Pd/PDMC-*T*-16 materials. On the other hand, the poorly performing catalyst, Pd/PDMC-500-16, has the least amount of electron-rich pyrrolic-N and pyridinic-N groups. Since the electron-rich pyrrolic-N and

pyridinic-N groups are generally unlikely to form at pyrolysis temperatures less than 600 °C,<sup>28-32</sup> their absence in Pd/PDMC-500-16, and thus Pd/PDMC-500-16's low catalytic activity, are perhaps not surprising.

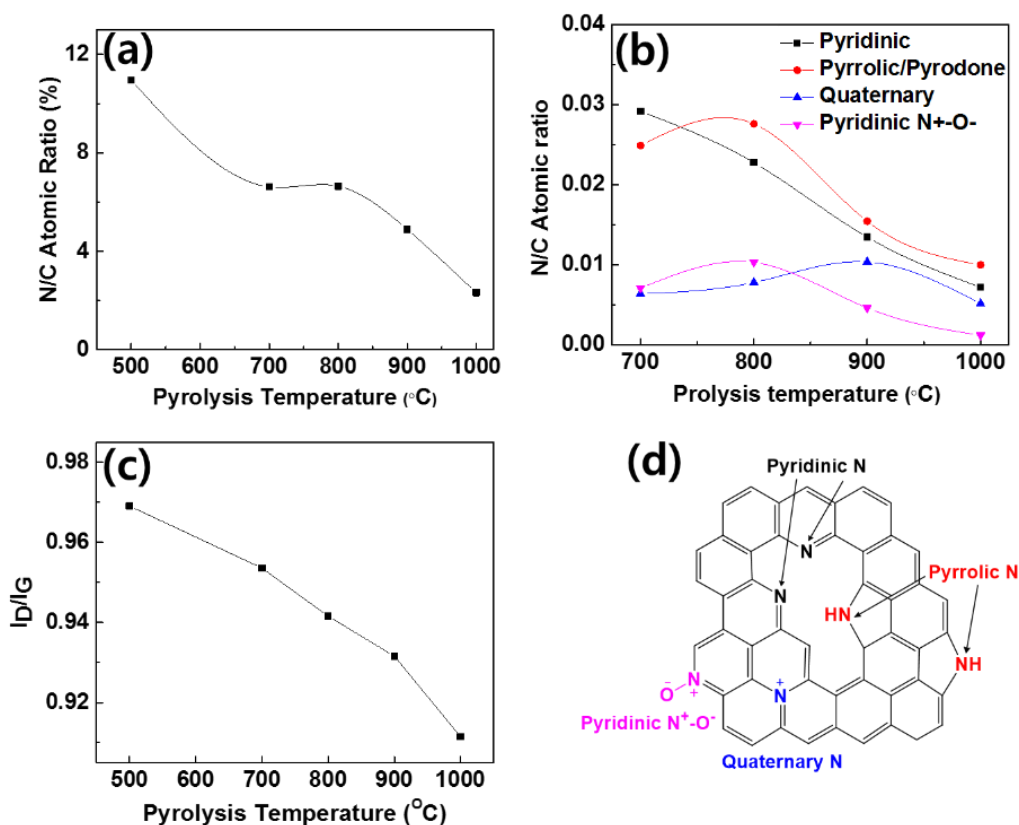


**Figure 4.9.** Results based on XPS and Raman spectra for different Pd/PDMC-*T*-16 materials (where *T* = 500, 700, 800, 900, and 1000 °C): (a) N/C atomic ratio for the total N and C in the materials, (b) N/C ratio for the different types of N species analyzed by XPS, (c)  $I_D/I_G$  ratio (ratio of intensity of D and G bands based on Raman spectra), and (d) plausible structures of the N species present in the N-doped carbon materials.

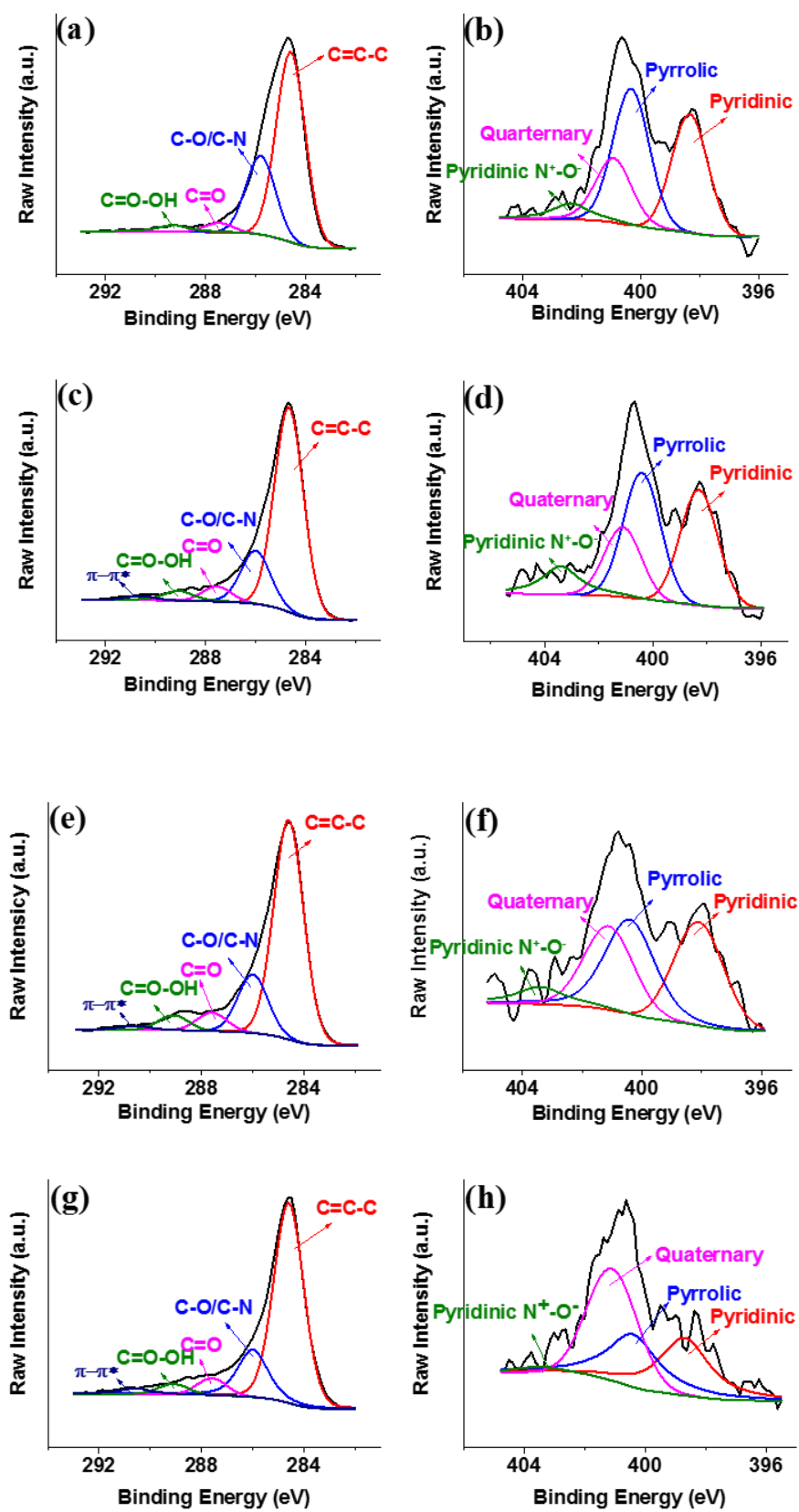


**Figure 4.10.** High-resolution, deconvoluted XPS spectra of C1s (left panels) and N1s (right panels) for the series of Pd/PDMC-*T-x* materials synthesized: (a-b) Pd/PDMC-700-16, (c-d) Pd/PDMC-800-16, (e-f) Pd/PDMC-900-16, and (g-h) Pd/PDMC-1000-16.

The deconvoluted XPS C1s peaks of the Pd/PDMC materials (**Figure 4.11**) also show peaks corresponding O and N species.<sup>32</sup> In the case of the XPS spectra of Pd3d, doublet XPS peaks corresponding to Pd(II) at *ca.* 343.0 eV (Pd 3d<sub>3/2</sub>) and 337.6 eV (Pd 3d<sub>5/2</sub>) and doublet peaks corresponding to Pd(0) at 340.9 eV (Pd 3d<sub>3/2</sub>) and 335.6 eV (Pd 3d<sub>5/2</sub>) are observed in all the materials.<sup>33,34</sup> The observed Pd(II) species are most likely due to the presence of Pd-O and/or Pd-N bonds in the materials (**Figure 4.11**). This is further corroborated by extended X-ray absorption fine structure (EXAFS) and near extended X-ray absorption fine structure (NEXAFS) analyses (*vide infra*).

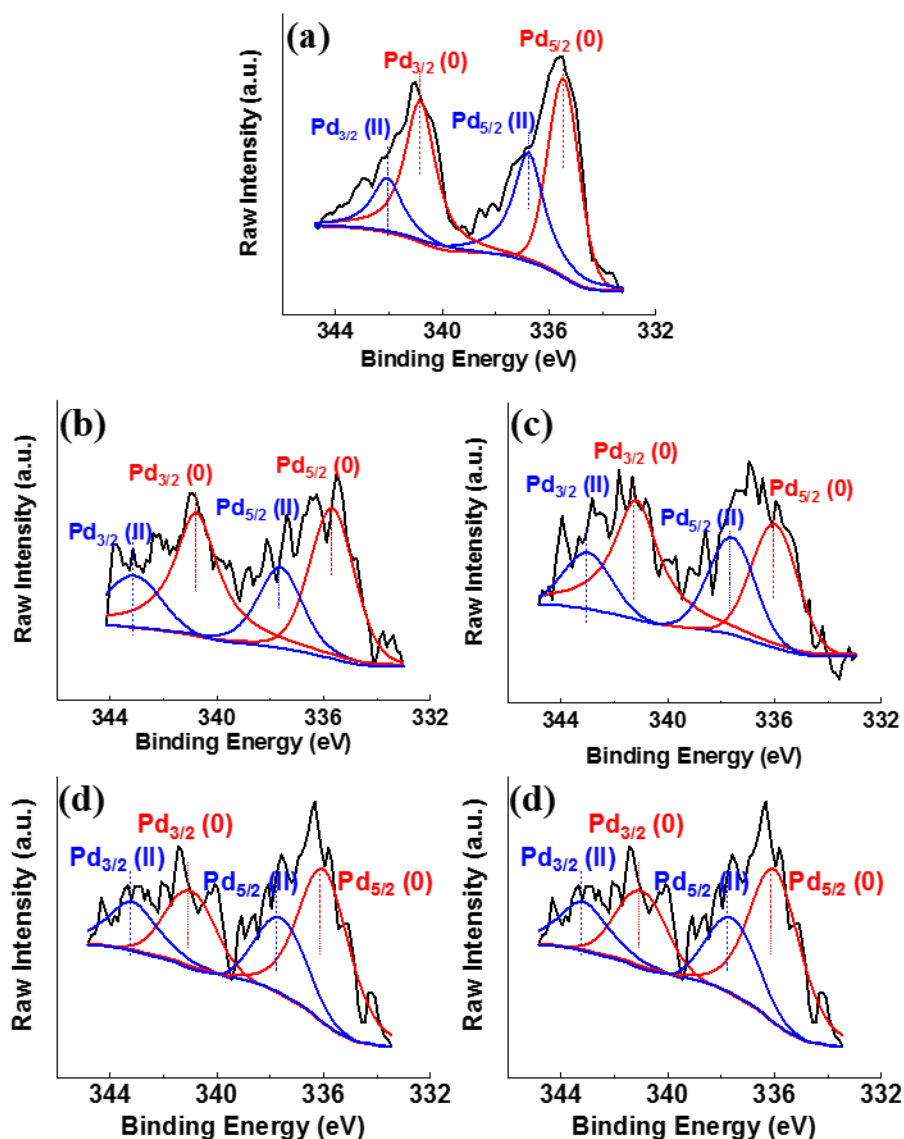


**Figure 4.11.** High-resolution XPS spectra of Pd3d region of the series of PDMC-*T*-16/Pd materials, namely: (a) Pd/PDMC-500-16, (b) Pd/PDMC-700-16, (c) Pd/PDMC-800-16/Pd, (d) Pd/PDMC-900-16, and (e) Pd/PDMC-1000-16.

Additionally, the PDMC-*T*-16 materials are characterized by Raman spectroscopy. Their Raman spectra show two first-order bands at  $1345\text{ cm}^{-1}$  and  $1580\text{ cm}^{-1}$  (**Figure 4.9**). These correspond to the characteristic D band (which is associated with the defects in carbon materials or which in our case is to do with the presence of N dopants in the

materials) and G band (due to the typical  $E_{2g}$  modes), respectively, of graphitic carbon materials. The ratio of intensity of the two peaks ( $I_D/I_G$  ratio) decreases from 0.97 to 0.91 as the pyrolysis temperature is raised from 500 to 1000 °C, indicating the increase in the degree of graphitization in the PDMC materials at higher pyrolysis temperatures (Figure 4.9 and Figure 4.12). According to these results, particularly the ones displayed in Figure 4.9b and Figure 4.10 the different N-dopant-associated species, which are present in the PDMC- $T$ - $x$  materials, are compiled and illustrated in Figure 4.9d.

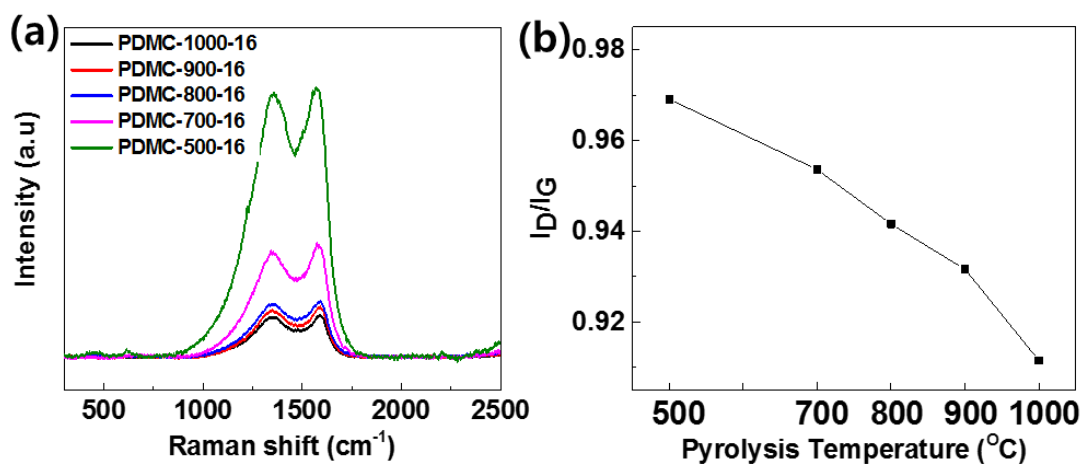


**Figure 4.12.** (a) Raman spectra of PDMC- $x$ -16 materials and (b) their  $I_D/I_G$  ratios as a function of their pyrolysis temperature.

#### 4.3.7. Investigation of metal–support interactions

To obtain more structural information about Pd/PDMC- $T$ - $x$  materials, including the possible presence of metal-support interactions in them, the materials are analyzed by EXAFS at Pd K-edge region (Figure 4.13 and Table 4.7) and by NEXAFS (Figure 4.14). The coordination numbers (CNs) of Pd-Pd bonding in all the Pd/PDMC- $T$ - $x$

materials ( $CN_{Pd-Pd} \approx 2$  to 4) are significantly less than that of bulk Pd foil ( $CN_{Pd-Pd} \approx 12$ ), confirming the presence of well dispersed Pd nanoclusters, each containing only few atoms, on the N-doped carbon support materials. This is also consistent with the observation made by STEM, in which small Pd nanoparticles with an average size of *ca.* 1.6 nm are seen (**Figure 4.2**). In addition, the EXAFS results indicate that the Pd nanoparticles in the PDMC materials are at least partially coordinated with O, N and/or C atoms of the support material, strongly suggesting the presence of metal–support interactions.

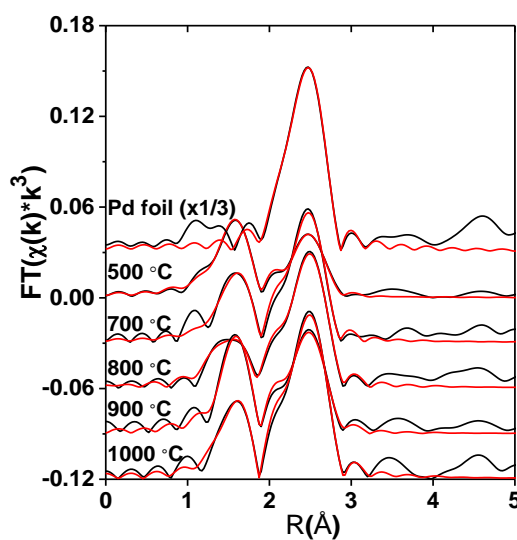


**Figure 4.13.** Fourier transformed EXAFS (black) of Pd/PDMC-*T*-16 materials (where *T* = 500, 700, 800, 900, or 1000 °C) and their best fits (red).

**Table 4.7.** Table for structural parameters obtained from EXAFS analyses.

	<i>Path</i>	<i>Coordination</i>	<i>Bond</i>	$\sigma^2$	$\Delta E_0$
		<i>Number</i>	<i>Length</i>	$[10^{-3}]$	$[eV]$
		<i>(CN)</i>	$[\text{\AA}]$	$\text{\AA}^2]$	
Pd/PDMC-	Pd-X <sup>a</sup>	2.4(2)	2.02(6)	4.6 (7)	0 (1)
500-16	Pd-Pd	2.4(3)	2.74(1)	8.8 (8)	-4 (2)
Pd/PDMC-700-	Pd-X <sup>a</sup>	2.0(3)	2.02(8)	4.0 (1)	1 (2)
16	Pd-Pd	3.6(4)	2.73(9)	7.0 (7)	-2 (1)
Pd/PDMC-800-	Pd-X <sup>a</sup>	2.0(3)	1.97(1)	7.0 (1)	-8 (3)
16	Pd-Pd	4.3(3)	2.74(3)	7.6 (5)	-1 (3)
Pd/PDMC-900-	Pd-X <sup>a</sup>	1.8(2)	2.01(5)	0.9 (9)	-0.4 (7)
16	Pd-Pd	3.4(5)	2.74(5)	8.0 (1)	-2 (1)
Pd/PDMC-	Pd-X <sup>a</sup>	1.8(3)	2.01(1)	3.0 (1)	-2 (3)
1000-16	Pd-Pd	4.5(5)	2.75(2)	6.6 (7)	-2 (1)
Pd foil	Pd-Pd	12(9)	2.74(4)	5.5 (4)	-2 (7)

<sup>a</sup>X could be O, C, or N, which are indistinguishable in EXAFS fitting analysis.

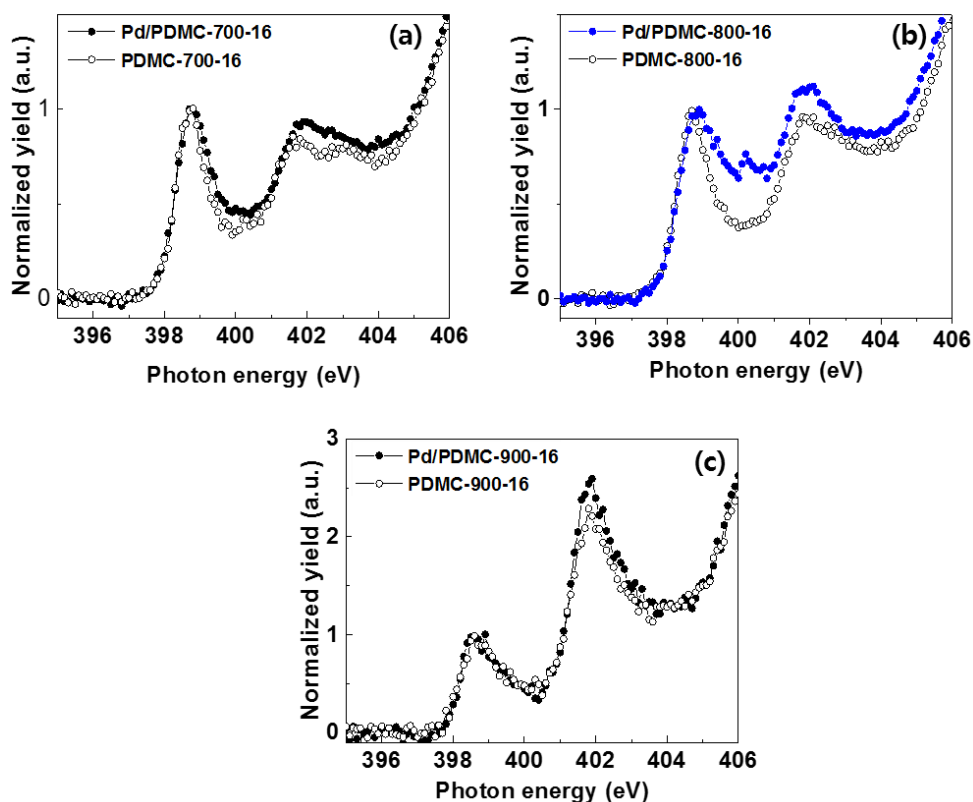


**Figure 4.14.** NEXAFS spectra of (a) Pd/PDMC-700-16, (b) Pd/PDMC-800-16, and (c) Pd/PDMC-900-16, along their corresponding control materials that contain no Pd nanoparticles.

Among all the Pd-X bond length of Pd/PDMC samples, Pd/PDMC-800-16 shows the shortest length, 1.97 Å (Table 4.7). This suggests that Pd/PDMC-800-16 has the strongest metal–support interaction. The shortest bond length and the strongest metal–support interactions of Pd/PDMC-800-16 (1.97 Å) may have been the result of the relatively higher density of electron rich pyrrolic and pyridinic groups in its N-doped carbon nanostructure.

The interface between Pd nanoparticles and PDMC is further investigated with NEXAFS, and the results are displayed in Figure 4.15. In the NEXAFS spectra,

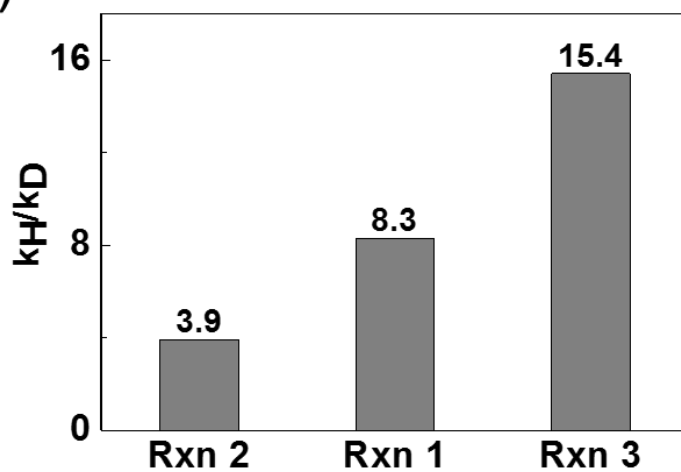
Pd/PDMC-800-16 is the only material that shows two different features of peak broadenings, the first at *ca.* 399.4 eV and the second at *ca.* 400.2 eV (**Figure 4.14b**). Both peaks can be assigned to Pd-N type interactions,<sup>35</sup> where the unoccupied N 2p states hybridize with the Pd 4d orbitals.<sup>36</sup> The result suggests that Pd/PDMC-800-16 displays a distinct, strong interaction between its Pd nanoparticles and the N-species on its support material. This result is in agreement with the one obtained by EXAFS above. So, it is not surprising then that this material is also the one that shows the highest catalytic activity for the  $\text{HCO}_2^-/\text{HCO}_3^-$  reversible reactions.

#### 4.3.8. Mechanistic studies

To elucidate the plausible reaction pathways by which the reversible  $\text{HCO}_2^-/\text{HCO}_3^-$  reactions take place over Pd/PDMCs, isotopic labeling studies are performed. Specifically three different kinds of isotopic labeling reactions are conducted with Pd/PDMC-800-16. The first one is  $\text{D-CO}_2^- + \text{H}_2\text{O}$ , which is named as Reaction 1; the second one is  $\text{H-CO}_2^- + \text{D}_2\text{O}$ , which is named as Reaction 2; and the third one is  $\text{D-CO}_2^- + \text{D}_2\text{O}$ , which is named as Reaction 3. The reactions are illustrated in detail in Scheme S1. The results from the reactions show kinetic isotope effects (KIE) (**Figure 4.15,I**), where the values of  $k_{\text{H}}/k_{\text{D}}$  follow the trend of: Reaction 3 (15.4)  $\gg$  Reaction 1 (8.3)  $>$  Reaction 2 (3.9). The results also indicate that both  $\text{H}_2\text{O}$  and  $\text{HCO}_2^-$  are involved in the rate-determining step. Moreover, the fact that Reaction 1 gives higher KIE value than Reaction 2 suggests that the bond cleavage of HO-H takes place prior to that of H- $\text{CO}_2^-$  during the dehydrogenation reaction (**Figure 4.15, I**). In the reaction mechanism, the final step involves the release of  $\text{H}_2$  *via* reductive elimination

from the H-Pd-H species.<sup>17</sup> The hydrogenation of  $\text{HCO}_3^-$  can essentially be thought of as the reverse of the above-discussed  $\text{HCO}_2^-$  dehydrogenation processes.

(I)



(II)

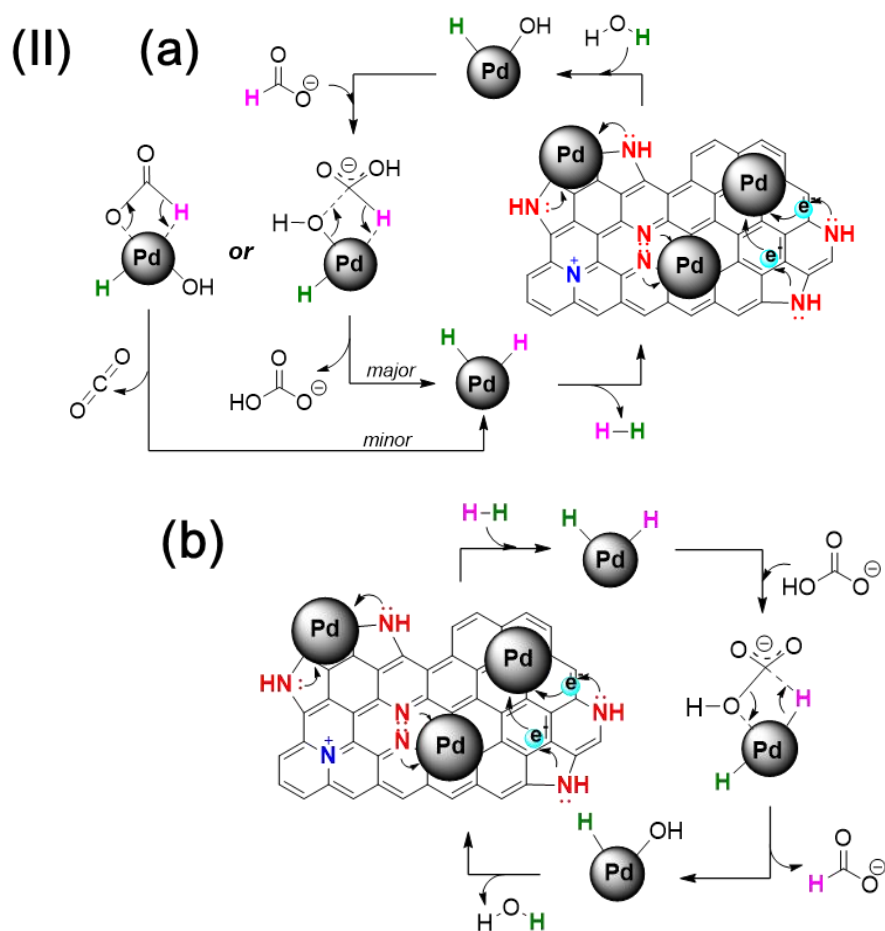


**Figure 4.15.** (I) Results of kinetic isotope effect (KIE) for different reactions over Pd/PDMC-800-16. **Rxn 1** is for  $\text{D-CO}_2^- + \text{H}_2\text{O}$ , **Rxn 2** is for  $\text{H-CO}_2^- + \text{D}_2\text{O}$ , and **Rxn 3** is for  $\text{D-CO}_2^- + \text{D}_2\text{O}$ . (II) Plausible reaction mechanisms for the  $\text{HCO}_2^-/\text{HCO}_3^-$  reversible reactions over the Pd/PDMC materials. The reactions allow reversible  $\text{H}_2$  storage/release: a) dehydrogenation pathway and b) hydrogenation pathways. (The pink and green colored H's indicate the H atoms originated from  $\text{HCO}_2^-$  and  $\text{H}_2\text{O}$ , respectively). The detailed stepwise pathways are further depicted in **Scheme 4.16**.

Supported by our various methods including XPS, Raman, EXAFS, NEXAFS, and isotopic labeling studies, the reaction mechanisms for the  $\text{HCO}_2^-/\text{HCO}_3^-$  reversible transformations over the Pd/PDMC material are then proposed, as shown in **Figure 4.15,II**. Notably, our results above suggest that the pyridinic/pyrrolic N species formed on the graphitic carbon surfaces upon pyrolysis are likely to accelerate the reversible  $\text{HCO}_2^-/\text{HCO}_3^-$  conversions by donating electron density to Pd *via* strong metal–support interactions. Moreover, the fact that the Pd nanoparticles in the catalyst are quite small in size, thanks to the synthetic route employed to make them, may have made the materials to show efficient catalytic activity towards the  $\text{HCO}_2^-/\text{HCO}_3^-$  reversible reactions.

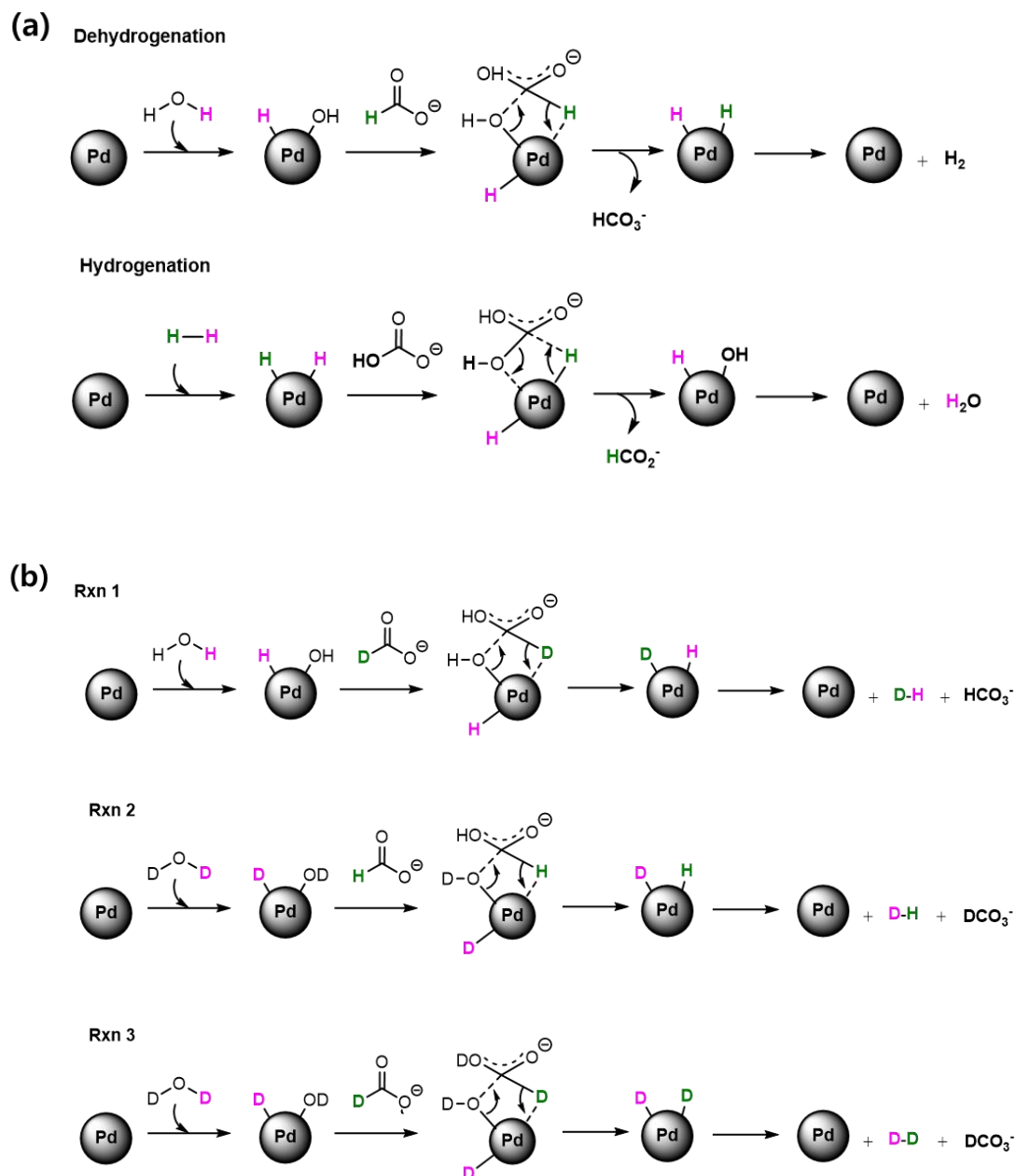


**Figure 4.16.** Schematic description for the possible reaction pathways of the dehydrogenation of formate and hydrogenation of bicarbonate. Schematic description for the possible reaction pathways of dehydrogenation with deuterium labeled reagents for the purposes of kinetic isotope effect (KIE) studies (**H** indicates hydrogen from water and **H** is related with formate species).

#### 4.4. Conclusion

In summary, I have presented the synthesis of polyaniline (PANI)-derived N-doped mesoporous carbons containing supported Pd nanoparticles (Pd/PDMCs) that show excellent catalytic activity for the  $\text{HCO}_2^-/\text{HCO}_3^-$  reversible reactions. The catalytic activity of the materials has been found to be dependent on their physical properties (*e.g.*, porosity and size of Pd nanoparticles) and chemical compositions (N-dopant associated species) of the materials. The structures and compositions of the catalysts have been controlled and optimized by varying the relative amount of colloidal silica templates and pyrolysis temperatures used to synthesize the materials. In addition, the pyrolysis temperature has been found to cause variations in the local N-C structures of the N-doped carbon support material. The N-dopant-associated species present in the materials have induced strong metal–support interactions, making the materials to exhibit excellent catalytic activity toward the  $\text{HCO}_2^-/\text{HCO}_3^-$  reversible reactions. The structural and composition parameters identified for the materials in relation to their catalytic properties toward these reversible reactions can provide valuable guidelines for the development of efficient catalysts for  $\text{H}_2$ -based energy storage/release catalytic systems for  $\text{H}_2$ -powered fuel cells and related applications.

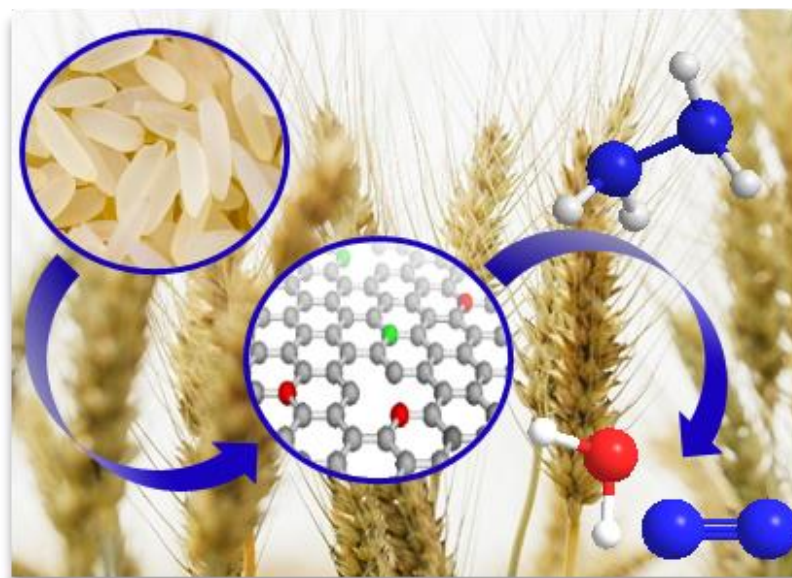
#### 4.5. Reference

- (1) Turner, J.A. *Science*, **2004**, *305*, 972-974.
- (2) Crabtree, G.W.; Dresselhaus, M.S.; Buchanan, M.V. *Phys. Today*, **2004**, *57*, 39-44.
- (3) Liu, C.; Li, F.; Ma, L.-P.; Cheng, H.-M. *Adv. Mater.* **2010**, *22*, E28-E62.
- (4) Armaroli, N.; Balzani, V. *Angew. Chem. Int. Ed.* **2007**, *46*, 52-66.
- (5) Dadfarnia, M.; Novak, P.; Ahn, D.C.; Liu, J.B.; Sofronis, P.; Johnson, D.D.; Robertson, I.M. *Adv. Mater.* **2010**, *22*, 1128-1135.
- (6) Graetz, J. *Chem. Soc. Rev.* **2009**, *38*, 73-82.
- (7) Li, L.; Mu, X.; Liu, W.; Mi, Z.; Li, C.-J. *J. Am. Chem. Soc.* **2015**, *137*, 7576-7579.
- (8) Yadav, M.; Xu, Q. *Energy Environ. Sci.*, **2012**, *5*, 9698-9725.
- (9) Demirci, U. B.; Miele, P. *Energy Environ. Sci.* **2009**, *2*, 627-637.
- (10) Çakanyildirim, Ç.; Gürü, M. *Int. J. Hydrog. Energy* **2008**, *33*, 4634-4712.
- (11) Stephens, F.H.; Pons, V.; Baker, R.T. *Dalton Trans.* **2007**, *25*, 2613-2626.
- (12) Grasmann, M.; Laurenczy, G. *Energy Environ. Sci.* **2012**, *5*, 8171-8181.
- (13) Loges, B.; Boddien, A.; Gärtner, F.; Junge, H.; Beller, M. *Top. Catal.* **2010**, *53*, 902-914.
- (14) Federsel, C.; Jackstell, R.; Boddien, A.; Laurenczy, G.; Beller, M.; *ChemSusChem* **2010**, *3*, 1048-1050.
- (15) Boddien, A.; Gärtner, F.; Federsel, C.; Sponholz, P.; Mellmann, D.; Jackstell, R.; Junge, H.; Beller, M. *Angew. Chem. Int. Ed.* **2011**, *50*, 6411-6414.
- (16) Papp, G.; Csorba, J.; Laurenczy, G.; Joó, F. *Angew. Chem. Int. Ed.* **2011**, *123*, 10617-10619.
- (17) Wiener, H.; Sasson, Y.; Blum, J. *J. Mol. Catal.* **1986**, *35*, 277-284.
- (18) Zaidman, B.; Wiener, H.; Sasson, Y. *Int. J. Hydrogen Energ.* **1986**, *11*, 341-347.
- (19) Bi, Q.-Y.; Lin, J.-D.; Liu, Y.-M.; Du, X.-L.; Wang, J.-Q.; He, H.-Y.; Cao, Y. *Angew. Chem. Int. Ed.* **2014**, *126*, 13801-11853.
- (20) Su, J.; Yang, L.; Lu, M.; Lin, H. *ChemSusChem* **2015**, *8*, 813-816.
- (21) Wang, F.; Xu, J.; Shao, X.; Su, X.; Huang, Y.; Zhang, T. *ChemSusChem* **2016**, *9*, 246-251.
- (22) Lee, J. H.; Ryu, J.; Kim, J. Y.; Nam, S.-W.; Han, J. H.; Lim, T.-H.; Gautam, S.; Chae, K. H.; Yoon, C. W. *J. Mater. Chem. A* **2014**, *2*, 9490-9495.
- (23) Koh, K.; Seo, J.-E.; Lee, J. H.; Goswami, A.; Yoon, C. W.; Asefa, T. *J. Mater. Chem. A* **2014**, *2*, 20444-20449.
- (24) Zhang, J.; Zhao, Z.; Xia, Z.; Dai, L. *Nat. Nanotechnol.* **2013**, *10*, 444-452.
- (25) Yoo, J. S.; Zhao, Z.-J.; Nørskov, J. K.; Studt, F. *ACS Catal.* **2015**, *5*, 6579-6586.
- (26) Wu, G.; Santandreu, A.; Kellogg, W.; Gupta, S.; Ogoke, O.; Zhang, H.; Wang, H.; Dai, L. *Nano Energy*, DOI: 10.1016/j.nanoen.2015.12.032.

- (27) Liu, Y.; Jin, Z.; Wang, J.; Cui, R.; Sun, H.; Peng, F.; Wei, L.; Wang, Z.; Liang, X.; Peng, L.; Li, Y. *Adv. Funct. Mater.* **2011**, *21*, 986-992.
- (28) Silva, R.; Voiry, D.; Chhowalla, M.; Asefa, T. *J. Am. Chem. Soc.* **2013**, *135*, 7823-7826.
- (29) Liang, H.-W.; Wei, W.; Wu, Z.-S.; Feng, X.; Müllen, K. *J. Am. Chem. Soc.* **2013**, *135*, 16002.
- (30) Yue, J.; Epstein, A. J.; Zhong, Z.; Gallagher, P. K.; Macdiarmid, A. G. *Synthetic Met.* **1991**, *41*, 765-768.
- (31) Pels, J. R.; Kapteijn, F.; Moulijn, J. A.; Zhu, Q.; Thomas, K. M. *Carbon*, **1995**, *33*, 1641.
- (32) Matter, P. H.; Zhang, L.; Ozkan, U. S. *J. Catal.* **2006**, *239*, 83-96.
- (33) Kumar, G.; Blackburn, J. R.; Albridge, R. G.; Modde-man, W. E.; Jones, M. M. *Inorg. Chem.* **1972**, *11*, 296-300.
- (34) Parambath, V. B.; Nagar, R.; Ramaprabhu, S. *Langmuir*, **2012**, *28*, 7826-7833.
- (35) Kaneko, S.; Kiguchi, M. *In Fullerenes, Nanotubes, and Carbon Nanostructures*, **2014**, *22*, 765-779.
- (36) Pinakidou, F.; Katsikini, M.; Paloura, E.C.; Akbari, A.; Riviere, J. P. *Mater. Sci. Eng. B.* **2011**, *176*, 473-476.
- (37) A. L. Ankudinov, B. Ravel, J. J. Rehr, S. D. Conradson *Phys. Rev. B* **1998**, *58*, 7565-7576.

## CHAPTER 5

### N- and O-Doped Mesoporous Carbons Derived from Rice Grains: Efficient Metal-free Electrocatalysts for Hydrazine Oxidation



#### 5.1. Overview

Nitrogen and oxygen co-doped, mesoporous carbon (RDMC) materials or metal-free electrocatalysts have been successfully synthesized using rice grains as precursors and silica nanoparticles as templates. Their synthesis involved three major synthetic steps: a low temperature hydrothermal treatment, followed by a high temperature pyrolysis in the presence of colloidal silica templates, and finally removal of the silica templates from the carbonized products with an alkaline solution. The as-obtained mesoporous carbons can effectively electrocatalyze the hydrazine oxidation reaction (HOR) with large negative onset potentials, low overpotential and high peak current densities, while also showing good long-term stability during the electrocatalytic reactions. The study

also shows that the electrocatalytic activity of the materials is dependent on the surface area of the materials and the heteroatom dopant-related species present in them. By optimizing the synthetic parameters, such as the amount of colloidal silica templates and the pyrolysis temperatures used for making them, the RDMC materials possessing optimized structures and compositions and exhibiting the best electrocatalytic performances are obtained. In particular, the RDMC material synthesized at pyrolysis temperature of 800 °C, following the hydrothermal treatment in the presence of a moderate amount of colloidal silica, denoted as RDMC-800-1, gives the best electrocatalytic activity toward HOR.

## 5.2. Introduction

The rapid rise in energy demands worldwide, coupled with the environmental issues caused by burning fossil fuels around the globe, have been pressing the scientific community to find solutions to these challenging problems. Fuel cells constitute one of the most promising solutions to these problems because they have the ability to convert chemical energy from various sustainable sources (such as hydrogen generated by solar-water electrolysis or ethanol derived from biomass hydrolysis) to electrical energy with reasonably high efficiency.<sup>1</sup> However, for fuel cells to work effectively, they require advanced, efficient and sustainable catalysts that promote the half reactions involved at the fuel cells' electrodes.<sup>2,3</sup> Among the many candidate catalysts developed so far for these purposes, heteroatom-doped carbon-based catalysts remain on the top of the list.<sup>4,5</sup> This is because these metal-free materials, which possess fascinating chemical and physical properties, have a great ability to effectively electrocatalyze some of the most important yet difficult reactions used in various fuel cells and solar-

powered electrolyzers, such as the oxygen reduction reaction (ORR),<sup>6,7</sup> the oxygen evolution reaction (OER),<sup>8,9</sup> the hydrogen evolution reaction (HER),<sup>10,11</sup> the hydrazine oxidation reaction (HOR),<sup>12</sup> and so on.

It has been reported that these metal-free carbon catalysts can be synthesized from different synthetic precursors, including phenol,<sup>13</sup> polymers,<sup>7,12</sup> and biological materials.<sup>14</sup> However, using these precursors for making electrocatalysts not only is costly but also can generate toxic chemicals and is not in line with ongoing worldwide initiatives on the development of green and sustainable chemistry and materials. To address this issue, biomass-derived materials, which are relatively inexpensive, abundant and renewable, are increasingly considered as precursors to make such metal-free catalysts. In fact, many previous studies in this area have shown that various carbon materials can be derived from biomaterials, such as peanut hulls, grass, or soy milk, using various synthetic methods.<sup>15,16</sup> Moreover, some of these biomass-derived carbon materials have been reported to have comparable catalytic activity as those derived from synthetic precursors.<sup>17</sup> Hence, research efforts have continued to find other natural, renewable precursors as well as facile synthetic routes that can convert such raw materials or biomass wastes to efficient carbon-based catalysts.

One of the simplest synthetic approaches applied to synthesize carbon nanomaterials is a low temperature hydrothermal carbonization (HTC).<sup>18,19</sup> This synthetic method generally produces carbon materials possessing amorphous structure, uniform chemical composition and high content of oxygen-based functional groups.<sup>18,19</sup> However, the method on its own is often ineffective to produce materials with high surface area—something that is highly required for many applications, including electrocatalysis.<sup>18,19</sup> To overcome this issue, I hypothesized that using sacrificial

templates along with the carbon precursors during the HTC and pyrolysis processes can potentially lead to carbon materials with highly porous structures, and thereby better electrocatalytic properties. While the use of hard templates to enable the formation of porous structures and high surface area in solid-state materials during synthesis is not new,<sup>20-22</sup> such an approach has never been combined with complimentary HTC and pyrolysis synthetic steps and applied together on biomass to produce carbon materials that are otherwise difficult to make.

To this end, herein I successfully demonstrate that HTC and pyrolysis can be successfully combined and applied together on milled rice grains (**Figure 5.1**) in the presence of colloidal silica templates and generate rice-derived N- and O co-doped mesoporous carbon (denoted as RDMC) materials. The resulting metal-free, high surface carbon materials are found to efficiently electrocatalyze HOR, a reaction that is relevant to direct hydrazine fuel cells. Rice grains are proven to be good choices to make these materials because they contain starch (90 %, dry basis) and some protein (7 %),<sup>23</sup> and can thus co-deliver both the carbon atoms and heteroatoms needed to make heteroatom-doped carbon electrocatalysts.<sup>24</sup> The synthesis of the materials is carried out through three major steps consisting of HTC (*step 1*), high temperature pyrolysis (*step 2*) and silica etching (*step 3*), as detailed in **Scheme 5.1**.

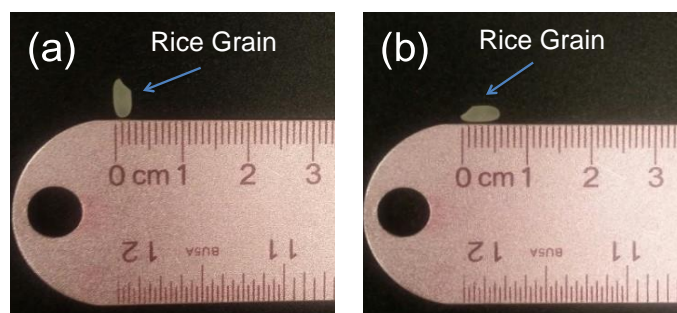
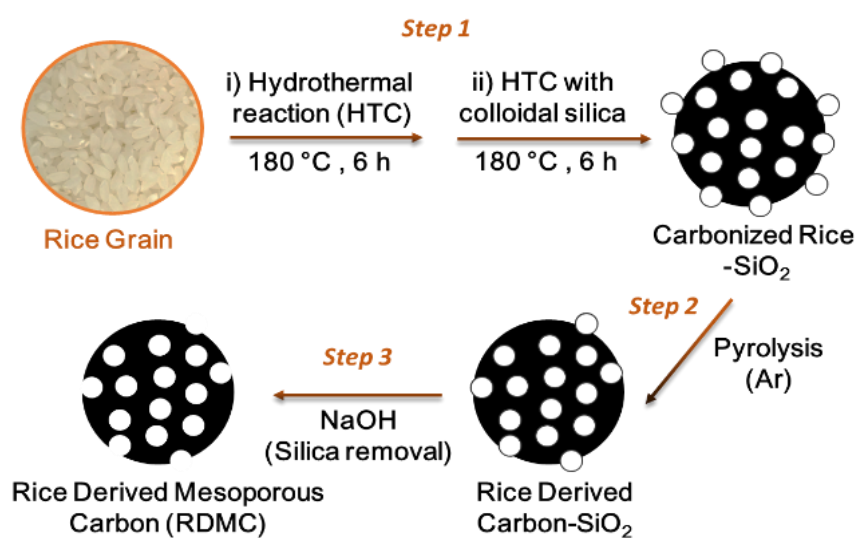


**Figure 5.1.** Picture of a rice grain and its size: a) width/diameter and b) length.

**Scheme 5.1.** Schematic procedure employed to synthesize the rice-derived mesoporous carbon (RDMC) materials.



### 5.3. Experimental Section

#### 5.3.1. Materials and Reagents

Colloidal silica dispersion (Ludox® HS-40, 40 wt. % suspension in water, particle size  $\approx$  12 nm), hydrazine monohydrate, phosphate buffer saline solution (PBS, 1X, pH = 7.4), and Pt/C (20 wt. %) were purchased from Sigma-Aldrich. Sodium hydroxide (NaOH) and absolute ethanol were obtained from Fisher Scientific. Raw rice was acquired from Seoul Trading Kyung-Gi rice (Product of 2014, Milled rice, purchased in USA). The rice grains have particles *ca.* 6 mm width and *ca.* 2 mm diameter. All the materials were used as received without any further purification. Deionized water was used throughout the experiments.

#### 5.3.2. Instrumentations and Characterizations

The nitrogen adsorption and desorption isotherms of the materials were measured with a Micromeritics TriStar-3000 (Micromeritics Instrument Corp.) at the liquid-nitrogen temperature. In order to remove any possible guest species adsorbed on the samples' surfaces, the samples were first degassed under nitrogen gas at 60 °C for 12 h before the measurements. From the adsorption/desorption data, the Brunauer-Emmett-Teller (BET) surface area and Barrett-Joyner-Halenda (BJH) pore size distribution of the samples were determined. Transmission electron microscope (TEM) images of the as-synthesized materials were acquired with a Topcon 002B TEM instrument. The FT-Raman spectra were acquired using a Raman spectrometer (Renishaw 1000) equipped with a 20 mW air-cooled argon ion laser ( $\lambda = 514.5$  nm), which served as the excitation lights source. The laser power at the sample position was typically 400  $\mu$ W and had an average spot-size of 1  $\mu$ m in diameter. X-ray photoelectron spectra were obtained using

a Thermo Scientific K-Alpha X-ray photoemission spectrometer (XPS) equipped with an Al K $\alpha$  as its X-ray source ( $h\nu = 1486.6$  eV), with an energy resolution of 0.6 eV for the survey scans and 0.1 eV for high resolution scans of individual peaks. Elemental analysis of the samples were performed at Robertson Microlit Laboratories, Ledgewood, NJ, USA.

### **5.3.3. Synthesis of RDMC Materials and Catalysts**

#### *Hydrothermal treatment of rice grains (step 1)*

The first HTC synthetic step was carried out in a 25 mL Teflon-lined stainless steel autoclave, which was placed in an oven and subjected to hydrothermal treatment. In a typical experiment, milled raw rice grains (Kyung-gi rice, purchased in USA) (1 g) were mixed with distilled water (10 mL) in a Teflon-lined stainless steel autoclave and then hydrothermally treated at 180 °C for 6 h. After letting the mixture cool down to room temperature, different amounts of colloidal silica (0, 0.5, 1, or 2 g per 1 g of rice grain) were added into the mixture. The mixtures were well dispersed under sonication for 30 min, and then subjected to a second hydrothermal treatment at the same temperature (180 °C) for another 6 h. The autoclave was let to cool down to room temperature. The solid products in the mixture were recovered by centrifugation, washed with distilled water and kept in oven at 100 °C for 12 h to let the solvent in them evaporate. This finally resulted in dark-brown, carbon/colloidal silica composite powder materials.

#### *High temperature pyrolysis (step 2)*

The carbon/silica composite materials obtained above were all pyrolyzed at 800 °C in a temperature-programmable tube furnace under a flow of argon at a flow

rate of ~30 mL/min. In the experiment, first the furnace temperature was raised to 300 °C with a ramp of 1 °C/min, and kept at this temperature for 3 h. The temperature was then increased to a final, desired temperature of 800 °C at a ramp of 10 °C/min, and kept at this temperature for another 2 h. Finally, the furnace was let to cool down to room temperature, producing different graphitized carbon/silica composite materials.

To study the effect of pyrolysis temperature, another set of materials were prepared from the carbon/colloidal silica composite powder material prepared above with 1 g colloidal silica per 1 g of rice grain. This carbon/silica composite material was pyrolyzed at four different high temperatures (600, 700, 800, or 900 °C) in a temperature-programmable tube furnace under a flow of argon at a flow rate of ~30 mL/min. First the furnace temperature was raised to 300 °C with a ramp of 1 °C/min, and kept at this temperature for 3 h. The temperature was then increased to a final, desired temperature of 600, 700, 800, or 900 °C at a ramp of 10 °C/min, and kept at this temperature for another 2 h. Finally, the furnace was let to cool down to room temperature, producing different graphitized carbon/silica composite materials.

#### *Removal of colloidal silica (step 3)*

To remove the silica templates from the graphitized carbon/colloidal silica products, typically 40 mg of the material was mixed with 1 M NaOH solution (20 mL) in autoclave and kept at 100 °C for 18 h. The dispersions were then centrifuged, and the resulting solid products were washed, first with distilled water and then with absolute ethanol (3 x 20 mL in each case). Finally, the obtained materials were dried in oven at 60 °C for 12 h. This led to black as-obtained rice-derived mesoporous carbon materials, which were denoted as RDMC- $T$ - $x$ , where  $T$  and  $x$  represent the final pyrolysis temperature and the amount of colloidal silica per 1 g of rice grains used to

make each material.

#### ***5.3.4. Synthesis of control materials***

For comparison, two control materials were synthesized. The first one was obtained by applying the two consecutive hydrothermal steps, followed by removal of the colloidal silica. The resulting material was denoted as RDC-HTC-1. The second material was prepared by applying only the pyrolysis step on a dried mixture of rice/SiO<sub>2</sub> (1:1 wt. ratio) (*step 2*) before proceeding to *step 3*. The product was denoted as RDMC-800-Py-1.

#### ***5.3.5. Electrochemical Tests and Electrocatalysis***

##### *Preparation of electrodes*

The electrochemical and electrocatalytic properties of all the mesoporous carbon and corresponding control materials were examined with a Versastat3 potentiostat (Princeton Applied Research, PAR). For the tests, a three-electrode cell, which consisted of a saturated calomel electrode (SCE) as the reference electrode, a graphitic carbon rod (diameter: 6 mm) as the counter electrode, and a glassy carbon disk (diameter: 3 mm) containing the catalysts as the working electrode, was used.

For the preparation the working electrode, 2 mg of catalyst was first dispersed in 200  $\mu\text{L}$  of 2-propanol under sonication to form a homogeneous suspension of the catalyst. Then, 2  $\mu\text{L}$  of the resulting suspension was pipetted and drop-casted onto the surface of a freshly polished glassy carbon electrode (GCE) (with diameter of 3 mm). The final loading of catalyst was 283  $\mu\text{g}/\text{cm}^2$ . After letting the catalyst-coated GCE dry under ambient conditions, a diluted solution of Nafion (10 %) (2  $\mu\text{L}$ ) was casted on it. The electrode was let to dry in air and then became ready for use.

To investigate the possible effect of the Nafion casting, a second working electrode was prepared using RDMC-800-1 and using 2  $\mu\text{L}$  of 20 % Nafion coating on it. When dried, this should give a thicker coating than than the one above, which was prepared from 2  $\mu\text{L}$  of 10 % Nafion.

The electrode containing Pt/C electrode, which I used for comparison, was also prepared in the same way. Typically, 2 mg of Pt/C catalyst was first dispersed in 200  $\mu\text{L}$  of 2-propanol under sonication to form a homogeneous suspension of the catalyst. Then, 2  $\mu\text{L}$  of the resulting suspension was pipetted and drop-casted onto the surface of a freshly polished glassy carbon electrode (GCE) (with diameter of 3 mm). The final loading of catalyst was 283  $\mu\text{g}/\text{cm}^2$ . After letting the catalyst-coated GCE dry under ambient conditions, a diluted solution of Nafion (10 %) (2  $\mu\text{L}$ ) was casted on it. The electrode was let to dry in air and then became ready for use.

#### *Cyclic Voltammetry*

Cyclic voltammetry (CV) curves during electrocatalysis over the materials synthesized above were performed in a phosphate buffered saline (PBS) solution (0.1 M, pH 7.4). In the CV measurements, the potential was scanned from -0.6 to 0.6 V vs. SCE with different scan rates, ranging from 10 to 100 mV/s, and the hydrazine concentration was varied from 10 to 100 mM. All the electrochemical measurements were carried out at room temperature and under ambient pressure.

#### *Rotating disc electrode (RDE)*

Linear sweep voltammograms (LSVs) over RDMC-800-1 were acquired with a Pine Bi-potentiostat (Pine Research Instrumentation), using a rotating disc electrode (RDE) (Pine Research Instrumentation). For the experiments, a three-electrode configuration

comprising a catalyst-modified glassy carbon as a working electrode was employed. The LSVs were scanned from -0.6 to 0.6 V at a scan rate of 10 mV/s and with the RDE rotating at 900 rpm.

#### *Stability Tests of the Electrocatalysts*

The stability of the mesoporous carbon materials during electrocatalysis of HOR was investigated by cyclic voltammetry in 50 mM hydrazine/0.1 M PBS solution. Typically, 500 cycles of LCVs were recorded, and the peak current densities for 50, 100, 150, 200, 250, 300, 350, 400, 450, and 500 cycles were obtained. Additionally, chronoamperometric measurement over the electrocatalysts was performed at a potential of -0.06 V (vs. SCE) in 50 mM hydrazine/0.1 M PBS solution.

#### **5.4. Result and Discussion**

As described in detail in the experimental section (**Section 5.3**), the synthesis of the rice derived mesoporous carbons (RDMCs) starts with a low temperature hydrothermal treatment of milled raw rice grains at 180 °C for 6 h. **Caution!** Autoclaves under hydrothermal conditions should be handled with extreme care and appropriate safety protocols. This is followed by an additional hydrothermal treatment of the materials in the presence of different amounts of colloidal silica templates at 180 °C for another 6 h. The carbonized rice/SiO<sub>2</sub> composite materials are then pyrolyzed at different high temperature (600, 700, 800 or 900 °C). Finally, the silica in the carbonized products is removed using concentrated NaOH solution, in order to create nanopores in the carbon materials. By varying the pyrolysis temperatures as well as the amount of colloidal silica

templates (0-2 g of colloidal silica per 1 g of rice grain), different RDMC materials, which are labeled as RDMC- $T$ - $x$ , where  $T$  and  $x$  represent the final pyrolysis temperature and the amount of silica in g per 1 g of rice, respectively, are then obtained. Additionally, the following two control materials are synthesized. The first one, named RDC-HTC-1, is synthesized by applying only the first two HTC treatment steps in the presence of 1 g of colloidal silica, followed by removal of silica templates (i.e., with no additional pyrolysis step). The second one, named RDMC-800-Py-1, is synthesized by directly pyrolyzing a dried physical mixture of milled rice grains and colloidal silica (1:1 wt. ratio) without the HTC treatment steps. The effects of these synthetic conditions on the composition, structure and electrocatalytic properties of the materials toward hydrazine oxidation reaction are then investigated.

The structures of RDMC- $T$ - $x$  and control materials are first examined by N<sub>2</sub> porosimetry (**Figure 5.2**). The results show that the surface area of the materials depends on both the amount of colloidal silica and the pyrolysis temperature used to synthesize them. As the amount of colloidal silica is increased, the Brunauer–Emmett–Teller (BET) surface area of the RDMC-800- $x$  materials gradually increase. For example, the surface area of the materials increase from 14 m<sup>2</sup>g<sup>-1</sup> for RDC-800-0 (which is synthesized without using colloidal silica templates) to 343 m<sup>2</sup>g<sup>-1</sup> for RDMC-800-0.5 (which is synthesized using a moderate amount or 0.5 g of colloidal silica templates for 1 g of milled rice grains), and then to 520 m<sup>2</sup>g<sup>-1</sup> for RDMC-800-2 (which is synthesized using the highest amount of colloidal silica templates) (**Table 5.1**). The Barrett–Joyner–Halenda (BJH) pore size distribution reveals that the pore size of RDMC-800- $x$  (where  $x > 0.5$  g) is centered at ca. 12 nm, which is comparable to the

size of colloidal silica used as templates for the synthesis of the materials. Note that RDC-800-0, which is synthesized without colloidal silica, is almost non-porous. The characterization results of the other relevant control materials are shown and compiled in **Figure 5.3–5.5** and **Tables 5.2** and **5.3**.

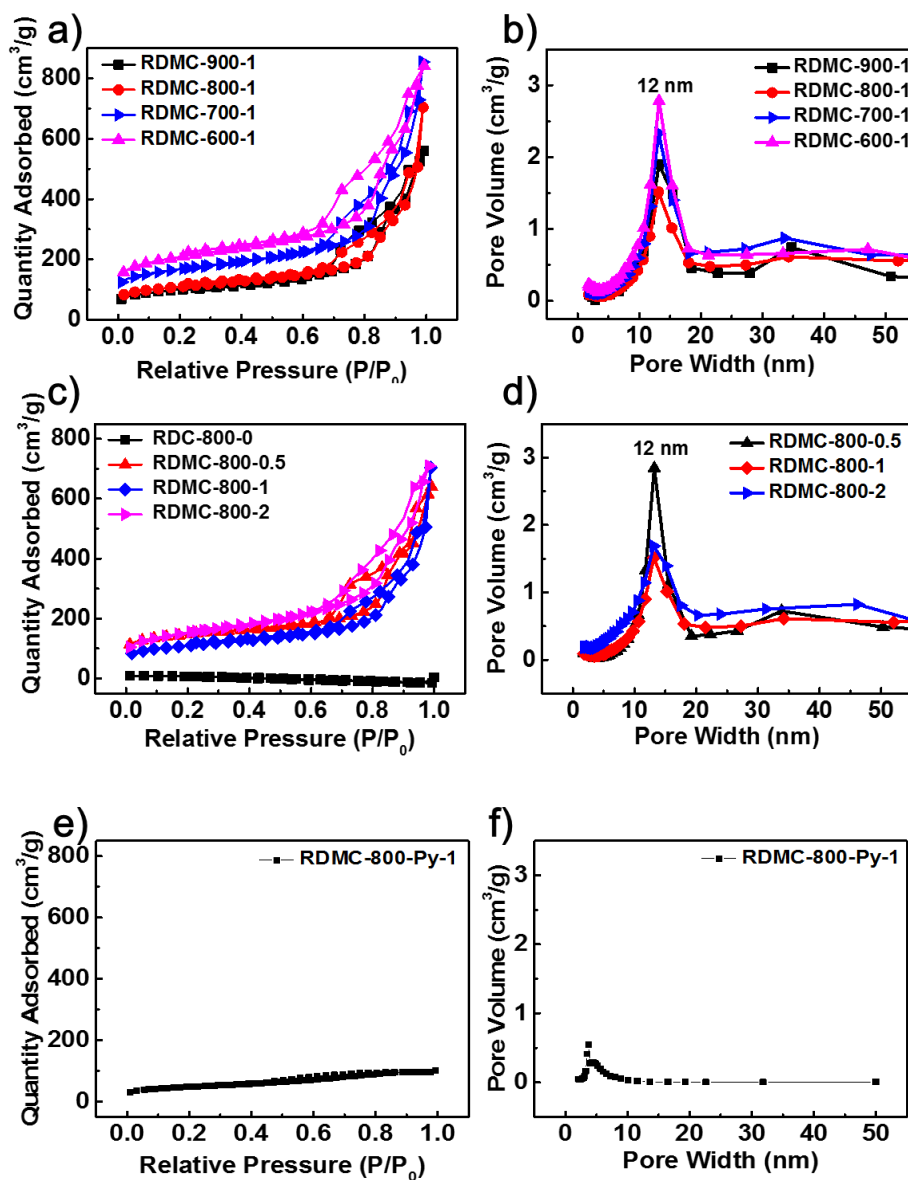


**Figure 5.2.** (Left panel)  $N_2$  adsorption/desorption isotherms and (right panel) BJH pore size distributions of: (a,b) the series of RDMC- $T$ -1 materials (where  $T$  is 600, 700, 800, or 900 °C), (c,d) the series of RDMC-800- $x$  (where  $x$  is the amount of colloidal silica

(in g) per 1 g of milled rice grains, and (e-f) the control material RDMC-800-Py-1.

**Table 5.1** BET surface area, average BJH pore size, and pore volume of a series of RDMC-T-x materials

<i>Entry</i>	<i>RDMC-T-x<sup>a</sup></i>		<i>BET</i> <i>surface</i> <i>area<sup>b</sup></i> <i>(m<sup>2</sup>/g)</i>	<i>Average</i> <i>Pore size</i> <i>(nm)<sup>b</sup></i>	<i>Pore</i> <i>volume</i> <i>(cm<sup>3</sup>/g)<sup>b</sup></i>
	<i>T</i>	<i>x</i>			
1	800	0	14	N/A	N/A
2	800	0.5	343	15.1	0.9
3	800	1	366	18.5	1.0
4	800	2	520	11.1	1.0
5	600	1	686	12.4	1.1
6	700	1	557	15.5	1.2
7	900	1	343	13.8	0.8
8 <sup>c</sup>	N/A	1	N/A	N/A	N/A
9 <sup>d</sup>	800	1	164	11.0	0.1

<sup>a</sup> *T* represents the pyrolysis temperature and *x* represents the amount of colloidal silica (in g) per 1 g of milled rice grain. <sup>b</sup> Measured by N<sub>2</sub> porosimetry. <sup>c</sup> A control material, which is denoted as RDC-HTC-1. <sup>d</sup> A control material, labeled as RDMC-800-Py-1.

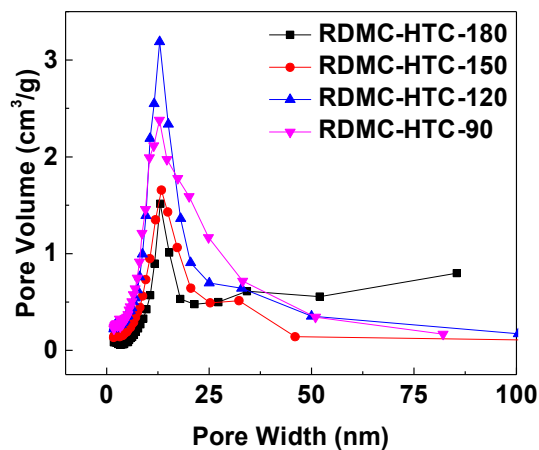


**Figure 5.3.** Pore size distribution of control RDMC materials prepared by varying the HTC temperature.

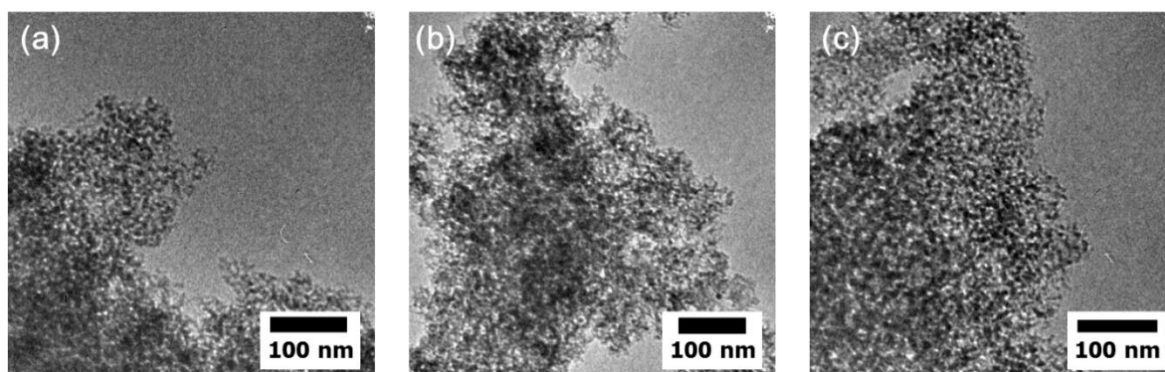


**Figure 5.4.** TEM images of the control materials synthesized by varying HTC temperature: a) RDMC-HTC-90, b) RDMC-HTC-120, and c) RDMC-HTC-150.

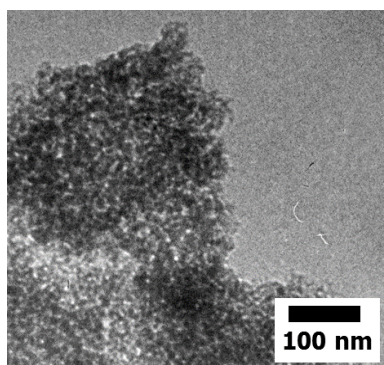


**Figure 5.5.** TEM images of time controlled HTC materials, RDMC-800-1 (0 h).

**Table 5.2.** Synthetic parameters, including HTC temperature and reaction time, employed to make the various (control) RDMC materials and results of their surface area

	<i>Step 1 (HTC Treatment)<sup>a</sup></i>		<i>BET Surface Area</i>
	<i>Part 1</i>	<i>Part 2</i>	<i>(m<sup>2</sup>/g)<sup>b</sup></i>
RDMC-HTC-90	90 °C, 6 h	90 °C, 6 h	604
RDMC-HTC-120	120 °C, 6 h	120 °C, 6 h	602
RDMC-HTC-150	150 °C, 6 h	150 °C, 6 h	357
RDMC-HTC-180 <sup>c</sup>	180 °C, 6 h	180 °C, 6 h	366

<sup>a</sup> In the first part (Part 1) of *Step 1*, the HTC treatment did not involve colloidal silica, and in the second part (Part 2) of *Step 1*, the HTC treatment in the presence of 1 g of colloidal silica. This step is followed by pyrolysis at 800 °C (*Step 2*). <sup>b</sup> Measured by N<sub>2</sub> porosimetry. <sup>c</sup> Same sample as RDMC-800-1 mentioned in the manuscript.

**Table 5.3.** Control samples synthesized by varying HTC reaction time and their surface area<sup>a</sup>

	<i>Step 1 =(HTC)</i>		<i>BET Surface Area<sup>b</sup></i>
	<i>Part 1</i>	<i>Part 2</i>	<i>(m<sup>2</sup>/g)</i>
RDMC-800-1 (0 h)	N/A	180 °C, 6 h	386
RDMC-800-1 (6 h) <sup>c</sup>	180 °C, 6 h	180 °C, 6 h	366

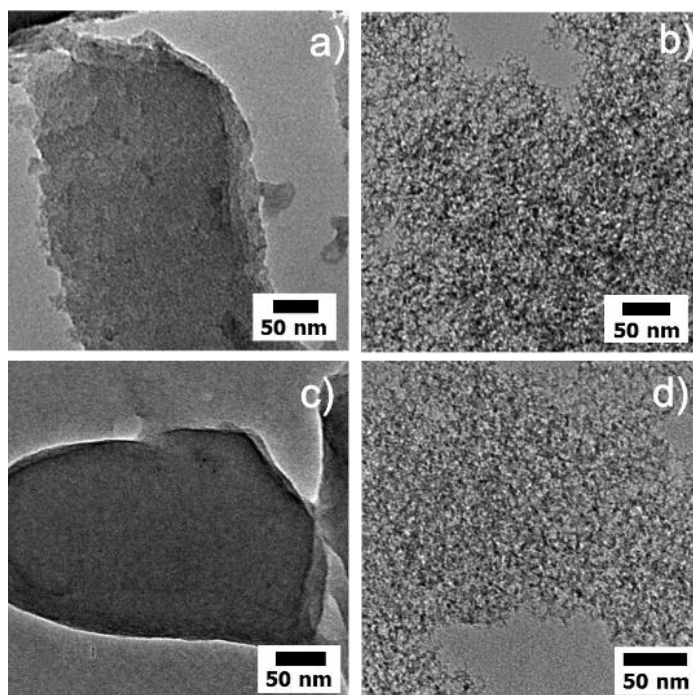
<sup>a</sup> All HTC controlled material proceed with 1 gram of silica colloidal at second part of *step 1* and proceed to 800 °C at *Step 2*; <sup>b</sup> Measured by N<sub>2</sub> porosimetry; <sup>c</sup> Same sample

with RDMC-800-1 in manuscript.

On the other hand, as the pyrolysis temperature increases, the BET surface area of the carbon materials decreases. For example, the surface area is  $686 \text{ m}^2\text{g}^{-1}$  for RDMC-600-1, but decreases to  $343 \text{ m}^2\text{g}^{-1}$  for RDMC-900-1 (**Table 5.1**, entries 5–7). This trend is similar to other carbon materials synthesized from other precursors by pyrolysis and that are reported before.<sup>25</sup> The decrease in surface area at higher temperatures is likely the result of the higher degree of cross-linkages that the aliphatic and aromatic carbon atoms in the precursors undergo during carbonization at increasingly higher temperatures.<sup>26</sup> Interestingly, there is no measurable porosity in RDC-HTC-1 (one of the control materials synthesized, entry 8 in **Table 5.1**). This indicates that the starch in the rice grains undergoes only hydrolysis, dehydration, and carbonization during the HTC step, and the silica nanoparticles cannot enter into the matrices of the resulting carbon material under the relatively low temperature employed during the HTC step. On the other hand, RDMC-800-Py-1 is nanoporous, and has a BET surface area of  $164 \text{ m}^2\text{g}^{-1}$  (entry 9 in **Table 5.1**). Its surface area is, however, still lower than those of the materials synthesized by combining HTC and high temperature pyrolysis (e.g., entry 3 in **Table 5.1**).

These results are further corroborated by TEM, which also show that the structures of the materials are changed from bulky, non-porous to highly nanoporous as colloidal silica is used in their synthesis. For example, TEM images of the control material RDC-HTC-1 show non-porous structures whereas those of RDMC-800-Py-1 show porous structures (**Figure 5.6c-d**) So, overall, the results above all indicate the importance of colloidal silica as templates and the HTC and high temperature pyrolysis steps to produce carbon materials, with desirable high surface area nanoporous structure,

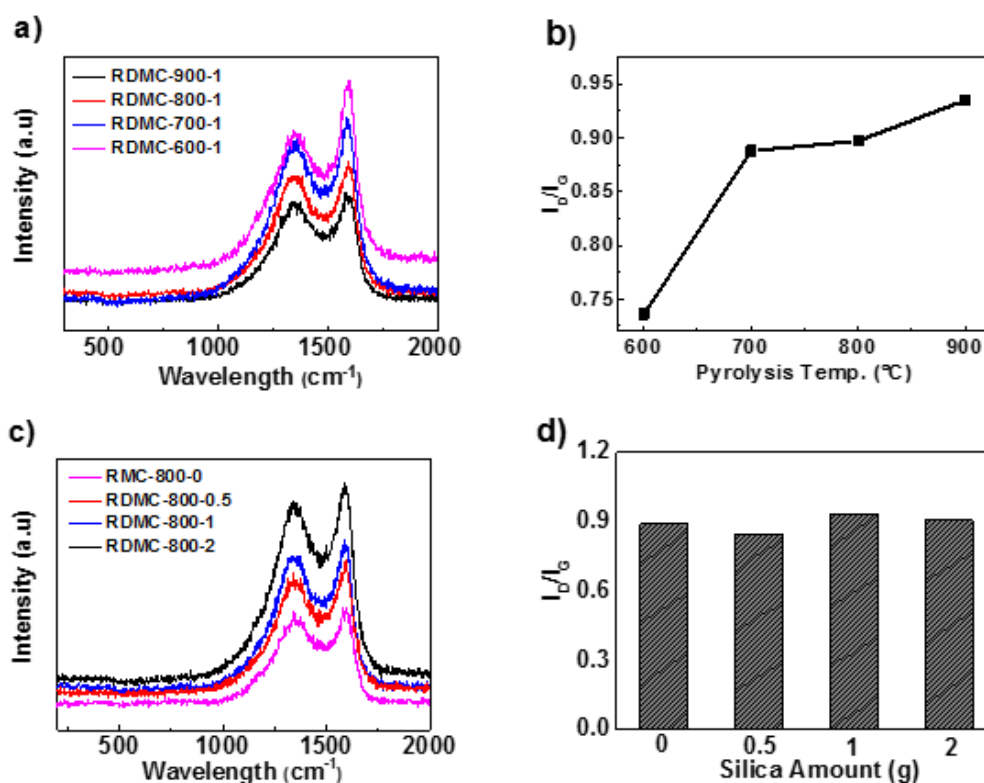
from rice grains.



**Figure 5.6.** TEM images of representative RDMC materials and their corresponding control materials: a) RDC-800-0, b) RDMC-800-1, c) RDC-HTC-1, and d) RDMC-800-Py-1.

The Raman spectra of RDMC- $T$ - $x$  materials display two broad peaks at *ca.* 1348 and 1586  $\text{cm}^{-1}$ , corresponding to the characteristic D and G bands, respectively, of graphitic carbon materials (**Figure 5.7**).<sup>27</sup> The D band in such materials is generally associated with structural defects from heteroatom dopants, while the G band commonly represents the typical ordered domains of graphitic carbon materials.<sup>7</sup> Specifically, in the case of the RDMCs materials, the D band predominantly stems from the presence of N dopant atoms in the carbon structure, whereas the G band is due to the  $\text{sp}^2$  carbon-related graphitic structure.<sup>28</sup> The value of  $I_D/I_G$  ratio of RDMC-800- $x$  materials, which represents the relative degree of disorder in the structure of carbon materials, is *ca.* 0.90 for all the materials (**Figure 5.7,c**). This suggests that the relative

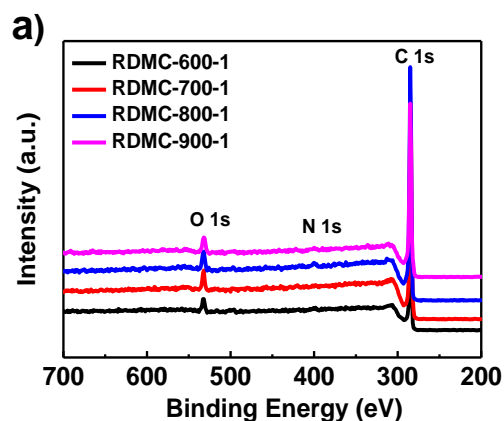
ratio of defect-to-ordered domains in the materials is not greatly affected by the amount of colloidal silica templates used for making the materials. However, in the case of the series of RDMC-*T*-1 materials, the value of  $I_D/I_G$  ratio increases significantly, from 0.74 to 0.94, when the pyrolysis temperature is raised from 600 to 900 °C.

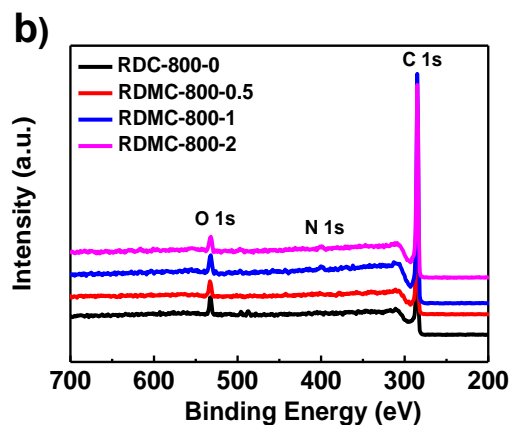


**Figure 5.7.** Raman spectra (left panel) and  $I_D/I_G$  ratios (right panel) of the RDMC materials obtained under different synthetic conditions: (a-b) the series of RDMC-*T*-1 materials and (c-d) RDMC-800-*x* materials.

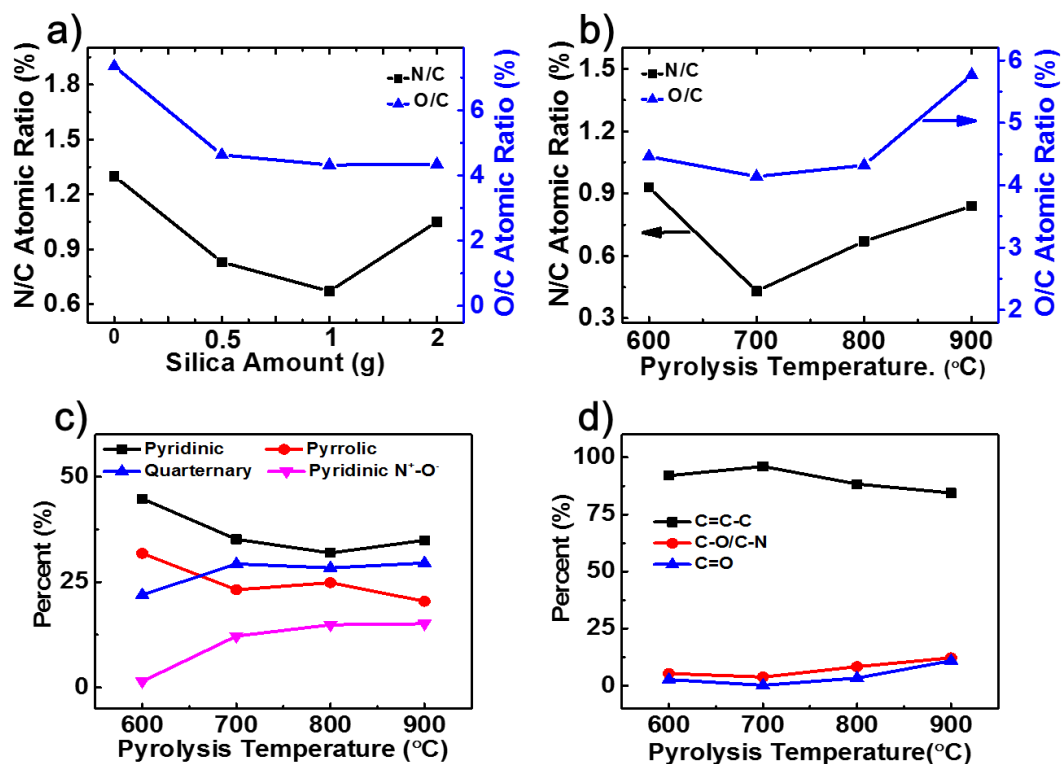
The elemental composition of the materials is determined by X-ray photoelectron spectroscopy (XPS). In the XPS survey spectra of the RDMC materials (**Figure 5.8**), peaks corresponding primarily to C and O, and some to N, are seen. While the O atoms may have predominantly come from the starch, the N dopants have most likely come from the small amount of protein present in rice. The ratio of N/C in the RDMC-*T*-1

materials varies slightly, between 0.4 and 1.3%, with RDMC-700-1 showing the lowest amount of N (**Figure 5.9**). There is some trend in O/C and N/C with respect to the amount of colloidal silica as well as the pyrolysis temperature used to make the materials. Although what may have caused the trends may need further investigations, some conclusions can still be drawn. It can be seen that, as the amount of colloidal silica increases up to a point, the porosity of the materials increases (**Table 5.1**), making the material easily lose N and O atoms, and have low N/C and O/C ratios. But, when the amount of colloidal silica increases further, despite the fact that the surface area of the material still increases, more oxygen from the colloidal silica also becomes available for the C atoms in the materials to escape with as CO<sub>2</sub>, leaving behind relatively more N dopants. These two opposite processes are what may have made the materials with less or more colloidal silica than RDMC-800-0.5 to have higher amounts of N/C and O/C ratios. Furthermore, at higher temperature pyrolysis, some N and O are also likely to remain in the samples in the form of siliconoxynitride.



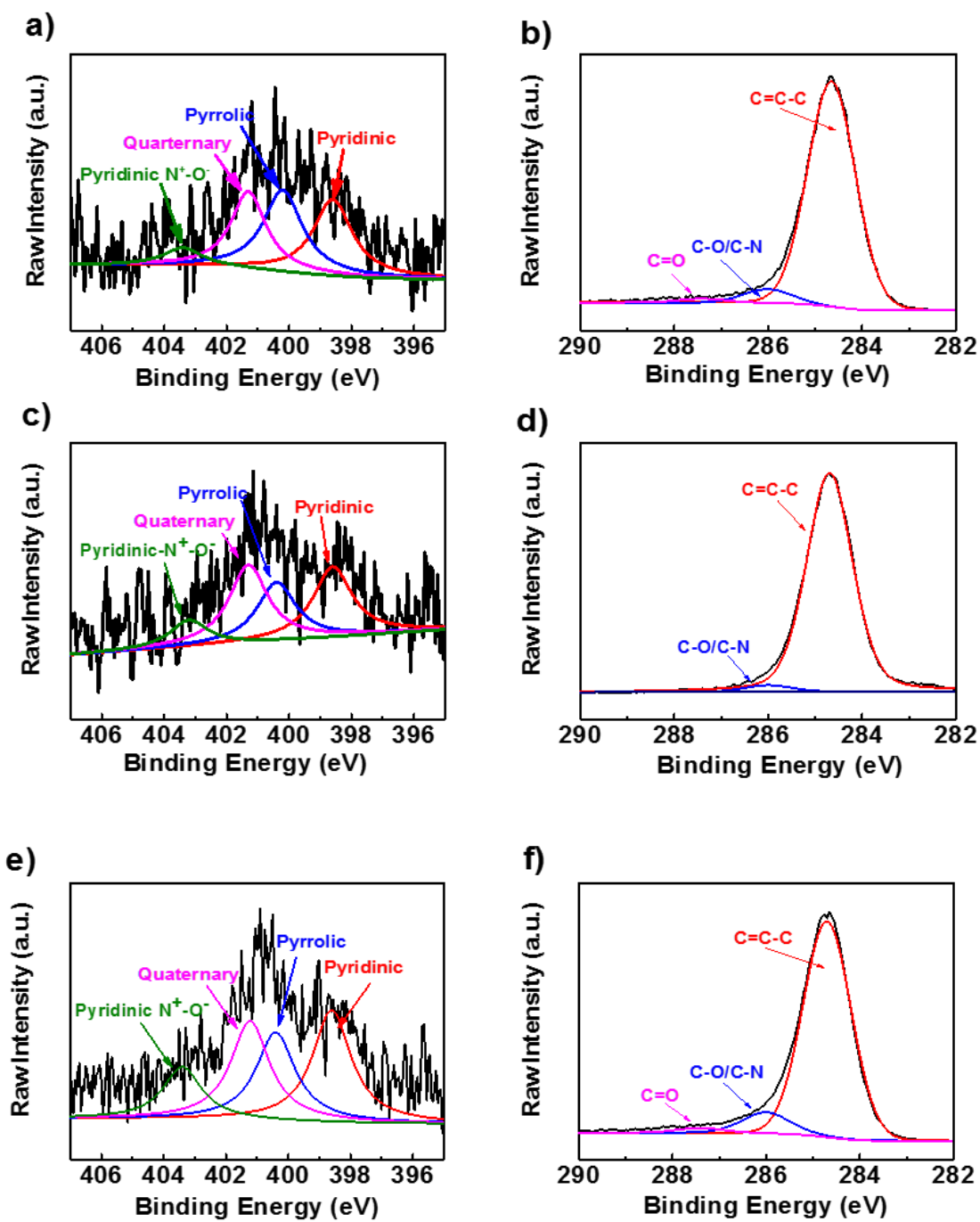


**Figure 5.8.** XPS survey spectra of the series of (a) RDMC-*T*-1 and (b) RDMC-800-*x* materials.



**Figure 5.9.** XPS results for RDMC-*T*-*x* materials. a) The N/C and O/C atomic ratios of the series of RDMC-800-*x* materials, b) the N/C and O/C atomic ratios of the series of RDMC-*T*-1 materials, and c) the percentages of the different types of N species and d) atomic percentages of the different C species in the series of RDMC-*T*-1 materials.

The chemical states of the nitrogen and carbon moieties in the materials are probed using high-resolution XPS (**Figure 5.10**). The peak corresponding to N1s is further deconvoluted into four different N dopant states, including pyridinic (398.7 eV), pyrrolic (400.3 eV), quaternary (401.2 eV) and pyridinic N<sup>+</sup>-O<sup>-</sup> (403.3 eV) species (**Figure 5.9**).<sup>29</sup> In all the RDMC-*T*-1 materials, although the pyridinic moieties are conspicuous, their amount gradually decreases as the pyrolysis temperature is increased. On the other hand, the amount of quaternary nitrogen increases as the pyrolysis temperature is increased from 600 to 700 °C, but then remains almost unchanged after 700 °C. The deconvolution of the XPS peak for C1s for the series of RDMC-*T*-1 materials into three different states, corresponding to C=C-C (284.6 eV), C-O/C-N (286.1 eV) and C=O (287.5 eV), is also included (**Figure 5.9d**). The result shows that all RDMC-*T*-1 materials possess more C=C-C type groups than C-O/C-N and C=O type groups in their structures.



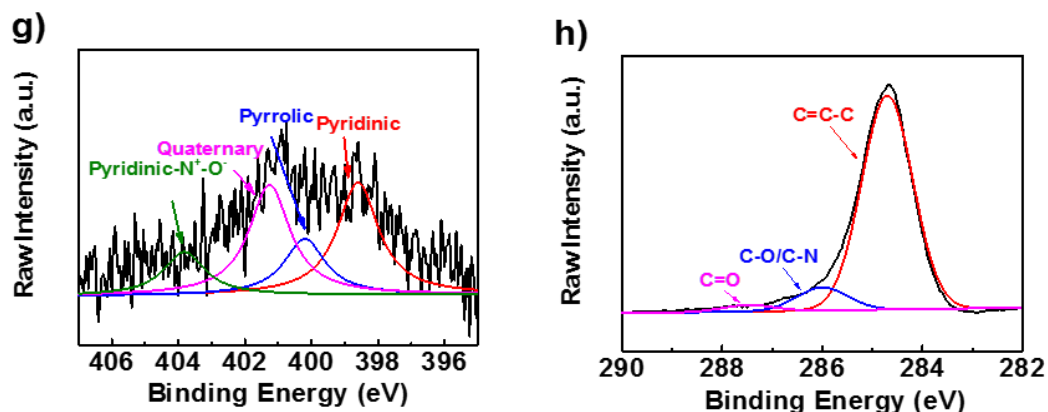
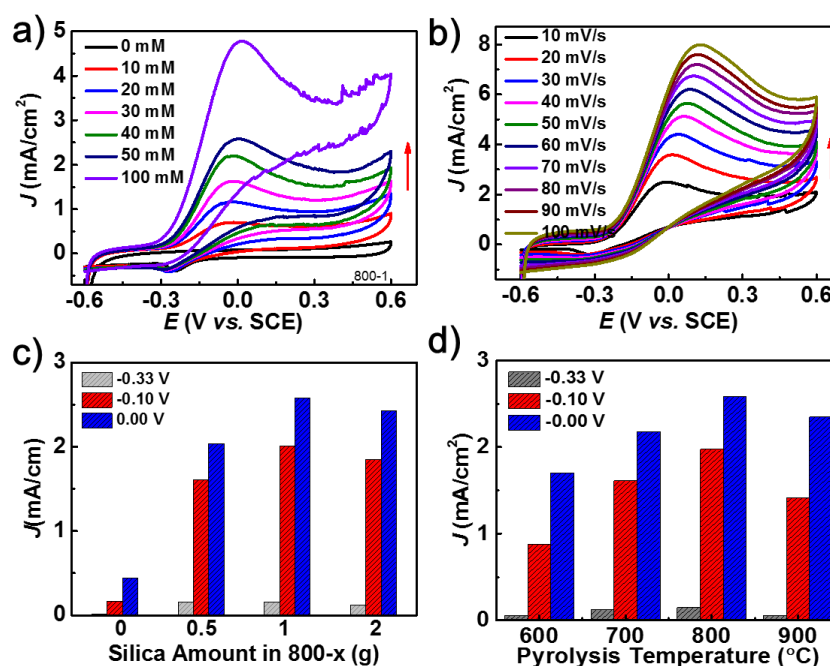


**Figure 5.10.** High-resolution XPS spectra of N1s peak (left panels) and C1s peak (right panels) of the series of RDMC-*T*-1 materials, which are synthesized at different pyrolysis temperatures: (a,b) RDMC-600-1, (c,d) RDMC-700-1, (e,f) RDMC-800-1, and (g,h) RDMC-900-1.

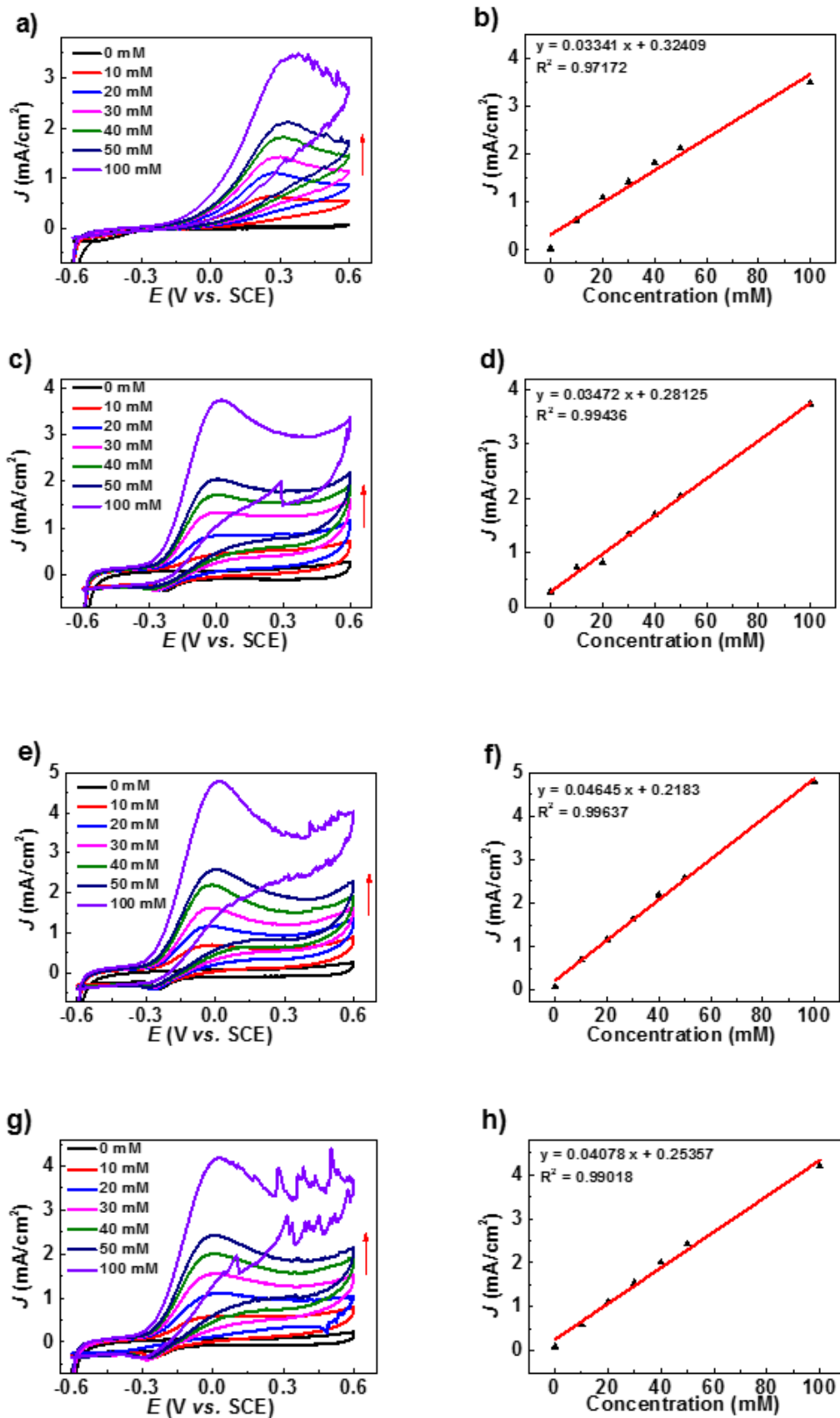
Cyclic voltammetry (CV) curves of HOR over the RDMC-*T*-*x* materials and the corresponding control samples from -0.6 V to 0.6 V (vs. SCE) at different scan rates for various hydrazine concentrations (**Figure 5.11-21**) demonstrate that all the series of RDMC-800-*x* and RDMC-*T*-1 materials can effectively electrocatalyze HOR. Of all the materials, RDMC-800-1 shows the best catalytic activity with a relatively large negative onset potential of -0.34 V (vs. SCE) (or low overpotential), a large negative peak potential of -0.02 V (vs. SCE), and a high peak current density of 2.6 mA cm<sup>-2</sup> in HOR of 50 mM hydrazine solution (**Figure 5.11a**). The values obtained for RDMC-800-1 are also either comparable with or better than those obtained for other electrocatalysts, including 20 wt% Pt/C (**Tables 5.4-5** and **Figure 5.18**).<sup>12,30</sup>

The current density produced during HOR over the RDMC materials increases linearly with the concentration of hydrazine (**Figure 5.11a** and **Figure 5.12e-f**). Moreover, kinetic studies show that increasing the electrochemical scan rates generates

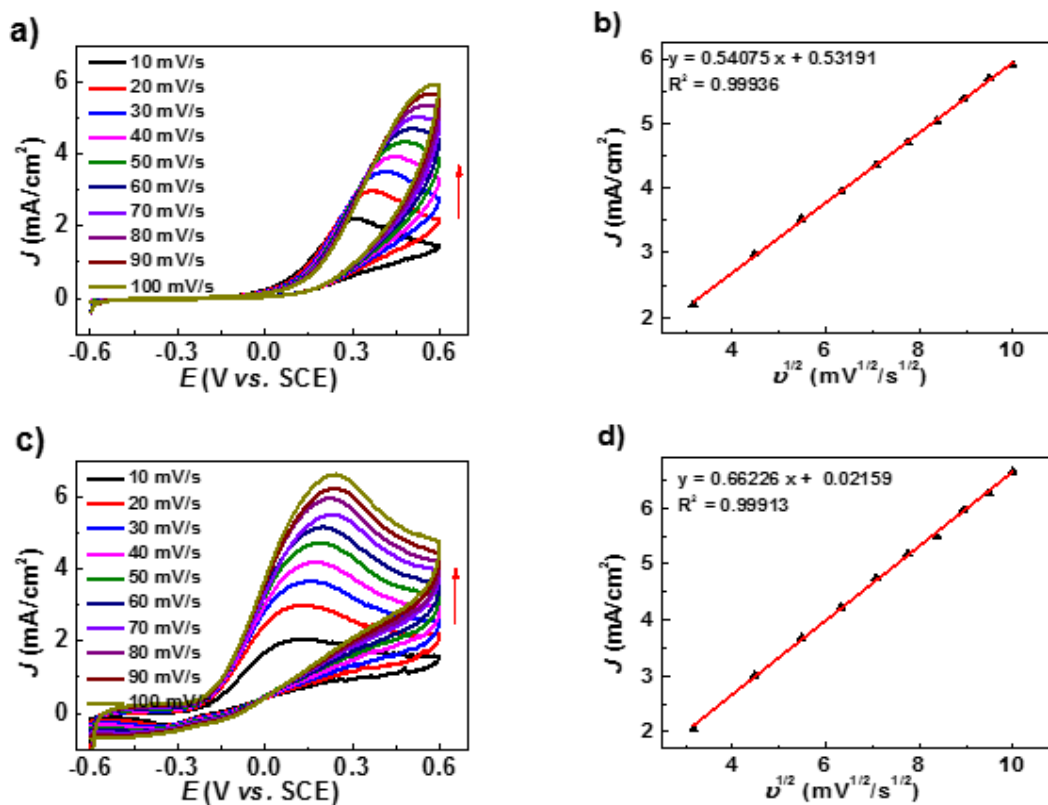
a more positive peak potential. The relationship between the peak current density and the square root of scan rate is linear, suggesting that the HOR over the materials involves a diffusion-controlled electrochemical process (**Figure 5.11b** and **Figure 5.13e** and f). Additionally, no cathodic peak is observed during the whole reverse scans, indicating that the reaction is irreversible. This behavior is further corroborated by linear sweep voltammetry (LSV) using a rotating disk electrode (RDE) for RDMC-800-1 (**Figure 5.13**).

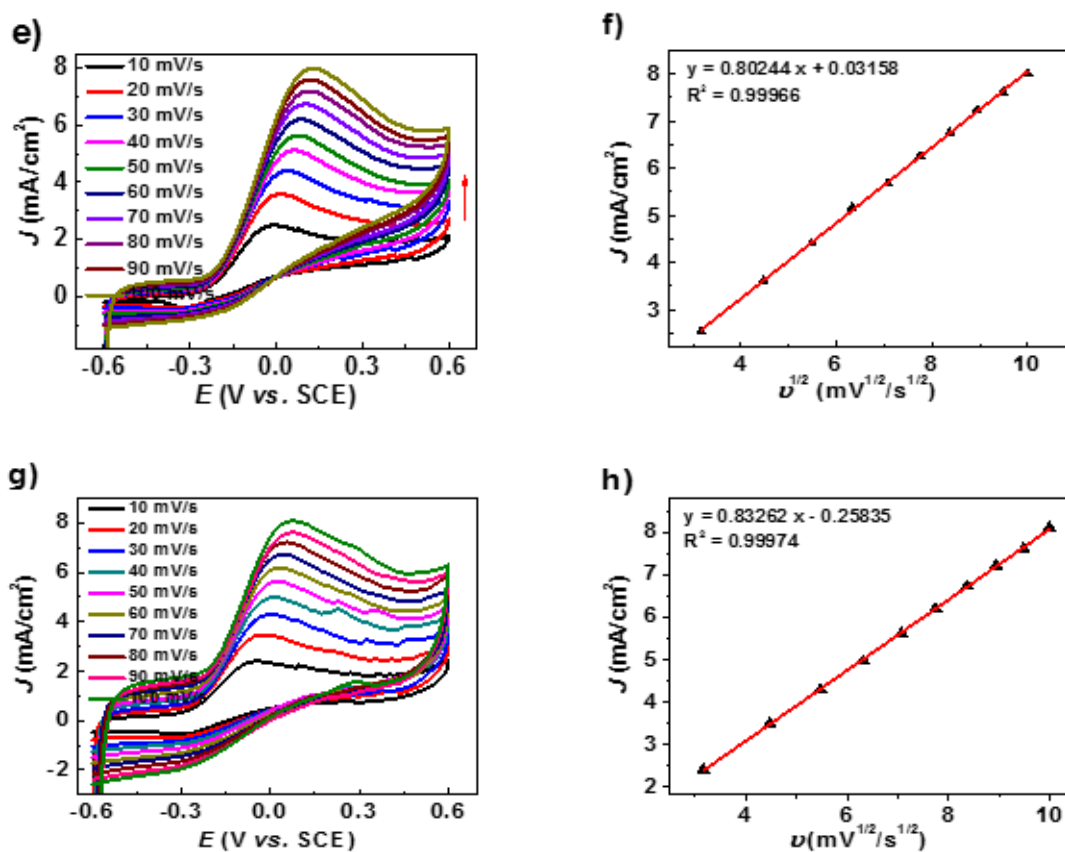


**Figure 5.11.** Electrocatalytic activity of RDMC-800-1 toward HOR: a) in different concentrations of hydrazine at a scan rate of 10 mV/s and b) at different scan rates in 50 mM of hydrazine. Current densities of different materials at three different potentials were compared over the series of c) RDMC-800- $x$  and d) RDMC- $T$ -1 materials in 50 mM of hydrazine at 10 mV/s scan rate in 0.1 M PBS, pH 7.4.

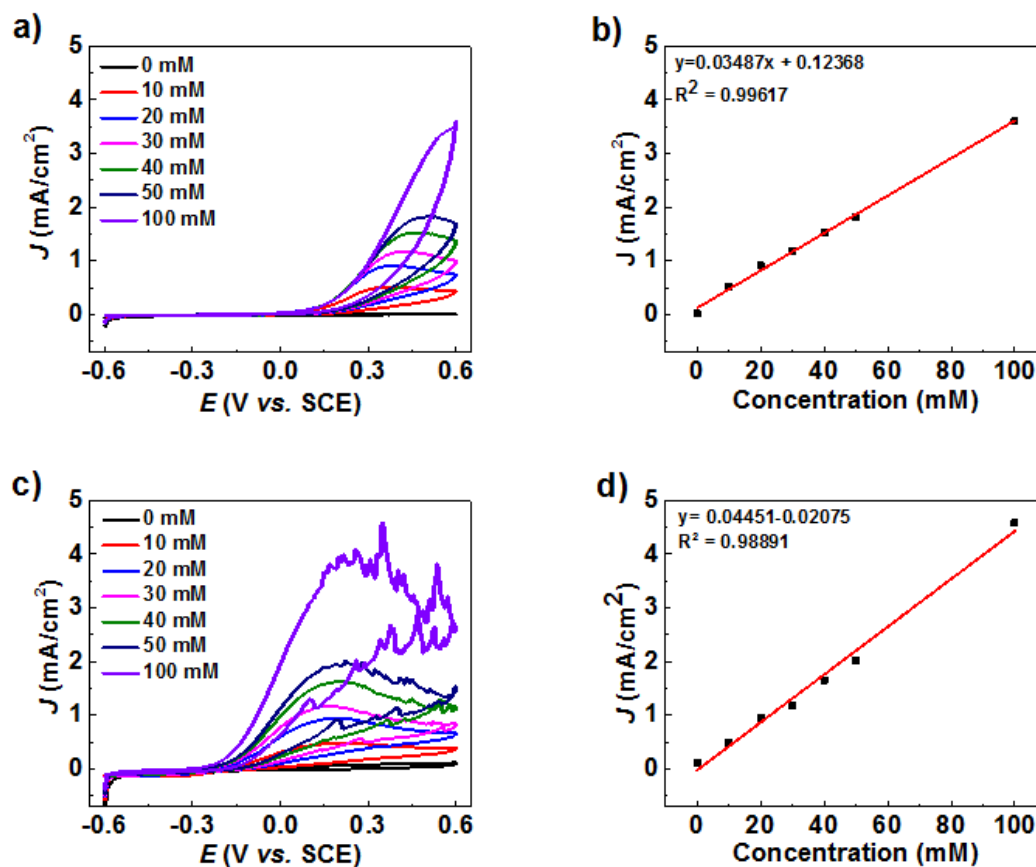


**Figure 5.12.** Cyclic voltammograms (CVs) of various concentrations hydrazine electrochemical oxidation with a scan rate of 10 mV/s at pH 7.4 in 0.1 M PBS over different RDMC-800-*x* materials/electrocatalysts (left panels) and their corresponding peaks current density versus hydrazine concentration graphs (right panels). The CVs are for: (a) RDC-800-0, (c) RDMC-800-0.5, (e) RDMC-800-1, and (g) RDMC-800-2. The corresponding current density versus concentration graphs are shown for: (b) RDC-800-0, (d) RDMC-800-0.5, (f) RDMC-800-1 and (h) RDMC-800-2.

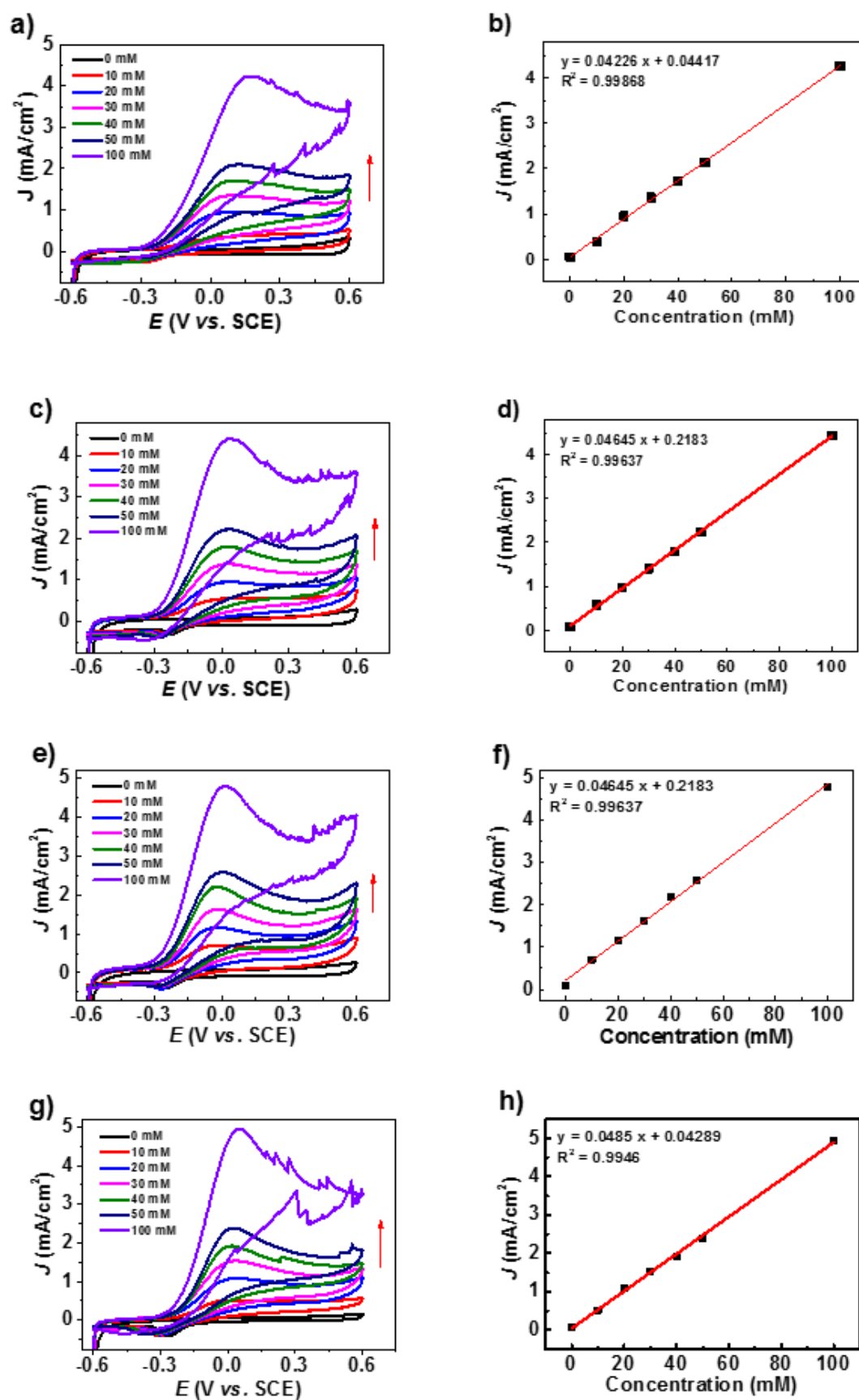




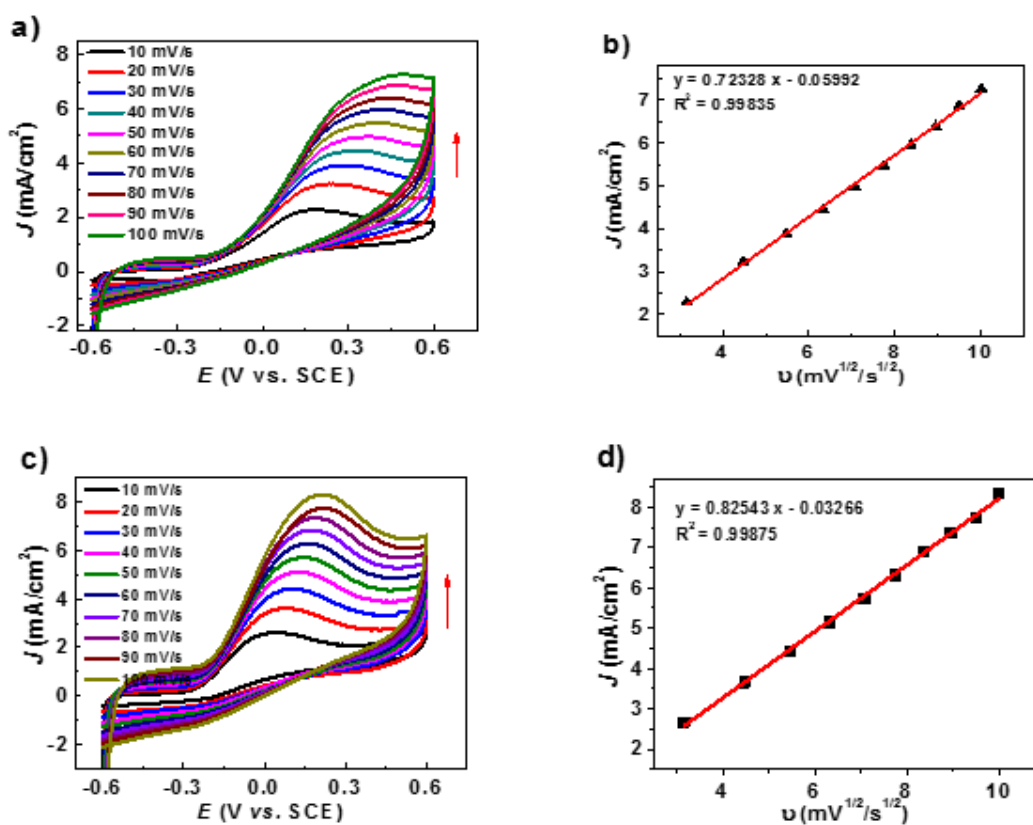
**Figure 5.13.** CVs for electrochemical oxidation of hydrazine (50 mM) at different scan rates, ranging from 10 mV/s to 100 mV/s, at pH at pH 7.4 in 0.1 M PBS over the series of RDMC-800- $x$  materials (left panels) and the corresponding plot for peak current density versus square of scan rate plots (right panels). The CVs include: (a) RDC-800-0, (c) RDMC-800-0.5, (e) RDMC-800-1 and (g) RDMC-800-2. The corresponding plots of current density versus scan rate are for: (b) RDC-800-0, (d) RDMC-800-0.5, (f) RDMC-800-1 and (h) RDMC-800-2.



**Figure 5.14.** (a-d) CVs for electrochemical HOR for various concentrations of hydrazine over two control materials (left panels) and their corresponding peaks current density versus hydrazine concentration graphs (right panels). The results are displayed for sample RDMC-HTC-1 (a,b) and RDMC-800-Py-1 (c,d).



**Figure 5.15.** CVs of HOR obtained for various hydrazine concentrations at a scan rate of 10 mV/s at pH 7.4 in 0.1 M PBS over the series of RDMC-*T*-1 materials (left panels) and their corresponding graph of peak current density versus hydrazine concentration (right panels). The CVs are for: (a) RDMC-600-1, (c) RDMC-700-1, (e) RDMC-800-1, and (g) RDMC-900-1. The corresponding plots of current density versus concentration are shown for: (b) RDMC-600-1, (d) RDMC-700-1, (f) RDMC-800-1, and (h) RDMC-900-1.



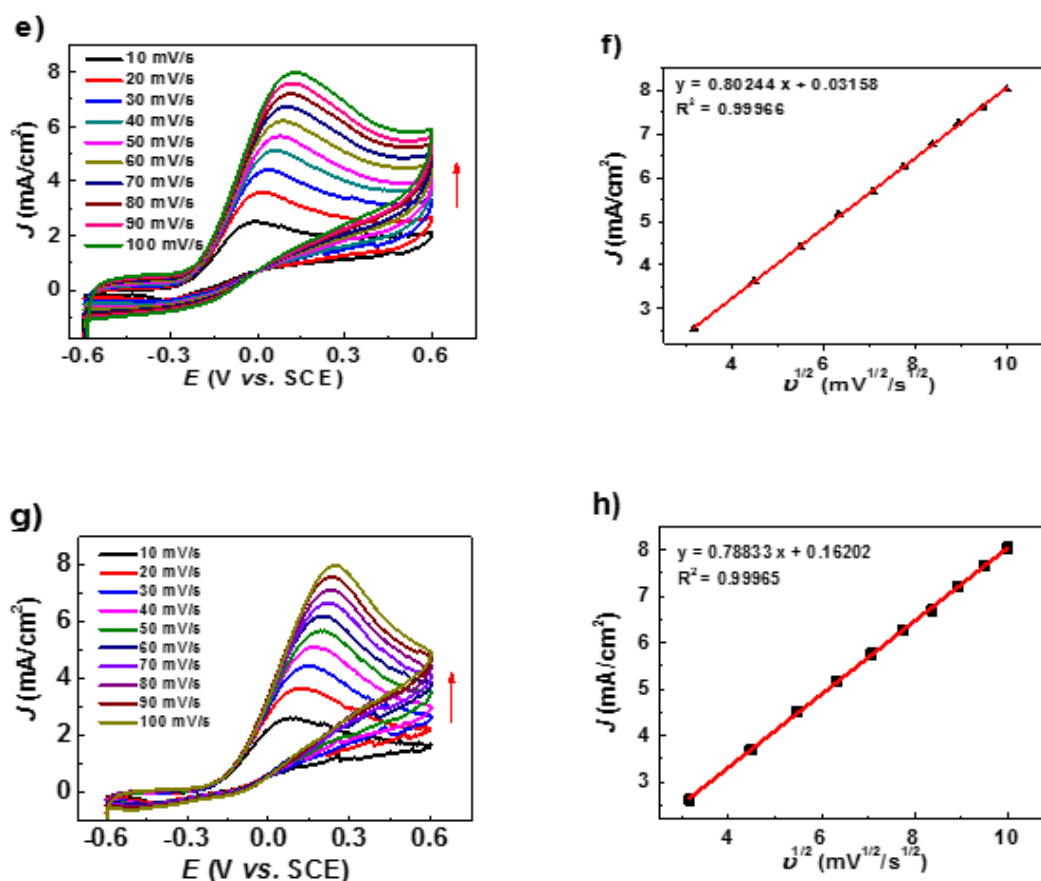


**Figure 5.16.** CVs of HOR for 50 mM hydrazine at different scan rates, ranging from 10 mV/s to 100 mV/s, at pH 7.4 in 0.1 M PBS over the series of RDMC-*T*-1 materials (left panels) and their corresponding peak current density versus square of scan rate plots (right panels). The CVs are for: (a) RDMC-600-1, (c) RDMC-700-1, (e) RDMC-800-1, and (g) RDMC-900-1. The corresponding plots of current density versus scan rate are for: (b) RDMC-600-1, (d) RDMC-700-1, (f) RDMC-800-1, and (h) RDMC-900-1.

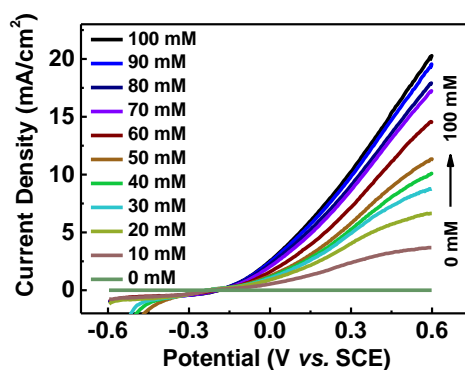


**Figure 5.17.** Polarization curves of hydrazine oxidation reaction (HOR) over RDMC-800-1. The measurement was performed at rotation speed of 900 rpm and at a scan rate 10 mV/s with different hydrazine concentrations in 0.1 M PBS solution.

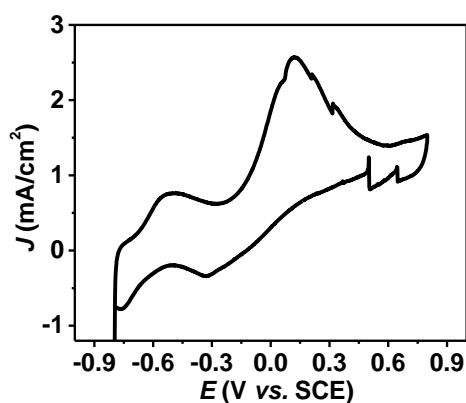


**Figure 5.18.** CVs of HOR obtained for 10 mM of hydrazine at 10 mV/s scan rate at pH 7.4 in 0.1 M PBS over Pt/C (20 wt. %) electrocatalyst.

Next, the effects of surface area and pyrolysis temperature of the materials on the materials' electrocatalytic activities were probed. As can be seen in **Figure 5.19**, the materials synthesized using relatively more colloidal silica templates show better electrocatalytic activity, with more negative onset and/or peak potential and higher peak current density. For example, as the amount of colloidal silica ( $x$ ) is increased from 0

to 0.5 and 1 g, the onset potential of the materials in HOR gets better or shifts to a more negative value (-0.16, -0.33, and -0.34, respectively). However, a further increase in the amount of silica, or concomitantly surface area, does not appear to improve the catalytic activity of the materials any more; for example, when  $x$  is increased from 1 to 2, the onset potential remains almost unchanged while the current density, in fact, slightly decreases (**Figure 5.11** and d and **Figure 5.20**).

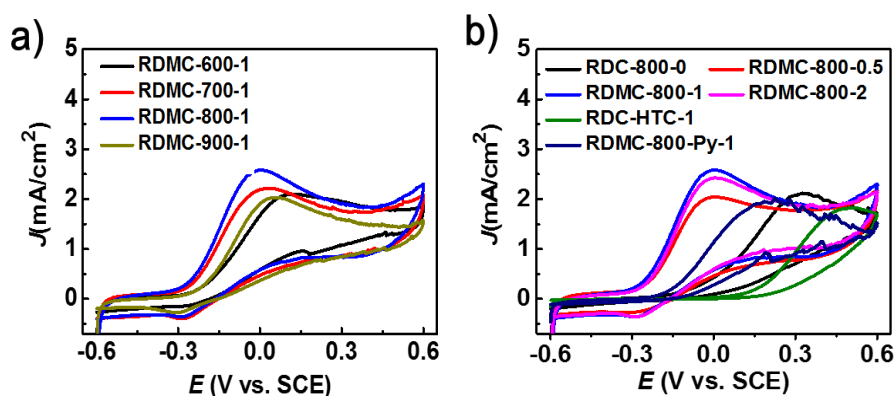


**Figure 5.19.** CVs of 50 mM hydrazine during electrochemical oxidation at pH 7.4 in 0.1 M PBS with scan rate of 10 mV/s over: a) the series of RDMC- $T$ -1 materials and b) the series of RDMC-800- $x$  materials and a corresponding control material.

On the other hand, when the pyrolysis temperature is increased from 600 to 800 °C, the materials' electrocatalytic activity gradually improves (**Figure 5.19**); however, when the pyrolysis temperature is increased from 800 to 900 °C, the materials' electrocatalytic activity decreases. The former may have to do with the increase in the dopant-related defect sites (**Figure 5.7**) and the higher density of certain heteroatom species favorable for the electrocatalytic reaction in the material, such as quaternary N-species (**Figure 5.9**).<sup>7,28</sup> This is also why, I believe, RDMC-800-1 shows the best catalytic activity among the RDMC- $T$ -1 materials I have investigated (**Figure 5.11**). Notably also, the control materials, RDC-HTC-1 and RDMC-800-Py-1, show poor

catalytic activity; this indirectly suggests that both HTC and high temperature pyrolysis are essential to make the highly active catalytic materials obtained here (Figure 5.14).

Next, the stability of the materials during electrocatalysis is evaluated (Figure 5.20). After 500 cycles, the current densities during HOR over RDMC-800-1 remain as much as the initial values (Figure 5.20a), indicating the stability of the material during catalysis. This is confirmed by chronoamperometry or  $i-t$  measurements (Figure 5.20b).

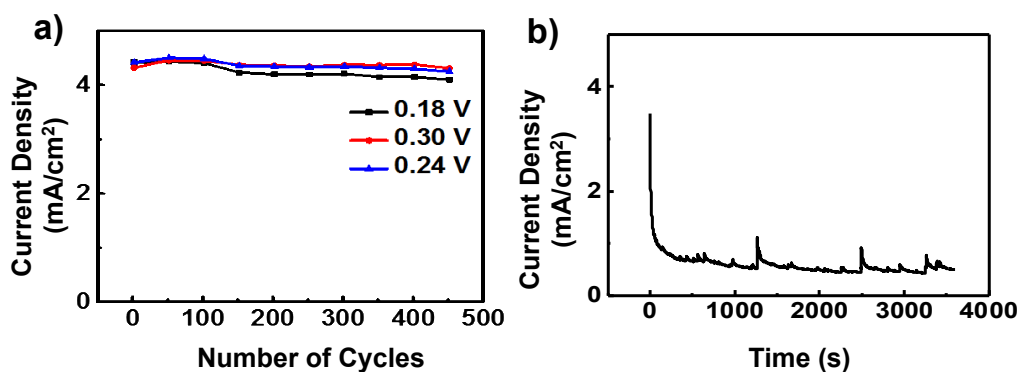


**Figure 5.20.** Stability test of RDMC-800-1 in 50 mM hydrazine, 0.1 M PBS at pH 7.4 during electrocatalysis of HOR over several cycles. a) Peak current density of hydrazine electro-oxidation as function of number of electrocatalytic cycles and b) chronoamperometric curve at working potential of 1 mV (vs. SCE).

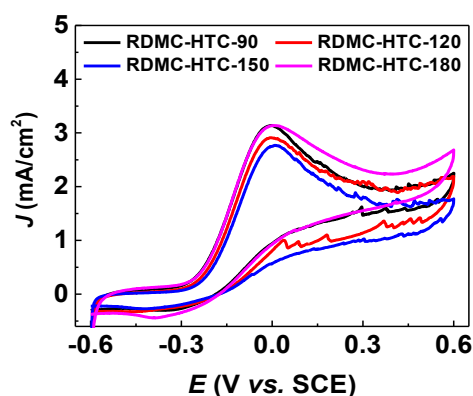


**Figure 5.21.** CVs of 50 mM hydrazine during electrochemical oxidation at pH 7.4 in 0.1 M PBS with scan rate of 10 mV/s over the different RDMC-HTC (control)

materials, synthesized by varying the HTC temperature.

**Table 5.4.** Comparison of the structures and the electrocatalytic activity of RDMC-800-1 for HOR with respect to other notable, recently reported carbon electrocatalysts for the same reaction.

<i>Sample</i>	<i>Onset/Peak Potential (vs. SCE)<sup>a</sup></i>	<i>BET Surface Area (m<sup>2</sup>/g)<sup>b</sup></i>	<i>BJH Average Pore Size (nm)<sup>b</sup></i>	<i>Atomic % of N<sup>c</sup></i>	<i>Ref.</i>
Carbon Nanoneedle	0.15 / 0.7 V	-	-	9	28
PPY-NOMPC-900	-0.36 / -0.06 V	400	3.7	3.29	12
YCWC <sup>d</sup>	-0.38 / 0.04 V <sup>e</sup>	912	2.6	-	30
PCDF-900	-0.3 / 0.1 V	493	4.3	0.4	31
<b>RDMC-800-1</b>	<b>-0.34 / -0.002 V</b>	<b>366</b>	<b>12</b>	<b>0.7</b>	<b>This work</b>

<sup>a</sup> Obtained from CV of 50 mM hydrazine at pH 7.4 in 0.1 M PBS. <sup>b</sup> Obtained from N<sub>2</sub> adsorption/desorption isotherms. <sup>c</sup> Obtained with XPS. <sup>d</sup> YCWC also have Fe species inside, and its excellent electrocatalytic activity of this material is believed to be partly due to the metal species in it. <sup>e</sup> Obtained from CV of 64 mM hydrazine at pH 7.4 in 0.1 M PBS.

**Table 5.5.** Selected recent literature results of electrocatalytic activities of different nanomaterials for HOR compared with our results.

<i>Electrode</i>	<i>Medium</i>	<i>Sweep Rate</i>	<i>Conc. [N<sub>2</sub>H<sub>4</sub>]</i>	<i>Onset / Peak Potential (vs. SCE)</i>	<i>Ref.</i>
Pd/C	0.05 M H <sub>2</sub> SO <sub>4</sub>	20 mV/s	10 mM	-0.05/0.1 V	32
Au/TiO <sub>2</sub> -NTs/Ti	0.1 M pH 7.0 PBS	100 mV/s	0.85 mM	-0.05/0.25 V	33
Au NP/GNP/GCE	0.1 M pH 6.0 PBS	100 mV/s	0.1 mM	-0.15/0.05 V	34
CeO <sub>2</sub> -RGO	3 M KOH	50 mV/s	22 mM	0.1/0.5 V	35
Nanoporous gold	0.1 M pH 8.5 PBS	20 mV/s	10 mM	-0.3/0.0 V	36
TiO <sub>2</sub> -Pt NFs/GCE	0.1 M pH 7.0 PBS	100 mV/s	4 mM	0/0.6 V	37
CM-MWCNT-GCE	0.5 M pH 8.0 PBS	25 mV/s	0.4 mM	0.05/0.2 V	38
Pd/MWCNTs@Pd	0.1 M K <sub>2</sub> SO <sub>4</sub>	50 mV/s	5 mM	0/0.3 V	39

Cu-GP	0.1 M KOH	100 mV/s	10 mM	-0.1/0.3 V	40
Pt/TiO <sub>2</sub> -NTs	0.1 M K <sub>2</sub> SO <sub>4</sub>	50 mV/s.	10 mM	0/0.25 V	41
Au-NPs/PAni/Ti	0.5 M H <sub>2</sub> SO <sub>4</sub>	100 mV/s	2 mM	0.4/0.7 V	42
RDMC-800-1	0.1 M pH 7.0 PBS	10 mV/s	10 mM	-0.34/-0.002 V	This work

---

## 5.5. Conclusion

In conclusion, nitrogen and oxygen co-doped mesoporous carbons have been synthesized from milled rice grains by combining hydrothermal carbonization with high temperature pyrolysis in the presence of colloidal silica templates. The as-obtained RDMCs have been demonstrated to serve as metal-free electrocatalysts for HOR. Their electrocatalytic performances have been found to depend on the synthesis parameters, particularly the pyrolysis temperature and the amount of colloidal silica templates used to make them.

## 5.6. References

- (1) Steele, B. C. H.; Heinzl, A. *Nature*, **2001**, *414*, 345-352.
- (2) Wei, L.; Karahan, H.E.; Zhai, S.; Yuan, Y.; Qiana, Q.; Goh, K.; Ng, A. K.; Chen, Y. *J. Energy Chem.*, **2016**, *25*, 189-191.
- (3) Zhou, W.; Zhou, J.; Zhou, Y.; Lu, J.; Zhou, K.; Yang, L.; Tang, Z.; Li, L.; Chen, S. *Chem. Mater.*, **2015**, *27*, 2026-2032.
- (4) (a) Liang, Y.; Li, Y.; Wang, H.; Zhou, J.; Wang, J.; Regier, T.; Dai, H. *Nat. Mater.*, **2011**, *10*, 780-786. (b) Yu, D.; Wei, L.; Jiang, W.; Wang, H.; Sun, B.; Zhang, Q.; Goh, K.; Sia, R.; Chen, Y. *Nanoscale*, **2013**, *5*, 3457-3464.
- (5) Zou, X.; Huang, X.; Goswami, A.; Silva, R.; Sathe, B.R.; Mikmekov, E.; Asefa, T. *Angew. Chem. Int. Ed.*, **2014**, *126*, 4461-4465.
- (6) Gong, K.; Du, F.; Xia, Z.; Durstock, M.; Dai, L. *Science*, **2009**, *323*, 760-764.
- (7) Silva, R.; Voiry, D.; Chhowalla, M.; Asefa, T. *J. Am. Chem. Soc.*, **2013**, *135*, 7823-7826.
- (8) Sakaushi, K.; Fellingner, T.-P.; Antonietti, M. *ChemSusChem* **2015**, *8*, 1156-1160.
- (9) Lu, X.; Yim, W.-L.; Suryanto, B. H. R.; Zhao, C. *J. Am. Chem. Soc.* **2015**, *137*, 2901-2907.
- (10) Zheng, Y.; Jiao, Y.; Jaroniec, M.; Qiao, S. Z. *Angew. Chem. Int. Ed.*, **2015**, *54*, 52-65.
- (11) Deng, J.; Ren, P.; Deng, D.; Bao, X. *Angew. Chem. Int. Ed.*, **2015**, *54*, 2100-2104.
- (12) Meng, Y.; Zou, X.; Huang, X.; Goswami, A.; Liu, Z.; Asefa, T. *Adv. Mater.*, **2014**, *26*, 6510-6516.
- (13) Yang, D.S.; Bhattacharjya, D.; Inamdar, S.; Park, J.; Yu, J. S. *J. Am. Chem. Soc.*, **2012**, *134*, 16127-16130.
- (14) (a) Wei, L.; Karahan, H. E.; Goh, K.; Jiang, W.; Yu, D.; Birer, Ö.; Jiang, R.; Chen, Y. *J. Mater. Chem. A*, **2015**, *3*, 7210-7214 (b) Wei, L.; Yu, D.; Karahan, H. E.; Birer, Ö.; Goh, K.; Yuan, Y.; Jiang, W.; Liang, W.; Chen, Y. *Catal. Today*, **2015**, *249*, 228-234.
- (15) Girgis, B.S.; Yunis, S.S.; Soliman, A.M. *Mater. Lett.* **2002**, *57*, 164-172.
- (16) Liu, S.; Tian, J.; Wang, L.; Zhang, Y.; Qin, X.; Luo, Y.; Asiri, A.M.; AlYoubi, A.O.; Sun, X. *Adv. Mater.* **2012**, *24*, 2037-2041.
- (17) Zhai, Y.; Zhu, C.; Wang, E.; Dong, S. *Nanoscale* **2014**, *6*, 2964-2970.
- (18) Yu, S.-H.; Cui, X.; Li, L.; Li, K.; Yu, B.; Antonietti, M.; Cölfen, H. *Adv. Mater.* **2004**, *16*, 1636-1640.
- (19) Yang, Y.; Cui, J.; Zheng, M.; Hu, C.; Tan, S.; Xiao, Y.; Yang, Q.; Liu, Y. *Chem. Commun.*, **2012**, *48*, 380-382.
- (20) Wei, L.; Sevilla, M.; Fuertes, A. B.; Mokaya, R.; Yushin, G. *Adv. Energy Mater.* **2011**, *1*, 356-361.
- (21) Liang, C.; Li, Z.; Dai, S. *Angew. Chem. Int. Ed.* **2008**, *47*, 3696-3717.
- (22) Liu, R.; Wu, D.; Feng, X.; Müllen, K. *Angew. Chem. Int. Ed.* **2010**, *122*, 2619-2623.
- (23) Juliano, B.O. *Chemical Aspects of Rice Grain Quality*, 1st Ed. International Rice Research Institute, Philippines, 1979.

- (24) Zheng, Y.; Jiao, Y.; Ge, L.; Jaroniec, M.; Qiao, S.Z. *Angew. Chem. Int. Ed.*, **2013**, *125*, 3192-3198.
- (25) Chen, Y.; Yang, H.; Wang, X.; Zhang, S.; Chen, H. *Bioresource Technol.* **2012**, *107*, 411-418.
- (26) Ishimaru, K.; Hata, T.; Bronsveld, P.; Meier, D.; Mamura, Y. *J. Mater. Sci.*, **2007**, *42*, 122-129.
- (27) Qian, W.; Hao, R.; Hou, Y.; Tian, Y.; Shen, C.; Gao, H.; Liang, X. *Nano. Res.*, **2009**, *2*, 706-712.
- (28) Silva, R.; Al-Sharab, J.; Asefa, T. *Angew. Chem. Int. Ed.*, **2012**, *51*, 7171-7175.
- (29) Matter, P.H.; Zhang, L.; Ozkan, U.S. *J. Catal.*, **2006**, *239*, 83-96.
- (30) Huang, X.; Zou, X.; Meng, Y.; Mikmeková, E.; Chen, H.; Voiry, D.; Goswami, A.; Chhowalla, M.; Asefa, T. *ACS Appl. Mater. Interfaces*, **2015**, *7*, 1978-1986.
- (31) Martins, C.; Huang, X.; Goswami, A.; Koh, K.; Meng, Y.; Almeida, V. C.; Asefa, T. *Carbon* **2016**, *102*, 97-105.
- (32) Liang, Y.; Zhou, Y.; Ma, J.; Zhao, J.; Chen, Y.; Tang, Y.; Lu, T. *Appl. Catal. B* **2011**, *103*, 388-396.
- (33) Hosseini, M.; Momeni, M.M.; Faraji, M. *J. Mol. Catal. A: Chem.* **2011**, *335*, 199-204.
- (34) Wana, Q.; Liua, Y.; Wang, Z.; Wei, W.; Li, B.; Zou, J.; Yang, N. *Electrochem. Commun.* **2013**, *29*, 29-32.
- (35) Srivastava, M.; Dasa, A.K.; Khanraa, P.; Uddina, M.E.; Kim, N.H.; Lee, J.H. *J. Mater. Chem. A* **2013**, *1*, 9792-9801.
- (36) Yan, X.; Meng, F.; Cui, S.; Liu, J.; Gu, J.; Zou, Z. *J. Electroanal. Chem.* **2011**, *661*, 44-48.
- (37) Ding, Y.; Wang, Y.; Zhang, L.; Zhang, H.; Li, C. M.; Lei, Y. *Nanoscale* **2011**, *3*, 1149-1157.
- (38) Zheng, L.; Song, J.-F. *Sens. Actuat. B: Chem.* **2009**, *135*, 650-655.
- (39) Ye, W.; Hu, H.; Zhang, H.; Zhou, F.; Liu, W. *Appl. Surf. Sci.* **2010**, *256*, 6723-6728.
- (40) Gao, H.; Wang, Y.; Xiao, F.; Ching, C. B.; Duan, H. *J. Phys. Chem. C* **2012**, *116*, 7719-7727.
- (41) Dong, B.; He, B.-L.; Chai, Y.-M.; Liu, C.-G. *Mater. Chem. Phys.* **2010**, *120*, 404-408.
- (42) Hosseini, M.G.; Momen, M.M.; Zeynali, S. *Surf. Eng.* **2013**, *29*, 65-69.

## Chapter 6.

### Summary and Future Prospect

My PhD research projects involve the design and synthesis of *i*) heterogeneous palladium nanocatalysts using amine grafted mesoporous SBA-15 silica, *ii*) nitrogen doped mesoporous carbon from polyaniline, which is nitrogen rich polymer, *iii*) N and O doped mesoporous carbon from biomass rice grain. Due to their unique properties, excellent catalytic activities have been shown toward each fuel cell applications such as formic acid dehydrogenation, formate/bicarbonate hydro-/dehydrogenation, and hydrazine oxidation. One of the most important part of catalysts, which resulted in excellent catalyst activity, is to obtain strong *metal molecular support interaction* (SMMSI) and this interaction strongly effects on metal catalysts' excellent activity than other supports. I also investigated how the modified supports (amine functionalized SBA-15 or N doped carbon) affect to Pd nanocatalysts through several instruments including TEM, XPS, XANES, NEAXFS etc.

In formic acid dehydrogenation reaction, amine plays important role than non-ligand material because: 1) amine group stabilizes palladium nanoparticles, 2) it acts as additional co-catalytic active i.e., first deprotonating part of dehydrogenation step ( $\text{HCOOH} + \text{NH}_2 \rightarrow \text{NH}_3^+ + \text{HCOO}^-$ ) and 3) it donates electron to Pd NPs, and perturbed Pd NPs to increase the catalytic activities. However, all amine groups not play important role. I investigated three different amine functional groups on SBA-15

mesoporous silica to see several effects on Pd NPs including *i*) electronic effect, *ii*) size of Pd NPs, *iii*) steric effect, and *iv*) hydrophobicity/ hydrophilicity of tethered amine functional groups. I concluded the amines' effects on Pd NPs are not even electronic effects but also steric effects play important role during rotation of the formate species part (2<sup>nd</sup> step of formic acid dehydrogenation), so steric tertiary amine gives lowest activity toward formic acid dehydrogenation.

Several research has been focusing on Lewis basic sites to enhance Pd catalysts' activity through electron donation to Pd NPs, however, what active site and catalytic mechanism in enhancement of Pd NPs for formic acid dehydrogenation are still underdeveloped. In this context, my Pd/SBA-15-Amine studies with different amine functional group works will help to give some insight for understanding catalytic mechanisms but more research are still needed for this. Moreover, one of biggest challenge for formic acid is still remain. Most of heterogeneous catalysts are based on the novel metals especially Au, Pt, Pd and Pd based catalysts so it should be changed to non-novel metals or metal free catalyst to be commercialized. Although this is difficult to do, developing less expensive catalysts will help to go one step further toward the commercialized formic acid based fuel cell.

The formate/bicarbonate reversible reaction has advantage of easiness of reversible reactions compared to formic acid one, however, it still needs some temperature and pressure e.g., 80 °C for formate dehydrogenation and 80 °C with 40 bar in the case of bicarbonate hydrogenation. I envision this bicarbonate hydrogenation can lower the reaction temperature and pressure with some additives or other modified catalysts. In formate/bicarbonate reversible cycle, I developed polyaniline derived

mesoporous carbon, which is N-rich carbon and investigated the difference of structural upon pyrolysis temperatures. The pyrolysis temperature of 800 °C showed the best catalytic activity for both reactions and this is because nitrogen is more closely attached and affected to Pd NPs thereby increase the catalytic activities. In here, direct mechanism isn't figured out but I proposed plausible mechanisms for formate/bicarbonate cycle: pyridinic/pyrrolic N species donating electron to Pd NPs and based upon strong metal-support interaction with small size of particles, it accelerates the reaction. I believe this investigation is important contribution to formate/bicarbonate reversible cycle and look forward to apply this Pd/PDMC material to other applications such as electrocatalysts or other hydrogenation reactions.

In hydrazine oxidation reaction, I synthesized the catalysts from the biomass materials and tried different synthetic methods. Through investigation with modified synthetic parameters, combination of hydrothermal and pyrolysis under Ar gas showed the best physical and chemical structure of materials for giving high catalytic activity. This demonstration can potentially provide better catalysts for next future biomass derived carbon. Moreover, I believe, in future work, besides this combination of hydrothermal and pyrolysis synthetic methods, and post-modification of material can be applied for another biomass materials and enhance their catalytic activities.

In summary, design and synthesis of sustainable heterogeneous catalysts are demonstrated in this thesis. Nitrogen functional group helped to be excellent multifunctional catalysts in terms of selectivity and catalytic activity for formic acid dehydrogenation without any additives at room temperature. Moreover, nitrogen doped carbon also tailoring the catalytic activity toward formate/bicarbonate reversible cycle.

In those works, strong metal support interaction plays important role and this interaction can broadly apply to other application too.

## Appendices



RightsLink®

Home

Create Account

Help



RSC Publishing

**Title:** Ultrasmall palladium nanoparticles supported on amine-functionalized SBA-15 efficiently catalyze hydrogen evolution from formic acid

**Author:** K. Koh, J.-E. Seo, J. H. Lee, A. Goswami, C. W. Yoon, T. Asefa

**Publication:** Journal of Materials Chemistry A

**Publisher:** Royal Society of Chemistry

**Date:** Oct 15, 2014

Copyright © 2014, Royal Society of Chemistry

LOGIN

If you're a copyright.com user, you can login to RightsLink using your copyright.com credentials. Already a RightsLink user or want to [learn more?](#)

This reuse request is not allowed. If you need further assistance, please contact Royal Society of Chemistry at [contracts-copyright@rsc.org](mailto:contracts-copyright@rsc.org).

BACK

CLOSE WINDOW

Copyright © 2017 Copyright Clearance Center, Inc. All Rights Reserved. [Privacy statement](#). [Terms and Conditions](#). Comments? We would like to hear from you. E-mail us at [customercare@copyright.com](mailto:customercare@copyright.com)



RightsLink®

[Home](#)[Create Account](#)[Help](#)RSCPublishing **Title:**

Formic Acid Dehydrogenation  
over Pd NPs Supported on  
Amine-Functionalized SBA-15  
Catalysts: Structure-Activity  
Relationships

**Author:** Tewodros Asefa, Katherine  
Koh, Mina Jeon, Chang Won Yoon

**Publication:** Journal of Materials Chemistry A

**Publisher:** Royal Society of Chemistry

**Date:** Apr 12, 2017

Copyright © 2017, Royal Society of Chemistry

[LOGIN](#)

If you're a [copyright.com user](#), you can login to RightsLink using your copyright.com credentials. Already a [RightsLink user](#) or want to [learn more?](#)

This reuse request is not allowed. If you need further assistance, please contact Royal Society of Chemistry at [contracts-copyright@rsc.org](mailto:contracts-copyright@rsc.org).

[BACK](#)[CLOSE WINDOW](#)

Copyright © 2017 [Copyright Clearance Center, Inc.](#) All Rights Reserved. [Privacy statement](#). [Terms and Conditions](#).  
Comments? We would like to hear from you. E-mail us at [customercare@copyright.com](mailto:customercare@copyright.com)



RightsLink®

Home

Account  
Info

Help



**Title:** Novel nanoporous N-doped carbon-supported ultrasmall Pd nanoparticles: Efficient catalysts for hydrogen storage and release

**Author:** Katherine Koh, Mina Jeon, Daniel M. Chevrier, Peng Zhang, Chang Won Yoon, Tewodros Asefa

**Publication:** Applied Catalysis B: Environmental

**Publisher:** Elsevier

**Date:** April 2017

© 2016 Elsevier B.V. All rights reserved.

Logged in as:  
Katherine Koh

LOGOUT

### Order Completed

Thank you for your order.

This Agreement between Katherine Koh ("You") and Elsevier ("Elsevier") consists of your license details and the terms and conditions provided by Elsevier and Copyright Clearance Center.

Your confirmation email will contain your order number for future reference.

#### [Printable details.](#)

License Number	4085440921213
License date	Apr 10, 2017
Licensed Content Publisher	Elsevier
Licensed Content Publication	Applied Catalysis B: Environmental
Licensed Content Title	Novel nanoporous N-doped carbon-supported ultrasmall Pd nanoparticles: Efficient catalysts for hydrogen storage and release
Licensed Content Author	Katherine Koh, Mina Jeon, Daniel M. Chevrier, Peng Zhang, Chang Won Yoon, Tewodros Asefa
Licensed Content Date	April 2017
Licensed Content Volume	203
Licensed Content Issue	n/a
Licensed Content Pages	9
Type of Use	reuse in a thesis/dissertation
Portion	full article
Format	both print and electronic
Are you the author of this Elsevier article?	Yes
Will you be translating?	No
Order reference number	
Title of your thesis/dissertation	DESIGN AND SYNTHESIS OF NANOCATALYSTS FOR HYDROGEN STORAGE AND ELECTROCATALYSIS
Expected completion date	Oct 2017
Estimated size (number of pages)	162
Elsevier VAT number	GB 494 6272 12
Requestor Location	Katherine Koh 610 Taylor Rd  PISCATAWAY, NJ 08854 United States Attn: Katherine Koh
Publisher Tax ID	98-0397604
Total	0.00 USD

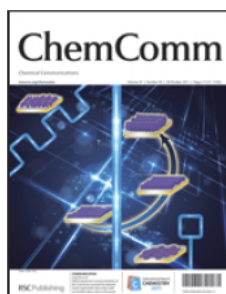
[ORDER MORE](#)

[CLOSE WINDOW](#)

Copyright © 2017 [Copyright Clearance Center, Inc.](#) All Rights Reserved. [Privacy statement.](#) [Terms and Conditions.](#)



RightsLink®

[Home](#)[Account Info](#)[Help](#)

**Title:** N- and O-doped mesoporous carbons derived from rice grains: efficient metal-free electrocatalysts for hydrazine oxidation

**Author:** Katherine Koh, Yuying Meng, Xiaoxi Huang, Xiaoxin Zou, Manish Chhowalla, Tewodros Asefa

**Publication:** Chemical Communications (Cambridge)

**Publisher:** Royal Society of Chemistry

**Date:** Oct 17, 2016

Copyright © 2016, Royal Society of Chemistry

Logged in as:  
Katherine Koh

[LOGOUT](#)

This reuse request is not allowed. If you need further assistance, please contact Royal Society of Chemistry at [contracts-copyright@rsc.org](mailto:contracts-copyright@rsc.org).

[BACK](#)[CLOSE WINDOW](#)

Copyright © 2017 Copyright Clearance Center, Inc. All Rights Reserved. [Privacy statement](#). [Terms and Conditions](#).  
Comments? We would like to hear from you. E-mail us at [customercare@copyright.com](mailto:customercare@copyright.com)